TÉCNICO LISBOA

UNIVERSIDADE DE LISBOA

INSTITUTO SUPERIOR TÉCNICO

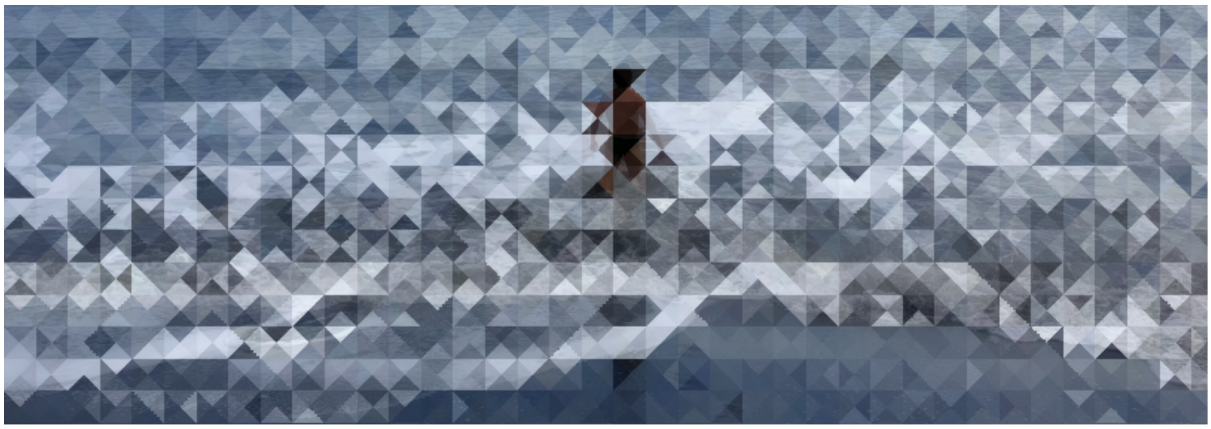

Changes in Hydrological Extremes: Advances in Climate-Induced Extremes Focusing on a Small North Atlantic Island

Luis Angel Espinosa Villalpando

Supervisor: Doctor Maria Manuela Portela Correia dos Santos Ramos da Silva

Co-supervisor: Doctor Rui José Raposo Rodrigues

Thesis approved in public session to obtain the PhD Degree in Civil Engineering

Jury final classification: Pass with Distinction and Honour

2021

TÉCNICO LISBOA

UNIVERSIDADE DE LISBOA
INSTITUTO SUPERIOR TÉCNICO

Changes in Hydrological Extremes: Advances in Climate-Induced Extremes Focusing on a Small North Atlantic Island

Luis Angel Espinosa Villalpando

Supervisor: Doctor Maria Manuela Portela Correia dos Santos Ramos da Silva
Co-supervisor: Doctor Rui José Raposo Rodrigues

Thesis approved in public session to obtain the PhD Degree in Civil Engineering

Jury final classification: Pass with Distinction and Honour

Jury

Chairperson: Doctor António Heleno Cardoso, Instituto Superior Técnico, Universidade de Lisboa

Members of the Committee:

Doctor João Luis Mendes Pedroso de Lima, Faculdade de Ciências e Tecnologia, Universidade de Coimbra
Doctor António Alberto do Nascimento Pinheiro, Instituto Superior Técnico, Universidade de Lisboa
Doctor Maria Manuela Portela Correia dos Santos Ramos da Silva, Instituto Superior Técnico, Universidade de Lisboa
Doctor Rodrigo Jorge Fonseca de Oliveira Maia, Faculdade de Engenharia, Universidade do Porto
Doctor Eduardo Manuel Vieira de Brito de Azevedo, Faculdade de Ciências Agrárias e do Ambiente, Universidade dos Açores
Doctor Rodrigo de Almada Cardoso Proença de Oliveira, Instituto Superior Técnico, Universidade de Lisboa

Funding Institutions

Fundação para a Ciência e a Tecnologia (FCT), The Portuguese Foundation, for Science and Technology, grant No. PD/BD/128509/2017.

2021

Abstract

Recent climate model projections have pointed up increased frequency, magnitude, and intensity of some of the extreme hydrological events, such as droughts and floods, for many regions of the world. Most of those issues were addressed in this thesis by adopting theoretical and conceptual approaches, focusing on a small island of the North Atlantic, i.e., on Madeira Island. The criteria for selecting Madeira Island as case study was its fragility to extreme hydrological events, the lack of knowledge regarding the behaviour of those events and their drivers, aggravated by the scarcity of hydrological data to support the studies on the previous issues. These constraints — commonly present in small island environments — made the research even more challenging from the beginning, reinforcing its relevance. The studies in this work included, but were not limited to, novel approaches of filling daily rainfall data gaps, trend analysis and change point detection, climate regionalisation, regional drought analysis, multivariate modelling of heavy rainfall, and links related to teleconnection patterns (indices) — particularly the North Atlantic Oscillation (NAO) index. The data used in the studies referred to teleconnection indices and, resulting from the implemented innovative gap-filling procedure, to 80 years of daily rainfall, from 1937/1938 to 2016/2017, at 41 rain gauges in the island. Based on regionalisation analysis three homogeneous regions with different temporal climatic variability were identified and used in some of the studies: the northern slope, the southern slope, and the central region. Special attention was given to the latter region due to its relevance for the island's water security, since it is the main region for the replenishment of the groundwater reservoirs.

Furthermore, to achieve the objectives set in this thesis, commonly used techniques such as the Mann-Kendall test and Sen's slope estimator for trend detection, the Standardized Precipitation index (SPI) for drought characterisation, and the principal component analysis for climatic regionalisation, were adjusted for the characteristics of Madeira. Additionally, novel approaches were proposed, for instance, the Multivariate Imputation by Chained Equations (MICE) applied for the first time for gap-filling of daily rainfall series, and the multivariate modelling with copulas for characterisation of hydrological extremes and for teleconnection. Results show that in the northern slope and central region there is an increase in the magnitude and frequency of drought and heavy rainfall as the likely consequence of changes in large-scale atmospheric patterns. Overall, this research provides mounting evidence that in Madeira Island: (i) seasonal rainfall (e.g. winter and annual rainfall) has shown a gradual, yet marked, decrease since the end of 1960's with the uncertainty regarding to whether rainfall will continue to decrease or it will counterbalance the already experienced rainfall deficits; (ii) the variability of seasonal and annual rainfall is highly correlated with the large-scale atmospheric circulation pattern of NAO; (iii) droughts in the island have become worse and more frequent than in the past; and that (iv) heavy rainfall is clearly intensified by the persistent changes in the NAO, mainly during its negative phases. These findings highlight the importance of the detection, and characterisation of changes in hydrological extremes, as well as the multivariate modelling for teleconnections to extreme rainfall in North Atlantic regions, especially in small islands which are highly vulnerable to the effects of climate change and abrupt climate variability.

Keywords:

Hydrological extremes; North Atlantic Oscillation; teleconnection; rainfall trends; Madeira Island.

Resumo

Recentes projeções de modelos climáticos apontam o agravamento em várias regiões da frequência, magnitude e intensidade de alguns dos eventos hidrológicos extremos, como secas e cheias. A maior parte desses aspetos foi analisada nesta tese mediante a adoção de abordagens teóricas e conceituais, embora restringidas ao contexto de uma pequena ilha do Atlântico Norte, a Ilha da Madeira. A seleção da Ilha da Madeira como estudo de caso decorreu do reconhecimento da sua fragilidade a eventos hidrológicos extremos, associada a um relativo desconhecimento sobre o comportamento desses eventos e dos mecanismos a que podem ser associados, fatores estes agravados pela escassez de dados hidrológicos que suportem os estudos daqueles eventos. Tais restrições — aliás, bastante vulgares em pequenos ambientes insulares — tornaram a pesquisa mais desafiadora desde o início, reforçando, assim, a sua relevância. Os estudos incluíram, embora sem caráter limitativo, novas abordagens de preenchimento de lacunas em séries diárias de precipitação, a análise de tendência e a deteção de pontos de quebra em séries temporais, a regionalização climática, a análise regional de secas, a modelação multivariada de precipitações intensas e sua relação com padrões de teleconexão (índices) — em particular, o índice de Oscilação do Atlântico Norte (NAO). Os dados utilizados incluíram índices de teleconexão e, em resultado da implementação de um procedimento inovador de preenchimento de lacunas da precipitação, 80 anos de precipitação diária, de 1937/1938 a 2016/2017, em 41 postos udométricos da Ilha. A análise da regionalização permitiu identificar três regiões homogéneas, caraterizadas por diferente variabilidade temporal climática, zonas essas sobre as quais incidiram algumas das análises efetuadas: a encosta norte, a encosta sul e a região central da Ilha. Importa realçar a relevância desta última região para a segurança hídrica da ilha, uma vez que é aí que principalmente se processa a recarga dos aquíferos.

Para atingir os objetivos definidos para a investigação, técnicas comumente utilizadas, como sejam, o teste de Mann-Kendall e o estimador de declive de Sen para reconhecimento e caraterização de tendências, o índice de precipitação estandardizada (SPI) para a caraterização das secas, ou ainda as técnicas de regionalização baseadas em análise de componentes principais, foram ajustadas às características da Ilha. Adicionalmente foram propostas novas abordagens, como seja o preenchimento de falhas diárias de registos de precipitação com base no algoritmo MICE (*Multivariate Imputation by Chained Equations*), nunca antes aplicado a séries temporais de variáveis hidrológicas àquele nível temporal, e a modelação multivariada com recurso a cópulas para caracterizar os eventos extremos de precipitação e sua dependência de padrões de teleconexão. Os resultados mostram que a magnitude e a frequência das secas e das precipitações intensas têm vindo a aumentar na encosta norte e na região central da Ilha da Madeira, provavelmente em consequência de mudanças nos padrões atmosféricos de grande escala. No geral, esta pesquisa fornece evidências crescentes de que na Ilha da Madeira: (i) algumas das precipitações sazonais, como sejam durante o inverno, mas também a nível anual, têm vindo a diminuir gradualmente, tendência essa que se acentuou desde o final da década de 1960, embora não seja possível concluir se tal tendência se manterá ou se se inverterá, neste caso, eventualmente contrabalançando a diminuição antes registada; (ii) a variabilidade da precipitação sazonal e anual está altamente correlacionada com o padrão de circulação atmosférica de grande escala da NAO; (iii) as secas na Ilha agravaram-se e tornaram-se mais frequentes; e que (iv) as precipitações intensas são claramente acentuadas por mudanças persistentes na NAO, principalmente durante as fases negativas do fenómeno. Tais conclusões destacam a importância da deteção e caracterização de tendências em extremos hidrológicos, bem como da modelação multivariada entre teleconexões e precipitações intensas em regiões do Atlântico Norte, especialmente em pequenas ilhas dada a sua maior vulnerabilidade aos efeitos das mudanças climáticas e à própria variabilidade climática.

Palavras-chave:

Extremos hidrológicos; Oscilação do Atlântico Norte; teleconexão; tendências de precipitação; Ilha da Madeira.

A mis padres María del Rosario y Mario Fernando, a quienes amo profundamente, les dedico esta tesis de doctorado por haberme brindado su comprensión y apoyo incondicional durante toda mi carrera permitiéndome hacer lo que más me gusta, por sus consejos que me orientaron a tomar las mejores decisiones y por creer en mí...

Acknowledgments

Throughout the writing of this doctoral thesis I have received a great deal of professional assistance and personal support.

I would first like to thank my supervisor at Instituto Superior Técnico (IST), Professor Maria Manuela Portela, whose expertise in statistical analysis of hydrologic variables was invaluable in formulating the research questions and methodology. Your insightful and continuos feedback pushed me to sharpen my thinking and brought my work to a higher level. You provided me with the tools that I needed to choose the right direction and successfully complete my thesis.

I would like to acknowledge my colleagues from IST and Laboratório Nacional de Engenharia Civil (LNEC) for their wonderful collaboration — Aldo, Alexandre, Ana Clara, Joana, João, Marta, Rui, and Soraia. I would particularly like to single out my supervisor at LNEC, Doctor Rui Raposo Rodrigues, I want to thank you for your support and help throughout my studies to materialise my idea about climate studies in small islands, and for all of the opportunities I was given to further my research.

I gratefully acknowledge the funding received towards my PhD from the International Doctoral Programme H2Doc - Environmental Hydraulics and Hydrology supported by the Fundação para a Ciência ea Tecnologia (FCT). Thanks to Dulce Fernandes for her amazing work ensuring the smooth and effective functioning of the bureaucracy processes before and during my studies.

I appreciate the support received through the collaborative work undertaken with the Hydraulic and Environmental Engineering Department of the Federal University of Ceará (Brazil), and the Department of Environmental Engineering of Technical University of Kosice (Slovakia). Special thanks to João Dehon and Martina Zelenakova for making possible such an amazing collaboration reflected in the publication of three scientific papers.

My thesis would not have been possible without data. Therefore, I am also very grateful to all those at the Instituto Português do Mar e da Atmosfera (IPMA) office, especially to Doctor Victor Prior and others who were always so helpful and provided me with their assistance throughout the time-consuming data collection process.

In addition, I would like to thank my parents for their wise counsel and sympathetic ear, and to my siblings Aldo and Marifer for being there for me all the time. Thanks to Achim Ströhle for always believing in me and encouraging me to follow my dreams. Finally, I could not have completed this dissertation without the support of Doctor Armando Graziano and João Carlos Teixeira (...), who provided stimulating discussions based on their own professional experiences as well as happy distractions to rest my mind outside of my research.

Contents

THIS PAGE INTENTIONALLY LEFT BLANK

List of Figures

List of Tables

Acronyms and Symbols

ACF Autocorrelation Function

AIC Akaike Information Criterion

ANNs Artificial Neural Networks

AR5 Fifth Assessment Report

ATP areal-influence

AZ Azores — Ponta Delgada

CCF Cross-correlation Function

CDF cumulative distribution functions

Csa temperate with hot and dry summer

Csb temperate with dry and warm summers

Csc temperate with dry and cool summers

DJF December to February

ENSO El Niño Southern Oscillation

ETCCDMI Expert Team on Climate Change Detection, Monitoring and Indices

EW east–to-west

FLAD *Fundação Luso-Americana para o Desenvolvimento*

GCMs Global Climate Models

GEFS/R Global Ensemble Forecasting System Reforecast2

GSa greenhouse gases

GTS global surface temperature

HadCM3 Hadley Centre Coupled Model Ver. 3

HDY year time-span

IDW Inverse Distance Weighting

IFM Inference Functions from Margins

IPCC Intergovernmental Panel on Climate Change

IPMA Portuguese Institute for Sea and Atmosphere

IQR interquartile range

KORE kernel occurrence rate estimator

LOWESS Locally Weighted Scatterplot Smoothing

MA moving average

MAE mean absolute error

MAR Missing At Random

MCMC Markov Chain Monte Carlo

MD Madeira Island

MI Multiple Imputation

MICE Multivariate Imputation by Chained Equations

MK Mann-Kendall

MLE Maximum Likelihood Estimation

NA not available

NAO North Atlantic Oscillation

NAOI North Atlantic Oscillation index

NCAR National Center for Atmospheric Research

NDJ November to January

NRI National Rainfall index

NRMSE normalised root mean squared error

PC principal component

PCA principal components analysis

PDSI Palmer Drought Severity index

PFA principal factors analysis

PMM predictive mean matching

POT peaks over threshold

RAM Autonomous Region of Madeira

RK Iceland — Reykjavik

RPC rotated principal component

SIDS Small Island Developing States

SLP sea-level pressure

SNIRH *Sistema Nacional de Informação de Recursos Hídricos*

SOI Southern Oscillation index

SPEI Standardized Precipitation Evapotranspiration index

SPI Standardized Precipitation index

SQMK Sequential Mann-Kendall

TDC tail-dependence coefficient

Latin lower case

a_m, chosen percentile rank

f, LOWESS span factor

l, lag between the smoothed series and the occurrence of an extreme rainfall event

m, imputed plausible completed data sets, running length

n, length of smoothed series, number of rows, number random correlated variables

ni, opposite previous NAOI value

p-value, probability of the occurrence of a given event

r, Pearson correlation coefficient

r_i, ranked value

rn, extreme rainfall value

s', standard deviation

t_i, statistic of SMQK

u, drought threshold

$u(t_i)$, progressive-trend series

$u'(t_j)$, retrograde-trend series

$\mathbf{v}$, eigenvectors

w_1, first variable with missing values

w_2, second variable with missing values

w_j, multidimensional value referred to as factor score coefficient

Latin upper case

A and B, Borel sets

$\mathbf{C}$, associated dependence function copula

$\mathrm{C}(u_1, u_2, ..., u_n)$, copula function

$\mathbf{C}(u, v)$, bivariate copula

Dd, drought duration

Dm, drought magnitude

Dmi, drought maximum intensity

E, expected value

$E(L)$, expected interarrival time

F, factor

F, distribution function

$F_{Dd}(d)$ or $F_{Dm}(m)$, drought characteristics marginal distributions

F_X and F_Y, marginals

F_{XY}, joint distribution

H_0, null hypothesis

H_A, alternative hypothesis

L, interarrival time

M, running length

NI, opposite previous NAOI series

$\bar{P}$, mean monthly rainfall

Par, copula parameter

Par1 and Par2, marginal distribution parameters

Q, estimate of the slope

Q_i, slope of paired data

RN, extreme rainfall series

S, test statistic

$\mathrm{T}_{Dd\,\&\,Dm}$, joint return period of drought characteristics

T_{Dd}, return period of drought duration

$\mathrm{T}_{Dm|Dd\geq d}$, return period of drought magnitude given drought duration exceeding a certain threshold

T_{Dm}, return period of drought magnitude

$\mathrm{T}_{NI\,\&\,RN}$, joint return period of the previous NAOI and extreme rainfall events

$\mathrm{T}_{NI\,\&\,RN}$, the return period for $NI \geq ni$ and $RN \geq rn$

$\mathrm{T}_{RN|NI\geq ni}$, conditional return period for extreme rainfall given NAOI

U and V, non-exceedance probabilities

Var, variance

$\boldsymbol{X}$, matrix array

$\mathbf{X}_{29200\times 41}$, matrix of the daily rainfalls

X_i, variable in year i

X_h and X_0, one-dimensional strictly stationary series

X_t, NAOI series

Y_t, rainfall series

Z, standard normal deviate

Greek symbols

α, significance level

δ, consecutive month

$\lambda(t)$, annual frequency of the periods under drought conditions, eigenvalues

$\sum$, summation

τ, Kendall tau

φ, copula generator function

Chapter 1

Introduction

Hydrological extremes have been the primary drivers of many natural disasters, leading to large economic losses and damage to infrastructures, and might further bring unprecedented threats to human societies due to the expected increase in their magnitude and frequency [344, 89] under a changing climate. In fact, the climate-induced changes have increased over many regions of the world during the past decades, and this trend seems likely to continue in the future [145, 428]. Therefore, there is a growing need to improve the understanding about changes in hydrological extremes and their related impacts for current and future risks management and strategic adaptation related to water resources. To achieve these goals, for instance, hydrologists have been improving physically-based models for comprehensive assessment of the impacts of hydrological extremes. The assessment should be done from global to regional and local setups, also ascertaining different time scales. However, identifying, modelling and understanding the changes in hydrological extremes under the current climate conditions still constitute a scientific and technological challenge since they vary spatially and temporally in nature.

In recent years, the rapid development of technology has made available more conventional ground-based data (e.g., hydroclimatic observations) and non-conventional data (e.g., paleo-data proxies or new satellite-based data) — related to large-scale physical factors and to fresh surface water occurrence [42, 150, 184]. This has facilitated the modelling of hydrological extremes and related changes which, however, is still insufficient in some regions [338]. Thus, the recognition of changes in climate-induced hydrological extremes could be addressed by synthesising emerging global and local datasets and by improved hydrological models.

1.1 Motivation

Usually climate change studies are developed for large continental areas, leaving aside island environments that are more susceptible since all the adaptation strategies must come from a limited area with no land connections. Then comes the specificity of "Island Hydrology" that is a combination from the surrounding ocean's climatology; the orographic obstruction of the island; its sometimes steep slopes; the specific soil types that have a strong volcanic component, with groundwater recharge implications [123] — in short,

great variability within small areas. This challenge coupled with the possibility of a better insight into the teleconnection pattern's detection, due to its singularity, was one of the main driving forces.

This research, which was carried out from 2017 through 2021, focuses on changes in hydrological extremes for a small island in the last century and earlier years of present century. The changes in hydrological extremes were examined and associated to atmospheric processes linking both dimensions through teleconnection patterns that drives research towards a better understanding of the hydrological extremes' variability [1]. Overall this research aims at addressing these issues by identifying the potential for changes in water availability in vulnerable regions to hydrological extremes, increases in the magnitude and occurrence of droughts and heavy rainfall, and teleconnection patterns in a changing climate. This research followed up on climatic and hydrological processes with a theoretical and conceptual approach.

1.2 An intensified climate crisis

The numerous extreme rainfall events and their most common outputs, such as droughts and floods, only add to experts' awareness of the current intensified climate crisis [377, 400]. These types of extreme hydrological events have been intensifying globally but not at the same pace as they could be perceived. Increases in magnitude and frequency in hydrological extremes have been predicted by successive scientific assessments from the Intergovernmental Panel on Climate Change (IPCC) [e.g., 255, 310, 31]. Recent hydrological extremes give a clear picture of the impacts, associated costs and risks that come with a warming climate [392]. For instance, climate change increases the odds of worsening drought duration and drought magnitude in many parts of the world in the decades ahead making periods with low rainfall amounts drier than they would be in a no-change scenario. On the other hand, heavy rainfall events have become more common since the 1950s. However, increases (decreases) in rainfall may not always lead to an increase (decrease) in total rainfall over a season or over the year.

Nowadays, the progressive mounting costs of climate-induced changes in both natural and man-made systems are an emergent and undeniable reality [37] — e.g., negative impacts on crop yields, alteration in the distribution of some water-borne illnesses, and progressive expansion of oxygen minimum zones and anoxic "dead zones". By witnessing and learning about it, an increasingly compelling story has been constructed: to limit future risks associated to climate change, governments must act more urgently and firmly measures are required to reduce greenhouse emissions. This should be accompanied with continuous evidence of the pace or magnitude of climate change from the scientific community. Scientists have been making projections of future global warming using climate models of increasing complexity for the past four decades and linking climate extremes to global warming intensity [480]. For instance, looking back at the first IPCC report [190], the observed rate of global warming was accurately predicted.

Since the publication of that IPCC report, experts have learned more about the global climate interactions from thoughtful, data and analyses, theoretical approaches, developments and improvements in complex characterisations identifying and quantifying Earth systems processes via in climate models [135]. There are examples where this continuously improved learning has led to an upward risk revision,

[1] The effects of climate on the changes in hydrological extremes were separated from the impact of human activities by using climate indices time series and not global emissions nor temperature data.

most notably for future global warming scenarios towards a worsening climate. Furthermore, increased number of observations have led to better analyses on impacts of climate change on the hydrological cycle — e.g., as air temperatures increase, more water evaporates into the air which can lead to changes in precipitation and rainfall, and to an increase in extreme events such as droughts and floods [405]. To adjust to and prepare for the current and future impacts on the hydrological cycle, measures can be based on existing IPCC global projections supplemented by high-resolution observations and by comprehensive regional analyses on past and projected trends in vulnerability and exposure to hydrological extremes.

What can be said with enough confidence based on scientific evidence is that global warming is unfolding as projected. According to the IPCC Fifth Assessment Report (AR5) in 2014 [31], the global temperature has been projected to rise. For instance, the decade from 2000 through 2009 was about 0.2°C warmer than in the previous decade as foreseen. Such upward temperature trend has sustained until now. The 2014 IPCC assessment report also stated that climate models projected short term increases in the duration, magnitude, intensity and spatial extent of heatwaves and warm spells, which is exactly what has been now documented [e.g., 299, 479, 503]. Examples are the multiple heatwaves that were reported during the 2018 summer in Europe and East Asia which happened earlier than ever before [316]. According to Albergel et al. [12] Central Europe, and some other areas, experienced in 2018 one of the most severe and long-lasting summer drought and heat wave ever recorded which is somewhat in accordance to the drought increases as projected in the AR5 by IPCC in 2014. In addition to the predicted drought conditions, the AR5 and some more recent reports also summarise the following:

1. Flooding is expected to intensify and be more widespread throughout the whole year — both coastal and inland [346]. Through most of Europe, the increasing frequency of relevant heavy precipitation events in summer and especially in winter were detectable, and there is a strong theoretical basis for these hydrological extremes strengthening by different rates per degree of global warming [511]. In general, the number of daily and multi-day extreme rainfall events has increased at a lower rate than the number of sub-daily events over many European regions [290]. This upward trend is predicted to continue particularly for sub-daily events.

2. Hydrological events described by distributions with a heavy tail of low probability — events that by definition are unlikely to occur — received less attention than the most likely estimates of future climate change, although with high-impact outcomes [96]. Previous IPCC reports largely focused on discussing plausible estimates of future state of nature. Nevertheless, it is necessary to consider the low probability futures, and those ones where climate change has low risk and unnecessary actions might be discarded. Risks are considered when examining future climate projections from the latest set of climate simulations. Several of these new models show considerably more warming over the XXI century compared with the previous versions of these models, with one model suggesting less warming [138]. Other variety of evidence from observations and theoretical approaches, including how well these models represent current global warming trends, suggest that predictions of high warming futures are unlikely, but these scenarios cannot be excluded. Thus, they constitute a risk that needs to be also considered in future planning.

3. Evidence of climate change impacts is growing. As impacts become more easily discernible, so does the sense of an intensified climate crisis and urgency. Many impacts are yet to emerge from the day-to-day and month-to-month natural variations in the weather, with the most difficult and potentially devastating likely to be those affecting human health and biodiversity worldwide [e.g., 312, 174, 472].

Complex impacts related to extreme hydrological events in small areas, such as in small islands, are sometimes underestimated or not well reproduced by climate models — e.g., Global Climate Models (GCMs) — since the spatial and temporal resolutions of impacts across the models are often large [391]. This emphasises the urgency of action to build climate change resilience through water management. To achieve that purpose, the understanding of recent changes in hydrological extremes at different spatial and temporal scales of interest, based on as much data as possible, is still a growing relevant issue.

1.3 Thesis outline

This document represents (i) a generalised assessment of the changes in hydrological extremes, i.e., in droughts and heavy rainfall, mostly based on rainfall data at different scales, and (ii) teleconnections between these changes and changes in some large-scale atmospheric processes.

This is a thesis encompassing a collection of peer-reviewed scientific research papers. Under this model, this PhD thesis consists of papers prepared from 2017 through 2021, all of them already published. The list of papers as first and second author is:

- Espinosa, L. A., Portela, M. M., and Rodrigues, R. (2019). Spatio-temporal variability of droughts over past 80 years in Madeira Island. *Journal of Hydrology: Regional Studies*, 25, 100623.
- Espinosa, L. A., Portela, M. M., Pontes Filho, J. D., Studart, T. M. D. C., Santos, J. F., and Rodrigues, R. (2019). Jointly modeling drought characteristics with smoothed regionalized SPI series for a small island. *Water*, 11(12), 2489.
- Espinosa, L. A., and Portela, M. M. (2020). Rainfall trends over a small island teleconnected to the North Atlantic oscillation-the case of Madeira Island, Portugal. *Water Resources Management*, 34(14), 4449-4467.
- Espinosa, L. A., Portela, M. M., and Rodrigues, R. (2020). Significant Extremal Dependence of a Daily North Atlantic Oscillation Index (NAOI) and Weighted Regionalised Rainfall in a Small Island Using the Extremogram. *Water*, 12(11): 2989.
- Espinosa, L. A., Portela, M. M., and Rodrigues, R. (2021b). Rainfall trends over a North Atlantic small island in the period 1937/1938–2016/2017 and an early climate teleconnection. *Theoretical and Applied Climatology*, 144(1-2): 469–491.
- Espinosa, L. A., Portela, M. M., Pontes Filho, J. D., and Zelenakova, M. (2021a). Bivariate Modelling of a Teleconnection Index and Extreme Rainfall in a Small North Atlantic Island. *Climate*, 9(5): 86.

- Portela, M. M., Espinosa, L. A., Studart, T., and Zelenakova, M. (2019). Rainfall Trends in Southern Portugal at Different Time Scales. In *INCREaSE 2019. International Congress on Engineering and Sustainability in the XXI Century*, pages 3–19, Springer.

- Portela, M. M., Espinosa, L. A., and Zelenakova, M. (2020). Long-Term Rainfall Trends and Their Variability in Mainland Portugal in the Last 106 Years. *Climate*, 8(12): 146.

The scientific research papers as first author adopting the Portuguese island, namely Madeira Island, as study area are directly reproduced in Chapters 3 to 8. The Chapters' titles are slightly different from those of the published material to better conduct the reader through the logic and evolution of the approach. With regard to the papers as second author, only the last one is presented in Appendix A because it can be considered a generalisation to mainland Portugal of the paper but preceded it. To "conduct along the pathway" of the research, the content of the papers from Chapters 3 to 8 are summarised and interconnected in this chapter based on their respective abstracts. In addition, some inevitable repetition of concepts, methods, and study area description in the following chapters is still present, but it was decided not to purge any redundancy in Chapters 3 to 8 in order to preserve the peer-reviewed structure of the contents.

As mentioned, Chapters 3 to 8 and Appendix A are presented in a progressive fashion as a way of reflecting the learning process of the author and deepening of the research into changes in hydrological extremes, and not in chronological order of their publication. The generalised ideas and theories for grasping the research in this document, and additional concepts are reviewed in Chapter 2. Finally, in Chapter 9, the main findings and further developments of this thesis and future implications for water resources management under a changing environment are summarised.

In Chapter 3, changes in the rainfall amounts in a small Portuguese island in the North Atlantic Ocean — Madeira Island — are analysed based on complete daily rainfall series aggregated into 1, 3, 6 and 12-month rainfall, and annual maximum rainfalls of 41 rain gauges from October 1937 through September 2017. The gaps of the daily rainfall data are filled in by the multivariate imputation by chained equations whose performance is also evaluated. The Mann-Kendall test coupled with the Sen's slope estimator are applied to detect and quantify trends along with the Sequential Mann-Kendall test to identify abrupt changes in trends. An association between the rainfall trends and those of mathematical definition of the North Atlantic Oscillation (NAO), i.e., of the North Atlantic Oscillation index (NAOI) is also discussed. New insights into the understanding of the rainfall patterns in small island environments in the North Atlantic are presented. These findings are pursued and reinforced in Chapter 4 for the same 41 rain gauges but spanning from October 1940 to September 2017. Through the application of the same models for the rainfall trend analysis focusing on the wet season, results suggest considerably and statistically significant decreases in rainfall, exacerbated in recent years at the central region of Madeira Island — an important location for fresh water security. Furthermore, Chapter 4 provides a solid basis to explain the climate change effects on the Madeira rainfall, suggesting that abrupt changes of the island's rainfall variability can be directly linked to those of the North Atlantic Oscillation climatic driver [426] based on the strong established teleconnection.

Chapter 5 presents an analysis on droughts from January 1937 to December 2016, using monthly rainfall at 41 rain gauges covering most of Madeira Island. The drought conditions are assessed by means of the Standardized Precipitation index (SPI). Drought variability and climate regionalisation (homogeneous climatic regions) are addressed with clustering techniques and principal components analysis (PCA). The droughts are characterised in terms of drought duration and magnitude from the run theory. Based on a kernel occurrence rate estimator (KORE), the frequency of the periods under drought conditions is discussed. The climatic drivers, namely the El Niño Southern Oscillation (ENSO) and the NAO are teleconnected to the drought variability at the identified homogeneous regions. This chapter shows that the spatial and temporal drought variability in the island has been subjected to noticeable changes in recent years with a considerable higher number of periods under drought conditions than in the past. Chapter 6 deepens the analysis on dependent drought events by introducing a copula-based bivariate cumulative distribution function for coupling drought duration and magnitude, and their related univariate and bivariate return periods. A broad discussion on the moving average filter applied to SPI series in drought analysis is also part of Chapter 6.

Extreme rainfall or heavy rainfall and its apparent dependence on a large-scale dominant mode of winter climate variability is addressed in Chapter 7. The extremal dependence between a North Atlantic Oscillation index (NAOI) and rainfall is assessed from January 1948 to September 2017 at multi-year dominance of negative and positive NAOI, i.e., –NAOI and +NAOI dominance subperiods, respectively. The datasets used are daily NAOI, and daily weighted regionalised rainfall series computed based on factor analysis and the Voronoi polygons method from 40 rain gauges in the small Portuguese island of Madeira. The extremogram technique is applied for measuring the extremal dependence within the NAOI univariate series. The cross-extremogram is the main tool applied for the dependence between the upper tail of the weighted regionalised rainfalls, and the upper and lower tails of daily NAOI. Results of Chapter 7 suggest systematic evidence of statistical dependence over Madeira between exceptionally –NAOI records and extreme rainfalls, which is stronger in the –NAOI dominance subperiods. Further development of the dependence between NAO forces and winter daily extreme rainfall at six representative rain gauges of Madeira is quantified in Chapter 8 via copula-based models for studying the return period of the extreme events from December 1967 to February 2017. The hypothesis in this chapter is that the observed influence of the NAO on extreme rainfall is largest in the North Atlantic sector, with the likelihood of an increased rainfall event from December through February in Madeira under the negative phase of the NAO. Results show the characteristics of the underlying joint distributions of two likely dependent random variables which highlights the importance of multivariate modelling for teleconnections to extreme rainfall in small islands.

Additionally, in Appendix A, the long-term rainfall trends, their temporal variability and uncertainty are addressed but this time over mainland Portugal. The study is based on monthly, seasonal and annual rainfall series at 532 rain gauges, spanning for the period of 106 years (1913–2019) utilising most of the same models as in Chapters 3 and 4. Results are in accordance to those for Madeira showing that from late 1960's on, the rainy season pattern has changed, with the last months prior to the dry season showing a sustained decrease of their relative contributions to the annual rainfalls.

Chapter 2

Theoretical and Methodological Background

This doctoral thesis aims at providing contributions on hydrological extremes based on long datasets assembled and homogenised in a way as to foster improved modelling approaches that lead to a better understanding of extreme hydrological events under climate change and abrupt climate variability. The themes of the this thesis include but are not limited to:

1. Novel approaches of filling rainfall data gaps (Chapter 3).
2. Trend analysis and change point detection (Chapters 3, 4, and Appendix A).
3. Climate regionalisation (Chapters 5, 6, and 7).
4. Regional drought analysis (Chapters 5, 6).
5. Bivariate copulas functions for extreme events analysis (Chapters 6 and 8).
6. Extremal dependence measure (Chapter 7).
7. Teleconnection indices (Chapters 3, 4, 5, 7, and 8).

This chapter provides an overview and some concepts about the previous themes intending to be different from the content of the chapters in which they are presented and applied, by complementing or synthesising such content or by just stressing relevant or some additional features of the aforementioned themes.

2.1 Multiple imputation for filling data gaps

Multiple imputation provides a useful strategy for dealing with datasets with data gaps [269]. Instead of filling in a single value for each missing value or data gap (hereafter used interchangeably), Rubin [368] proposes a multiple imputation procedure that replaces each missing value with a set of plausible values that represent the uncertainty about the right value to impute. These multiply imputed datasets are then

analysed by using standard procedures for complete data and combining the results from these analyses. Regardless which complete-data analysis is used, the process of combining results from different imputed datasets is essentially the same. This translates into valid statistical inferences that properly reflect the uncertainty due to missing values. Multiple imputation techniques are very flexible and can be used in a broad range of settings [365]. Since multiple imputation involves creating multiple predictions for each data gap, the analyses of multiple imputed data take into account the uncertainty in the imputations and yield accurate standard errors. Generally, with a high concentration of missing values in the observed data, the imputations might be extremely variable, leading to high standard errors in the analyses [162]. Conversely, if the observed data are highly predictive of the data gaps, the imputations are likely to be more consistent across imputations with smaller and accurate standard errors.

Multivariate Imputation by Chained Equations (MICE) is a particular multiple imputation technique — and the main model used in Chapter 3 for filling of the rainfall data gaps. MICE operates under the assumption that given the variables used in the imputation procedure, the data gaps are Missing At Random (MAR). This means that the probability that a value is missing depends only on observed values and not on unobserved values [454]. In the MICE procedure a series of regression models are run whereby each variable with data gaps is modelled conditionally upon the other variables in the data. Thus, each variable can be modelled according to its distribution, with, for instance, continuous variables modelled using linear regression [261]. The MICE can be summarised into six general steps:

Step one: A simple imputation is performed for every data gap in the dataset. These imputations, via the mean imputation for instance, are considered as placeholders.

Step two: The placeholders imputations for variable one (VAR1) are set back to missing.

Step three: The observed values from VAR1 in Step two are regressed on the other variables in the imputation model. Namely, VAR1 is the dependent variable in a regression model and all the other variables are independent variables in the regression model.

Step four: The data gaps for VAR1 are then replaced with imputations from the regression model. When VAR1 is afterwards used as an independent or predictor variable in the regression models for other variables, both the observed and these imputed values are to be used.

Step five: Steps two, three, and four are then repeated for each variable that has data gaps. The cycling through each of the variables constitutes one cycle. At the end of one cycle all of the data gaps have been replaced with imputations, or predictions, from regressions that reflect the relationships observed in the data.

Step six: Steps two through four are repeated for a number of cycles, with the imputations being updated at each cycle.

The number of cycles to be performed should be adapted to each specific case and take account of the nature of the problem and the required computation time. At the end of these cycles the final imputations are retained, resulting in one imputed dataset. Overall, by the end of the cycles the distribution of the

parameters governing the imputations should have converged in the sense of becoming stable avoiding dependence on the order in which the variables are imputed.

Despite multiple imputation methods can be computationally demanding and the fact that they make more parametric assumptions which are often chosen arbitrarily, their main advantage is that they allow more flexible conditioning sets and thereby better capture the relations between variables. Thus, a novel multiple imputation approach, i.e., MICE is tested and discussed in Chapters 3 and 5 for gap-filling daily and monthly rainfall respectively.

2.2 Trend analysis and change point detection

Both, trend analysis and change point detection in a time series are frequent analysis tools [403]. Change point detection is the identification of abrupt variation in the process behaviour due to distributional changes, whereas trend can be defined as estimation of gradual departure from past norms. A change point can be defined as unexpected, structural, changes in time series properties such as the mean or variance [501]. Many change point detection algorithms have been proposed for single or multiple changes assuming, for instance, discrete time and known pre-change and post-change distributions [323].

Trend analysis is defined as a process of estimating gradual change based on previous data. Different parametric and non-parametric techniques are used to estimate trends. The Mann-Kendall test and Sen's slope estimator [80], Spearman rho [477], seasonal Kendall [187], and Cox–Stuart [371], are the most frequently used approaches. An analysis based solely on the change point, neglecting the trends or vice versa may mislead the interpretation of results. For instance, estimating only the trend could provide little information by implying that the data series simply denotes either and upward, downward, or no trend. This issue is overcome when the trend and change point are coupled together which results in an improved trend assessment and, in some cases, less uncertain future events predictions.

Though there are several studies related to trend analysis specifically of climatic variables, change point analysis has recently gained importance all over the globe [54]. This is highlighted for rainfall series and a teleconnection index in Chapters 3, 4, and Appendix A.

2.3 Climate regionalisation

Climate regionalisation studies have made a thorough use of eigenvector analysis [66, 132], particularly utilising variations of principal components analysis (PCA), and common factor analysis, also called principal factors analysis (PFA), which seek the least number of components and factors, respectively, accounting for the common variance or correlation of a set of climatic variables [157, 110]. These eigenvector analysis methods, also including empirical orthogonal functions [173], are generally used to temporally and spatially reduce climatic data to manageable, physically coherent abstractions by expressing the variance of a sampled data field in a reduced number of variables, and also to transform multiple climatic signals, or data series, into representative ones. These abstractions aim at providing a comprehensive understanding of local climate patterns across a specific region.

The many procedural options that exist in eigenvector analysis may produce widely differing results, such as the truncation of insignificant components or factors, and the use of orthogonally and obliquely rotated or unrotated solutions [46]. Several solutions are possible using orthogonally and obliquely rotated PCA or PFA since rotation of the principal components or factors, respectively, about a fixed configuration of the variable vectors in multidimensional space is dependent on one of several algebraic formulae. For unrotated and orthogonally rotated PCA or PFA, no single position of the component vectors best represents the configuration of variable vectors [358].

For different analytical purposes, such as temporal trends and frequency analysis, it is convenient to divide the spatial continuum of a climatic variable or index — e.g., rainfall or a drought index, such as the Standardized Precipitation index (SPI) which is derived from rainfall data [167] — into a manageable number of homogeneous areas, i.e., with similar or correlated temporal pattern, based on the reduction of variables [30]. Specifically, climate regionalisation using eigenvector analysis is a practical technique that enables generalisation about areas derived from a spatially and temporally varying climate variable. These techniques have been helpful for delimiting climate regions, and such approaches have successfully delimited spatially cohesive rainfall or SPI regions considering similar seasonality and long-term variability characteristics [5, 84].

One of the main goals of PCA and PFA is to summarise the correlations among a set of observed variables, or weather stations in some cases, with a smaller set of linear combinations. For instance, the rain gauges with the same seasonal timing of rainfall — or, as it was done in the drought analysis, of SPI [40] — at a selected timescale are correlated and grouped together, presumably because of the same atmospheric controls. Generally in climate regionalisation, after the application of PCA or PFA, no clustering algorithm is implemented [66]. Alternatively, the correlation values for each principal component or factor are mapped. Depending on the interpolation technique used, different isolines can be produced, and thus, homogeneous regions can be identified using correlation contours with given prefixed values as boundaries.

Climate regionalisation, with the use of PCA and PFA, is implemented in Chapters 5 and 6 to identify representative homogeneous regions drawn around rain gauges assigned to the same principal component or factor based on SPI for regionalised drought analysis, and in Chapter 7 to group rain gauges with similar daily rainfall variability for extreme rainfall. The evaluation of the regionalisation is established on a maximum-correlation approach in which rain gauge is assigned to the component or factor upon which it correlates most highly. Altogether this application intends to acquire a high accurate climate regionalisation for the development of a classification that identifies sub-regional differences of changes in hydrological extremes.

2.4 Regionalised drought analysis

Droughts that are triggered by persistent lack of rainfall are among the hydrological events with the most disastrous consequences for society and economy [102]. Information on the duration, magnitudes, and frequencies of droughts is essential for sustainable water resources management, agricultural management,

and for studies related to impacts of climate change [230].

To minimise the risk associated to droughts, statistical and probabilistic methods are applied to previous drought events to characterise both the phenomena and their changes. However, reliable drought estimates require, generally, representative data series, or regionalised series, instead of single station data due to the large-scale nature of the drought phenomenon itself [355]. Regional drought analysis is therefore used to provide a framework for drought characterisation [233].

The Standardized Precipitation index (SPI) — developed by McKee et al. [257] — is a flexible index used by a variety of research institutions, universities, drought response managers, and National Meteorological and Hydrological Services worldwide. This index is straightforward given that rainfall data is the only required input parameter. The SPI is both effective assessing wet and dry periods [257]. Ideally to calculate the SPI, at least twenty to thirty years of monthly rainfall values are needed, but fifty to sixty, or more, years of data is optimal. The SPI is an index based on the probability of occurrence of a certain deviation from an average amount of precipitation and for a given timescale. This index is based solely on precipitation data and is of relatively simple calculation, and can be computed for different timescales, which allows it to describe different drought conditions. Furthermore, due to the standardisation of the SPI index, the frequency of extreme events at any location and at any timescale is consistent and comparable. The considered timescales — normally 3, 6, 12, 24 and 48 months — reflect the drought impact on the depletion of the different reservoirs of fresh water at the level of the watershed, from rivers, soil, groundwater and artificial reservoirs. When SPI is computed for medium accumulation periods (e.g., 6 months, i.e., SPI-6 as implemented in Chapters 5 and 6), it can be used as an indicator for reduced stream flow and reservoir storage.

Regionalised droughts are addressed in Chapters 5 and 6 based on the regionalised SPI after the application of eigenvector transformation techniques to the drought indexes series. The main objective of the implementation of this approach is to analyse different drought characteristics (e.g., magnitude, and duration of periods under drought conditions) from the regionalised SPI series based on the theory of runs [257].

2.5 Analysis of extreme events using copulas

The assessment of extreme events requires a characterisation of the probabilistic properties of hydrological variables. In many cases, this characterisation is addressed from a univariate point of view, whereas most hydrological events are intrinsically multivariate [375]. In this context, copulas have recently received attention in the multivariate frequency analysis of extreme hydrological events [356]. On one hand, multivariate extreme events analysis is concerned with the extremes in a multivariate random sample, i.e., points of which at least some of the components have exceptionally large values or have values above an adopted threshold [395]. On the other hand, an univariate approach summarises only one variable at a time. However, multivariate approaches consider more than one factor of independent variables that influence the variability of dependent variables, which may lead to more accurate conclusions from the studied phenomenon. Thus, copulas can be used to provide appropriate models for the dependence

structure among multivariate extreme events [166].

Generally speaking, copulas have been used as a way of studying scale-free measures of dependence, and as a starting point for constructing families of bivariate, or multivariate, distributions [220]. Copulas are functions which join or "couples" multivariate distribution functions to their uni-dimensional marginal distribution functions. Copulas can be used to model n-dimensional probability distributions. The n-dimensional distribution function is said to be a copula if all n marginal distributions are uniform on the interval $(0, 1)$. Specifically, copulas are an important part of the study of dependence among variables since they separate the effect of dependence from the effects of the marginal distributions [112].

In this thesis, the copulas applied were restricted to the bivariate type. The use of copulas is justified because traditional approaches often fail to analyse the characteristics of extreme events within a bivariate framework under changing environment. With that in mind, the joint behaviour of correlated drought characteristics and its changes over time is evaluated in Chapter 6. Furthermore, the bivariate curves under different levels of joint return periods for historical and future periods are derived by copula functions and the most likely realisations are estimated in in Chapter 8 between the persistence of the North Atlantic Oscillation (NAOI) and extreme rainfall.

2.6 The extremal dependence and the extremogram

The probabilistic characterisation of the relationship between two or more random variables calls for a notion of dependence [339]. In Chapter 7, the concept of extremal dependence is explored upon tails of random vectors — a daily North Atlantic Oscillation index (NAOI) and daily regionalised rainfall. The extremal positive dependence analyses both upper tails of the previous random vectors, while the concept of extremal negative dependence arises when the lower tail of one vector is involved, such as the dependence between observations in the lower tail of NAOI (extreme negative values) and high positive rainfall extremes in the upper tail.

The upper tail contains the upper values in a distribution. If any distribution is graphed on a Cartesian plane with the traditional coordinate system, the highest values will always appear on the right, because the highest values on a number line are to the right. Similarly, the lower tail contains the lower values in a distribution, with the lowest set of values appearing on the left of any graphed distribution [175].

In the mathematical modelling of a random phenomenon or experiment, the quantity of interest is described by a measurable function $X : \Omega \to \mathbb{R}$ from a pre-assigned atomless probability space $(\Omega, A, \mathbb{R})$ to some other measurable space, which will be chosen as the real line in what follows [339]. This X is called a random variable. A random variable, if considered as an individual entity, is univocally described by its distribution:

$$F(x) := \mathbb{P}(X \leqslant x), x \in \mathbb{R}. \tag{2.1}$$

Exploring the relationship between two or more random variables is crucial to stochastic modelling in many applications and requires a much more complex statistical analysis. Usually, an number of $d \geqslant 2$ random variables $X_1, ..., X_d : \Omega \to \mathbb{R}$ are gathered into a random vector $\boldsymbol{X} := (X_1, ..., X_d) : \Omega \to \mathbb{R}^d$. A

full model description of $(X_1, ..., X_d)$ can be provided in the form of its joint distribution function:

$$F(x_1, ..., x_d) := \mathbb{P}(X_1 \leqslant x_1, ..., X_d \leqslant x_d), x_1, ..., x_d \in \mathbb{R} \tag{2.2}$$

where $\boldsymbol{X} \sim F$ and the univariate distributions $F_j(x := \mathbb{P}(X_j \leqslant x), j = 1,$ are referred to as the marginal distributions of F. When $d \geqslant 2$, the full knowledge of the individual models $F_1, ..., F_d$ is not sufficient to determine the joint distribution F. To address this issue, it is necessary to establish the dependence relationship among a set of given marginal distributions, i.e., to make a rearrangement to describe dependence among a set of random variables as done in Chapter 7 via the extremogram and cross-extremogram [251].

The extremogram is related to the extreme dependence functions and extremal coefficient function introduced by Fasen et al. [127]. These concepts are generalisations in a stochastic processes context of the coefficient of tail dependence. In Chapter 7, the decay of extremal dependence between two distinct variables — both daily NAOI and rainfall — in a regularly varying strictly stationary time series is addressed based on the extension of the extremogram, i.e., the cross-extremogram.

2.7 Teleconnection indices in the climate system

Rainfall extremes and their underlying causes are important processes to plan appropriate adaptation measures. Large-scale climate patterns and weather indices, such as North Atlantic Oscillation index (NAOI) [362], are the major factors that affect the weather variations and climate from far away distances, which in turn can be linked to extreme hydrological events. Based on some definitions, weather patterns and indices are indicators, by which temporal changes in intensity and spatial changes in atmospheric circulation patterns are measured. Thus the significant relationship and correlation between temporal changes of two circulation systems or patterns, that are at long distance from each other (such as links between the North Atlantic Oscillation and outputs of extreme rainfall), is called teleconnection. The teleconnection is associated with fluctuations in the atmosphere, usually defined as indices [141], furthermore, it is a way to summarise the climate modes to describe the process of transferring heat, energy, moisture, and momentum of the earth atmosphere, and to get a better understanding of how climate change affects hydrological extremes.

The largest global climate pattern and the most well-known of the developed teleconnections is the El Niño-Southern Oscillation (ENSO), expressed as the Southern Oscillation index (SOI), which is governed by a shift in ocean temperatures affecting trade wind magnitudes in the central Pacific. ENSO is a periodic fluctuation in sea surface temperature and the air pressure of the overlying atmosphere across the equatorial Pacific Ocean [353]. This feature, while spatially disconnected from Europe and the North Atlantic region, has well-established, but few, relationships with warm and cool-season climate scale phenomena including wintertime temperature and rainfall patterns, tropical cyclone frequency, and even severe weather outbreaks on the North Atlantic and European sector [263]. ENSO events often reach maturity by the end of dry season, whereas the effects in northern and central Europe are expected to be largest in late winter for rainfall [225]. While ENSO is more appropriate for the Pacific, the NAO

has been well-established for teleconnection on winter weather in Europe, Greenland, northeastern North America, North Africa, and northern Asia.

The NAO is an irregular fluctuation of atmospheric pressure over the North Atlantic Ocean. The NAO can occur from daily to yearly basis, or the fluctuations can take place decades apart [426]. It is an oscillation due to the changes in atmospheric pressure which are essentially a back-and-forth switching between two prevailing patterns, i.e., positive and negative NAO phases. The NAO can be defined as the North Atlantic Oscillation (NAOI) index NAOI generally based on the surface sea-level pressure difference between sub-polar low and the subtropical high [482]. The NAO exhibits considerable interseasonal and interannual variability, and prolonged periods of both positive and negative phases.

The positive phase of the NAOI — an increased difference in pressure between the two dipoles — reflects above-normal temperatures in the high latitudes of the North Atlantic and across northern Europe and below-normal temperatures in Greenland and oftentimes across southern Europe and the Middle East [447]. The positive NAOI phases also reflect below-normal heights and pressure across the high latitudes of the North Atlantic and above-normal heights and pressure over the central North Atlantic, and western Europe. They are also associated with above-normal rainfall over northern Europe and Scandinavia and below-normal rainfall over southern and central Europe. Opposite patterns of height and pressure, temperature, and specially rainfall anomalies are typically observed during strong negative phases of the NAOI over these regions [340].

Both phases of the NAOI are associated with wide changes in the intensity and location of the North Atlantic jet stream and storm track, and in large-scale modulations of the normal patterns of zonal and meridional heat and moisture transport, which in turn results in changes in temperature and rainfall patterns often extending from eastern North America to western and central Europe [142]. In addition, during particularly prolonged periods dominated by one particular phase of the NAOI, abnormal height and temperature patterns are also often seen extending well into central Russia and north-central Siberia.

Relationships between (i) rainfall trends, drought, and heavy rainfall, at different timescales; and (ii) the two teleconnection patterns mentioned in this Section — with special focus on the NAO — form a large part of this thesis, namely, the effects of NAO, based on two NAOI definitions, on rainfall trends are investigated in Chapters 3 and 4. Chapter 5 intends to link drought, derived from the SPI signal, to both indices of ENSO and NAO, i.e., to SOI and NAOI. In Chapters 7 and 8, the links between the NAO and extreme rainfall are addressed based on the cross-extremogram and bivariate copulas, respectively.

Chapter 3

Filling Rainfall Data Gaps, Rainfall Trends, and a Teleconnection

This chapter has been published as: Espinosa, L. A., Portela, M. M., and Rodrigues, R. (2021b). Rainfall trends over a North Atlantic small island in the period 1937/1938–2016/2017 and an early climate teleconnection. *Theoretical and Applied Climatology*, 144(1-2): 469–491, https://doi.org/10.1007/s00704-021-03547-7

Abstract

Changes in the rainfall amounts in a small island in the North Atlantic Ocean — Madeira Island — were analysed based on complete daily rainfall series aggregated into 1, 3, 6 and 12-month rainfall, and annual maximum rainfalls of 41 rain gauges (1937/38–2016/17). The gaps of the daily rainfall data were filled in by the multivariate imputation by chained equations whose performance was evaluated. The Mann-Kendall test coupled with the Sen's slope estimator were applied to detect and quantify trends. The Sequential Mann-Kendall test was used to identify abrupt changes in trends. Results show a widespread downward trend in seasonal and annual rainfall, with the highest values in Madeira's central region. A strong association between the downward rainfall trends and the upward trends of the North Atlantic Oscillation index was found. New insights into the understanding of the rainfall patterns in small island environments in the North Atlantic were produced.

Keywords:

Rainfall trend; multivariate imputation by chained equations; Mann-Kendall test; Sen's slope; change-point detection; North Atlantic Oscillation; Madeira Island.

3.1 Introduction

Studying climate variability, hydrological extreme events, trends in hydrological variables, along with their prediction, from global to regional and local scales, are of primary importance in agricultural, forestry and water management activities. These activities are scheduled or designed mainly in accordance to rainfall seasonality and spatio-temporal distribution [468]. However, assessing climate variability, the mechanisms that cause the changes and their related impacts is rather difficult. In recent years, unevenly distributed changes have led to an increased temporal variability mostly on rainfall, streamflow and

evaporation patterns [20, 226]. For the purpose of understanding the potential effects of climate change, trend analysis and change-point detection in the time series of climatic variables, such as temperature and rainfall, have been the focus of research worldwide.

Small island environments, i.e., islands with areas between 100 km^2 and 5,000 km^2 [123], have fragile ecosystems often with limited water resources and great care of the environment is required for support of their inhabitants. The hydrological features of small islands, such as reduced catchment areas and the generally limited surface and groundwater storage capacity, make their hydrology and water resources development and management issues very distinct from those on larger islands or continental areas. According to Santos et al. [380], these islands constitute very important assets for the countries they integrate for many reasons (e.g., for their strategic and economic advantages, and for their often unique landscapes and ecosystems). Therefore, understanding the behaviour of climatic variables on small islands and being able to detect their trends are fundamental issues in water planning and management in a changing environment [351]. Due to their limited area and isolated nature, the effects but mainly the consequences of climate change are generally magnified compared to continental areas and may cause freshwater supply failures on a background of decreasing rainfall and increasing temperature reports [310, 31].

The Intergovernmental Panel on Climate Change (IPCC), in its periodical assessment reports [255, 310, 31], has stressed that the vulnerability and exposure of island environments to changes of extreme rainfall episodes and their outputs (e.g. floods and droughts) will increase. However, the high spatial and seasonal variability of those events makes it difficult to analyse their behaviour, including the identification of rainfall trends. Furthermore, because of climate change, a significant reduction in freshwater availability is expected in many of the North Atlantic small islands [31]. Masson-Delmotte [250] also report an increasing water stress, although specifically in Small Island Developing States (SIDS), due to global warming.

In the last decades the volume of literature in refereed international journals relating to rainfall trends has increased for different climate zones [e.g., 289, 352]. For instance, rainfall records over the Caribbean region in the period 1900–2000 showed a continuing rainfall decline of 0.18 $mm\,year^{-1}$ [206]. Similar studies have been carried out focused on the rainfall, however, over mainland Portugal and not over the Portuguese Islands. Those studies have reported a generalised decreasing tendency in seasonal and annual rainfall amounts [268, 379, 507]. An equivalent characterisation in the European Macaronesia [252] also reported generalised decreasing trends in different periods of the year. Specifically for the Portuguese island of Madeira, Miranda et al. [268] investigated the presence of linear monotonic trends based on 135 years (1865–2000) of annual rainfall data at Funchal meteorological station — located in the capital of the Autonomous Region of Madeira (RAM), very close to the coast of the southern slope — and Santos et al. [380] utilised rainfall data from 14 rain gauges coupled with the atmosphere-ocean general circulation model Hadley Centre Coupled Model Ver. 3 (HadCM3) to produce scenarios of rainfall anomalies, with particular attention given to the winter and summer seasons in the late 21^{st} century. Nevertheless, the number of independent scientific studies on rainfall trends in small islands, specifically for the North Atlantic region, is still quite limited. This is mainly because there are few long-term rainfall records

available for individual small island locations [31].

For statistical reasons, valid climatic analyses require continuous, complete, and long-time series [111]. However, the climatic datasets often contain missing values or gaps [393] caused, for instance, by equipment failures, errors in measurements, budget cuts, and natural hazards, which affect the variables' estimates [424]. The problem of missing values, as those of rainfall [10], is relatively common in almost all research related to hydrology and can have a significant effect on the conclusions that can be drawn from the data [159]. Moreover, the temporal variability of the climatic variables combined with the irregular spatial distribution of the measuring stations are sources of uncertainty when trends in these variables are addressed, once more, such as in rainfall [106]. Rebuilding a series, i.e., filling in its gaps, may have a more beneficial effect on the analyses' outputs rather than just ignoring the missing data [349].

Different univariate and multivariate methods for imputation of missing rainfall data can be adopted depending on the length of the gaps, the availability of data from neighbouring rain gauges, the climatic region under consideration, the length of existing records, and the performance of the implemented model for gap-filling [282, 283, 49]. Univariate imputation methods are largely used in hydrological analysis including, for instance, the mean substitution [236] and the linear interpolation method [243] both based only on the series with missing values, or the closest station method and the inverse distance method which use information from other rain gauges rather than the one with missing data [498, 497]. However, univariate imputation is usually incapable of providing a reasonable imputation for a variable when periods of missing values are large [57]. Gap-filling in a multivariate setting includes multivariate versions of univariate methods, data driven methods, such as Artificial Neural Networks (ANNs) [221], self-organizing maps [282, 283, 8, 284], and the k-nearest neighbor approach [401, 273]. The techniques mentioned so far, fill in each missing value exactly once. In contrast, model-based approaches, specifically the machine learning method for Multiple Imputation (MI), fill in at the same time missing values of multiple incomplete series in a dense network of neighbouring stations [269, 342].

The aim of this paper is to provide a comprehensive characterisation of the variation in rainfall and of the recent dynamics of its change over a small island environment as is the case of Madeira Island — located in the North Atlantic Ocean, in the European part of Macaronesia [235]. To overcome the issue of the incompleteness of the rainfall data at Madeira Island, MI was applied to fill in the missing daily rainfalls. Different from the previous studies about rainfall trends in the island, whose results were based on a very small number of rain gauges or even on a single rain gauge, this study used complete daily rainfall series spanning from October 1937 to September 2017 (i.e., 80 hydrological years, starting on October 1^{st}, from 1937/38–2016/17) at 41 rain gauges (Table 3.1) covering most of the island, as depicted in Figure 3-1. It is, therefore, the first comprehensive and detailed study about rainfall trends in Madeira Island, thus providing new insights into the understanding of the rainfall patterns in recent decades.

For that purpose, monthly, quarterly (4-month), semester (6-month), yearly, and annual maximum (from 1 to 7 days) rainfall series were obtained from the complete daily data (after applying the gap-filling procedure) and analysed, aiming at identifying significant linear monotonic trends based on the non-parametric Mann-Kendall (MK) statistical test. To quantify the trends, the non-parametric Sen's

slope estimator test was used. Furthermore, the Sequential Mann-Kendall (SQMK) test was applied as a change-point detection technique, in order to identify breakpoints in the rainfall series. Finally, an exploratory analysis was conducted on the relationship between the seasonal rainfall trends and the mathematical description of the North Atlantic Oscillation (NAO) phase, i.e., the North Atlantic Oscillation index (NAOI).

3.2 Material and methods

3.2.1 Study area

Madeira is the largest island of the Madeira Archipelago with an area of 741 km^2, a length of 57 km and a maximum width of 22 km. Centred at 32° 44.34' N and 16° 57.91' W, approximately 600 km northwest of the Western African coast, Madeira Island has a steep topography and is completely formed by volcanic materials, consisting of an enormous central E-W oriented mountainous system (Pico Ruivo, 1862 m.a.s.l., Pico do Areeiro, 1818 m.a.s.l., and Paúl da Serra region, above 1400 m.a.s.l.) cut by deep valleys (Figure 3-1). Except for the higher areas, where very low temperatures may occur during winter, the differences between winter and summer temperatures are generally small. According to the Koppen's classification [58], the climate is predominantly temperate with dry and warm to hot summers as approaching the coastal zones of Madeira.

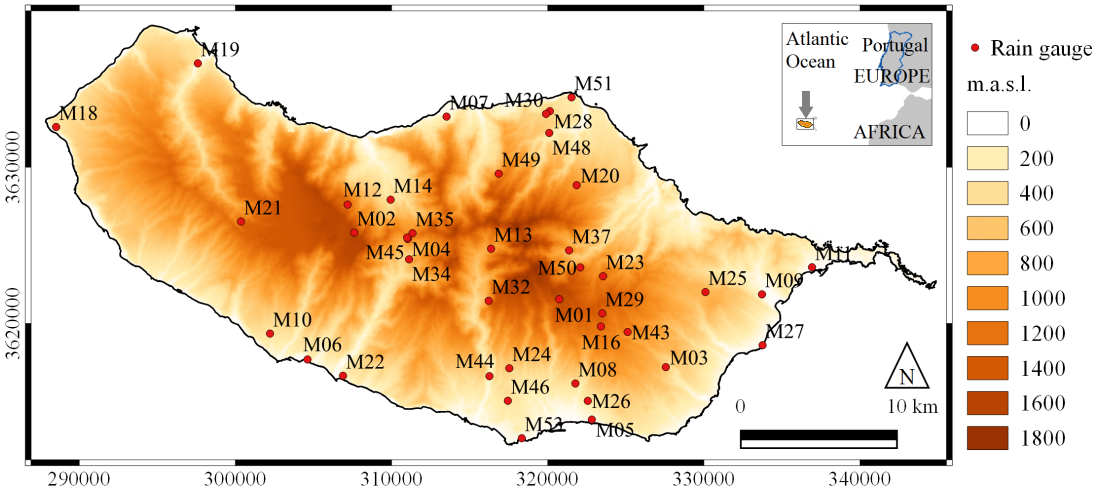

Figure 3-1: Location of the 41 selected rain gauges used in the study (bullets with identification codes) over the elevation map of Madeira Island. Referencing system: World Geodetic System 1984 (WGSM84); UTM zone 28N.

Due to the Madeira Island's E-W oriented mountainous system, which divides the island into east and west from an orographical perspective, the rainfall is strongly influenced by the topography, falling predominantly in the north facing slope because of the prevailing N-E trade winds [235]. The rainfall regime is not only affected by the local circulation, but also by synoptic systems (such as fronts and extratropical cyclones which are typical in mid-latitudes) and the Azores Anticyclone in the summer season [140].

The rainfall quantity and its high variability, with respect to time and space, play an important role

on the availability of Madeira's freshwater resources. The rainfall in Madeira is more abundant during the months of December and January. From June to August the average rainfalls are low [58] and close to zero in July. There is a wide variation in rainfall between lower and higher elevations with the lowest amounts occurring along the southern slope. Regions with smaller amounts of rainfall are more susceptible to the rainfall temporal variability in terms of water availability. This is the case of the southern slope [70].

As can be seen in Figure 3-2**a**, the average annual rainfall in Madeira Island presents a very uneven distribution in which the dominant factors are the elevation and exposure to the prevailing trade winds, as mentioned previously. The highest average annual values, exceeding 2200.0 mm, are observed at the higher elevations located in the central region of the island (e.g., the rain gauges of M01, M02, and M04 with 2592.2, 2605.7, and 2410.4 mm, respectively) and also in the northern slope, while the smallest annual averages, less than 650.0 mm, occur in the lowland areas of the southern slope (e.g., the rain gauges of M05, M06, and M53 respectively with 608.4, 597.7, and 340.1 mm).

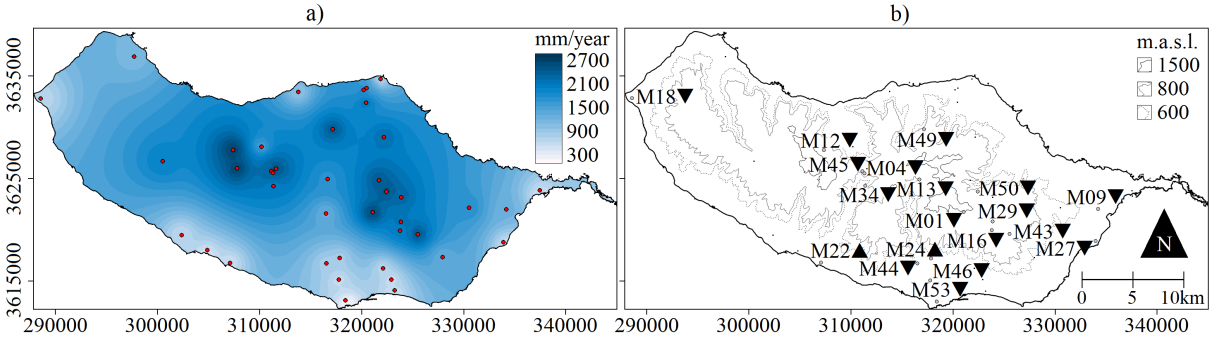

Figure 3-2: Madeira Island. **a)** Average annual rainfall surface based on the completed daily series at the 41 rain gauges (red bullets) for the reference period from 1937/38–2016/17. The spatial interpolation technique applied was the Inverse Distance Weighting (IDW) with an exponent of 2. **b)** Contour lines of three elevations in which most of the extensive network of small canals or *levadas* develops; and location of the rain gauges (identification codes) with statistically significant rainfall trends at any of the considered time-spans (whether positive or negative depicted by the upward or downward triangles direction, respectively).

In Madeira Island, groundwater is the main source of freshwater for its 267,785 inhabitants and about 500,000 tourists per year [199]. The island's population is concentrated primarily in the coastal areas, almost exclusively on the southern slope where most of the larger towns are located and where most of the economic activity of Madeira takes place.

The groundwater exploitation, for domestic and industrial use, as well as for irrigation and electrical production purposes, is made by means of water galleries, tunnels, wells and springs and by an extensive network of small canals or *levadas* supplying water to the northern and southern slopes. The *levadas* network, whose origin dates back to the first settlements of Madeira Island in the first quarter of the 15^{th} century, mostly borders the mountains at elevations from 600 to 1500 m.a.s.l. (Figure 3-2**b**). With more than 1000 km long, the network has been classified as an Outstanding Universal Value due to its uniqueness [104]. The groundwater flows from the central regions to the coast, where the aquifers discharge to the sea [333]. The main natural groundwater recharge areas are located in the highlands, where the rainfall values and permeability of rocks are higher (e.g., the rain gauges of M01 and M02 – Figure 3-1). These areas are therefore critical for the island's water security.

3.2.2 Rainfall data

Daily rainfall series at the 41 rain gauges (Table 3.1 and Figure 3-1) for the time-frame from October 1937 to September 2017 were made available by Portuguese Institute for Sea and Atmosphere (IPMA) (https://www.ipma.pt/en/). IPMA is the national authority in the fields of meteorology, aeronautical meteorology, climate, seismology, and geomagnetism, and an institution of reference at international level also devoted to the promotion and coordination of scientific research. It has very high data quality standards and is the most reliable source of Portuguese hydrological and hydrometeorological data.

Table 3.1: 41 rain gauges adopted in the study. Identification (code and name), coordinates, elevation, and areal-influence (ATP) according to the Thiessen polygons method. Average rainfalls for January (JAN), August (AUG), second quarter (QT2), first semester (SM1), year (HDY), and annual daily maximum (AM1), in the reference period of 80 hydrological years, from October 1937 to September 2017 (data obtained from the reconstructed daily dataset).

Code	Name	Lat-N	Lon-W	Elevation	ATP	Average rainfall (mm)					
				(m.a.s.l.)	(km^2)	JAN	AUG	QT2	SM1	HDY	AM1
M01	Areeiro	32.7200	-16.9170	1610	13.67	354.5	26.8	936.8	2078.9	2592.2	181.3
M02	Bica da Cana	32.7562	-17.0554	1560	22.06	352.0	40.2	933.0	2009.6	2605.7	141.8
M03	Camacha-Valparaiso	32.6763	-16.8421	675	28.58	202.6	13.5	520.5	1117.8	1406.8	113.3
M04	Encumeada de São Vicente	32.7503	-17.0169	900	1.12	334.7	31.5	900.8	1883.2	2410.5	145.1
M05	Funchal Observatório	32.6476	-16.8924	58	7.08	87.5	2.7	230.7	501.4	608.4	62.2
M06	Lugar de Baixo	32.6790	-17.0832	15	10.94	87.0	4.0	221.6	485.3	597.7	54.3
M07	Ponta Delgada	32.8213	-16.9920	123	17.27	142.0	24.6	368.8	821.3	1070.2	85.2
M08	Sanatório	32.6687	-16.9006	384	11.76	112.5	6.3	302.4	657.8	809.7	81.0
M09	Santana	32.7220	-16.7742	80	16.47	176.4	37.0	441.7	999.8	1338.9	104.2
M10	Canhas	32.6942	-17.1098	400	25.20	112.4	7.4	288.4	621.5	779.2	64.1
M11	Caniçal	32.7374	-16.7387	15	11.35	85.2	13.4	231.6	519.8	674.6	54.7
M12	Caramujo	32.7694	-17.0585	1214	30.43	352.5	49.5	945.0	2025.3	2653.0	130.4
M13	Curral das Freiras	32.7456	-16.9599	787	20.09	253.4	10.4	695.5	1437.9	1754.7	141.5
M14	Loural	32.7727	-17.0292	368	19.38	229.7	20.7	607.4	1283.9	1600.6	121.1
M16	Montado do Pereiro	32.7019	-16.8839	1260	6.54	285.7	25.4	761.0	1659.1	2080.4	134.2
M18	Ponta do Pargo	32.8108	-17.2589	339	40.68	118.2	13.5	296.3	625.5	817.8	62.1
M19	Porto do Moniz	32.8492	-17.1628	64	52.22	157.9	34.6	404.6	908.3	1234.2	70.3
M20	Queimadas	32.7831	-16.9022	881	34.68	275.9	61.2	731.2	1632.0	2207.3	122.7
M21	Rabaçal	32.7585	-17.1311	1233	88.95	274.8	28.7	735.9	1567.2	2005.3	115.8
M22	Ribeira Brava	32.6740	-17.0630	25	24.14	104.1	4.5	261.9	572.4	703.1	66.6
M23	Ribeiro Frio	32.7309	-16.8830	1167	19.08	300.7	41.0	810.6	1775.6	2276.1	149.1
M24	Santo António	32.6768	-16.9459	525	10.83	135.9	6.1	359.1	757.1	929.8	78.1
M25	Santo da Serra	32.7260	-16.8170	660	36.10	236.0	40.5	626.1	1367.2	1790.1	124.3
M26	Bom Sucesso	32.6620	-16.8960	291	6.98	101.3	4.9	269.4	587.7	719.6	66.8
M27	Santa Catarina	32.6936	-16.7731	49	7.75	93.3	7.6	240.7	526.8	660.3	62.2
M28	Cascalho	32.8290	-16.9250	430	1.83	190.8	47.5	496.8	1103.7	1537.8	72.8
M29	Poiso & Posto Florestal	32.7130	-16.8870	1360	4.60	286.6	29.0	769.1	1692.0	2134.5	135.6
M30	Vale da Lapa	32.8270	-16.9280	346	5.32	237.1	55.1	625.0	1373.2	1882.3	86.6
M32	Lapa Branca-Curral das F.	32.7190	-16.9650	610	22.46	190.0	14.2	515.0	1098.6	1360.0	82.5
M34	Serra de Água	32.7420	-17.0200	573	24.35	274.1	21.0	737.4	1574.8	1971.0	113.9
M35	Chão dos Louros E.	32.7570	-17.0180	895	9.55	344.3	30.1	926.7	1983.0	2509.7	153.4
M37	Lombo Furão	32.7490	-16.9110	994	13.62	338.0	34.6	891.9	1914.3	2416.2	163.0
M43	Meia Serra	32.7020	-16.8700	115	12.48	325.5	43.5	881.5	1887.0	2444.0	106.8
M44	Covão ETA	32.6750	-16.9630	510	22.46	132.4	5.9	353.3	760.4	930.3	88.8
M45	Encumeadas Casa EEM	32.7540	-17.0210	1010	2.32	304.2	26.3	816.0	1742.2	2202.4	132.7
M46	Santa Quitéria ETA	32.6610	-16.9510	320	9.20	103.9	4.2	274.9	597.5	726.5	70.6
M48	ETA São Jorge	32.8160	-16.9260	500	10.43	266.8	60.6	687.7	1531.1	2093.7	113.4
M49	Fajã Penedo	32.7920	-16.9600	620	23.84	322.6	45.9	836.8	1823.8	2378.8	148.5
M50	Cabeço do Meio-Nogueira	32.7357	-16.8987	995	4.08	350.2	34.8	921.2	1978.4	2477.9	170.0
M51	Ponta de São Jorge	32.8337	-16.9067	266	6.15	105.7	20.3	264.7	584.9	779.3	57.0
M53	Lido-Cais do Carvão	32.6366	-16.9365	20	4.99	48.4	1.7	127.3	278.4	340.1	30.5
Total area		–	–	–	741.00	–	–	–	–	–	–

The 41 rain gauges were selected to obtain the longest continuous daily rainfall series possible. However, all the rainfall series had missing data, as characterised in Figure 3-3. The missing data were filled in using the gap-filling method described in the next section. Based on the aggregation of the complete

daily rainfall data at each rain gauge, rainfall series for the following time-spans were obtained: month, quarter, semester, year, and annual maximum rainfall from 1–7 cumulative days.

3.2.3 Gap-filling of missing daily rainfall data. Multivariate imputation by chained equations (MICE)

The daily rainfall series were organised into a matrix with 29200 rows (cases, under a multivariate perspective) and 41 columns (variables), $\mathbf{X}_{29200 \times 41}$. The number of cases is equal the number of daily rainfalls, i.e., 80×365, and the number of columns, to the number of rain gauges. The leap days were discarded. The missing daily rainfalls were identified in the matrix by not available (NA).

The estimation of the missing data at daily level was addressed by Multiple Imputation (MI) which is a statistical technique that uses the distribution of the observed data to estimate a set of plausible values for the missing data [390, 365, 369]. The MI process may be summed up as: i) generating multiple imputed datasets in which the unknown missing data are replaced by m independent simulated values with a random component; ii) analysing multiple imputed datasets; and iii) combining estimates from multiple imputed datasets, i.e., the m estimates are combined into an overall estimate and variance-covariance matrix using Rubin's rules [367].

In order to perform MI, the Multivariate Imputation by Chained Equations (MICE) approach was explored for the Madeira Island's missing daily rainfalls, assuming that the mechanism under which the gaps occurred was Missing At Random (MAR). All simple imputation methods for missing data, i.e., listwise and pairwise deletion, arithmetic mean imputation, may give biased results in datasets with missing data at MAR [320]. Unbiased results can be obtained in this case by applying more sophisticated imputation methods, however, including either single or multiple imputations [10], such as the MICE. This multivariate imputation technique was applied because it is a practical approach for creating imputed datasets that has shown to perform well, although in different contexts and types of variables, when handling a great amount of missing values, especially in large datasets [366, 487, 114]. In climatic and hydrological settings, good estimates of missing values have been obtained by applying the MICE algorithm in comparison to other methods like multiple linear regression, inverse distance, Kriging [92] and Co-Kriging methods — e.g., solar radiation values by Turrado et al. [450], wind speed data by Wesonga [484], and daily rainfall values by de Carvalho et al. [81]. Despite its advantages, the MICE requires statistical and computation sophistication, and for this reason, single imputation methods seem to be more frequently used in hydrology [144].

MICE is also known as fully conditional specification and sequential regression multivariate imputation [22]. It involves filling in the missing values multiple times m through a specified algorithm — implemented in the package 'mice' in R (https://cran.r-project.org/) and described in more detail by Van-Buuren and Groothuis-Oudshoorn [454] — and creating multiple complete datasets for each missing value. Because of this, the analyses of multiple imputed data take into account the uncertainty in the imputations and yield accurate standard errors which depend mainly on the information in the observed data [455]. That is, observed data that are highly predictive of the missing values will make more consistent imputations resulting in smaller standard errors [453].

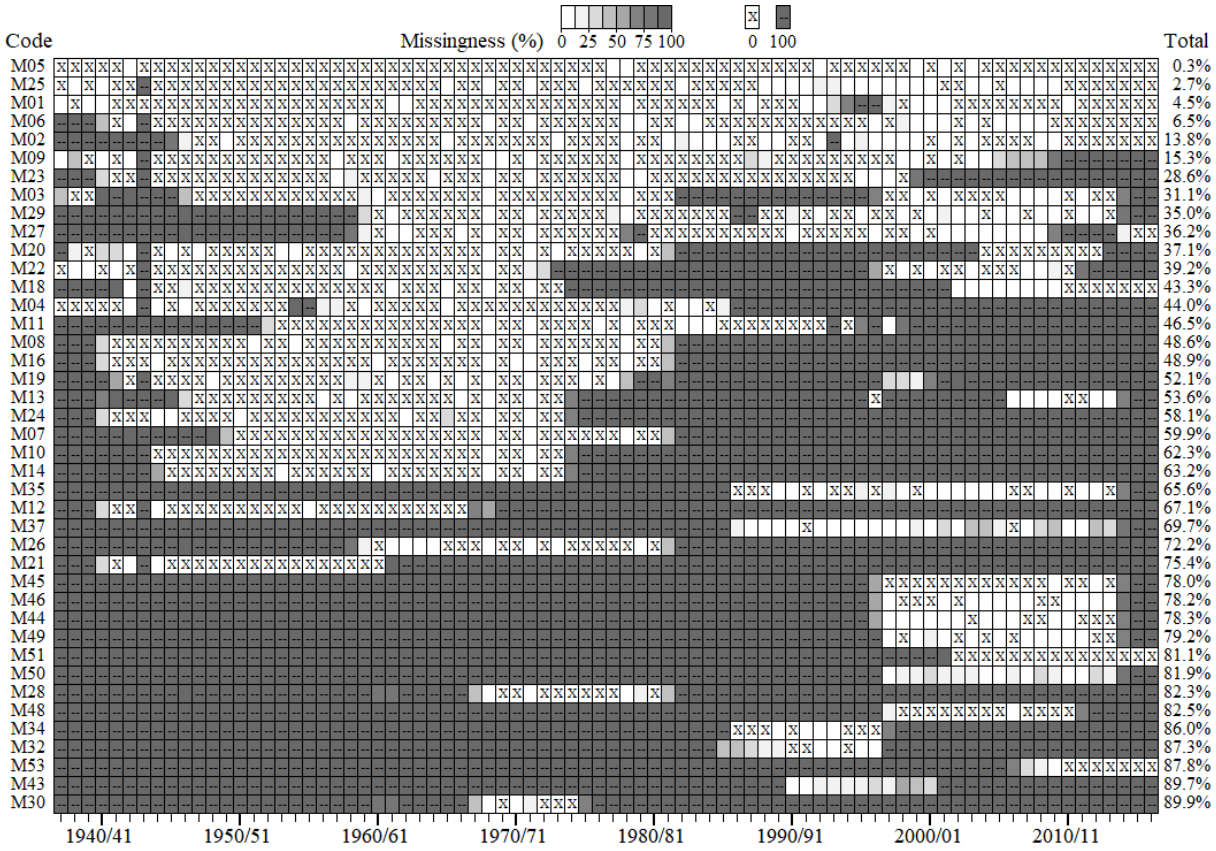

Figure 3-3: Characterisation of the missing daily rainfalls. On the left column, identification code of the rain gauge, and on the right column, total percentage of missing daily rainfalls in the 80-year reference period. Between the previous two columns, daily missingness in each year, ranging from 0% (crossed white cell) to 100% (dotted dark cell).

In the MICE algorithm, all missing values are initially filled in by simple random sampling with replacement from the observed values [487]. The first variable with missing values, i.e., w_1, is regressed on all other $(k-1)$ variables w_2, ..., w_k, restricted to individuals with the observed w_1. Missing values in w_1 are replaced by simulated draws from the corresponding posterior predictive distribution of w_1. Then, the next variable with missing values, i.e., w_2, is regressed also on all other $(k-1)$ variables w_1, w_3, ..., w_k, restricted to individuals with the observed w_2, and using the imputed values of w_1. Once again, missing values in w_2 are replaced by draws from the posterior distribution of w_2. These steps are repeated for all other variables with missing values in turn. This repeated process is called a cycle. It should be noted that the historical values are not replaced or changed throughout the gap-filling procedure.

In this regard, the application of the MICE algorithm based on the matrix of the daily rainfalls at Madeira Island, including both observed daily data and NAs, $\mathbf{X}_{29200 \times 41}$, was done by adopting $m = 30$ imputed plausible completed datasets and 50 maximum cycles for the 41 variables, following the logic already mentioned for the MI process (Figure 3-4). Although standard texts on MI suggest that small numbers of m (from 3 to 5) are adequate, a higher number was implemented as done by Graham et al. [160], however highly restricted to computation time, expecting lower differences between imputations and observed data [487]. The imputations were generated according to the predictive mean matching method [469] which is the default method for quantitative variables.

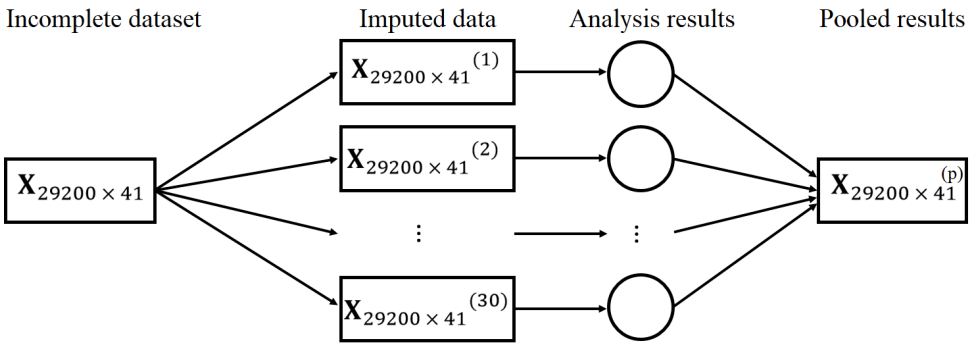

Figure 3-4: The three main steps of the MI algorithm applied to the gap-filling of the daily rainfalls, i.e., MICE. The incomplete data was organised into a matrix with 29200 rows (cases or days in the 80-year reference period) and 41 columns (variables or rain gauges), imputed for $m = 30$ plausible datasets which are analysed and pooled into a single completed dataset. Adapted from Van-Buuren and Groothuis-Oudshoorn [454].

In addition, the performance of MICE was examined based on the Pearson's correlation coefficient r [169] between observed values and their corresponding imputed values from synthetically generated missing rainfalls. For this purpose, synthetic false missing daily rainfalls, from sampling without replacement, were obtained for the rain gauge of M01-Areeiro (originally with only 5% of missing daily data). For this rain gauge, six scenarios of rainfall series with different total percentages of missing data were assembled — namely, 15%, 30%, 50%, 70%, 80%, and 90% — and filled in with the MICE algorithm. The observed data and imputations were compared at both daily and monthly (aggregated from the daily data) levels, expecting that the higher proportions of missing data, the lower the r coefficient would be.

3.2.4 Trend analysis

At each of the 41 rain gauges, 26 rainfall series, each 80-year long, were analysed for monotonic trends by means of the non-parametric Mann-Kendall and Sen's slope estimator tests: the series related to the twelve months of the hydrological year (OCT-SEP), the quarters (Q1-Q4), the semesters (SM1 and SM2), the year (HDY), and annual maxima (AM1-AM7). The tests applied are described in the next sections.

Mann-Kendall test

The presence of temporal trends and their statistical significance were verified by using the non-parametric Mann-Kendall (MK) test [247, 211]. This statistical method detects the presence of monotonic trends and is widely used in trend detection but also to ascertain the spatial variation of the temporal trends of climatic and hydrological time series when various stations are tested simultaneously [180]. It is a simple method, which does not require assuming normality, is robust against outliers, and can handle missing values [149, 370].

The null hypothesis H_0 of no trend is tested, i.e., for a time series, $X = \{x_1, x_2, ..., x_n\}$, the x_i observations are randomly ordered in time, against the alternative hypothesis, H_A, where the data follow a monotonic trend whether increasing or decreasing. In cases where the sample size $n > 10$, three values are calculated by the MK test: the test statistic S, the variance of S, $\mathrm{Var}(S)$, and the standard normal deviate Z. Positive values of Z indicate upward trends while negative values show downward trends.

In this research, the significance level of $\alpha = 0.05$ was adopted. When testing upward or decreasing monotonic trends at the α significance level, H_0 is rejected for an absolute value of Z greater than $Z_{1-\alpha/2}$. For $\alpha = 0.05$, $Z_{1-\alpha/2} = 1.96$. Although the MK method can be applied to discontinuous series, in its application to the rainfall series at Madeira Island an infilling was done before performing the trend analysis, as further discussed.

Sen's slope estimator test

The magnitude of the linear trends was computed using a non-parametric procedure developed by Sen [396], i.e., the Sen's slope estimator test. The test was used for all the time series regardless the statistical significance of the MK test. To derive an estimate of the slope Q, the slopes of all data pairs are calculated as follows:

$$Q_i = \frac{x_j - x_k}{j - k}, i = 1, 2, ..., N, j > k \tag{3.1}$$

where x_j and x_k are the values in years j and k, $j > k$, respectively. If there are n values x_j in the same time series, there will be $N = n(n-1)/2$ slope estimates, Q_i, whose median is the Sen's slope estimator. If the N values of Q_i are ranked from the smallest to the largest one, the Sen's estimator is defined as:

$$Q = \begin{cases} Q_{\frac{N+1}{2}} & \text{, if } N \text{ is odd} \\ \frac{1}{2}(Q_{\frac{N}{2}} + Q_{\frac{N+2}{2}}) & \text{, if } N \text{ is even} \end{cases} \tag{3.2}$$

Q is calculated by a two sided test at 100 $(1 - \alpha)\%$ confidence interval and a true slope can be obtained by the non-parametric test. A positive value of Q indicates an increasing (or upward) trend and a negative value of Q a decreasing (or downward) trend in the time series. The application of the Sen's Slope test requires continuous rainfall data.

Sequential change-point detection

The Sequential Mann-Kendall (SQMK) test was applied to the second quarter, first semester, hydrological year, and annual daily maximum rainfall series with statistical significant trends according to the MK test, in order to detect the approximate year of the start of changes in trend over time, i.e., change-points or breakpoint positions in the data. A change-point is a point in a time series at which the statistical properties of the distribution change [219]. The SQMK test also shows fluctuation in the trends over time [343]. The test sets up two standardised series, a progressive series $u(t)$ and a retrograde one $u'(t)$, which are both expected to fluctuate around zero [7, 422]. The following steps were applied to calculate $u(t)$ and $u'(t)$:

1. The values of the original series X_i were replaced by their ranks r_i, arranged in ascending order.

2. The magnitudes of r_i, $(i = 1, 2, ..., n)$ were compared with r_j, $(j = 1, 2, ..., i - 1)$, and at each comparison, the number of cases $r_i > r_j$ were counted and denoted by n_i.

3. A statistic t_i was defined as follows:

$$t_i = \sum_{k=1}^{i} n_k \tag{3.3}$$

4. The mean and variance of the test statistic were computed as:

$$E(t_i) = \frac{i(i-1)}{4} \text{ and } \mathrm{Var}(t_i) = \frac{i(i-1)(2i+5)}{72} \tag{3.4}$$

5. The sequential values of the statistic $u(t_i)$ were then calculated as:

$$u(t_i) = \frac{[t_i - E(t_i)]}{\sqrt{\mathrm{Var}(t_i)}} \tag{3.5}$$

Similarly, $u'(t_j)$ was calculated backward, starting from the end of the series. The point at which the progressive series $u(t)$ crosses the retrograde series $u'(t)$ and diverges beyond the specified confidence value (in this study, 95%, i.e., $\alpha = 0.05$), is considered as a statistically significant change-point in trend within the time series — rejecting the null hypothesis H_0 of no detectable abrupt change.

3.3 Results

The trend analysis at 41 rain gauges in Madeira Island was done based on 80 hydrological years of rainfall data, from 1937/38 to 2016/17. The Mann-Kendall and the Sen's slope estimator tests were used to identify trends for different time-spans (month, quarter, semester, year and annual maximum from 1–7 cumulative days). In addition, change-point of the trends were obtained by applying the SQMK test to those series with statistically significant trends for different time-spans. Table 3.1 presents some of the rainfall characteristics at the 41 rain gauges in the studied reference period. Before going into the results from the trend analysis those related to the validation of the MICE procedure are presented.

3.3.1 Performance of the gap-filling procedure (MICE)

The MICE algorithm was utilised on the dataset with $80 \times 365 = 29200$ cases or days (with both recorded and missing values) and 41 variables (the selected rain gauges), aiming at reconstructing the daily rainfall database used throughout this work. Thus, 80 years of complete daily rainfall data at 41 rain gauges were obtained. As mentioned, leap days were discarded.

Aiming at demonstrating that the MICE algorithm is able to make accurate estimates of the missing daily rainfall, observed data were compared to their respective imputations of synthetic missing data at the M01-Areeiro rain gauge. For that purpose, some observed daily rainfalls were randomly considered as false missing values and added to the original 5% of missing daily data in order to generate the six scenarios of missing data percentage defined in Section 3.2.3.

At the daily level, the Pearson's correlation coefficient r showed a strong association between the observed data and the corresponding imputations of false missing values for any of the different percentages of missing data (specified between brackets): $r = 0.91$ (15%), $r = 0.89$ (30%), $r = 0.89$ (50%), $r = 0.88$

(70%), $r = 0.88$ (80%), and $r = 0.87$ (90%). At the monthly level, r were even higher, ranging from 0.95 to 0.99, as indicated in Figure 3-5. The figure shows that, even in the scenarios with high percentages of missing daily rainfalls (e.g., 50%, 70%, 80%, and 90%), there is still a very good correspondence between the monthly rainfalls aggregated from solely daily records and those aggregated from both observed and imputed daily values. These results confirm the ability of the MICE as a rainfall gap-filling technique. It should be noted that the comparison between false incomplete and completed series could only be done for those months originally with complete records. Because the 5% of daily gaps occurred in a continuous and concentrated period, the percentage of months with gaps was also 5%, meaning that the maximum number of months that could be considered in the previous comparison was 912 months ($80 \times 12 \times 0.95$).

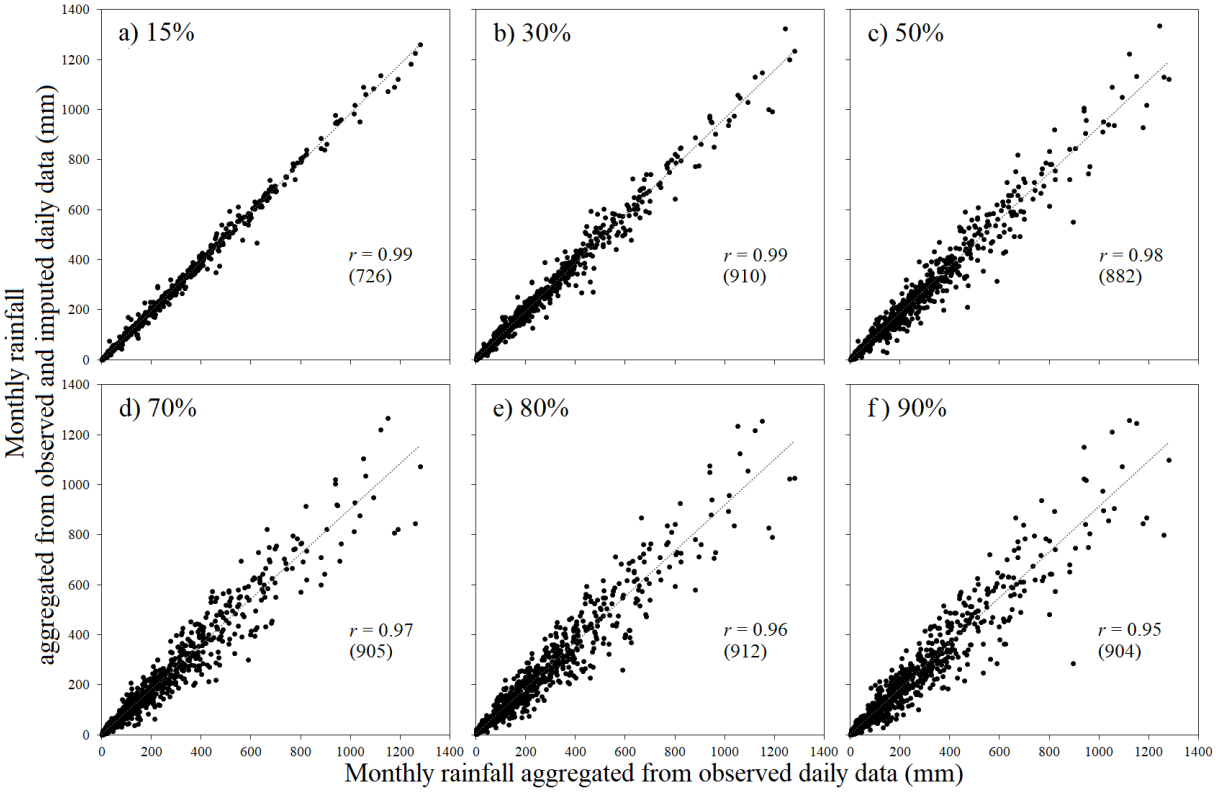

Figure 3-5: Performance of the MICE algorithm at M01-Areeiro rain gauge for different percentages of missing daily rainfalls, from **a)** 15% to **f)** 90%. Scatter plot of observed vs imputed monthly data. In each plot, r relates to the monthly Pearson's correlation coefficient, and the number of months under comparison is specified between brackets.

3.3.2 Spatial distribution of the rainfall over Madeira Island

Table 3.1 shows that the average rainfall in January ranges from 300.0–350.0 mm at the central region and northern slope, and from 50.0–80.0 mm at the southern slope. The average rainfall in August ranges from 40.0–60.0 mm at the central region and northern slope (e.g., the rain gauges of M01-Areeiro and M49-Fajã Penedo), and from 2.0–6.0 mm at the southern slope (e.g., M05-Funchal Observatório and M44-Covão ETA), respectively. This suggests that, areas with generally small rainfall amounts are located at the lowlands (up to 200 m.a.s.l.) of the southern slope, comprehending rain gauges such as M10-Canhas in the southwest, and M27-Santa Catarina (situated in the vicinity of Madeira International Airport Cristiano

Ronaldo CR7) in the southeast. Although these areas are the most important agricultural regions of the island [294], very small rainfall amounts were recorded in the rainiest quarter of the hydrological year, i.e., QT2.

In general, the results confirm that the spatial distribution of the rainfall in Madeira Island is highly variable and strongly affected by its complex topography, with the highest amounts occurring at the higher elevations of the central region, regardless the time-span.

3.3.3 Monthly, quarterly, semesters, and annual rainfall trends

Clearly, establishing the robustness of trend detection methods is vital to a comprehensive definition of changes in rainfall rates. Applying a trend test to data series with gaps, as it happens in Madeira, may result in overestimation or underestimation of the trends, i.e., in an unreliable characterisation [348].

Because the MK test allows for gaps or missing value, as previously mentioned, an exploratory analysis was done prior to its comprehensive application aiming at understanding the influence of the gaps in the results from the trend analysis. For this purpose, the annual rainfall series with more than 10 values were selected. The analysis showed that, as for the Z values, the results based on the original and on the after-filling rainfall data could differ significantly.

Figure 3-3 shows that the gaps in the rainfall series in Madeira occur mostly concentrated in some subperiods. At the same time, the effects of the climate change became worldwide visible after the middle 1960's [31], by means of increasing air temperature and, for the regions located at lower latitudes, decreasing rainfall. The combined effect of the gaps distribution and of the expected consequences of the climate change fully support the comparison of the results from the trend test applied to the series before and after the gap-filling procedure. In fact, for the rainfall series with gaps mostly concentrated in more recent years (expectably, the driest ones), the trend analysis often resulted, comparatively to the after gap-filling dataset, in less pronounced downward trends — such as in M12-Caramujo with Z of -0.63, for the incomplete dataset, and of -1.82, for the completed dataset. The opposite occurs for the series with gaps occurring essentially at early years of the study period (the wettest ones): the downward trends based on the incomplete dataset are much more pronounced than those from the completed series (e.g., M29-Poiso & Posto Florestal with Z of -3.02 before MICE application, and of -1.98 after gap-filling). Therefore, the incomplete series, mainly those with high number of gaps, are unsuitable for the trend analysis because they do not capture the effect of climate change as is portrayed, for instance, in M01-Areeiro, almost without gaps and denoting a pronounced decrease of the rainfall in recent years.

The results from the rainfall trend analysis for the completed data at different time-spans are reported in Table 3.2. The following time-spans without statistically significant trends at any of the 41 rain gauges were not included: October, December, February, April and May.

According to Table 3.2, the second quarter (January-March, QT2) showed eight significant downward trends while each of the remaining three quarters showed only two. For the first and wettest semester, from October to March (SM1), the month of January denoted the highest number of rain gauges with significant trends. The same applies to August in the second and driest semester, from April to September (SM2). This last semester is the only one in which upward trends may also occur. At the yearly level (HYD),

Table 3.2: Sen's slope estimates in mm year^{-1} at the 41 rain gauges in the reference period (1937/38 to 2016/17) for different time-spans. The statistically significant results (based on the MK test for $\alpha = 0.05$) are highlighted in bold. QT1, QT2, QT3, and QT4 stand for, respectively, first quarter (October-December), second quarter (January-March), third quarter (April-June), and fourth quarter (July-August). SM1 and SM2 stand for first semester (October-March) and second semester (April-September), respectively. The year time-span (HDY) is from October to September. AM1 stands for annual daily maximum.

Code	Month							Quarter				Semester		Year	Daily
	NOV	JAN	MAR	JUN	JUL	AUG	SEP	QT1	QT2	QT3	QT4	SM1	SM2	HDY	AM1
M01	-2.29	***-2.14**	-1.34	0.01	***-0.06**	***-0.21**	-0.44	-2.15	***-5.64**	-0.55	-0.74	***-7.70**	-1.35	***-9.30**	-0.50
M02	-1.13	-1.81	-0.24	0.05	-0.02	-0.23	-0.26	-1.08	-3.18	-0.43	-0.52	-4.65	-0.84	-3.53	0.12
M03	-0.14	-0.89	-0.67	0.06	0.01	0.00	-0.09	1.14	-2.45	0.36	-0.05	-1.13	0.37	-0.59	0.36
M04	-0.34	***-1.98**	-1.04	0.11	***0.24**	0.09	-0.07	0.98	***-3.81**	-0.33	0.25	-2.73	-0.05	-2.00	0.37
M05	-0.05	-0.28	-0.26	0.00	0.00	0.00	0.00	0.47	-0.60	0.07	-0.02	-0.30	0.19	-0.12	0.18
M06	0.13	-0.10	-0.43	0.00	0.00	0.00	0.00	0.80	-0.38	0.19	-0.02	0.46	0.27	0.48	0.17
M07	-0.75	-0.47	-0.16	0.03	0.06	-0.13	-0.25	-0.78	-0.86	0.04	-0.39	-1.83	-0.26	-2.20	0.11
M08	-0.08	-0.37	-0.24	0.04	***0.04**	0.00	0.01	0.42	-0.82	0.09	-0.01	-0.38	0.21	-0.26	0.14
M09	-0.43	-0.50	-0.13	0.02	-0.04	***-0.27**	***-0.44**	-0.38	-0.35	-0.16	***-0.86**	-0.71	-0.85	-1.49	0.10
M10	0.23	-0.26	-0.45	0.04	***0.06**	0.00	0.04	0.86	-0.93	0.10	0.11	-0.05	0.16	0.33	0.07
M11	-0.24	-0.18	-0.08	0.04	0.02	-0.07	-0.09	0.07	-0.12	0.19	-0.15	-0.02	0.05	0.20	0.12
M12	-1.20	***-2.11**	-1.04	0.24	0.22	-0.12	0.05	-0.77	***-5.18**	-0.39	0.00	-6.13	-0.64	-5.96	***-0.37**
M13	-0.30	-1.46	-1.03	0.04	***0.00**	0.00	0.08	1.10	***-3.70**	-0.64	0.10	-2.84	-0.66	-3.17	0.09
M14	-0.78	-1.18	-0.36	0.13	***0.11**	0.00	-0.08	0.29	-2.31	0.03	-0.01	-2.59	-0.13	-2.71	-0.15
M16	-1.48	***-1.85**	-0.88	0.15	***0.18**	-0.02	-0.31	-1.87	***-4.25**	-0.04	-0.23	***-5.94**	-0.47	***-5.92**	-0.15
M18	***-0.68**	***-0.91**	***-0.52**	-0.06	0.00	0.00	-0.11	***-1.78**	***-1.97**	***-0.60**	-0.10	***-3.78**	***-0.79**	***-4.25**	***-0.29**
M19	-0.48	-0.27	0.00	0.12	0.15	0.03	0.03	-0.59	-0.38	0.51	0.01	-0.82	0.49	0.14	0.07
M20	-0.87	-1.11	-0.06	***0.38**	0.19	-0.21	-0.12	-1.53	-1.48	***1.35**	-0.24	-3.33	1.11	-2.66	0.02
M21	-0.04	-1.37	-0.72	***0.25**	***0.03**	0.16	-0.02	0.88	-2.61	0.28	0.42	-2.42	0.72	-2.00	-0.01
M22	0.55	-0.09	-0.32	0.03	***0.00**	0.00	0.07	***2.16**	-0.20	0.34	0.10	1.66	***0.56**	***2.35**	***0.34**
M23	-0.67	-1.08	-0.09	0.22	0.10	-0.14	-0.24	-0.21	-1.66	0.87	-0.32	-1.58	0.58	-1.17	0.02
M24	0.21	-0.48	-0.37	***0.08**	***0.07**	***0.05**	0.09	1.39	-1.32	0.19	0.28	-0.51	0.56	0.19	0.15
M25	-0.88	-0.73	-0.17	0.11	0.05	-0.15	-0.38	-0.78	-1.61	0.40	-0.71	-2.56	-0.48	-2.78	0.00
M26	-0.10	-0.37	-0.30	0.02	0.02	-0.02	0.00	0.62	-0.84	0.07	-0.01	-0.60	0.15	-0.28	0.08
M27	-0.09	-0.24	-0.15	-0.02	-0.02	***-0.06**	-0.03	0.44	-0.48	0.16	-0.14	0.05	0.05	0.25	0.20
M28	-0.63	-0.70	-0.03	0.20	0.10	-0.14	-0.15	-1.07	-0.73	0.56	-0.29	-1.80	0.32	-1.44	0.12
M29	-1.43	***-1.82**	-0.82	-0.07	-0.07	***-0.25**	-0.37	-1.55	***-3.94**	-0.51	-0.69	-5.11	-1.41	***-5.88**	-0.12
M30	-0.38	-0.70	-0.22	0.24	0.14	-0.14	-0.12	-0.41	-1.28	0.77	-0.18	-1.83	0.55	-1.59	0.17
M32	-0.47	-0.90	-0.49	0.05	0.01	-0.06	-0.06	0.35	-1.98	0.12	-0.09	-1.63	-0.09	-1.84	0.13
M34	-0.44	-1.14	-0.04	0.03	-0.03	***-0.14**	-0.09	1.08	-2.14	0.33	-0.21	-0.62	0.01	0.01	0.06
M35	-1.22	-1.86	-0.37	0.10	-0.05	-0.18	-0.15	-0.31	-3.47	0.34	-0.33	-3.64	-0.23	-3.36	-0.01
M37	-0.97	-1.23	-0.04	0.06	-0.03	-0.20	-0.31	1.24	-2.19	0.47	-0.49	-1.11	-0.28	-1.30	-0.05
M43	-0.88	-1.42	-0.86	0.25	0.22	-0.05	0.00	0.16	***-3.99**	0.20	0.08	-3.98	0.15	-3.77	0.07
M44	0.00	-0.51	-0.33	0.00	-0.01	***-0.05**	0.01	0.97	-1.09	0.05	-0.01	-0.36	0.28	-0.07	***0.38**
M45	-0.64	-1.40	-0.04	0.04	-0.06	***-0.18**	-0.15	0.95	-2.19	0.19	-0.31	-1.02	-0.08	-0.51	***0.32**
M46	-0.10	-0.31	-0.18	0.01	-0.01	***-0.03**	0.00	0.89	-0.62	0.19	-0.01	0.02	0.35	0.65	***0.33**
M48	-0.51	-0.59	0.11	0.19	0.03	-0.28	-0.55	0.00	-0.38	0.36	-0.75	-0.93	-0.28	-1.02	0.31
M49	-0.86	-1.30	-0.01	0.10	0.01	***-0.30**	-0.44	0.65	-1.99	0.27	-0.72	-1.07	-0.37	-1.46	0.30
M50	-1.07	-1.22	-0.11	-0.02	-0.06	***-0.25**	-0.34	0.71	-2.27	0.17	-0.60	-1.68	-0.63	-1.36	0.14
M51	-0.08	-0.10	-0.02	0.06	-0.02	-0.11	-0.18	0.33	0.10	0.12	***-0.34**	0.67	-0.07	0.55	0.16
M53	0.01	-0.09	-0.07	0.00	0.00	***-0.02**	0.02	0.57	-0.16	0.17	0.00	0.24	0.27	0.50	0.08

the rainfalls followed a downward trend in 30 rain gauges, four of which with statistical significance. Figure 3-2b summarises the output from the trend analysis, by showing the location of the rain gauges with statistically significant trends (p-value $< \alpha$, with $\alpha = 0.05$) and the sign of those trends (positive or negative) at any of the following five periods: January, August, second quarter (QT2) and first semester (SM1), and year (HDY). These periods were selected because of the high number of significant trends during the same according to Table 3.2 (e.g., January has the highest number of significant trends out of the dry months, the same for August out of the wet months; July also complies with the previous criteria but it was not chosen because it represents redundant information regarding August). Figure 3-2b shows that there is enough evidence to reject the null hypothesis, H_0, of no trend at 19 out of the 41 selected rain gauges.

The Inverse Distance Weighting (IDW) with exponent 2 [32] was applied to the Sen's slope estimates aiming at characterising the spatial distribution of the trends in the selected five periods, as shown in

Figure 3-6. Although the figure was based on the results at the 41 rain gauges, only those with statistical significant trends are highlighted by their codes and trend estimates (between brackets).

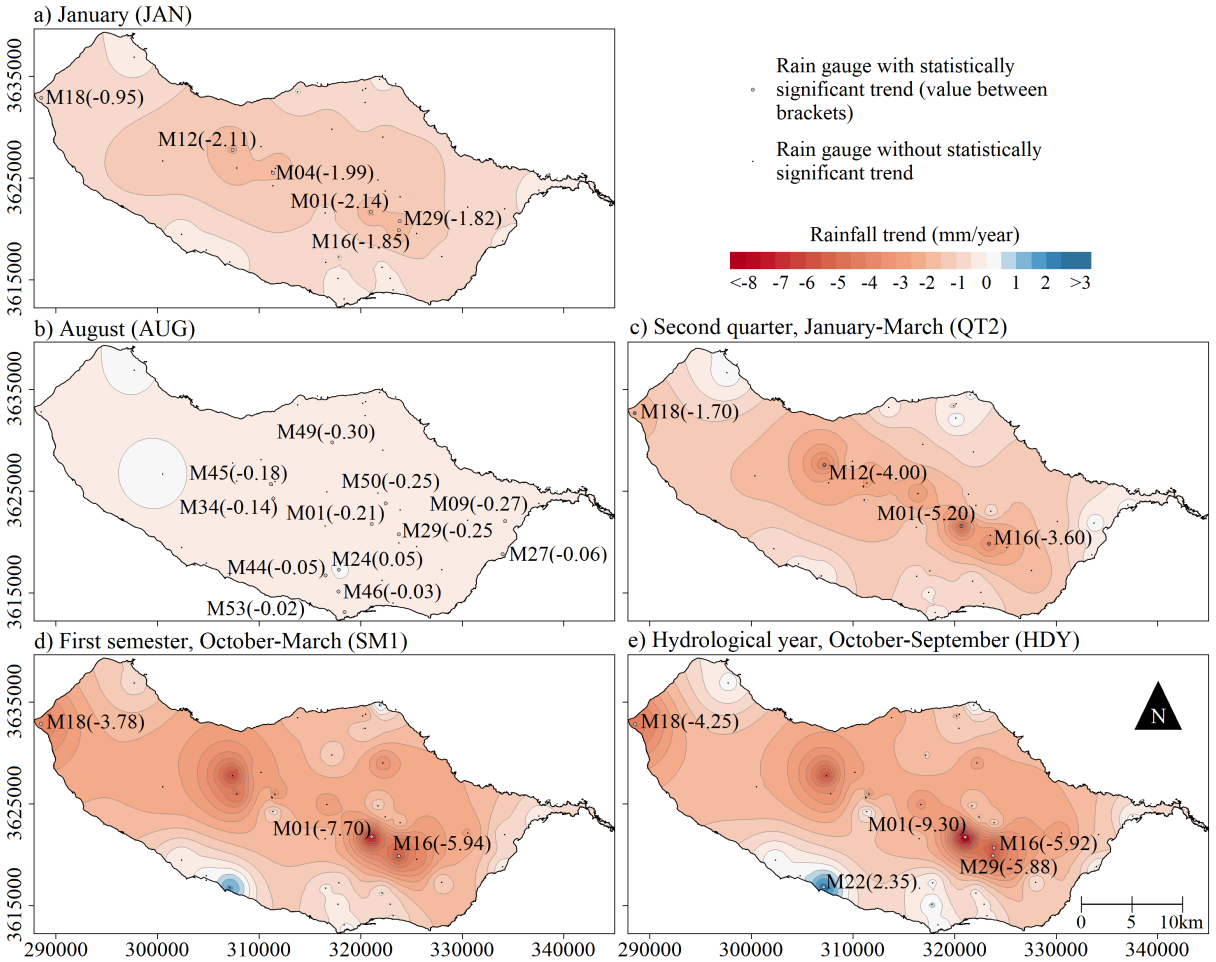

Figure 3-6: Spatial distribution of the rainfall trends in mm year^{-1} (1937/38–2016/17) for January and August, for the second quarter and first semester of the hydrological year, and for the hydrological year itself.

For January (Figure 3-6**a**), only six rain gauges denote significant trends with a weighted average of -1.58 mm year^{-1}. The weighted average trend in August is less pronounced compared to the one in January: of -0.15 mm year^{-1} at the 12 rain gauges with statistical significance (Figure 3-6**b**). When accounting for the previous rates one should keep in mind the differences between rainfalls in January and August.

For the second quarter, QT2, all the 41 rainfall series revealed downward trends (Figure 3-6**c**), however, only 10% with statistical significance (Table 3.2). From the figure, it is evident that the higher decreases occur in the central part of Madeira Island, with magnitude varying from -3.60 mm year^{-1}, at the rain gauge of M16-Montado do Pereiro, to -5.20 mm year^{-1} at the M01-Areeiro rain gauge (the rain gauge at the highest elevation).

The trends in the first semester (SM1 — Figure 3-6**d**) and in the year (HDY — Figure 3-6**e**) followed a pattern similar to the one of QT2, i.e., with more pronounced downward trends in the highlands (central region), although with a smaller percentage of significant trends: respectively, 7% and 12%

(Table 3.2). However, for both SM1 and HDY, the number of upward trends increased at the southern slope, specifically, in the coastal region that goes from the rain gauges of M22-Ribeira Brava to M05-Funchal Observatório. In general terms, Figures 3-6**d** and 3-6**5** show that the rainfall decrease in the wet semester and in the year is much more pronounced than in the other time-spans.

Overall, the results suggest a downward trend in all the rainfall time series at the central region of Madeira Island (e.g., M01-Areeiro, M29-Poiso & Posto Florestal, and M50-Cabeço do Meio), and an upward trend, although very small, in a narrow coastal strip of the southern slope (e.g., M22- Ribeira Brava). Decreasing rainfall in the high central region may exacerbate the already existing water scarcity problems [104] because, as mentioned, the replenishment of groundwater is dependent on the rainfall in that region.

3.3.4 Annual maximum (from 1–7 cumulative days) rainfall trends

Regarding the annual maximum short duration series, Figure 3-7 depicts the spatial distribution of the Sen's slope estimates from 1 to 7 cumulative days highlighting only the significant rainfall trends, as done for Figure 3-6. Table 3.1 indicates that the highest values for 1-day maximum rainfall (AM1) are systematically recorded at the island's highlands (the average values for the 41 rain gauges are also reported in the table). The trend analysis (Figure 3-7) showed that the highest number of rain gauges with statistically significant trends occurred for AM1 (Figure 3-7**a** — Table 3.2) ranging approximately from -0.30 to 0.40 $\mathrm{mm\,year^{-1}}$. The spatial distribution of the AM1 trends, whether significant or not, showed positive values over most of the island except for rain gauges at higher elevations (e.g., M01-Areeiro).

For longer cumulative periods, from 2 to 6-day (Figures 3-7**b** to 3-7**f**), the trends are mostly negative (downward) — although with a smaller number of significant trends — and the spatial distribution of the trends is similar to that of HDY, but with smaller rates. For the 7-day annual maximum rainfalls (AM7) the trends range from -1.17 to -0.65 $\mathrm{mm\,year^{-1}}$ (Figure 3-7**g**). Some of the downward trends from AM3 to AM6 at the high central switched to upward trends for AM7, although without statistical significance.

3.3.5 Sequential change-point detection in rainfall trends

The SQMK test was used to obtain fluctuations in the trends over time, and possible abrupt temporal shifts in the rainfall series. The analysis considered some time-spans and for each one of them, only the rain gauges with rainfall series denoting significant trends according to the MK and Sen's slope tests (identified in Table 3.2), as follows:

- Second quarter (QT2): M01-Areeiro, M04-Encumeada de São Vicente, M12-Caramujo, M13-Curral das Freiras, M16-Montado do Pereiro, M18-Ponta do Pargo, M29-Poiso & Posto Florestal, and M43-Meia Serra. All these rain gauges are located in the central highlands.
- First semester (SM1): M01-Areeiro, M16-Montado do Pereiro, and M18-Ponta do Pargo.
- Hydrological year (HDY): M01-Areeiro, M16-Montado do Pereiro, M18-Ponta do Pargo, M22-Ribeira Brava, and M29-Poiso & Posto Florestal.

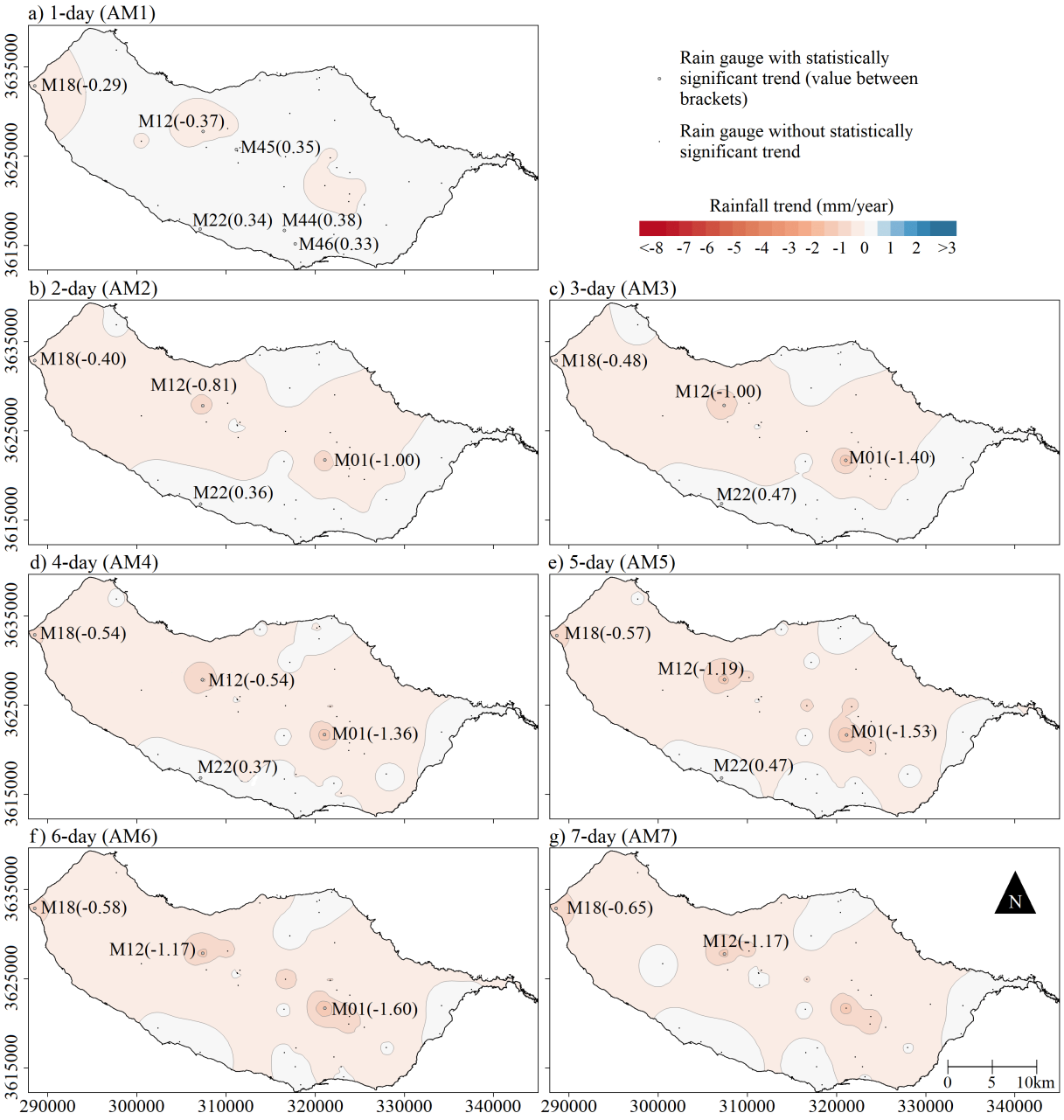

Figure 3-7: Spatial distribution of the rainfall trends in mm year^{-1} (1937/38–2016/17) for annual maximum rainfall series, from 1 to 7 cumulative days (AM1 to AM7).

– Annual daily maximum (1-day, AM1): M12-Caramujo, M18-Ponta do Pargo, M22-Ribeira Brava, M44-Covão ETA, M45-Encumeadas Casa EEM, and M46-Santa Quitéria ETA.

The results of the probable change-point were evaluated for a significance level of 5% based on the p-value and are shown in Figure 3-8.

For the eight rain gauges in which QT2 was analysed, the intersections of $u(t)$ and $u'(t)$ allow to identify several change-points between the years 1965/66 and 1974/1975, and only a few ones between 1989/90 and 1990/91. In regards to the progressive series $u(t)$, the rainfall shows an increasing trend from 1937/38–1969/70 followed by a general decrease.

A similar behaviour is observed regarding SM1, however, the abrupt shifts are significant only from

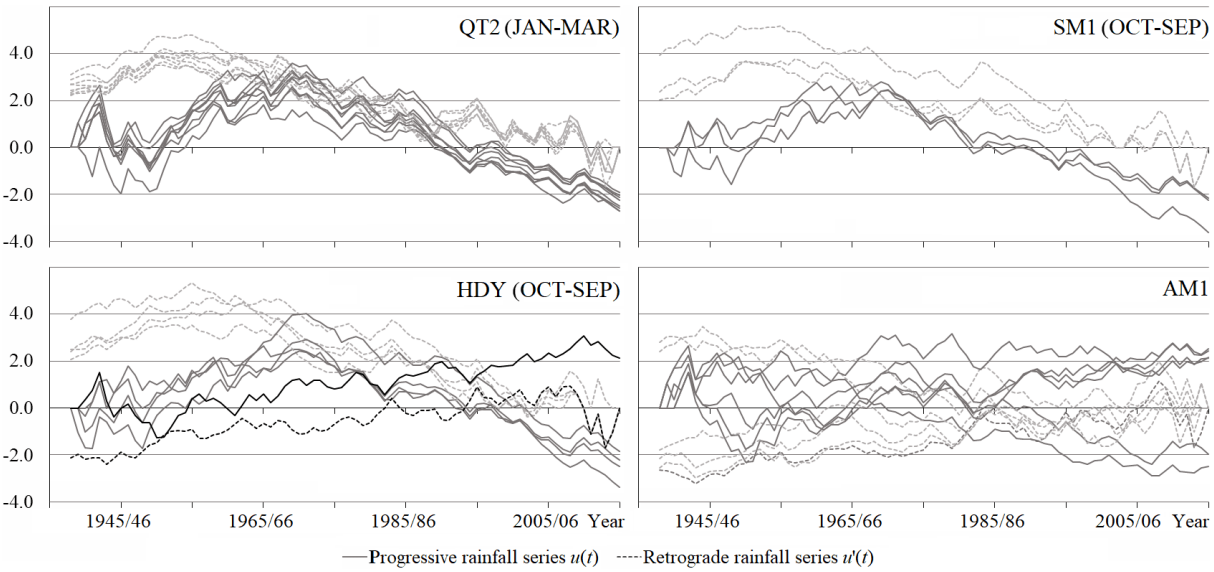

Figure 3-8: Change-point detection results from the SQMK test at the rain gauges with significant trends for different time-spans (number of rain gauges for QT2, SM1, HDY, and AM1, of 8, 3, 5, and 5, respectively). Several statistically significant breakpoints — given by the intersection of progressive, $u(t)$ (solid line), and retrograde, $u'(t)$ (dashed line), rainfall series — can be detected between 1965/66 and 1974/75.

1965/66–1974/75. In what concerns to HDY, the trends are clearly positive from 1937/38–1969/70 and negative from 1970/71–2016/17. That is, the $u(t)$ series have gradual upward trends from the very beginning of the reference period, then, converge to the $u'(t)$ series, which are intersected around 1969/70. From this year onward, such trends switch to very steep downward trends (except for the only southern slope rain gauge with significant trend, M22-Ribeira Brava, with a sustained upward trend and no temporal shifts).

AM1 shows an unclear behaviour without pronounced trends and only with two rain gauges denoting abrupt changes — M22-Ribeira Brava and M18-Ponta do Pargo, respectively, in 1951/52 and in 1970/71.

3.4 Discussion

3.4.1 Reconstruction of the 80-year rainfall database

Unlike single imputation, MI considers uncertainty in predicting missing values by creating multiple complete datasets [22, 208, 512, 13, 261]. Results confirmed that MI, performed by the implementation of the MICE algorithm, is a potentially useful method to fill in missing daily rainfall data in datasets with large percentages of NAs — as was performed and corroborated at monthly scale for Madeira Island in a previous work [117]. Despite these advantages, and others recognised by different authors from different scientific fields [such as 126, 213], it should be acknowledged that the major drawback of the MICE algorithm is the lack of a robust theoretical justification compared to other approaches [22] when performing MI to handle missing data – such as Markov Chain Monte Carlo (MCMC) random sampling method with Monte Carlo integration using Markov chains [143]. Thus, justification of the MICE procedure has rested on empirical studies rather than theoretical arguments [487] as done in the

present work, namely, by means of the validation presented in Section 3.3.1. Hence, care should be taken when generalising the MICE algorithm, like any other powerful technique, to fill in missing data. Another drawback is the fact that the MICE algorithm is very time-consuming when applied to large incomplete datasets. In its application to Madeira Island, the time required to get one complete dataset performed on a computer with a processor Intel Core i3 and an installed memory of 4.00 GB was more than two days.

The overall spatial distribution of the average annual rainfall in Madeira Island in the 80 years analysed (Figure 3-2**a**) is in accordance with other studies [331, 335] being characterised by more abundant rainfall in the central and northern regions (especially at higher elevations) than in the southern slope. Baioni et al. [26], among other authors, analysed historical data regarding flood events in Madeira Island based on climate data. The authors reported average annual rainfalls which concur well with the ones obtained in this work. For M27-Santa Catarina, they present an average annual rainfall from 1941/42–1991/92 of 681.4 mm, which is very close to the 660.3 mm of Table 3.1. According to the Climate Atlas of the Archipelagos of Canary Islands, Madeira and Azores [58], the average annual rainfalls in the 30-year period from 1971/72–2000/2001 at M02-Bica da Cana and M01-Areeiro were 2635.0 mm and 2620.0 mm, respectively; these values are approximately 1.5% higher than those now obtained based on 80 years of data, which also supports the decrease of the rainfall towards the present. The overall comparison of these annual averages highlights the Madeira's rainfall pattern stability, a typical characteristic of islands within Macaronesia [72].

At monthly scale, differences may occur between the rainfall amounts for recording periods shorter than the one adopted in the present work. An example is the average rainfall in December at M05-Funchal Observatório: according to Chazarra et al. [58] from 1971/72–2000/01 it accounted for 109.4 mm. Although this value is relatively close to our estimate for the same 30-year period (approx. 116.0 mm), it is higher than the 95.1 mm now obtained for the 80-year period, from 1937/38–2016/17. In the specific case of this rain gauge, the rainfall data shows that shorter and more recent periods recorded smaller amounts of rainfall in December (the average rainfall from 2001/02–2016/17 is 90.0 mm), although without significant trends.

The coherence of the rainfall amounts from the present work and from the previous ones reinforces the applicability of the MICE algorithm to fill in daily rainfall series.

3.4.2 Spatio-temporal rainfall trends

In terms of seasonality, the first semester (SM1, October-March), i.e., Madeira Island's rainy season, is becoming drier with downward rainfall trends occurring in the months of November, January, February and March. It should be noted that although the average monthly rainfalls vary widely from one rain gauge to another, the obtained rainfall trends denote a spatial regularity. Regarding the within-the-year distribution of the rainfall, some transition zones can be identified. For instance, in the first semester the highest average monthly values occur in the month of November at the highlands (central region) and northern slope (e.g., rain gauges of M01-Areeiro and M14-Loural, respectively, with 420.9 mm and 247.5 mm) whereas at the southern slope and in a few parts of the central region, December is the wettest

month of the first semester and also of the hydrological year (e.g., M05-Funchal Observatório, M29-Poiso & Posto Florestal, with 95.4 mm and 336.1 mm, respectively). Nevertheless, the average rainfalls in November, December and even January only differ slightly.

The semester from April to September (SM2) exhibits minor downward rainfall trends in April, August and September, while the months of June, July and August present upward trends, also very small. In any case, it is acknowledged that the SM1 and SM2 rainfall amounts in recent periods have changed. An example is the rain gauge of M01-Areeiro — of great importance for water management in Madeira Island. In the last fifteen years, i.e., since 2002/03, eleven SM1s (73%) were drier than the long-term average while in the period of sixty-five years, from 1937/38–2001/2002, only thirty (46.2%) evenly distributed and with rainfall below average occurred. In the same rain gauge and semester, since 2013/14 the rainfall from October to March has been consistently below the long-term 80-year average (decrease of the rainfall from 13% — year of 2016/17 — to 61% — year of 2013/14). Out of the last fifteen SM2s in M01-Areeiro, fourteen exhibited below-average conditions (decrease of rainfall from 6%, year of 2015/16, to 69%, year of 2004/05). In contrast, at two lowland southern slope rain gauges — M05-Funchal Observatório and M22-Ribeira Brava — the same semesters (SM2) were above their respective long-term average (nine out of fifteen, and ten out of fifteen, respectively), which suggests wetter conditions. In fact, the 80-year Sen's slope estimates for SM2, ranging from -1.41 to 1.11 $\mathrm{mm\,year^{-1}}$ (not reported), were positive in more than half of the forty-one rain gauges, although only one estimate had statistical significance.

From an annual point of view, downward rainfall trends predominated in the northern slope and central region of Madeira Island. Most annual rainfall series at a narrow coastal strip of the southern slope presented upward trends, which were confirmed as significant by the MK test only in one case (M22 with 2.35 $\mathrm{mm\,year^{-1}}$).

The rainfall trends given by the Sen's slope and their spatial distribution at both SM1 and HDY time-spans are quite similar (Figures 3-6**d** and 3-6**e**). This is not a surprising result, given the higher contribution of that semester to the annual amount. The previous similarity coincides with the findings, based on different methodologies, from other researchers studying past, present, and future climate, more specifically, of small islands of Macaronesia, that show evident decreases in annual rainfall over northern slopes and neglectable changes over southern slopes [380, 268, 72, 252]. Regarding Madeira Island, Cropper and Hanna [73] when applying the Theil–Sen slope estimator [11], to the data at M05-Funchal Observatório from 1981/82–2010/11, detected an upward trend (not statistically significant) of 6.1 millimetres per decade ($\mathrm{mm\,dec^{-1}}$). This result differs from the one now obtained, which suggests a decreasing trend of 1.2 $\mathrm{mm\,dec^{-1}}$ (Table 3.2), although also not significant. For this very reason, when analysing results from different researchers, care should be taken because there may be discrepancies due to the length of the recording periods. Therefore, establishing continuous rainfall time series as long as possible is necessary to more accurately characterise the rainfall regime, and, consequently, detect changes in rainfall patterns.

An increasing rainfall trend in the annual maximum 1-day series (AM1) was recorded over 64.44% (477.49 $\mathrm{km^2}$) of Madeira Island. Only the results for AM1 are discussed because the time of concentration, defined as the response of a watershed to a rainfall event [165], in the island's catchments is less than

1 day [467] which makes the intense rainfall for longer duration less important. It should be noted that annual maximum daily rainfall data represents one of the most important and readily available measures of extreme rainfall and is employed to evidence how rainfall extremes have changed over time [266, 133, 485]. Moreover, an increase in extreme rainfall is projected for many areas worldwide, including the North Atlantic region, in the coming decades [109]. In Madeira Island, very short duration intense or extreme rainfall events (typically within 1-hour duration) can trigger flash floods, landslides and debris flows particularly in the wet season, as those registered in the years of 1920, 1929, 1956, 1979, 1993, 1997, and more recently, in February 2010 which caused almost 50 casualties and about 1.4 billion euros of material losses [360, 26, 78, 158].

Overall, the maximum daily rainfall trends obtained in this work (Figure 3-7) are consistent with numerous studies such as the outputs of climate models in other regions of the globe — more specifically, employing global coupled general circulation models (CGCMs) — which suggest that the intensity of extreme rainfall will increase under global warming, including many regions where average annual rainfall decreases [471, 216, 485, 270].

3.4.3 Rainfall areal-anomalies in the wet seasons and year

The anomalies of the spatial rainfall distribution and their temporal evolution were computed for the wet seasons (QT2 and SM1) and for the year (HDY). For each year from 1937/38 to 2016/17, the rainfall anomaly at a given rain gauge and time-span was defined as the ratio between the rainfall at that time-span and the corresponding long-term average, and assigned to an anomaly class. The following five anomaly classes were considered: below 0.5, from 0.5 to 0.8, from 0.8 to 1.2, from 1.2 to 1.5, and above 1.5. The anomalies thus obtained for the 41 rain gauges were spatially weighted according to the Thiessen method [441] — Table 3.1, ATP column — and made dimensionless by reference to the island's area. The results achieved are depicted in Figure 3-9. The figure shows that the dry spells over the island (first two classes, for anomalies < 0.5 and from 0.5–0.8) occurred periodically, however at irregular time intervals. In contrast, the wet ones (class of > 1.2) were spatially more extensive and concentrated until the end of the 1960's.

3.4.4 Abrupt shifts and a North Atlantic Oscillation teleconnection

The continuing rainfall decline in recent wet seasons, detected for Madeira, has been previously acknowledged in other latitudinal locations and climate zones [e.g., 318, 456, 443, 289, 352]. Some of the studies focused on the sustained decreasing trends and below-average-conditions (in terms of hydrological droughts, in some cases), their related impacts on water resources, and on the possibility of rainfall reduction in the wet season being part of global climate drivers' variability. One of these drivers is the North Atlantic Oscillation (NAO) which can be defined as the measure of the strength of the Icelandic Low and the Azores High and it accounts for much of the rainfall variability over the Euro-Atlantic area, and it is an important teleconnection pattern to explain the changes in rainfall [193].

Aiming at understanding the possible effects of climate change over Madeira Island for QT2, SM1,

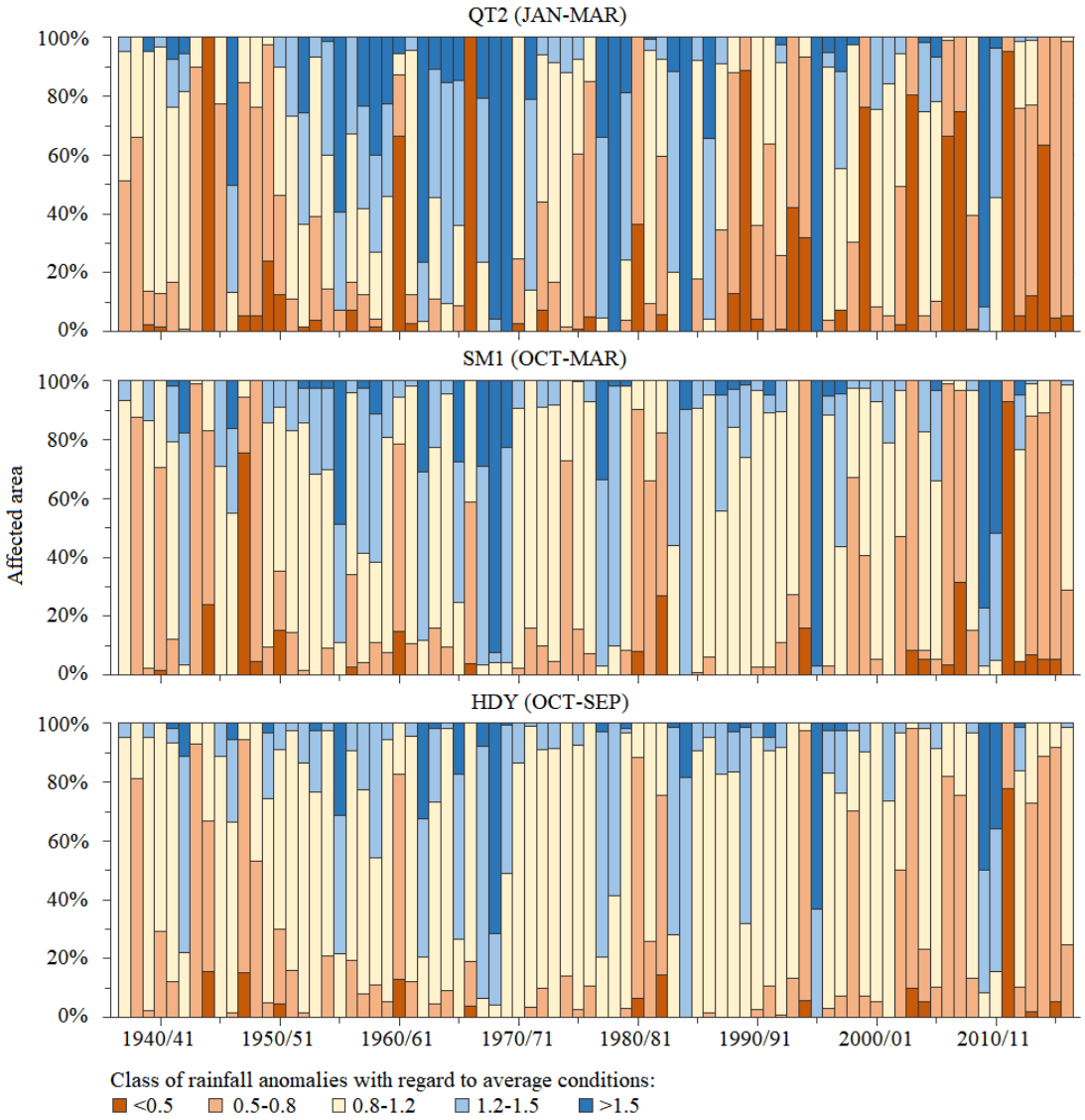

Figure 3-9: Dimensionless areal weighted rainfall anomalies for the second quarter (QT2), first semester (SM1), and year (HDY). The 100% of affected area refers to 741 km^2.

and HDY, the 80-year period was divided into two subperiods, based on the change-point findings from Figure 3-9, and analysed by applying the same previously used trend models (the coupled MK and Sen's slope tests). The results are shown in Table 3.3. For the sake of comparison, the results for the reference period (Table 3.2) were also included.

Table 3.3 shows that from 1937/38–1969/70 the rainfall over the study area had a particularly pronounced upward trend, followed by a downward trend from 1970/71–2016/17 with a noticeable increase in the number of rainfall trends with statistical significance in both subperiods. It should be noted that the SQMK results (not reported) denoted no change-points for these two subperiods.

Additionally, the SQMK test was also applied to the Seasonal (JFM, JAN-MAR) North Atlantic Oscillation index (NAOI) and Annual NAOI signals, both station-based and defined by Jones et al. [204]. The station-based data was retrieved from National Center for Atmospheric Research (NCAR) — [194]. The analysis was conducted over the same 80-year period (1937/38–2016/17). The SQMK results of both NAOI signals and the progressive series $u(t)$ from Figure 3-8, are depicted in Figure 3-10 which indicates:

Table 3.3: Sen's slope estimates in mm year^{-1} for the 41 rain gauges in the reference period and in two subperiods (accounting for 80, 33, and 47 hydrological years, respectively). The statistically significant results (based on the MK test for $\alpha = 0.05$) are highlighted in bold with an asterisk.

Code	QT2 (Jan-Mar)			SM1 (Oct-Mar)			HDY (Oct-Sep)		
	1937/38 – 2016/17	1937/38 – 1969/70	1970/71 – 2016/17	1937/38 – 2016/17	1937/38 – 1969/70	1970/71 – 2016/17	1937/38 – 2016/17	1937/38 – 1969/70	1970/71 – 2016/17
M01	***-5.64**	***25.94**	***-11.13**	***-7.70**	***36.86**	-13.98	***-9.30**	***40.46**	***-23.37**
M02	-3.18	***23.86**	***-8.23**	-4.65	***44.09**	***-14.97**	-3.53	***48.73**	***-21.22**
M03	-2.45	***11.42**	***-4.99**	-1.13	***17.05**	-3.92	-0.59	***16.51**	-4.55
M04	***-3.81**	***22.74**	***-11.61**	-2.73	***33.01**	***-15.46**	-2.00	***35.52**	***-20.61**
M05	-0.60	***4.91**	-1.19	-0.30	4.70	-1.71	-0.12	3.69	-1.73
M06	-0.38	5.87	-1.36	0.46	6.44	-1.08	0.48	5.22	-0.43
M07	-0.86	***8.13**	-3.20	-1.83	***12.64**	-4.79	-2.20	***11.7**	-5.20
M08	-0.82	***7.5**	-2.46	-0.38	8.14	-3.45	-0.26	6.78	-3.75
M09	-0.35	***7.09**	-3.21	-0.71	***13.21**	-3.16	-1.49	12.68	-4.83
M10	-0.93	***7.01**	-2.53	-0.05	7.43	-3.12	0.33	***8.36**	-2.56
M11	-0.12	3.98	-1.95	-0.02	***7.58**	-2.94	0.20	***6.55**	-3.69
M12	***-5.18**	14.23	***-8.79**	-6.13	18.53	-10.56	-5.96	14.46	-13.42
M13	***-3.70**	***23.52**	***-7.29**	-2.84	***31.07**	-8.18	-3.17	***33.07**	-11.35
M14	-2.31	***17.31**	-4.03	-2.59	***25.06**	-3.58	-2.71	***21.77**	-4.04
M16	***-4.25**	***16.11**	***-7.1**	***-5.94**	***28.17**	-10.14	***-5.92**	***28.42**	***-13.08**
M18	***-1.97**	***7.86**	***-3.78**	***-3.78**	***9.63**	***-7.33**	***-4.25**	***7.41**	***-9.75**
M19	-0.38	***7.61**	***-5.39**	-0.82	***13.8**	***-6.78**	0.14	***16.47**	***-8.96**
M20	-1.48	7.12	-3.84	-3.33	13.53	-5.04	-2.66	7.70	-5.27
M21	-2.61	***20.7**	***-7.51**	-2.42	***29.57**	-8.71	-2.00	***29.52**	***-10.94**
M22	-0.20	***6.94**	-0.84	1.66	6.32	1.51	***2.35**	4.79	2.53
M23	-1.66	7.14	***-7.98**	-1.58	17.38	-9.63	-1.17	20.83	-12.26
M24	-1.32	***12.07**	-2.88	-0.51	***17.02**	-3.70	0.19	***16.45**	-3.97
M25	-1.61	5.49	***-6.79**	-2.56	4.84	***-11.1**	-2.78	5.86	***-15.78**
M26	-0.84	***7.26**	-1.83	-0.60	***8.51**	-2.74	-0.28	***7.82**	-2.07
M27	-0.48	***5.84**	***-2.59**	0.05	***8.58**	-2.73	0.25	***5.7**	-3.14
M28	-0.73	5.66	***-4.88**	-1.80	11.81	-6.11	-1.44	10.92	***-7.49**
M29	***-3.94**	***20.73**	***-8.56**	-5.11	***34.02**	***-14.35**	***-5.88**	***39.38**	***-18.48**
M30	-1.28	8.47	***-5.42**	-1.83	***16.3**	-6.71	-1.59	12.85	***-7.53**
M32	-1.98	***13.16**	***-5.13**	-1.63	***16.97**	-6.30	-1.84	***15.86**	-7.25
M34	-2.14	***20.49**	-5.99	-0.62	***28.33**	-5.67	0.01	***31.4**	-7.38
M35	-3.47	***27.26**	***-7.98**	-3.64	***38.83**	-11.78	-3.36	***42.17**	***-14.84**
M37	-2.19	***25.31**	-6.77	-1.11	***34.29**	-2.66	-1.30	***34.55**	-5.26
M43	***-3.99**	***18.06**	***-6.47**	-3.98	***22.55**	-7.24	-3.77	***20.87**	-8.99
M44	-1.09	***10.73**	-2.51	-0.36	***14.5**	-3.07	-0.07	***14.75**	-2.79
M45	-2.19	***23.96**	-5.95	-1.02	***38.1**	-7.30	-0.51	***37.75**	-10.82
M46	-0.62	***7.47**	-1.50	0.02	8.04	-0.95	0.65	7.13	-0.49
M48	-0.38	***8.87**	-4.96	-0.93	***18.99**	-4.09	-1.02	***15.66**	-6.69
M49	-1.99	***25.13**	***-6.87**	-1.07	***38.03**	-6.74	-1.46	***34.83**	-10.48
M50	-2.27	***28.23**	-7.72	-1.68	***38.37**	-5.93	-1.36	***39.22**	-9.06
M51	0.10	2.96	-1.26	0.67	5.28	-0.31	0.55	3.97	-0.91
M53	-0.16	2.36	-0.76	0.24	3.24	-0.49	0.50	2.29	-0.55

i) for the seasonal NAOI, two statistically significant breakpoints in 1968/69 and 1973/1974; and ii) for the annual NAOI, six breakpoints in 1969/70, 1974/75, 1980/81, 1983/84, 1988/89, and 1990/1991. Some of these change-points are close to those for QT2 and HDY (see also Figure 3-8), i.e., are close to the year 1969/70. Besides the year-to-year fluctuations whether in the seasonal or in the annual signals, approximately from the middle 1960's onwards, Figure 3-10 suggests downward linear trends of the progressive series of the rainfall, and upward trends in the case of NAOI progressive series. These results are in accordance with a trend analysis of a NAOI based on the difference of normalised pressures between Lisbon, Portugal, and Stykkisholmur, Iceland [193].

Several studies have been looking at the increasing capacity to correlate accurately the NAO patterns and rainfall changes [249]. In fact, significant relationships between changes in rainfall and the NAO signal

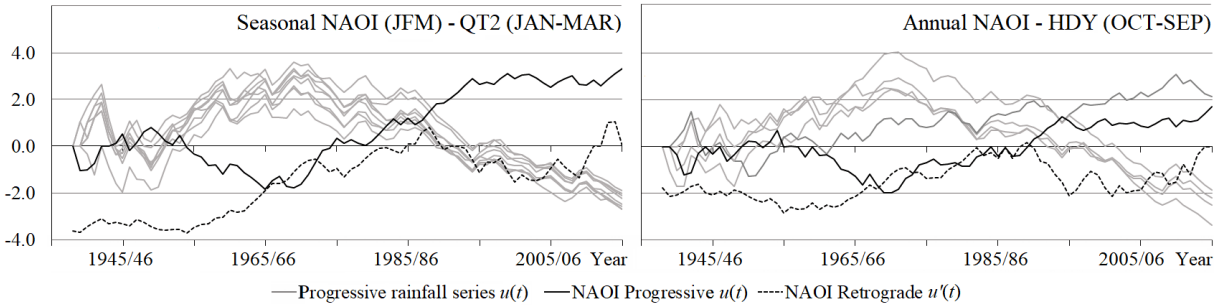

Figure 3-10: Change-point detection results from the SQMK test applied to Seasonal NAOI (JFM, Station-Based) and Annual NAOI data (1937/38 to 2016/17). The NAOI progressive $u(t)$ and retrograde $u'(t)$ series are marked in solid and dotted black lines, respectively; the progressive rainfall series $u(t)$ at the rain gauges with statistically significant rainfall trends are marked in solid grey lines (QT2 and HDY from Table 3.2, also reported in Figure 3-8).

in small islands of Macaronesia has been found by different authors [183, 380]. Hence, the results from the SQMK analysis for rainfall and NAOI, were compared considering all the 41 rain gauges adopted in this study, even though only a few ones denoted significant trends. Figure 3-11 shows the spatial distribution of the Pearson correlation coefficient r between the NAOI progressive series, and those of the QT2 and HDY rainfall series.

Figure 3-11 relates only to the correlation between progressive series $u(t)$, because for retrograde series $u'(t)$ the results are close albeit symmetric. According to the figure, correlations are stronger for the second quarter (QT2), ranging from $r = -0.90$ (rain gauges of M12-Caramujo, M16-Montado do Pereiro, M18-Ponta do Pargo, all of them denoting significant downward trends) to $r = 0.17$ (M23-Ribeiro Frio with a non-significant downward trend). Concerning the year, correlation values range from $r = -0.86$ (M16-Montado do Pereiro with a significant trend of -5.92 mm year^{-1}) to $r = 0.46$ (M22-Ribeira Brava with a significant upward trend of 2.35 mm year^{-1}). This clearly indicates a coherent link between rainfall changes in Madeira Island and the NAO signal. Such link is negatively stronger in the high central region where the most pronounced downward rainfall trends occur (e.g., the rain gauge of M16-Montado do Pereiro has a notable downward annual rainfall trend and a correlation with NAOI trend of $r = -0.86$). Overall, the NAOI trends are also associated to upward rainfall trends in the lowland areas but to a lower degree.

According to Cropper and Hanna [73] for Macaronesia, significant negative correlations between the NAOI and rainfall are displayed for the Azores, across all seasons, and for Madeira Island, from October to March, though these conclusions were based only on the data in one rain gauge, the M05-Funchal Observatório. Thus, changes in NAO seem to explain the reason for the significant decrease in the rainfall amounts in the wet season. This is in accordance with the findings in this work — additionally supported by a much higher number of rain gauges with complete long rainfall series — regarding the rainfall trends and the proposed NAOI teleconnection. Also a similar strong relationship between NAO and winter rainfall has been observed for the Canary Islands — located about 450 km south of Madeira Island, and part of Macaronesia too [183], with clear correlations between NAO and rainfall at southern slopes of the western islands. As stated by Cropper [72], the strong rainfall reduction in Canary Islands and Madeira Island from October to March may be associated with a migration of the Azores high-pressure system

[200] in a warmer climate.

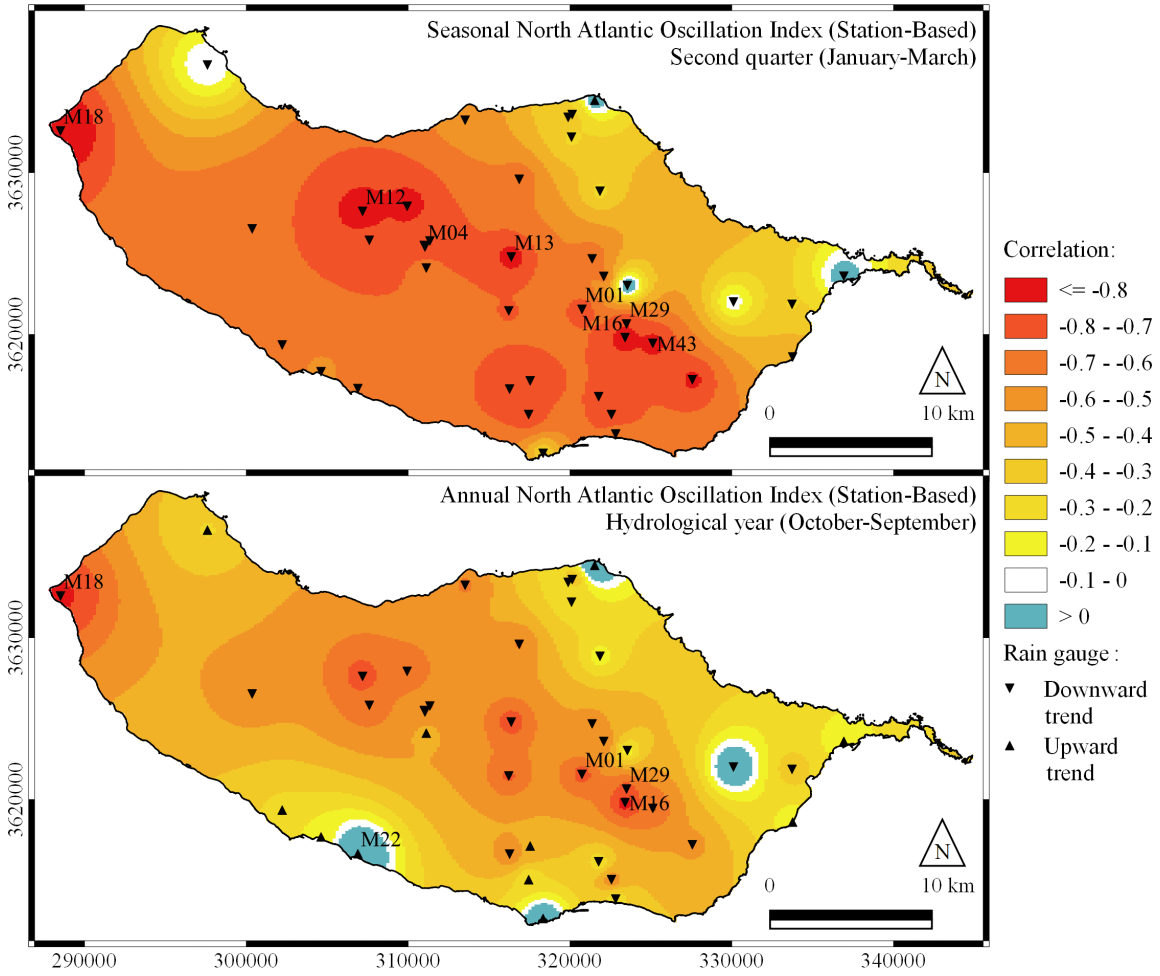

Figure 3-11: Spatial distribution of the Pearson correlation coefficient between the progressive series $u(t)$ from the SQMK test (1937/38–2016/17) of the North Atlantic Oscillation index (NAOI) and of the rainfall series for the second quarter (QT2) and the year (HDY). The rainfall trends (Table 3.2) are depicted as triangles with different orientation according to the trend sign. The rain gauges with statistically significant rainfall trends are identified by their codes.

3.5 Conclusions

The current consensus on the increasing climate variability, rainfall extremes, and their related outputs may compromise water security (for sustained decreasing rainfall conditions) and, on the other hand, be the trigger of landslides and floods occurrence. Small islands, like Madeira, with limited surface water resources but also with a relief that boost debris flows and flash floods, are particularly vulnerable to the effects of climate change.

The objective of the research underlying this work was to provide a comprehensive characterisation of the rainfall trends at different time-spans in Madeira Island, from short durations to the year, to identify shifts in the temporal patterns of the rainfall series, and to investigate possible connections between those shifts and climate driver's signals, such as the NAOI, that could be used for forecasting purposes.

Although some of the previous objectives have been addressed by other authors, the combined number

of rain gauges analysed and the length of the time series was always very small. Differently from those studies, the present one utilised 80 years of daily rainfall data (from 1937/38 to 2016/17) at 41 rain gauges evenly distributed over the Island, which makes it the first investigation on rainfall data to be conducted under such conditions, in terms of high number of rain gauges, length of complete time series, and continuous spatial characteristics of the phenomenon.

Due to the several gaps of the rainfalls, a robust machine learning method for Multiple Imputation, namely the Multivariate Imputation by Chained Equations (MICE), was applied and validated, also for the first time, to fill in the gaps of daily rainfalls. The rainfalls for the time-spans greater than the day were obtained by aggregating the daily data as has been performed in similar analyses [507, 146, 306].

The planning and management of freshwater resources in Madeira Island aiming at ensuring the water security, especially under the background of global warming [250], requires the understanding of the rainfall behaviour. Madeira's climate is projected to become hotter and drier [380], with much less rainfall at the northern and central regions in the wet season. These expectations are aligned with the results from the research. Decreases of the rainfall, namely in the wet months and seasons, may end in significant loss of freshwater, imposing serious water stresses on the island's hydrological resources which depend mostly on the rainfall capturing in the highlands.

It should be acknowledged that there is more than one way in which gap-filling, rainfall trends, change-point detection, rainfall areal-anomalies, and climate driver teleconnections may be calculated. Whether the spatio-temporal distribution of rainfall and its changing patterns are important or not will depend on how the results are to be used and so, therefore, any characterisation cannot be considered as the final one. Maps, as those produced by the study, showing the rainfall trends in any specific place of Madeira or even for the link between rainfall and NAO trends provide detailed tools for the planning and management of freshwater resources. To anticipate future changes in Madeira water resources availability is of the utmost importance, because of the island's groundwater recharge process which will be severely affected if the present downward rainfall trends persist.

Nevertheless, it is uncertain whether the more pronounced decreasing rainfall trends in recent years can be considered as lasting or not. Despite the good results achieved, a comprehensive analysis between the continuing upward trend of NAO during the last five decades and the consequences for rainfall is still necessary and left open for further investigation, eventually based on a better defined NAOI for Madeira Island.

Chapter 4

Winter Rainfall Trends Teleconnected to the North Atlantic Oscillation

Due to the length constraints imposed by the Editors of Water Resources Management journal, this chapter is a moderately extended version of: Espinosa, L. A., and Portela, M. M. (2020). Rainfall trends over a small island teleconnected to the North Atlantic oscillation-the case of Madeira Island, Portugal. *Water Resources Management*, 34(14), 4449-4467, https://doi.org/10.1007/s11269-020-02668-4

Abstract

For improving sustainable water resources management and planning at local and regional scales, specifically in small islands, long-term and recent rainfall trends due to temporal shifts in major climatic drivers should be investigated based on dense and long-running ground data series — as done in this research work for the North Atlantic Portuguese island of Madeira (741 km^2). Monthly, wet season and annual rainfall trends have been obtained via the non-parametric Mann-Kendall (MK) and the Sen's slope estimator tests for 41 rain gauges spanning from 1940/41 to 2016/17 (77 hydrological years, each starting on October 1). By means of the Sequential Mann-Kendall (SQMK) test, abrupt temporal shifts in the wet season and annual rainfall, and in the North Atlantic Oscillation index (NAOI) series have been identified on the late 1960's — sandwiched by two subperiods with clearly opposite trends. In general, the results suggest considerably and statistically significant decreases, exacerbated in recent years, at the central region of the island which is one of the most important locations in terms of fresh water security. Additionally, this work provides a solid basis to explain the climate change effects on the Madeira rainfall, suggesting that abrupt changes of the North Atlantic Oscillation (NAO) climatic driver can be directly linked to rainfall variability based on the established strong teleconnection. These findings are expected to contribute to improve the actions towards sustainable water management in the island, and of some other small islands with similar climatic characteristics influenced as well by large-scale circulation patterns.

Keywords:

Rainfall trends; small island; Madeira Island; teleconnection; North Atlantic Oscillation index.

4.1 Introduction

The lack of resolution in current Global Climate Models (GCMs), ground-based data and long-term analyses at small spatial scales with respect to components of both, weather and climate systems —

such as temperature and rainfall — make climate change monitoring systems integration a challenging task [226]. These constraints result, at local and regional scales, in a poorly understood present climate, and in highly uncertain future climatic conditions. Nevertheless, on wider scales recent studies suggest nonuniform and rapidly increasing shifts in long-term patterns of rainfall, streamflow, and evaporation with direct impact on fresh surface and groundwater availability [20, 226]. Rainfall in particular, is a critical component of the water and energy cycles [189], and due to its high spatio-temporal variability is one of the most difficult fluxes to analyse. So, as critical as the rainfall role is in those cycles, analyses to address its variability, trends, change-points, and its possible teleconnection to major climatic drivers are of the utmost importance for sustainable water resources management and planning. These circumstances show the need of such analyses moving from global to local or regional scales with emphasis on small islands as in the case of the present work which focuses on rainfall trends and their possible teleconnection to a climatic driver's trends for a North Atlantic small island, namely, Madeira Island.

According to Falkland et al. [123], based on the size, island environments with less than 2,000 km^2 or with a maximum width less than 10 km can be categorised as small islands — sub-classifications according to their topography as either "high" or "low" can be also adopted. These environments provide important ecosystem services [83] due to their unique landscapes; and are major assets for the countries they often integrate, for their strategic and economic benefits [380]. The hydrology, water resources development, assessment and management issues of small islands are more noticeable and distinct from the ones faced by larger islands or even continental areas [185] as a result, generally, of their inherent climatic conditions and physical characteristics (e.g., high rainfall variability, small catchment areas, limited groundwater and surface water storage capacity). The high level of vulnerability to natural hazards (e.g., extreme hydrological events) and multiple climate stressors have been recognised as threats to sustainable water management in small islands. However, the distinction between observed and projected impacts of climate stressors, especially climate change, is often not clear in the literature [303]. Thus, understanding the long-term and up to date climatic variables trends and teleconnections, particularly for rainfall on small islands are fundamental issues in a changing environment.

The scientific evidence and information presented on the periodical assessment reports by the Intergovernmental Panel on Climate Change (IPCC) [255, 310, 185] have stressed that the vulnerability and exposure of small islands to rainfall changes would continue to escalate — with increased frequency of extreme rainfall events and their related outputs, i.e., droughts and floods, increased rainfall during the summer months, and a decrease in rainfall during the wet or rainy seasons. Owing to the effects of climate change, a significant reduction in freshwater availability is expected in small islands of the North Atlantic Ocean due to the decrease of the rainfall during the wet season [185]. However, the identification of significant changes in freshwater availability, derived from rainfall trend analysis, is hampered by the high spatial and temporal variability of rainfall itself and commonly, by the short length of the available rainfall data series [510] and the lack of rainfall records at daily and sub-daily scales due to the very coarse density of observation stations [440].

In small islands the rainfalls might be influenced by a same weather phenomenon and affected whether in the same direction or in the opposite one [476]. Weather phenomena — such as the North Atlantic

Oscillation (NAO), frontal structures, and low-pressure systems — can be defined as natural events that occur as a result of one or a combination of the water cycle, pressure systems and the Coriolis effect [437]. NAO defined as fluctuations in the difference of atmospheric sea-level pressure (SLP) between two dipoles, often the Icelandic Low and the Azores High [195], is a driver of rapid climate change in the Northern Hemisphere. In fact, it is one major mode of climate variability that influences the rainfall amounts trends in the North Atlantic [430]. Therefore, different NAO phases can be associated with the rainfall trends direction, i.e., either upward or downward trend [271].

During the last two decades, the number of scientific studies and publications has increased regarding rainfall trends for different climate zones [268, 379, 507, 481]. For instance, a significant decline in rainfall of the wet period in Southern Australia has been observed from 1958 to 2007 which has been found to be closely related to variations in SLP (10-40° S, 110-155° E) and projected to continue decreasing [289]. In contrast, the tropical climate region of Myanmar has been predicted to encounter excessive precipitation especially in the rainy season according to future climate impact on streamflow study [300]. For Southern Continental Portugal, a recent study on long-term rainfall trends has been carried out at different time-spans based on complete monthly data from 1910/11 to 2017/18; the research showed that the rainfall is noticeably diminishing and that its within-the-year pattern is changing, with reduction of the duration and of the relative contribution of the rainy period [329]. The variability and trends of rainfall and the influence of various climate indices has been assessed in previous studies [352]. Nevertheless, the number of independent scientific studies on rainfall trends in small islands, specifically for the North Atlantic Ocean region, has still been quite limited. This is mainly due to the inadequate capacity to collect continuous long-running rainfall records for individual locations [185].

Trend analyses for the European Macaronesia (comprehending the Canary Islands, the Azores and the Madeira Archipelago, which main island is Madeira) have reported generalised downward rainfall trends in different periods of the year, although based on a relatively small number of rainfall series [252, 73]. Expressly for the Portuguese island of Madeira, the presence of linear monotonic trends has been previously investigated based on 135 years (from 1865 to 2000) of annual rainfall records, however, at only one rain gauge located very close to the coast of the southern slope [268]. Rainfall data from 14 rain gauges of Madeira Island coupled with GCMs have been used to produce scenarios of rainfall anomalies [380], with particular attention given to the wet and dry seasons in the late XXI century. Those scenarios indicated that the annual rainfall in the island would continue to decrease in the 2070–2099 period, with wet seasons even drier than those of the 30-year control period, from 1961 to 1990.

On this basis, the present work aims at (i) providing new insights into wet season and annual rainfall trends, and (ii) proposing a NAO–rainfall trend teleconnection for the small island environment of Madeira. To this end, a comprehensive rainfall trends characterisation was made based on a much denser network of 41 rain gauges, as depicted in Figure 4-1, and also on continuous longer-running rainfall time series — from October 1940 to September 2017, i.e., 77 hydrological years. Hence, this is the first thorough and broad study on rainfall trends in Madeira Island addressing the long-term wet season and annual rainfall changes, but also the recent rainfall trends dynamics, whose results may improve the water resources management and planning of the island.

Though several studies have been conducted on trends and abrupt changes in rainfall for larger areas, few have ever focused on rainfall changes and probable driving factors associated for small islands such as Madeira. The structure of this paper is (i) quantifying significant linear monotonic trends via the non-parametric Mann-Kendall (MK) and the Sen's slope estimator tests applied to monthly, wet season, and annual rainfall series — aggregated from the complete daily data; (ii) ascertaining the possible effects of climate change on rainfall trends based on a change-point technique, i.e., Sequential Mann-Kendall (SQMK) test; and (iii) conducting an exploratory analysis, at seasonal and annual scales, on the teleconnection between rainfall trends and those of a mathematical definition of the NAO, i.e., the North Atlantic Oscillation index (NAOI) due to the possibly strong effects of NAO changes on the rainfall variability.

4.2 Material and methods

4.2.1 Study area

The archipelago of Madeira with a total area of 797 km^2, is formed by (i) the selected case study, i.e., Madeira Island (Figure 4-1) which is the most important and largest island within the archipelago with an approximate area of 741 km^2, a length of 57 km in the E-W direction and a maximum width of 22 km in the N-S direction, by (ii) Porto Santo Island, with 42 km^2, and (iii) the Desertas Islands (Deserta Grande, Bugio and Ilhéu Chão) with 14 km^2 of total area. Madeira centred at 32°43'12" N 16°58'12" W, is located about 700 km from the Western African coast and 870 km from the Southern Continental Portugal.

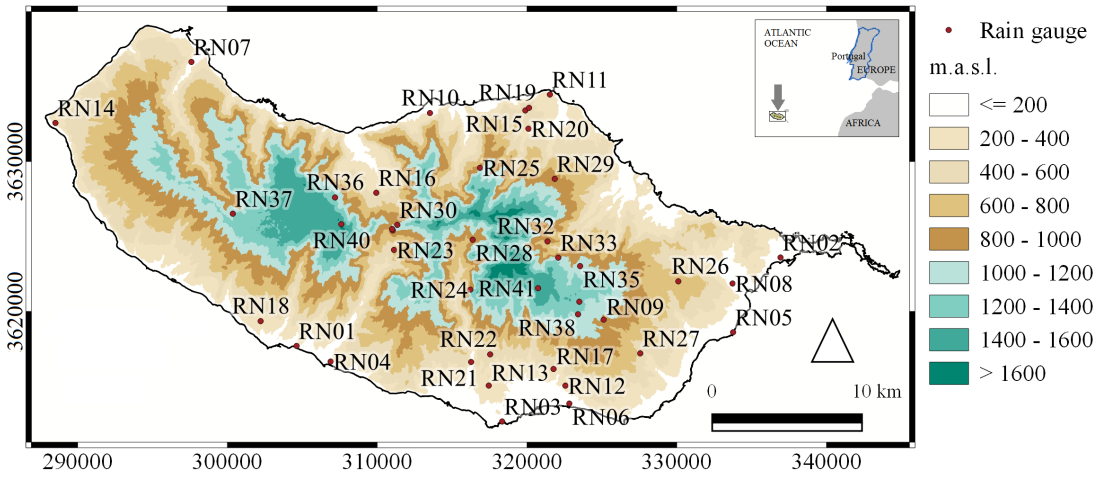

Figure 4-1: Elevation map of the Portuguese small island of Madeira. Location of the 41 rain gauges considered in the study identified by red bullets with their respective codes (RN01-RN41). System adopted: projection, UTM; zone; 28N; datum, the World Geodetic System 1984; and planar units, metres.

The island is almost entirely formed by volcanic rocks, mostly basalts [333], strongly conditioning its morphology. Despite its relatively small size, more than 30% of its surface lies above 1000 metres above sea level (m.a.s.l.). The highly rugged topography of the island is characterised mainly by the deep valleys, the enormous mountain ridge extending along the centre with 1,861 m.a.s.l. at its highest point

(Pico Ruivo), and to a much lesser extent, by the flat areas such as the plateau of Paul da Serra lying at an average altitude of 1,450 m.a.s.l. (Figure 4-1). The relief of this high volcanic island, additionally to the effect of altitude, result in a local climatic differentiation which in accordance with the Koppen's classification [58] is temperate with dry and warm summers (Csb) for most of the island, temperate with hot and dry summer (Csa) in the lower coastal zones (e.g., RN06 rain gauge in Figure 4-1), and temperate with dry and cool summers (Csc) in small areas of altitude above 1,610 m.a.s.l. (e.g., RN41).

The prevailing meteorological conditions on the island are mainly determined by the local circulation, the trade winds, the intensity and location of the subtropical anticyclone of the Azores, and the morphology and orientation of the relief [140]. The relative orientation of the mountain ridge (E-W), which is nearly perpendicular to the direction of the prevailing trade winds (N-SE), induces a remarkable variation of air temperature and rainfall amounts [235] between the northern and southern slopes (Figure 4-2). Cold fronts are much more frequent and more active than warm fronts, whose activity is generally weak, both being more frequent in the first half of the hydrological year (from October to March) than in the second one (from May to September). The passage of fronts usually causes heavy rainfalls, especially in the highlands. The island has rainfall all year round, with high quantities during the wet season [158], and with a very dry short period regularly in July [58].

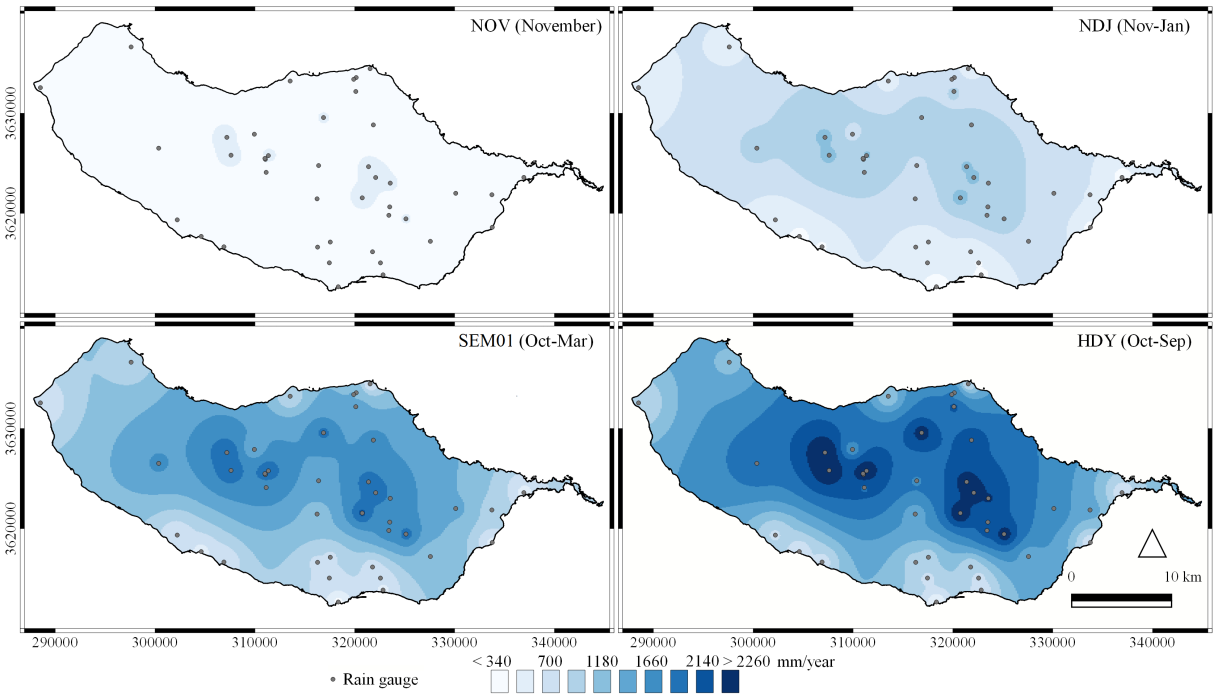

Figure 4-2: Average rainfall surfaces based on the 41 rain gauges (bullets) and on the reference period from 1940/41 to 2016/17 for NOV, NDJ, SEM01 and HDY. The Inverse Distance Weighting (IDW) with an exponent of 2 was applied as spatial interpolation technique (UTM zone 28N, WGS 84).

In most cases, the average rainfall increases with altitude, being higher, for the same altitude, in the northern slope than in the southern slope due to the mentioned dominant factors. Figure 4-2 depicts the average rainfalls for the first month of the wettest trimester (November, NOV) ranging from 52.0–419.5 mm, for this trimester (November to January, NDJ) ranging from 154.0–1182.2 mm, for the first semester (October to March, SEM01) ranging from 278.7–2073.0 mm, and for the hydrological year (October to

September, HDY) ranging from 600.1–2663.6 mm. Regardless the time-span, the highest average values are observed at the higher elevations located in the central and northern highlands (e.g., RN31, RN40, and RN41 rain gauges), while the smallest averages, occur in the lowlands (e.g., RN01, RN03 and RN06 rain gauges).

In Madeira, perennial streams and, especially, groundwater are the main source of freshwater for its about 270,000 inhabitants and half a million tourists per year [199]. Thus, groundwater resources are consequently of key importance for the endogenous environmental potential of the island. The exploitation of these resources for different uses (e.g., water supply for human settlements, industrial, and agricultural) is made by galleries, tunnels, wells and springs, and by an extensive system of more than 1000 km of open aqueducts, the *levadas*, which, bypassing the slopes and precipices of the streams, capture and transport water to the northern and southern slopes. The groundwater flows from the planaltic highlands, where rainfall and rock permeability are higher, and discharges to sea [333]. The main natural groundwater recharge areas are located in the central region of the island, which makes them critical for the island's fresh water security (e.g., the rain gauge of RN40-Bica da Cana located in the vicinity of the plateau of Paul da Serra). Paul da Serra plateau, with approximately 24 km^2, is the most important hydrogeological and water resources unit, due to its slightly rugged topography, highly favourable to the retention of rainfall, and to its geological nature enhancing both, infiltration and aquifer formation [333].

4.2.2 Data from October 1940 to September 2017

Rainfall data. The series at the different timescales (1, 3, 6, and 12 months) were established by aggregating the daily rainfalls for each rain gauge of Figure 4-1 and Table 4.1. The daily rainfall data was obtained via the procedure implemented by Espinosa et al. [118] to the records made available by the Portuguese Institute for Sea and Atmosphere, IPMA (https://www.ipma.pt/en/oipma/), which is the main source of hydrological and hydrometeorological characteristics for Portugal. Because the analysis addressed the wet season, the data used were the first month of that season, November (NOV), its first trimester, from November to January (NDJ), and the wet season itself, from October to March (SEM01). The annual rainfall (HDY) data was also considered.

North Atlantic Oscillation index (NAOI) data. The NAOI represents a pattern of low-frequency tropospheric height variability. It is based on centres-of-action of 500 millibars constant pressure (mb) height patterns. The adopted station-based index of the NAO considers the difference of normalised SLP between Lisbon, Portugal, and Stykkisholmur/Reykjavik, Iceland, since 1864. The station-based data (3-month, from November to January, NDJ NAOI, and annual) was retrieved from National Center for Atmospheric Research (NCAR) (https://climatedataguide.ucar.edu/climate-data).

4.2.3 Trend analysis and change-point detection

The non-parametric Mann-Kendall and Sen's slope estimator tests, and the sequential version of Mann–Kendall test, described in this section, were used to establish the rainfall monotonic trends and to, determine the period of abrupt changes or the trends slope break, and also to identify a climatic driving factor defining

Table 4.1: The 41 rain gauges analysed in the study sorted by increasing elevation. Identification, coordinates (UTM zone 28N, WGS 84), elevation, and average rainfalls in the reference period of 77 hydrological years, from October 1940 to September 2017, for November (NOV), the wettest trimester from November to January (NDJ), the first semester from October to March (SEM01), and the hydrological year (HDY).

Code	Name	Coordinate (m)		Elevation	Average values of rainfall in mm			
		X	Y	(m.a.s.l.)	NOV	NDJ	SEM01	HDY
RN01	Lugar de Baixo	304,617.00	3,617,700.00	15	91.2	269.9	487.3	600.1
RN02	Caniçal	336,935.00	3,623,598.00	16	101.3	287.6	522.7	677.7
RN03	Lido-Cais do Carvão	318,344.00	3,612,661.00	20	52.0	154.0	278.7	340.6
RN04	Ribeira Brava	306,894.00	3,616,657.00	25	105.9	319.7	574.3	705.6
RN05	Santa Catarina	333,770.00	3,618,611.00	49	100.3	298.2	530.3	664.3
RN06	Funchal Observatório	322,831.00	3,613,854.00	58	95.1	277.7	501.8	609.1
RN07	Porto do Moniz	297,595.00	3,636,640.00	64	186.7	516.3	912.1	1,238.9
RN08	Santana	333,732.00	3,621,863.00	80	201.7	575.9	1,006.5	1,346.5
RN09	Meia Serra	325,125.00	3,619,453.00	115	353.2	1,050.6	1,895.1	2,452.8
RN10	Ponta Delgada	313,526.00	3,633,233.00	123	167.1	461.9	826.2	1,075.9
RN11	Ponta de São Jorge	321,533.00	3,634,467.00	266	114.0	335.1	587.6	782.1
RN12	Bom Sucesso	322,571.00	3,615,052.00	291	111.3	325.5	590.8	723.3
RN13	Santa Quitéria	317,452.00	3,615,056.00	320	116.6	332.3	600.2	729.6
RN14	Ponta do Pargo	288,513.00	3,632,570.00	339	120.2	355.9	629.4	821.7
RN15	Vale da Lapa	319,893.00	3,633,407.00	346	264.3	766.3	1,375.6	1,886.0
RN16	Loural	309,941.00	3,627,916.00	368	250.5	727.5	1,293.2	1,611.6
RN17	Sanatório	321,777.00	3,616,160.00	384	129.3	366.2	661.9	814.5
RN18	Canhas	302,217.00	3,619,353.00	400	115.4	344.2	623.6	781.9
RN19	Cascalho	320,142.00	3,633,581.00	430	214.6	616.6	1,106.7	1,542.3
RN20	São Jorge	320,102.00	3,632,187.00	500	300.3	871.0	1,536.3	2,100.2
RN21	Covão	316,274.00	3,616,629.00	510	146.4	424.9	765.5	936.2
RN22	Santo António	317,545.00	3,617,136.00	525	140.0	419.0	761.9	935.1
RN23	Serra de Água	311,124.00	3,624,104.00	573	292.4	882.3	1,582.9	1,981.5
RN24	Lapa Branca-Curral das Freiras	316,222.00	3,621,455.00	610	208.3	607.2	1,104.3	1,365.2
RN25	Fajã Penedo	316,868.00	3,629,581.00	620	352.5	1,036.8	1,835.3	2,392.4
RN26	Santo da Serra	330,110.00	3,622,009.00	660	267.6	767.7	1,353.3	1,774.4
RN27	Camacha-Valparaiso	327,570.00	3,617,207.00	675	213.1	643.0	1,127.8	1,419.1
RN28	Curral das Freiras	316,377.00	3,624,782.00	787	263.6	802.8	1,446.5	1,765.6
RN29	Queimadas	321,860.00	3,628,847.00	881	314.4	910.5	1,632.1	2,209.3
RN30	Chão dos Louros Encumeada	311,346.00	3,625,775.00	895	369.0	1,118.1	1,991.4	2,521.1
RN31	Encumeada de São Vicente	311,042.00	3,625,405.00	900	350.3	1,043.6	1,888.2	2,421.4
RN32	Lombo Furão	321,375.00	3,624,670.00	994	365.4	1,091.4	1,924.7	2,428.7
RN33	Cabeço do Meio-Nogueira	322,092.00	3,623,586.00	995	390.2	1,124.5	1,989.0	2,490.8
RN34	Encumeadas Casa	310,999.00	3,625,497.00	1,010	323.1	973.1	1,754.2	2,216.9
RN35	Ribeiro Frio	323,551.00	3,623,025.00	1,167	351.1	1,005.6	1,782.4	2,285.4
RN36	Caramujo	307,186.00	3,627,603.00	1,214	382.9	1,129.2	2,033.6	2,663.6
RN37	Rabaçal	300,361.00	3,626,520.00	1,233	288.9	866.8	1,572.9	2,012.7
RN38	Montado do Pereiro	323,413.00	3,619,809.00	1,260	330.5	940.0	1,667.4	2,089.8
RN39	Poiso & Posto Florestal	323,500.00	3,620,648.00	1,360	336.4	960.9	1,697.1	2,141.0
RN40	Bica da Cana	307,604.00	3,625,815.00	1,560	381.3	1,133.0	2,019.9	2,619.9
RN41	Areeiro	320,746.00	3,621,552.00	1,610	419.5	1,182.2	2,073.0	2,588.2

the Madeira's rainfall trends based on seasonal and annual NAOI trends. To this end, the NOV, NDJ, SEM01 and HDY rainfall series (77-year long each) at the 41 rain gauges of Figure 4-1 were considered. The steps of the research methodology steps are summed up in Figure 4-3.

Mann-Kendall test. The presence of temporal trends and their statistical significance were verified by using the non-parametric Mann-Kendall (MK) test [247, 211] at a significance level of $\alpha = 0.05$. This statistical test detects the presence of monotonic trends and is widely used in trend detection but also to ascertain the spatial variation of the temporal trends of climatic and hydrological time series when various time series or rain gauges data are tested at the same time [180]. The hypothesis that there is no significant trend, the null hypothesis H_0, assumes that the X_i observations are independent

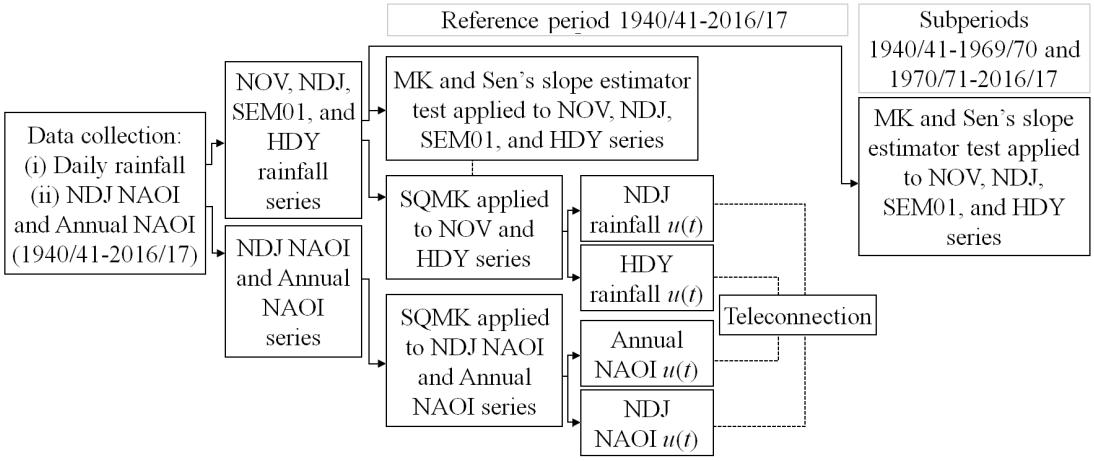

Figure 4-3: Flowchart of the methodology adopted: trends analysis, change-point detection, and teleconnection.

and randomly ordered in time, whereas the alternative hypothesis, H_A, considers that the data follow a monotonic trend, either increasing or decreasing.

Sen's slope estimator test. The magnitude of the linear trends was computed using a non-parametric procedure developed by Sen [396], i.e., the Sen's slope estimator test. This test was applied to all the rainfall series notwithstanding the statistical significance results from the MK test. To derive an estimate of the slope Q, the slopes of all data pairs are calculated as follows:

$$Q_i = \frac{x_j - x_k}{j - k}, i = 1, 2, ..., N, j > k \tag{4.1}$$

where x_j and x_k are the values in years j and k, $j > k$, respectively. If there are n values x_j in the same time series, there will be $N = n(n-1)/2$ slope estimates, Q_i, whose median is the Sen's slope estimator. If the N values of Q_i are ranked from the smallest to the largest one, the Sen's estimator is defined as:

$$Q = \begin{cases} Q_{\frac{N+1}{2}} & \text{, if } N \text{ is odd} \\ \frac{1}{2}(Q_{\frac{N}{2}} + Q_{\frac{N+2}{2}}) & \text{, if } N \text{ is even} \end{cases} \tag{4.2}$$

A $(1-\alpha)$ two-sided confidence interval about the slope estimate is obtained by the non-parametric test based on the normal distribution. A positive value of Q indicates an upward or increasing trend in the time series whereas a downward or decreasing trend is represented by a negative value of Q.

Sequential Mann-Kendall test. The Sequential Mann-Kendall (SQMK) was used to test assumptions about the start of a trend and to detect change-points or breaking point positions in the rainfall and NAOI series. A change-point is a point in a time series at which the statistical properties of the distribution change [219]. The SQMK test also distinguishes the irregular upward and downward trends with respect to a reference period of time [343].

The SQMK test sets up two standardised series, a progressive-trend series $u(t)$ and a retrograde-trend one $u'(t)$, which are both expected to fluctuate around zero.

The values of the original series X_i were replaced by their ranks r_i, arranged in ascending order. The

magnitudes of r_i, $(i = 1, 2, ..., n)$ were compared with r_j, $(j = 1, 2, ..., i-1)$, and at each comparison, the number of cases $r_i > r_j$ were counted and denoted by n_i. A statistic t_i was defined as follows:

$$t_i = \sum_{k=1}^{i} n_k \tag{4.3}$$

The mean and variance of the test statistic were computed as:

$$E(t_i) = \frac{i(i-1)}{4} \text{ and } \mathrm{Var}(t_i) = \frac{i(i-1)(2i+5)}{72} \tag{4.4}$$

The sequential values or progressive-trend series $u(t_i)$ was then calculated as:

$$u(t_i) = \frac{[t_i - E(t_i)]}{\sqrt{\mathrm{Var}(t_i)}} \tag{4.5}$$

Analogously, the retrograde-trend series $u'(t_j)$ was also computed, although starting from the end to the beginning of the time series.The point at which the progressive-trend series $u(t)$ crosses the retrograde-trend series $u'(t)$ and diverges beyond the specified confidence level (in this study, 0.95 for $\alpha = 0.05$ was adopted), is considered as a statistically significant change-point in trend within the time series.

4.3 Results

A rainfall trends characterisation was obtained for the 77-year reference period. On account of the breaking point analysis results, two distinctly characterised subperiods were analysed, the initial one from 1940/41–1969/70 and the final one from 1970/71 on. For the reference period, a strong teleconnection between the progressive-trend series of rainfall and NAOI was determined.

4.3.1 Reference period from 1940/41 to 2016/2017

Rainfall trends. The Sen's slope estimates (Equations 4.1 and 4.2) in mm year^{-1} are presented in Table 4.2 for November (NOV), the trimester from November to January (NDJ), the first semester from October to March (SEM01), and for the hydrological year starting in October (HDY). For the 77-year reference period (from October 1940 to September 2017), the table shows that there is a generalised downward trend in the rainfall at the different timescales. The same table illustrates that, overall, there is enough evidence to reject the null hypothesis, H_0, of no trend at one or more of the considered timescales at eight out of the forty-one analysed rain gauges. Seven rain gauges located, except for one (RN11), in the southern region of the island, denote upward trends of which only one with statistical significance (RN04). According to the table, the number of rain gauges with statistically significant downward trends is one, for NOV, and four, for the wettest trimester, NDJ, these last trends also being recognised as significant for SEM01. At the annual timescale, HDY, rainfalls from thirty-six rain gauges show downward trends of which seven with statistical significance. The only significant upward trend occurs at this timescale (RN04).

Table 4.2: Rainfall trend estimates in mm year^{-1} for the 41 rain gauges in the complete 77-year reference period and in two subperiods based on the SQMK results (accounting for 30 and 47 years, respectively) for November (NOV), the wettest trimester from November to January (NDJ), the first semester from October to March (SEM01), and the hydrological year starting in October (HDY). Results with statistical significance, based on the MK test (p-value $< \alpha = 0.05$), are highlighted with an asterisk.

Code	1940/41–2016/17 (mm year^{-1})				1940/41–1969/70 (mm year^{-1})				1970/71–2016/17 (mm year^{-1})			
	NOV	NDJ	SEM01	HDY	NOV	NDJ	SEM01	HDY	NOV	NDJ	SEM01	HDY
RN01	0.1	0.3	0.4	0.4	0.1	3.2	8.0	6.5	0.2	-1.7	-1.1	-0.4
RN02	-0.3	-0.4	-0.2	-0.2	-0.2	4.0	*9.5	*8.4	-0.1	-2.0	-2.9	-3.7
RN03	0.0	0.1	0.3	0.6	0.1	2.8	*4.4	3.1	-0.1	-1.2	-0.5	-0.6
RN04	0.6	1.3	1.7	*2.5	0.1	3.3	9.1	6.8	0.8	-0.3	1.5	2.5
RN05	-0.2	-0.5	-0.3	-0.1	0.4	3.5	*9.2	*5.8	0.1	-2.1	-2.7	-3.1
RN06	-0.1	-0.4	-0.3	-0.1	0.2	3.6	6.2	5.3	-0.3	-2.5	-1.7	-1.7
RN07	-0.6	-1.6	-1.4	-0.4	2.3	*7.8	*18.8	*21.2	0.3	*-4.2	*-6.8	*-9.0
RN08	-0.5	-0.9	-1.4	-2.3	2.0	7.1	13.5	12.0	0.9	-2.9	-3.2	-4.8
RN09	-1.3	-3.8	-5.0	-5.1	0.9	7.1	23.7	20.4	0.3	-6.7	-7.2	-9.0
RN10	-0.9	-1.7	-2.7	*-3.0	-0.8	4.4	*12.7	11.0	0.2	-3.3	-4.8	-5.2
RN11	-0.1	0.1	0.6	0.4	0.4	3.2	6.5	4.6	0.4	-1.1	-0.3	-0.9
RN12	-0.2	-0.7	-0.9	-0.5	0.2	4.4	*10.1	*8.5	-0.2	-3.4	-2.7	-2.1
RN13	-0.2	-0.2	-0.1	0.5	-0.4	5.3	10.3	9.3	0.1	-1.9	-0.9	-0.5
RN14	*-0.9	*-3.3	*-4.8	*-5.2	-1.9	0.0	8.8	6.2	-0.3	*-4.6	*-7.3	*-9.7
RN15	-0.5	-1.7	-2.4	-2.1	2.0	6.1	*19.1	16.2	0.8	-4.2	-6.7	*-7.5
RN16	-1.2	-3.0	-4.0	-4.6	-1.8	6.6	*24.9	19.2	1.0	-3.4	-3.6	-4.0
RN17	-0.3	-1.1	-0.7	-0.7	0.2	3.4	9.5	6.9	-0.2	-3.4	-3.4	-3.7
RN18	0.1	-0.2	-0.3	0.1	-0.1	3.1	9.8	*10.2	0.5	-3.1	-3.1	-2.6
RN19	-0.8	-1.8	-2.4	-2.1	0.9	3.8	12.8	11.0	0.8	-4.7	-6.1	*-7.5
RN20	-0.6	-0.6	-1.4	-1.8	1.3	9.7	*21.9	*16.3	1.4	-2.9	-4.1	-6.7
RN21	-0.1	-0.6	-0.8	-0.5	1.1	7.8	*16.1	*16.5	0.0	-2.9	-3.1	-2.8
RN22	0.1	-0.2	-1.0	-0.2	2.1	*9.8	*20.3	*20.2	0.1	-4.1	-3.7	-4.0
RN23	-0.8	-1.7	-1.3	-1.2	0.7	15.1	*34.7	*34.8	0.6	-6.2	-5.7	-7.4
RN24	-0.7	-1.6	-2.4	-2.3	0.2	7.6	*18.7	*19.4	0.0	*-5.6	-6.3	-7.2
RN25	-1.3	-2.2	-2.4	-3.4	2.1	14.7	*42.3	*40.4	1.1	-6.2	-6.7	-10.5
RN26	-0.9	-1.6	-1.5	-1.4	0.6	8.4	17.9	17.2	-1.1	-6.6	*-11.1	*-15.8
RN27	-0.5	-1.8	-2.2	-1.8	-2.5	3.5	16.1	13.2	-0.1	*-5.6	-3.9	-4.5
RN28	-0.6	-2.8	-4.3	-5.1	1.9	16.0	*36	*36.4	0.3	-6.5	-8.2	-11.4
RN29	-1.2	-2.9	-3.9	-3.4	-1.1	0.7	13.4	6.3	0.8	-3.5	-5.0	-5.3
RN30	-1.6	-4.6	-5.0	-5.4	0.8	16.7	*45.8	*49.6	-0.1	-9.7	-11.8	*-14.8
RN31	-0.8	-2.6	-3.5	-3.3	4.2	19.2	*43.5	*46.5	-0.3	*-10.5	*-15.5	*-20.6
RN32	-1.3	-2.0	-2.1	-2.6	0.6	17.7	*39.5	*41.7	0.5	-4.5	-2.7	-5.3
RN33	-1.5	-2.3	-3.0	-2.7	-0.6	18.5	*45.3	*43.2	0.5	-6.9	-5.9	-9.1
RN34	-1.1	-2.3	-2.6	-2.1	2.0	*17.9	*43.1	*42.9	0.5	*-6.8	-7.3	-10.8
RN35	-1.1	-2.0	-2.2	-2.0	0.4	10.7	20.2	24.9	-0.1	-7.9	-9.6	-12.3
RN36	-1.5	-4.4	*-7.8	*-8.2	-1.2	8.4	17.4	12.1	0.3	-7.8	-10.6	-13.4
RN37	-0.2	-1.7	-3.1	-3.0	2.2	8.8	*36.5	*35.0	0.3	-7.2	-8.7	*-10.9
RN38	-1.9	*-5.4	*-7.4	*-7.3	-0.5	9.5	29.2	*28.8	-0.9	*-9.0	-10.1	*-13.1
RN39	-1.7	*-4.5	*-6.3	*-7.3	2.1	*17.7	*46.4	*46.9	-1.1	*-9.7	*-14.4	*-18.5
RN40	-1.5	-4.2	-6.7	*-6.6	3.8	*18.5	*49.1	*53.6	0.1	-9.4	*-15.0	*-21.2
RN41	-2.5	*-6.0	*-8.2	*-10.6	1.2	19.5	*46.9	*47.8	-2.0	*-11.1	-14.0	*-23.4

The spatial distribution of the trend magnitude of Table 4.2 was characterised using the Inverse Distance Weighting (IDW) with an exponent of two [279] — Figure 4-4. It should be noted that the figure is based on statically significant and non-significant trends. From Figure 4-4, it is evident that for all the timescales the higher rainfall decreases occur in the central part of Madeira. The magnitudes of the trends in NDJ are almost three times those in NOV which suggests that the rainfall trends might be somewhat equally distributed in November, December and January, months also with close average rainfalls (not shown here). The trends for SEM01 and for HDY followed a spatial pattern similar to the one of NDJ, i.e., with more pronounced downward rainfall trends at the central highlands, and also at

large part of the northern slope. Compared to the shorter timescales, the area of the southern slope with upward annual trends, though with very small magnitude, expanded.

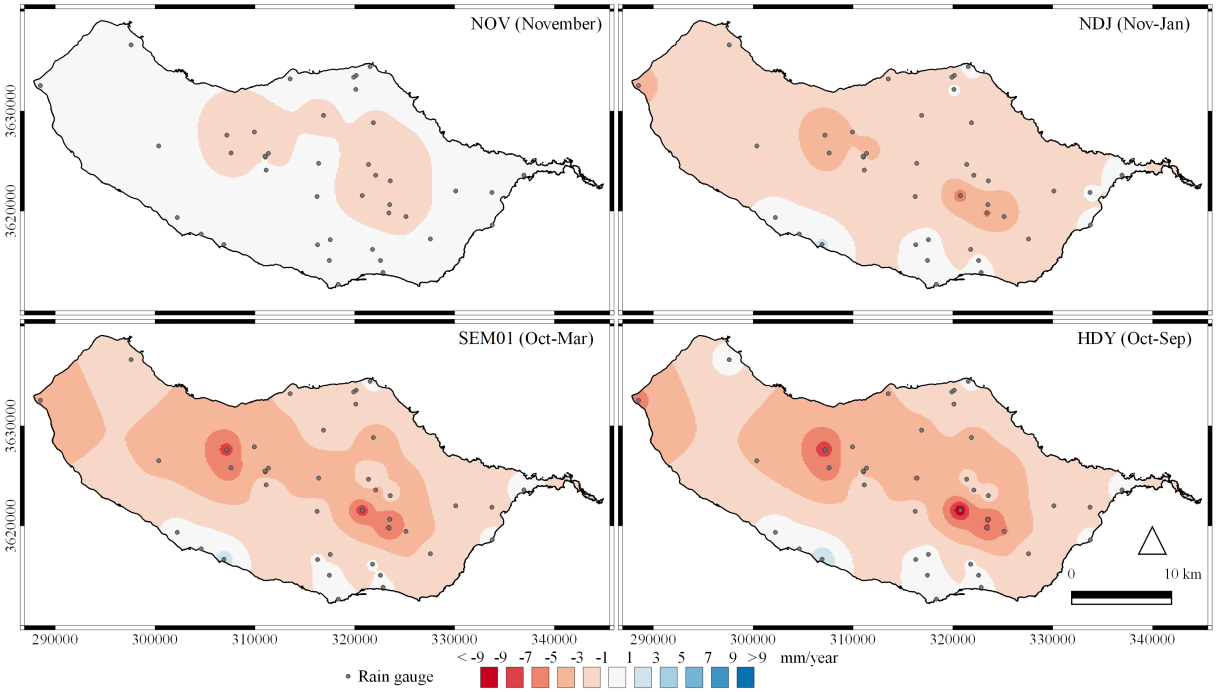

Figure 4-4: Spatial distribution of trend magnitude at different timescales, obtained from the Sen's slope estimator for the reference period, from 1940/41–2016/17. The Inverse Distance Weighting (IDW) with an exponent of 2 was applied as spatial interpolation technique (UTM zone 28N, WGS 84).

In general, the results suggest considerably and statistically significant decreases in rainfall at the central region of the island and in many locations of great importance in terms of water security (such as the HDY trends of -10.6, -6.6, and -8.2 mm year^{-1}, for RN41, RN40, and RN36, respectively). As mentioned, groundwater is replenished in central highlands, therefore, such continuing decrease may exacerbate the impacts associated with the lack of Madeira's freshwater resources [105].

Change-point detection in rainfall and NAOI time series. The Sequential Mann-Kendall test was used (Equations 4.3–4.5) to obtain fluctuations in the trends over time, and possible abrupt temporal shifts or slope break in the rainfall and NAOI trend series. For each timescale, the change-point technique was applied to the rainfall series denoting significant trends in the reference period (accounting for 1, 4, 5, and 8 series for NOV, NDJ, SEM01 and HDY, respectively — Table 4.2). Regarding the NAOI, only seasonal NDJ and annual time series were considered, being consistent with the rainfall NDJ and HYDY series.

The results of the probable changes were evaluated for a $(1-\alpha) = 0.95$ confidence level based on the p-value. Because all the rain gauges denoted a similar progressive $u(t)$ and retrograde $u'(t)$ trend development and for the sake of readability, only the results for NDJ and HDY at one rain gauge (RN14) paired with the NAOI trends are exemplified in Figure 4-5. For the wettest trimester (NDJ) as well as for the seasonal NAOI the intersection of each paired progressive-trend $u(t)$ and retrograde-trend $u'(t)$ series allows to identify a change-point between the years 1969/70 and 1970/71 — Figure 4-5, left graph. In regards to the progressive-trend series $u(t)$, the NDJ rainfall shows an upward trend (dimensionless)

from 1940/41 to 1970/71 followed by a general decrease. In contrast, the progressive-trend series $u(t)$ for NDJ NAOI develops a decline before the change-point in 1969/70, and a sustained increase after this point.

A similar behaviour in the $u(t)$ and $u'(t)$ is observed regarding HDY rainfall and annual NAOI — Figure 4-5, right graph. Although several change points were detected for the HDY rainfalls, except the one in 1968/69, they were statistically non-significant. In the same figure, there are two abrupt temporal shifts for the annual NAOI series, of which the one in 1969/70 is statistically significant. Other authors have shown that a number of important characteristics of the global atmospheric circulation and climate rapidly changed in a near-monotonic fashion over the decade, or less, centred on the late 1960's [25]. This motivated the study of the rainfall trends before and after the statistically significant breaking point centred between 1969/70 and 1970/71.

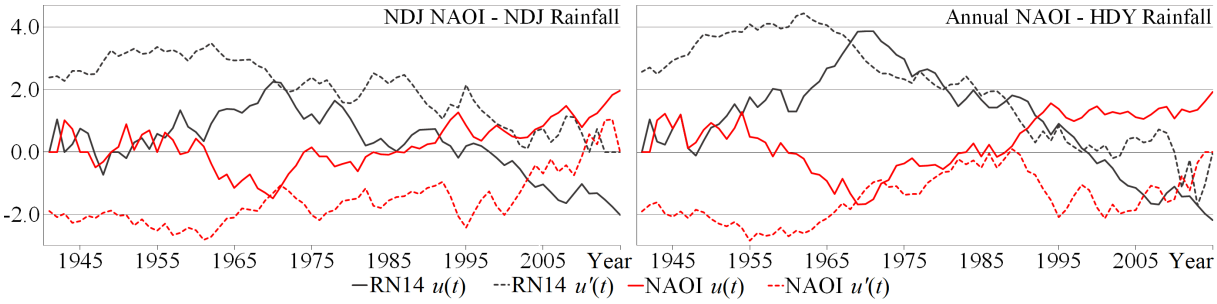

Figure 4-5: Sequential Mann-Kendall test for rainfall and NAOI with progressive-trend series $u(t)$ (solid line), and retrograde-trend series $u'(t)$ (dashed line) at seasonal NDJ (left graph) and annual (right graph) timescales for the westernmost rain gauge of RN14 Ponta do Pargo. The resulting series for the NAOI are in red and those for the rainfall in grey.

4.3.2 Subperiods from 1940/41 to 1969/1970, and from 1970/71 to 2016/17

To understand the possible effects of climate change on the island's rainfall, a trend analysis, using the same models as for the reference period, was done for two subperiods based on the change-point results as described in Section 4.3.1 — (i) from October 1940 to September 1970, and (ii) from October 1970 to September 2017.

The trend estimates for the different timescales are reported in Table 4.2. In general, the table shows that during the initial subperiod the rainfall denoted particularly pronounced upward trends, followed by equally particularly pronounced downward trends in the years afterwards. Comparatively to the 77-year period, both subperiods show a noticeable increase in the number of trends with statistical significance, namely, for SEM01 and HDY (although with opposite signs from one subperiod to the other). Figure 4-6 and Figure 4-7 show the spatial distribution of the previous trends.

4.3.3 Teleconnection between the rainfall trends and the NAOI trends at seasonal and annual timescales for the reference period

As previously described, the SQMK test was used to graphically illustrate the progressive and retrograde trends of rainfall and NAOI (see Figure 4-5). In general, rainfall presents a downward trend for the

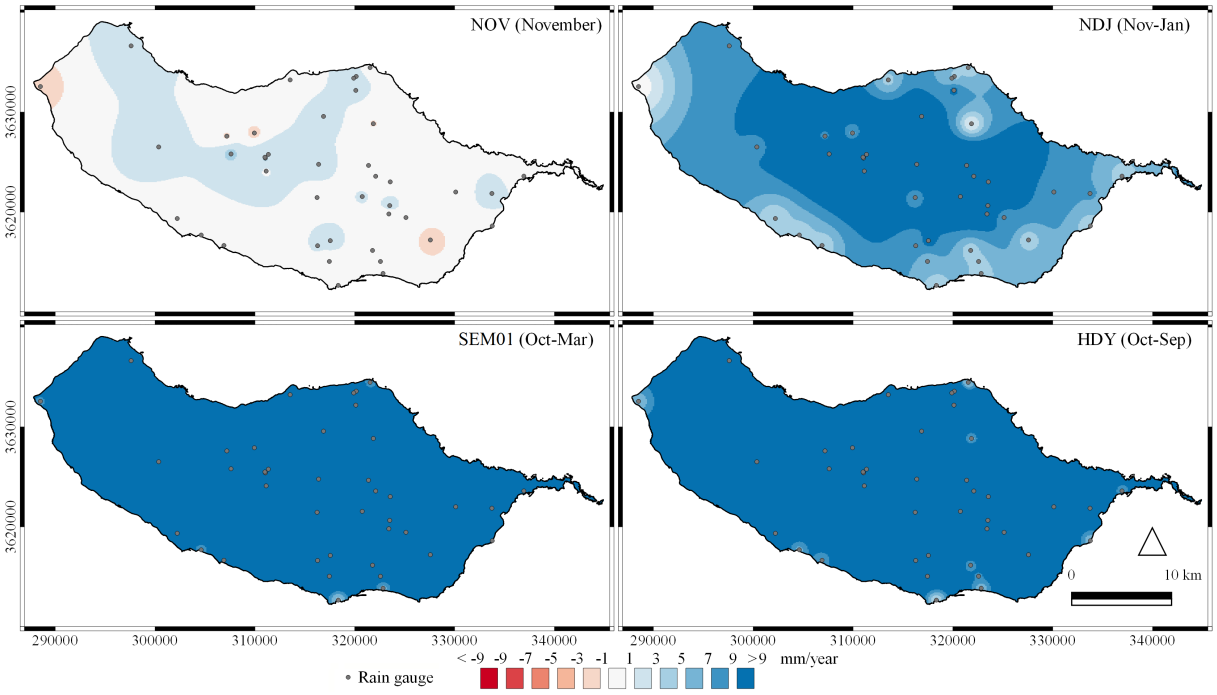

Figure 4-6: Spatial distribution of trend magnitude at different timescales, obtained from the Sen's slope estimator for the 30-year subperiod, from 1940/41–1969/70. The Inverse Distance Weighting (IDW) with an exponent of 2 was applied as spatial interpolation technique (UTM zone 28N, WGS 84).

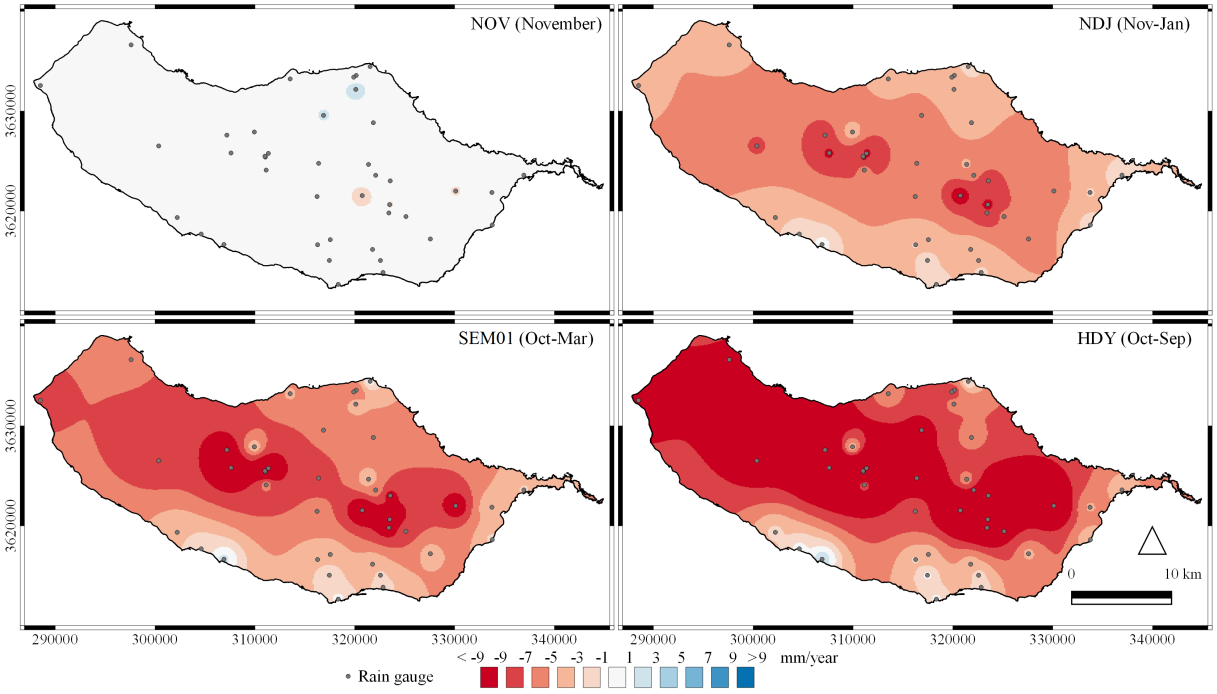

Figure 4-7: Spatial distribution of trend magnitude at different timescales, obtained from the Sen's slope estimator for the 47-year subperiod, from 1970/71–2016/17. The Inverse Distance Weighting (IDW) with an exponent of 2 was applied as spatial interpolation technique (UTM zone 28N, WGS 84).

reference period with a shorter upward trend during the initial subperiod, and a much stronger downward, and apparently sustained, trend for the final subperiod. Such trend behaviour is mirrored for the NAOI, i.e., generalised upward trend, being slightly more pronounced in the case of NDJ NAOI than the annual

NAOI. Supported by the change-point results, an exploratory correlation analysis was performed to detect how consistent the linkage between NAOI and rainfall trends could be.

For teleconnection, only the linear correlation between the progressive-trend series $u(t)$, computed by using Equation 4.5, for rainfall and for NAOI of the 1940/41–2016/17 period was measured by means of the Pearson correlation coefficient r — considering rainfall as the dependent variable, and NAOI as the explanatory one. Figure 4-8 depicts the spatial distribution of such correlation for the wet season and annual timescales. According to the figure, for the wettest trimester (NDJ) most of the locations exhibit a strong negative correlation (e.g., rain gauges of RN41, RN40, RN38, and RN39 with $r < -0.8$, and also with high downward rainfall trends). The only positive correlation was obtained for the RN04 ($r = 0.3$ and a rainfall trend of 1.3 mm year^{-1} — Table 4.2). Concerning the annual timescale, the correlation values range from $r = -0.9$ (RN39 with a statistically significant trend of -7.3 mm year^{-1}) to $r = 0.3$ (RN04 with a statistically significant rainfall trend of 2.5 mm year^{-1} — Table 4.2).

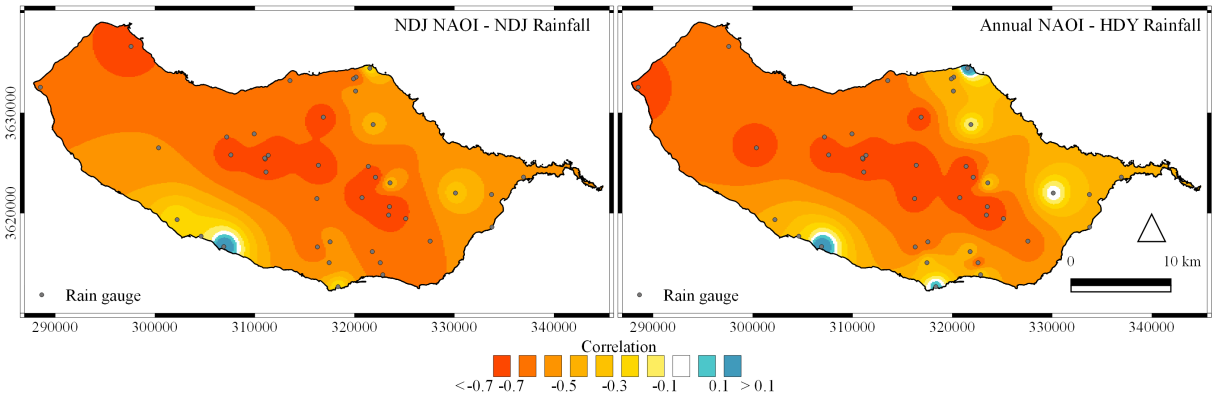

Figure 4-8: Teleconnection between rainfall trends (statistically significant and non-significant) and NAOI trends based on the SQMK results for the reference period from 1940/41 to 2016/17. Spatial distribution of the Pearson correlation coefficient between the progressive-trend series $u(t)$ of rainfall and NAOI for NDJ and annual timescales (IDW with an exponent of 2, UTM zone 28N, WGS 84).

This proposed teleconnection at seasonal and annual timescales, clearly indicates a coherent relationship between the changes in the NAO mode and in the rainfall in Madeira, with negative strong correlations in the high central region and large part of the northern slope where the most pronounced downward rainfall trends are registered. It should be noted that the negative trends in the NAOI time series are also associated to upward rainfall trends but to a lesser extent.

4.4 Discussion and conclusions

For sustainable water resources management and planning under climate change, long-term and recent changes in rainfall and their characteristics due to temporal shifts in climatic drivers should be investigated not only at global scale (e.g., GCMs), but also at a regional scale, based on ground data as done in the present paper. The objectives underlying this research work were (i) to analyse rainfall trends at different timescales by applying climate trends techniques to the 41 rain gauges data for the small island of Madeira, (ii) to detect the possible trend turning points in the rainfall and climatic driver data, and (iii) to explain rainfall trends changes based on a proposed teleconnection.

Rainfall trends. The study showed that, from the 1970's on, Madeira's climate is becoming drier with well-established decrease of the rainfall in the central region and northern slope (e.g., the significant -10.6 mm year^{-1} detected for the central RN41 rain gauge for the reference period from 1940/41–2016/17). Only a narrow coastal strip of the southern slope presented upward trends. It should be noted that although the rainfall amounts vary widely from one rain gauge to another, the rainfall trends denote a spatial regularity. These findings are in line with numerous studies in other latitudinal locations and climate zones such as the outputs of GCMs suggesting seasonal (wet season) and annual rainfall decreases under global warming — e.g., the rainfall analysis done over a period of 81 years (1934/35–2014/15) revealing that the annual rainfall has decreased from -0.3 to -0.9 mm year^{-1} in the United Arab Emirates [262], the analysis for eastern of the Spanish part of Iberian Peninsula denoting significant downward trends of 51.0 mm year^{-1} from 1955/56–2016/17 [270], the rainfall variability over the most important river basin in Morocco tending towards drier conditions according to the noticed deficits for seasonal and annual rainfall [302]. The same applies at finer spatial scales as it was confirmed for Madeira. For instance, other researches based on different methodologies and on past conditions of the climate components for small islands of Macaronesia, have identified a pronounced decline in annual rainfall over the highlands and changes of minor importance over southern slopes [380, 268, 73, 252].

Regarding Madeira, few studies have reported rising temperature and wetter conditions in recent years. An exception is Cropper and Hanna [73] who applied the Theil–Sen slope estimator to the rainfall data from 1980/81 to 2010/2011 at rain gauge of RN06-Funchal identifying an upward trend in temperature of 0.33 degrees Celsius per decade and a non-statistically significant rainfall increase in the wettest trimester of the rainy season of 0.6 mm year^{-1}. This rainfall trend differs from the one now obtained for the same location, which suggests a decrease, also not significant, of 2.5mm year^{-1} in the last 47 years (Table 4.2). This circumstance indicates that the rainfall variability is an active process and that care should be taken when comparing trends for same locations based on different time windows. However, to more accurately characterise the rainfall regime and, consequently, detect changes in its patterns, it is necessary to have long and updated rainfall data. In addition, as demonstrated in this paper, the island presents high spatio-temporal rainfall variability, so making assumptions about rainfall trends based on a single rain gauge may be a quite limited and distorted approach. In the specific case of RN06, its location near the southern coastline makes its rainfall records also not relevant for the water resources management and planning.

Teleconnection approach. Given that the NAO is one of the most important large-scale modes of atmospheric circulation in the Northern Hemisphere and particularly associated with rainfall variability [195], several studies have been looking for an increased capacity to ascertain such association. In some of the small islands of European Macaronesia, different authors have found significant relationships between changes in rainfall and the NAO mode [183, 380]. For this region, significant associations have been ascertained with strong negative correlations between changes in the rainfall and in mathematical definitions of the NAO displayed for the Azores and for Madeira Island in all the trimesters of the wet semester [73]. A strong relationship between NAOI and rainfall changes has been also observed at southern slopes of the western the Canary Islands [183] in the same seasons. Thus, changes in NAO

seem to be inextricably linked to those observed in rainfall of some North Atlantic Ocean islands. This may be attributable to NAO impacts on trade winds [147] corresponding to higher rainfall amounts on windward slopes when such winds are stronger. Consequently, the spatial variation in rainfall trends of Madeira may be explained by its high dependence on the dynamic interaction of the trade winds with the island's morphology as indicated in Section 4.2.1. For instance, the progressively strengthening of NAO, generally associated to strong positive NAOI phases, has been associated with weaker trade winds and drier conditions in recent years, specifically with the downward rainfall trends of the wet season [183, 380] which is in line with the findings in this work. The opposite pattern has been noted for northern Europe, i.e., strong positive NAOI phases connected with wetter conditions and significant upward rainfall trends in some cases [195].

Additionally, the teleconnection provides further indication that the continuing drier conditions, i.e., significant downward rainfall trends, in the wet or winter season and in the hydrological year over Madeira are related to the persistent upward NAOI trends in regard to the computed progressive-trend series $u(t)$. Such sustained upward trend in the NAOI since 1970/71 on has been previously acknowledged and linked not only to changes in rainfall — e.g., the significant negative correlation between snow depth and NAO in Western Italian Alps, i.e., upward NAO is unfavourable to snow pack persistence [439] — but to the quickly temperatures rise in the North Atlantic Ocean region [499, 197]. Some other authors have suggested that internal variability of the NAO imparts substantial uncertainty to future changes in regional climate over the coming decades [95]. Nevertheless, a thorough analysis on projected changes in the NAO mode and their effects on seasonal and annual rainfall variability for Madeira is beyond the scope of this paper, and therefore left open for further investigation.

In summary, this research work provides (i) a comprehensive rainfall trend analysis for the small island environment of Madeira with a much finer rainfall grid and longer-running series from a high number of rain gauges, (ii) a detailed description of the long-term and as well of recent years changes in rainfall with special attention to the wet season and annual timescales by analysing the reference period and the two subperiods supported by the change-point analysis results, and (iii) a solid basis to explain the climate change effects on the Madeira rainfall, suggesting that abrupt changes of the NAO climatic driver can be directly linked to rainfall variability based on the established strong teleconnection. A straight-forward improvement would be to build a teleconnection based on different NAOI definitions and regionalised rainfall, i.e., spatially representative rainfall series instead of individual locations. However, despite these possible extensions, the results presented here can be used for improving the water resources management and planning of the island, and of some other small islands with similar characteristics influenced as well by large-scale circulation patterns.

Chapter 5

Spatio-Temporal Variability and Regional Frequency Analysis of Droughts

This chapter has been published as: Espinosa, L. A., Portela, M. M., and Rodrigues, R. (2019). Spatio-temporal variability of droughts over past 80 years in Madeira Island. *Journal of Hydrology: Regional Studies*, 25, 100623, https://doi.org/10.1016/j.ejrh.2019.100623

Abstract

Droughts from January 1937 to December 2016, were studied using monthly rainfall at 41 rain gauges covering most of the island. The gaps of the original rainfall data were filled by Multiple Imputation by Chained Equations (MICE). The drought conditions were assessed by means of the Standardized Precipitation index (SPI), specifically the SPI6. To study the drought variability, some clustering techniques and principal components analysis (PCA) were applied to the SPI field. Three homogeneous regions (northern slope, southern slope, and central region), each of them with different temporal climatic variability may be identified. Furthermore, for each region, the droughts were characterised in terms of magnitude and duration, and based on a kernel occurrence rate estimator (KORE) as well as on frequency of the drought periods. Finally, two climatic drivers, namely the El Niño-Southern Oscillation (ENSO) and the North Atlantic Oscillation (NAO) were teleconnected to the drought variability at the identified homogeneous regions for the period under study. It was not possible to establish a clear relationship between ENSO/NAO and drought occurrence. Nevertheless, the results showed that the spatio-temporal drought variability in Madeira Island has been subjected to noticeable changes in recent years (2001–2016) with a considerable higher number of periods under drought conditions than in the past.

Keywords:

Drought; Standardized Precipitation index (SPI); MICE; Principal Components Analysis (PCA); occurrence rate; El Niño-Southern Oscillation (ENSO); North Atlantic Oscillation (NAO).

5.1 Introduction

Droughts, as natural phenomena, are part of Earth's climate and occur virtually in all climatic zones with neither warning nor recognition of administrative borders or of political and economic differences. Droughts can be perceived as prolonged and regionally extensive occurrences of below average natural water availability [435], either in the form of rainfall, river runoff, or groundwater. They are typically classified into meteorological, agricultural, hydrological, ground-water, stream-flow, and socio-economic drought [238]. Unlike other natural weather disasters, droughts start unnoticeably, develop cumulatively, produce snowballing impacts, and by the time damages are visible, it is too late to mitigate their consequences. Understanding the characteristics and consequences of droughts as well as modelling and forecasting their occurrences are major issues for a successful water policy, especially in regions more prone to extreme hydrological events. These issues become even more important under the climatic change perspectives. Indeed, despite the low confidence in observed global-scale trends in droughts, due to the lack of direct observations, their magnitude and frequency are likely to increase. The same applies to other extreme hydrological events [310, 31].

As stated by the Intergovernmental Panel on Climate Change, IPCC, in its periodical assessment reports [255, 310, 31], island environments are specifically more vulnerable and often affected by extreme hydrological events, i.e., floods and droughts, and climate change compared to continental areas, especially in small islands meaning those islands with areas between 100 km^2 and 5000 km^2 [123]. They have particular physical, demographic (usually with a high concentration of population), and economic features along with hydrological and water resources development and management problems that distinguish them from larger islands or continental areas.

In recent times, prolonged and more severe droughts have increased islands' vulnerability [256]. These prolonged periods of suppressed rainfall, together with their persistence and intensity, have raised the public and the political awareness to the many associated socio-economic impacts on water management and the need for drought mitigation measures. In fact, droughts are very particular problems in small islands — e.g., some of the Australian islands in the Pacific, but also the Cook Islands, the Federated States of Micronesia, the Republic of the Marshall Islands, New Zealand, Papua New Guinea, Pitcairn Islands, Samoa, Solomon Islands [256]; the Azores and the Madeira archipelagos, and the Canary Islands [123] — because of their relative fragile freshwater sources that can be depleted when precipitation drops down leading in many cases to groundwater and aquifer overexploitation; and often causing serious losses in productivity of agriculture, electricity, health, among other impacts [27].

In spite of their recurrent nature, particularly in regions with pronounced hydrological temporal variability, droughts are among the most complex and simultaneously the least understood extreme hydrological events [435] and have been lagging behind the development of flood related research. Thus, there is an urgent need to address the emerging issues on drought research and management as a first step for water resources management, aiming at preventing and mitigating the consequences of the future occurrences [363]. According to [423], this knowledge can be used as a basis for a better understanding of drought vulnerability in different climates. For this purpose, throughout the 20^{th} century, several

indices such as the Palmer Drought Severity index (PDSI) [305] and the Standardized Precipitation index (SPI) [258] were developed to evaluate the water deficit in relation to some average amount for a certain period of time [178]. The PDSI uses precipitation and temperature data in a water balance model to compare the meteorological and hydrological drought across space and time, whereas the SPI only considers precipitation as state variable. Indices based on different climatic and hydrological variables may exhibit different regional and temporal patterns, i.e., results vary depending on the drought index and on the timescale considered.

There are no generally applicable drought assessment methods for small island environments owing to the diversity of conditions. Examples are Madeira Island with notable differences in rainfall between north and south; Porto Santo, also belonging to Madeira archipelago, with some signs of aridity and relatively low rainfall [235]; the Azores archipelago with very wet high regions and drier coastal areas [380]; Anguilla in the Caribbean with a tropical climate ameliorated by marine influences notably the trade winds [308]; the islands of Antigua and Barbuda with a great variation in mean annual rainfall from year to year [260]; the islands of Bermuda with precipitation evenly distributed throughout the year and more intense in summer than in winter [364]; Mauritius, situated in the southwest part of the Indian Ocean, with a rainfall regime subject to large regional variation and two marked seasons [347]; and the Canary Islands archipelago which are placed in a dry belt, so rainfall is very low near the coast and in flat islands [123]. Due to this great diversity of conditions in small islands, characterisation methods taken directly from continental territory applications may be only crude or even irrelevant approaches to identify and characterise extreme hydrological events, such as droughts. For instance, indices like the National Rainfall index (NRI), defined as the national average of the total annual precipitation weighted by its long-term average, are more commonly used for agricultural drought recognition [155] in larger areas (e.g., an entire country) making them unsuitable to address droughts affecting smaller areas or of a different type (meteorological and hydrological droughts). Therefore, specific methods or indices to characterise drought should be applied or adapted for small islands which, additionally, are often subject to data availability constraints. Thus, consideration of each islands peculiarities must be taken into account when applying them.

Given the large spatial character of droughts, different authors have recommended that they should be studied within a regional context [432], because the results of individual case studies may be incomparable [93]. Consequently, the selected index should be standardised for the purpose of making the drought analyses results comparable, regardless of the studied region [238]. This is the most important characteristic of the SPI. At a given location, the SPI measures rainfall anomalies based on a comparison of observed rainfall amounts for an accumulation period of interest (usually, 1, 3, 6, 12-month), with the long-term historic rainfall record for that period. The historic record is fitted to a probability distribution, which is then transformed into a standard normal distribution such that the mean SPI value for that location and period is zero [427].

According to Lloyd-Hughes and Saunders [238], the SPI is one of the most commonly used multi-scalar indices in Europe to monitor all types of drought. It is also recommended by the World Meteorological Organization [493] and is likely to be the most frequently used drought indicator worldwide, because the

SPI is applicable in all climate regimes [461, 463, 385]. Furthermore, by using standardised anomalies, a reliable and simple comparison of historical and current droughts among different rainfall regimes and geographic locations is also feasible [274].

For many analytical purposes related to climate variability, like the analysis of drought patterns, it is convenient to divide the spatial continuum (e.g., of SPI) into a manageable number of homogeneous areas. Otherwise, such analysis may be difficult when data from several monitoring stations are used [337]. The clustering techniques, such as hierarchical and non-hierarchical clustering, and the principal component analysis (PCA) may help to disclose high-level regularities that enable the generalisation about areas based on a spatially and temporally varying parameter. These techniques have been widely used in climate regionalisation [45, 67, 451]. Many authors [e.g. 40, 462, 463, 385, 354] have applied the PCA to the SPI for analysing the spatial and temporal variability of droughts.

Moreover, in recent years, some authors have attributed the drought variability to natural climate variability [265, 121, 168]. Specifically, the El Niño and the La Niña phases, known as the El Niño Southern Oscillation (ENSO) signal across the equatorial Pacific Ocean, are widely recognised as major ocean–atmosphere climatic drivers causing, in some cases, rainfall variability and hydrological variable anomalies on a global scale mainly in the tropics of the Pacific coast of America [461]. Wikarmpapraharn et al. [488] explored the ENSO and drought variability relationships using the Southern Oscillation index (SOI) and the SPI time series from four representative rain gauges in the central plain of Thailand, finding that the SPI series (for accumulation periods of 1, 2, 3, and 4-month) are strongly correlated with the ENSO strength and phases. This suggests that apparently ENSO controls rainfall variability in that region. Nevertheless, the possible relationship between ENSO and drought events, analysed by using different indices like SPI, PDSI, and SOI, remains uncertain.

Another dominant pattern of interannual climate variability is the North Atlantic Oscillation (NAO) in the Northern Hemisphere extratropics [193] which is one of the most prominent teleconnection patterns in all seasons [29]. This climatic driver consists of a north-south dipole of anomalies, with one of its centres located over Greenland and the other one of opposite sign spanning the central latitudes of the North Atlantic (35^{o} N to 40^{o} N). In general terms, the NAO influences changes in the temperature and precipitation from eastern North America to western and central [291]. Different authors have acknowledged that the NAO is largely responsible for the periods of drought in Europe [e.g. 240, 465, 248].

In the current study, the SPI was applied to rainfall records (from January 1937 to December 2016), aiming at analysing droughts, from moderate to extreme according to Agnew [9], in Madeira Island by clustering rain gauges, and decomposing their corresponding SPI time series into principal components to identify homogeneous regions regarding temporal drought patterns. Madeira is a small Portuguese island of the North Atlantic which belongs to the Autonomous Region of Madeira (RAM) in the European part of Macaronesia — This work was motivated by the following issues:

1. The poor quality of the original rainfall data in Madeira Island (short series and numerous gaps) is not compatible with a comprehensive drought characterisation, despite the fragility of the island to rainfall shortness. To address this issue, a gap-filling procedure was implemented, resulting in long daily rainfall series (80 years, from January 1937 to December 2016) in 41 rain gauges (Table

5.1), which allowed a novel and detailed spatio-temporal characterisation of the droughts over the whole Island.

2. Furthermore, in many mountainous small islands, like Madeira (Figure 5-1), the exact rainfall distribution is strongly dependent on the complex topography and the prevailing winds [158], which still makes the estimation of extreme hydrological events highly uncertain issues in water resources management. Therefore, identifying homogeneous regions may be essential for a more comprehensive assessment of those events regarding their spatial extent, magnitude and frequency.

3. Because of its reduced area, Madeira Island has little visibility at a global scale. This may justify the absence of regional studies on droughts, as those done for the continental Portuguese territory [e.g. 385, 275]. There are some studies covering relatively short periods or well-recognised drought events, such as the exceptionally extreme drought that affected Madeira during the 2011–2012 hydrological year [235]; however, none of them provides a comprehensive overview of drought events that occurred in the last decades.

4. Although ENSO is commonly linked to climate patterns over the tropical Pacific, it has been proven that it can also affect other regions, such as the northern Europe that underwent a severe precipitation deficit during the Medieval Climate Anomaly, which was synchronous with droughts in various ENSO-sensitive regions worldwide [179]. Because the effects of ENSO on the small islands of the North Atlantic region are less understood [234], a comparison was performed between the phases of SOI and drought periods identified based on the SPI. In addition, the dominant periods of the cumulative SOI and the mathematical description of the NAO, i.e., the NAO index (NAOI), were related to some characteristics of the droughts in the island.

The paper is organised as follows: in section 5.2 there is a brief description of Madeira Island, its climate, hydrology and the main freshwater resources. Section 5.3 provides information on the available rainfall data and on the models utilised. Section 5.4 shows the main results and discussion obtained from the PCA applied to the SPI on a 6-month timescale, and from the relationship between climatic drivers and drought events. In section 5.5, the conclusions are given.

5.2 Study area

Madeira is the largest island of the Madeira Archipelago. It has an area of 741 km^2, a length of 57 km and a largest width of 22 km. Centered at 32º 44.34' N and 16º 57.91' W, Madeira has a steep topography and is completely formed by the volcanic materials, consisting of an enormous central E-W oriented mountainous ridge (Pico Ruivo, 1862 m.a.s.l., and Pico do Areeiro, 1818 m.a.s.l., and Paúl da Serra region, above 1400 m.a.s.l.) cut by deep valleys (Figure 5-1). According to the Koppen's classification, the climate is predominantly temperate with dry and warm summers, and temperate with hot and dry summer in the coastal zones of Madeira [58]. Except for the higher areas, where very low temperatures may occur during winter, the differences between winter and summer temperatures are generally small.

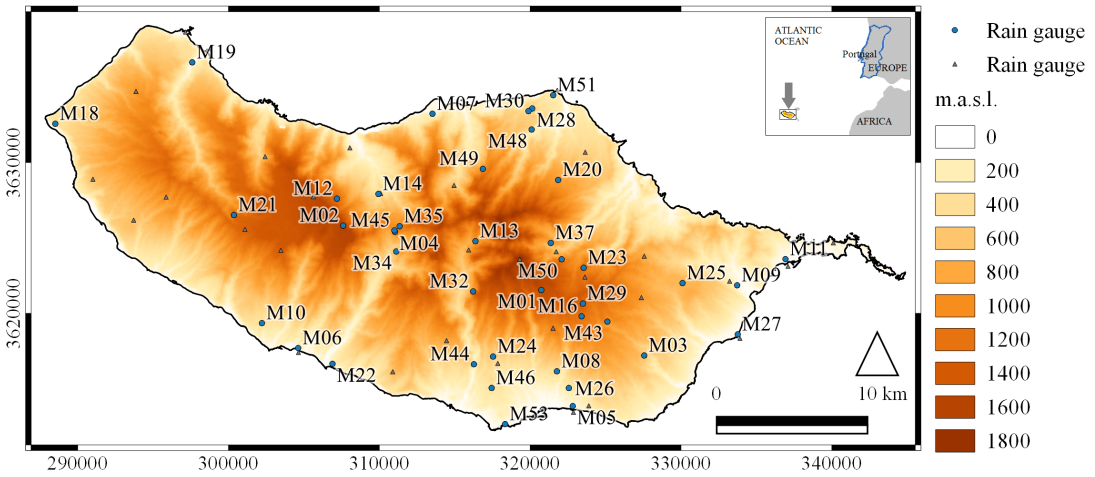

Figure 5-1: The elevation map of Madeira Island in meters above sea level (m.a.s.l.). Location of the set of 67 rain gauges: the 26 discarded ones (*triangles*), and the 41 selected for the study (*bullets* with identification codes). The referencing system adopted was the World Geodetic System 1984 (WGSM84); UTM zone 28N.

Due to its E-W oriented mountains, the precipitation is strongly orographically-generated, falling predominantly in the north facing slope because of the prevailing N-E trade winds [235]. The rainfall regime is not only affected by the local circulation, but also by synoptic systems — typical of mid-latitudes, such as fronts and extratropical cyclones, and the Azores Anticyclone in the summer season [140]. The rainfall quantity and its high variability with respect to time and space play an important role on the availability of the Madeira's freshwater resources. Regions with smaller amounts of precipitation are more susceptible to the rainfall temporal variability, in terms of water availability. This is the case of the southern slope of the island compared to the northern one. In addition, from an orographical perspective the island is also divided by deep valleys into east and west. However, based on the rainfall regime and the marked elevation differences (e.g., Figure 5-2), there are two distinct regions in Madeira, namely the northern slope (with large amounts of rainfall) and the southern slope (with less rainfall).

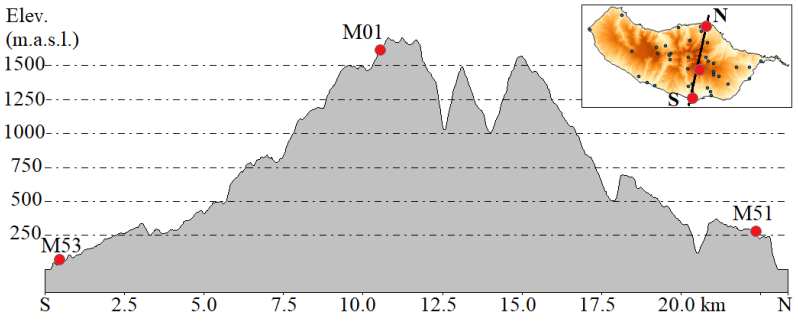

Figure 5-2: Topographic profile from a southern slope point, S, to a northern slope point, N. Intersected rain gauges: M53-Lido-Cais do Carvão, M01-Areeiro, and M51-Ponta de São Jorge. The northern slope profile (M01-M51-N) is mainly composed by steep mountains and high sea cliffs. In the southern slope profile (M01-M53-S), however, the descent to the shore takes longer with more relatively gentle slopes.

In Madeira Island, groundwater resources are the main source of freshwater for the 267,785 inhabitants and about 500,000 tourists per year [199]. Nearly all its population is concentrated in the southern slope (e.g., in the vicinity of the rain gauges M03, M05, M06, M08, M10, M22, M24, M44, M53 — Figure

5-1). The groundwater exploitation for domestic and industrial use, as well as for irrigation and electrical production purposes, is made by means of water galleries, tunnels, wells and springs and, remarkably, by an extensive network of small (originally stone) canals or *levadas* with more than 1000 km long. The *levadas*, whose origin dates back to the first settlements of Madeira Island in the first quarter of the 15^{th} century, mostly border the mountains at elevations from 600 to 1000 m.a.s.l., and are classified as an Outstanding Universal Value due to their uniqueness [104]. The groundwater flows from the central region to the coast, where the aquifers discharge to the sea [333]. The main groundwater natural recharge areas are located in the high central parts where the precipitation values and permeability of rocks are higher (e.g., the rain gauges M01 and M02).

5.3 Materials and methods

This study on droughts in Madeira Island for a 80-year reference period utilised five main models mostly implemented in R (https://cran.r-project.org/) related to: 1) rainfall data preparation, i.e., filling the gaps to have long and robust continuous time series (by implementing Multiple Imputation by Chained Equations, MICE); 2) the drought index calculation (based on the SPI); 3) clustering techniques and identification of homogeneous regions regarding temporal patterns of the drought indexes' series (by applying PCA); 4) validation of the identified homogeneous regions by characterising the moderate drought events in terms of magnitude and duration; 5) characterisation of the frequency of the periods under droughts conditions (based on a kernel occurrence rate estimator, KORE); and 6) a comparison between the SOI and SPI time series.

5.3.1 Data

The daily and sub-daily data from 67 rain gauges (Figure 5-1) in the reference period of 80 years, from January 1937 to December 2016, were made available by the Portuguese Met Office, IPMA (The Portuguese Institute for Sea and Atmosphere, https://www.ipma.pt), which has high data quality standards and is one of the main sources of Portuguese hydrological and hydrometeorological data. The rain gauges were selected aiming at establishing the continuous daily rainfall series as long as possible. The dataset thus assembled was highly variable in terms of length of the recording periods, missing values, and duration of the gap periods (Figure 5-3). Most of the rain gauges (45 rain gauges) had more than 60% of missing daily rainfalls and only 4 rain gauges had less than 10% of missing values. From these last rain gauges, only three (M01-Areeiro, M05-Funchal Observatório, and M25-Santo da Serra — Table 5.1) had less than 5% of missing values. The available data was sometimes redundant and even ill-defined, with rain gauges located in the same place but covering different periods. It should be noted that the studied period refers to 80 civil years (from January 1937 to December 2016).

5.3.2 Filling of missing data

The Multiple Imputation by Chained Equations (MICE) algorithm was used for completing the daily rainfall series of the rain gauges with missing values or gaps in the reference period, as it was applied

Table 5.1: The 41 rain gauges adopted in the study. Identification (code and rain gauge name), coordinates, elevation, and homogeneous regions (RG1, RG2, RG3) to which they belong. The percentage of missing daily records from January 1937 to December 2016. $\bar{P}$ and s' refer to the average and the standard deviation of the existing monthly rainfall records in the same period.

Code	Name	Lat-N	Lon-W	Elevation (m.a.s.l.)	Homogeneous region	Missing values (%)	$\bar{P}$ (mm)	s' (mm)
M01	Areeiro	32.7200	-16.9170	1610	RG3	4.5	210.5	212.5
M02	Bica da Cana	32.7562	-17.0554	1560	RG3	14.8	219.1	216.9
M03	Camacha-Valparaiso	32.6763	-16.8421	675	RG2	30.1	117.7	116.3
M04	Encumeada de São Vicente	32.7503	-17.0169	900	RG3	43.1	213.5	198.3
M05	Funchal Observatório	32.6476	-16.8924	58	RG2	0.3	50.7	50.6
M06	Lugar de Baixo	32.6790	-17.0832	15	RG2	7.4	50.3	49.6
M07	Ponta Delgada	32.8213	-16.9920	123	RG1	59.9	96.3	90.9
M08	Sanatório	32.6687	-16.9006	384	RG2	48.6	70.1	71.8
M09	Santana	32.7220	-16.7742	80	RG1	14.6	109.0	107.1
M10	Canhas	32.6942	-17.1098	400	RG2	62.3	64.9	66.3
M11	Caniçal	32.7374	-16.7387	15	RG1	46.5	60.4	56.8
M12	Caramujo	32.7694	-17.0585	1214	RG3	67.1	239.1	231.0
M13	Curral das Freiras	32.7456	-16.9599	787	RG3	53.6	149.5	143.3
M14	Loural	32.7727	-17.0292	368	RG3	63.2	145.5	127.4
M16	Montado do Pereiro	32.7019	-16.8839	1260	RG3	48.9	186.2	174.7
M18	Ponta do Pargo	32.8108	-17.2589	339	RG1	44.2	68.9	67.4
M19	Porto do Moniz	32.8492	-17.1628	64	RG1	52.1	106.2	98.8
M20	Queimadas	32.7831	-16.9022	881	RG1	37.1	187.3	186.8
M21	Rabaçal	32.7585	-17.1311	1233	RG2	75.4	161.0	161.9
M22	Ribeira Brava	32.6740	-17.0630	25	RG2	38.3	59.8	58.4
M23	Ribeiro Frio	32.7309	-16.8830	1167	RG3	28.6	200.5	192.7
M24	Santo António	32.6768	-16.9459	525	RG2	58.1	79.5	79.5
M25	Santo da Serra	32.7260	-16.8170	660	RG1	2.7	147.5	147.4
M26	Bom Sucesso	32.6620	-16.8960	291	RG2	72.2	62.6	56.1
M27	Santa Catarina	32.6936	-16.7731	49	RG2	37.1	55.2	54.2
M28	Cascalho	32.8290	-16.9250	430	RG1	82.3	132.9	117.8
M29	Poiso e Posto Florestal	32.7130	-16.8870	1360	RG3	35.0	179.3	175.1
M30	Vale da Lapa	32.8270	-16.9280	346	RG1	89.9	171.8	141.4
M32	Lapa Branca-Curral das F.	32.7190	-16.9650	610	RG2	87.0	126.1	145.9
M34	Serra de Água	32.7420	-17.0200	573	RG3	86.0	187.3	187.3
M35	Chão dos Louros E.	32.7570	-17.0180	895	RG3	65.6	201.9	210.7
M37	Lombo Furão	32.7490	-16.9110	994	RG3	69.7	178.4	187.3
M43	Meia Serra	32.7020	-16.8700	115	RG3	81.6	179.9	170.6
M44	Covão ETA	32.6750	-16.9630	510	RG2	78.3	75.6	76.7
M45	Encumeadas Casa EEM	32.7540	-17.0210	1010	RG3	78.0	168.3	192.2
M46	Santa Quitéria ETA	32.6610	-16.9510	320	RG2	78.2	63.4	60.3
M48	ETA São Jorge	32.8160	-16.9260	500	RG1	82.5	164.4	171.6
M49	Fajã Penedo	32.7920	-16.9600	620	RG3	79.2	182.9	188.1
M50	Cabeço do Meio-Nogueira	32.7357	-16.8987	995	RG3	81.9	165.8	192.1
M51	Ponta de São Jorge	32.8337	-16.9067	266	RG1	82.1	60.1	69.6
M53	Lido-Cais do Carvão	32.6366	-16.9365	20	RG2	88.8	26.5	26.5

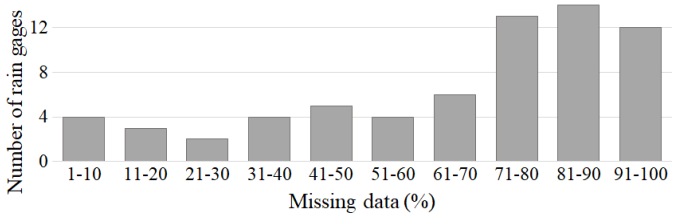

Figure 5-3: Characterisation of the missing daily rainfall (1937–2016).

in recent years to estimate the missing rainfall data at a daily scale [81]. In the MICE algorithm, each missing value is imputed m multiple times through a specified algorithm, that uses the observed data of every cell to find a plausible value for the missing cell. These algorithms are implemented in the package 'mice' in R and described in more detail in the article by Van-Buuren and Groothuis-Oudshoorn [454].

The application of the MICE algorithm to the rainfall records at Madeira Island adopted $m = 30$ imputed plausible completed datasets and 50 maximum iterations. The imputations are generated according to the default method, which is, for numerical data, predictive mean matching (PMM) to deal with the missing rainfall data. *MICE** and *MICE*** refer to the two completed datasets obtained by applying the algorithm, respectively: 1) to monthly rainfalls computed by accumulating the existing daily records, and 2) directly to daily rainfall records that afterwards were accumulated into monthly data. To validate these results a few error measures were applied to assess, at each rain gauge, the differences between the observed dataset and the reconstructed dataset (*MICE** or *MICE***). The measures applied were: the correlation coefficient, the mean absolute error (MAE), the normalised root mean squared error (NRMSE), and the Wilcoxon signed-rank test [350], which is a non-parametric statistical hypothesis test used to determine whether the time series before gap-filling and after gap-filling have the same empirical distribution.

5.3.3 Standardized Precipitation index (SPI)

The choice of the drought index depends on several aspects, such as the objective of the analysis, the specific features of the hydrological regime under consideration, or the data availability. In the study for Madeira Island, the droughts were assessed via the Standardized Precipitation index, SPI (specifically SPI6).

The SPI is an index based on the probability of occurrence of a certain deviation from an average amount of precipitation and for a given timescale. When computing the SPI at a timescale of δ-month, the variable to be analysed is the monthly precipitation, for $\delta = 1$, and the cumulative precipitation in periods of δ consecutive month, for $\delta > 1$. Although different timescales were analysed, only the SPI6 is mentioned because, besides being the recommended timescale when addressing agricultural droughts [176], it can also be associated with the precipitation shortfalls that, in some regions, begin to affect the streamflows and levels of reservoirs and lakes [427]. In the management of the water resources in Madeira, precipitation shortfalls for more than a few months are very important due to the island's dependency on precipitation for groundwater recharge.

To describe the monthly or the cumulative precipitation series, the *Pearson Type III* distribution with parameters given by the L-moments were applied [385]. According to the drought category for SPI proposed by Agnew [9], only values smaller than $u = -0.84$ were considered (moderate or worse droughts). The several consecutive time periods with SPI values below this threshold belong to the same drought event with duration (Dd), maximum intensity (Dmi), and magnitude (Dm), as defined in Figure 5-4. It is noteworthy that the magnitude and the duration of the drought events are somehow mutually dependent, because the longer the duration is, the higher the magnitude should be.

For pooling mutually dependent droughts and for removing minor droughts, which have little hydrological importance and may disturb the analysis, the moving average procedure [457, 136, 434] is applied to the SPI6 time series before selecting the droughts events (Figure 5-5). López-Moreno et al. [241] and Li et al. [232] also used the same technique (with a low pass filter of 5 months) although for the SPI based on discharges and at a longer timescale (12 months). Wen et al. [483] applied the moving average

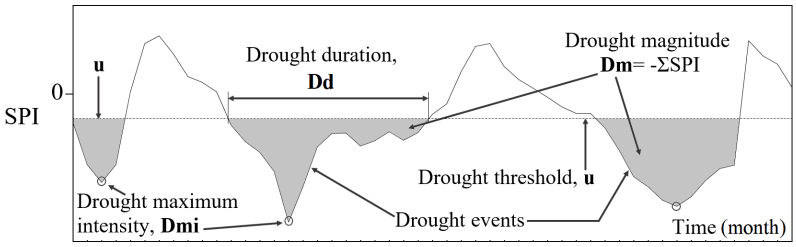

Figure 5-4: Definition of drought properties, namely, *Dmi*, *Dd*, *Dm* for SPI values below an adopted threshold, u — adapted from Santos et al. [384].

for SPI from 3 to 12 months with running-lengths equal to the SPI timescale. For the SPI at different timescales, Shin et al. [409] pooled the drought events when they reoccurred for at least 2 months and the SPI values of inter drought event time were less than zero. In the case study of Madeira Island, a filter of 5 months was adopted assuming that the hydrological processes that condition the freshwater availability are not very sensitive to very short and frequent droughts — because groundwater is their prime source.

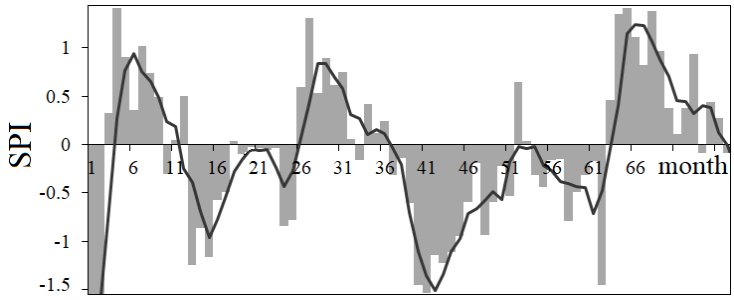

Figure 5-5: Moving average with a 5-month running-length (*smoothed black time series*) applied to an original SPI time series (*grey rectangular bars*).

5.3.4 Clustering and principal components analysis

For the purpose of characterising the spatio-temporal drought patterns in Madeira Island and obtaining a clearly defined regionalisation of drought homogeneous regions, cluster analysis coupled with principal components analysis (PCA) were applied to the smoothed SPI6 time series. These procedures intend to identify homogeneous regions by forming groups of rain gauges with similar temporal pattern of the SPI6 series [256].

The cluster analysis relies on the discriminant analysis to check the statistical significance of the formed groups [98]. Nevertheless, this does not ensure that the groups are actually meaningful. The objective of this step is to form clusters of rain gauges to have a regionalisation of droughts in Madeira, in case that there is one. It is important to mention that the groups' identification is very dependent on the particular metric to cluster, therefore, different metrics were used to get "stable" clusters, i.e., the rain gauges of a defined cluster do not change positions regardless of the method used. The clustering techniques applied were hierarchical clustering — the *Ward's* method as amalgamation rule combined with *Chebyshev*, *Manhattan*, and *Euclidean* distances; and non-hierarchical clustering like k-means. These techniques are the most popular techniques for clustering [169, 223].

PCA is a statistical procedure commonly used to transform an original set of variables into a different set of uncorrelated variables, through linear combinations of these variables aiming mainly at both data and dimensionality reduction [169]. To isolate the dominant patterns of co-variability of the droughts at the selected rain gauges, the PCA was applied to the SPI6 time series. The PCA provides a natural "smoothing" of the SPI field in terms of a reduced number of dominant patterns of variability or empirical eigenvectors [337]. The PCA consisted firstly by calculating the covariance matrix of the SPI6 data with the corresponding eigenvalues and eigenvectors. The principal components, or PC score time series, are given by the projection of the SPI6 fields on the orthonormal eigenfunctions [357]. It is noteworthy that the identification of the spatial patterns of SPI6 was based on the principal components loadings which represent the correlation, or covariance, between the SPI6 time series at each rain gauge and the corresponding PC score time series — considered as "regionalised" new SPI6 series. To more precisely locate spatial patterns of drought variability and to improve their interpretation, each principal component was rotated — rotated principal component (RPC) — using the Varimax technique, which is frequently used for performing these rotations [3].

5.3.5 Yearly frequency of the droughts

The analysis of the changes in the rate (or frequency) of occurrence of the periods under drought conditions, attempts to answer the question: regardless the scarcity of water, i.e., the precipitation deficit, how the frequency of the occurrence of droughts has changed over time? To tackle this question, a kernel occurrence rate estimator (KORE) was used, according to the stepwise approach applied by Silva et al. [413], Portela et al. [326], Silva [412], including the generation of pseudodata outside (before and after) of the observation interval, by the straightforward method of reflection for an amplitude of three times the bandwidth.

The kernel technique is a nonparametric model developed by Diggle [97] for smoothing point process data. In its application to the droughts in Madeira Island, it aimed at analysing how the annual frequency of the periods under drought conditions, $\lambda(t)$, change over time. For that purpose, the KORE analysis was applied to the times of occurrence of the periods under drought conditions, i.e., with values of the new regionalised SPI6 series (given by the RPC scores) representing moderate or worse droughts ($u < -0.84$). To select the bandwidth a straight-forward method, the Silverman's rule of thumb [414], was adopted [412].

To quantify the uncertainties of the results thus achieved, the pointwise confidence bands were constructed around $\lambda(t)$ by means of bootstrap simulations [71, 276]. The Kernel occurrence rate estimation method, coupled with the bootstrap confidence band construction, was first introduced into the analysis of climate extremes by Mudelsee et al. [277], with a detailed description given by Mudelsee et al. [278].

5.3.6 SOI and NAOI data

Although there are several slight variations in the SOI and NAOI [15, 193], in this study the standardised Tahiti-Darwin monthly SOI and the standardised Iceland-Azores monthly NAOI `https://crudata.ue`

a.ac.uk/cru/data/pci.htm — Figure 5-6) were used from January 1952 to December 2016. In order to establish a possible relationship between ENSO/NAO and drought occurrence in Madeira Island, the 6-month running-length of both, the SOI and NAOI were used — denoted in this work as SOI-6 and NAOI-6, respectively. For the same period, both climatic signals were compared to the SPI6 time series at the identified homogeneous regions by means of the Pearson correlation coefficient r and cross-correlation [169]. The previous period refers to the one with complete monthly SOI and NAOI data. Although Madeira Island is located at a latitude lower than Azores, 32º 44' N and 37º 46' N, respectively (MD and AZ in Figure 5-6), it was not possible to find a southern station that could better define a NAOI in this work, i.e., a station at a latitude lower than the one of Madeira Island with long enough surface pressure records.

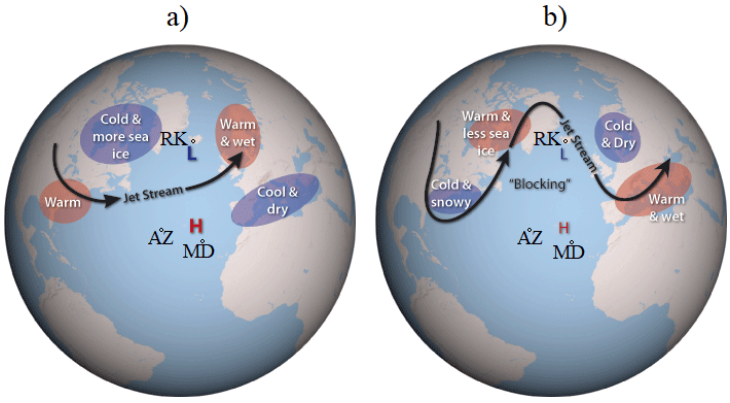

Figure 5-6: Location of Madeira Island (MD), as well as the station on the Azores — Ponta Delgada (AZ) and the one on Iceland — Reykjavik (RK) used to calculate the NAO index (traditionally defined as the normalised surface pressure difference between these two stations). Impacts on weather and climate patterns during: **a)** positive NAO phase; and **b)** negative NAO phase. L, low pressure, and H, high pressure; adapted from MetOffice [264].

5.4 Results and discussion

5.4.1 Filling of missing rainfall data

The reconstruction of the long-term rainfall time series at the 67 initial rain gauges (Figure 5-1) utilised the MICE algorithm. Because of the relative short distance between the rain gauges, the correlations among the observed data series are positively high in most cases. The data series with 90% or more missing values (for 12 rain gauges) were directly discarded. For the remaining rain gauges, the average $\bar{P}$, and the standard deviation (s') of the observed monthly data and of the reconstructed monthly data (identified as *MICE** or *MICE***, according to the time level at which the MICE algorithm was applied — monthly and daily, respectively) were, at first, compared using MAE and NRSME error measures with 0–16.5% of error; nevertheless, no rain gauges were discarded in this step. The Wilcoxon signed-rank test was also applied to the same long-term averages with the following null hypothesis: the observed data and the reconstructed data are not significantly different, i.e., p-value $> \alpha = 0.05$. The 14 rain gauges with p-value lower than the significance level $\alpha = 0.05$ were discarded at this stage. These procedures

resulted in a dense set of 41 rain gauges with long-term daily rainfall data for Madeira Island that were continuous and reliable, also identified in Figure 5-1.

For Rabaçal rain gauge, originally with 75% of missing daily data, Figure 5-7 exemplifies the long-term mean $\bar{P}$ and s' of the monthly rainfall before gap-filling (observed data with gaps), and the reconstructed dataset smoothed with a locally weighted scatterplot smoothing, LOWESS (Cleveland, 1979). The figure shows that, even in a rain gauge with such a significant number of missing daily rainfalls, there is a very good correspondence between the statistical characteristics of the observed rainfalls and the estimated rainfalls given by MICE.

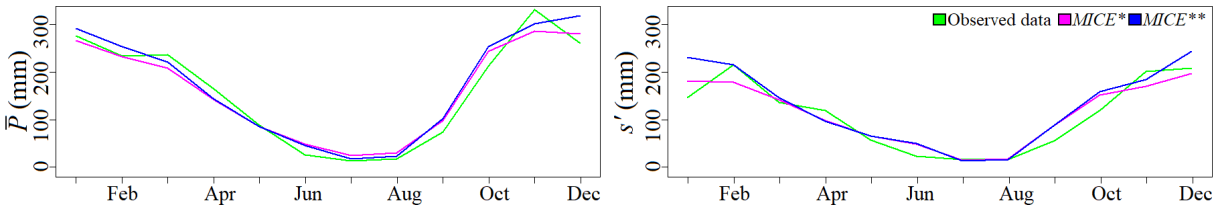

Figure 5-7: Monthly rainfall from 1937 to 2016 at Rabaçal (M21) rain gauge. Smoothed monthly long-term average ($\bar{P}$), and standard deviation (s') of the series of the observed data and the reconstructed data ($MICE*/MICE**$).

After the application of the adopted data quality criteria, the final network of complete daily rainfall series ($MICE**$) in a period of 80 years, from January 1937 to December 2016, was set up. The network, comprising of 41 rain gauges, is represented in Figure 5-8, and identified in Table 5.1. The spatial interpolation technique applied to obtain the map of the mean annual rainfall depicted in Figure 5-8 was the Inverse Distance Weighting (IDW) with an exponent of 2. IDW is based on a concept of distance weighting and can be used to estimate the unknown spatial rainfall data from the known data of rain gauges that are adjacent to the unknown site [47]. In most cases, the critical influence parameter of IDW is the distance [60] which may not be the case of Madeira Island, due to its topography. However, the elevation was not considered in the interpolation technique because there is a dense set of rain gauges at different elevations especially at the central highlands (Figure 5-1). Figure 5-8 clearly shows that the high central parts of the island have the highest long-term values of rainfall (ranging from 2500 to 2800 mm year^{-1}), the northern slope as well with high values, in contrast, the southern slope shows very low rainfall values (ranging from 300 to 700 mm year^{-1}).

The results confirmed that the MICE algorithm is an acceptable and potentially useful method, able to fill all the missing values simultaneously, preserving the original characteristics of the historical series, regardless of the timescale and the percentage of missing values. The advantage of the MICE algorithm is that it incorporates the uncertainty related to the missing data, which results in a valid statistical inference, in addition to, restoring the variability of missing rainfall data [208]. Similar consistent results were obtained by de Carvalho et al. [81], who applied and tested the MICE algorithm with the same predictive mean matching method to a sub daily rainfall dataset of a Brazilian region. The authors' results are very encouraging, because they performed approximately 25% better than two geostatistical methods to estimate the missing values (like the Kriging and Co-Kriging). Despite the already mentioned advantages of MICE, and other advantages recognised by different authors from different scientific fields

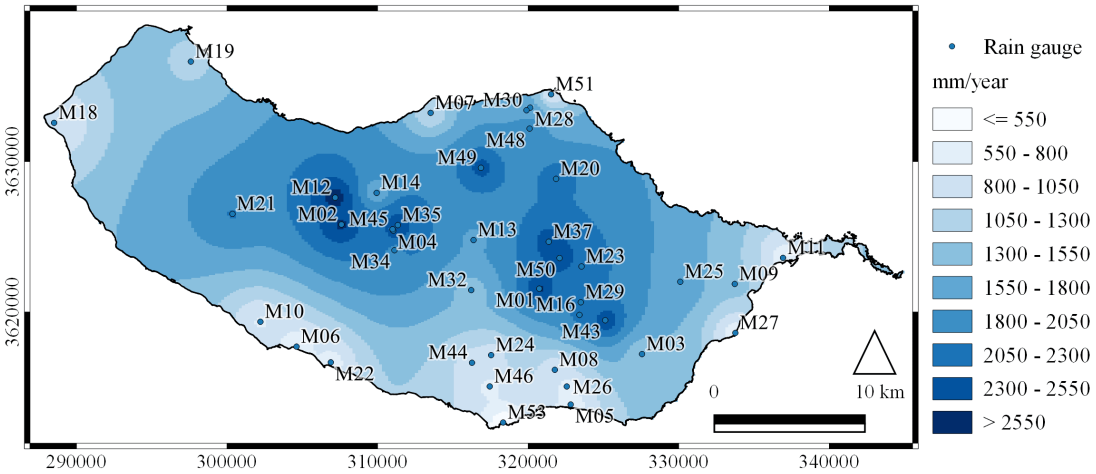

Figure 5-8: Map of the mean annual rainfall in Madeira Island (from 1937 to 2016) based on the daily rainfall data from the 41 selected rain gauges.

[such as 213, 126], it should be acknowledged that the major drawback of the MICE algorithm is the lack of a robust theoretical justification, as other approaches have in case of filling the missing data, as discussed by Azur et al. [22]. Hence, care should be taken to generalise the MICE algorithm to fill the missing rainfall data, but as a good alternative for datasets with large percentages of missing values, and its application must be carefully considered in the context of the problem.

5.4.2 Clustering of rain gauges based on SPI6

At each one of the rain gauges, the SPI6 series was next computed as described in section 5.3.3, based on the monthly rainfalls obtained by aggregating the daily rainfalls. This series was smoothed by applying a moving average. Consequently, for the reference period of 80 years, i.e., 960 months, the length of each smoothed SPI6 series is $n = 960 - 5 - 4 = 951$ months, where the 5 and 4 result from the 6-month SPI and the 5-month moving average calculations, respectively. The results of other moving average values show that the length of the series and the number of drought events decrease as the running-length increases. However, the major droughts are always recognised and their characteristics are almost the same regardless the running-length.

Aiming at grouping the drought index series, according to the similarities among their temporal patterns, the different clustering methods presented in section 3.4 were applied to the 41 smoothed SPI6 series of moderate or worse droughts. Table 5.2 summarises the results achieved for 3 possible representative clusters of drought temporal variability. The classifications with higher number of clusters were rejected, because the composition of the clusters (the rain gauges) were not stable, i.e., the elements in each cluster were very variable.

In most cases, the different classifications clearly grouped the rain gauges into three regions: northern slope (Cluster 1), southern slope (Cluster 2), and central area (Cluster 3) of Madeira Island. The clusters, that differ regarding the clustering method applied, are located in the transition between the northern and southern slopes. Nevertheless, these identified regions are not completely clear by applying *Ward's-Chebyshev* method, because the clusters' elements are more mixed, in comparison to the results, from the

Table 5.2: The clustering of the selected 41 rain gauges for the SPI6 time series (1937-2016), via hierarchical clustering (*Ward's-Chebyshev*, *Ward's-Manhattan*, *Ward's-Euclidean*) and non-hierarchical clustering (k-means). The 3 possible representative classifications were identified: northern slope (Cluster 1), southern slope (Cluster 2), and central area (Cluster 3).

Ward's-Chebyshev			*Ward's-Manhattan*			*Ward's-Euclidean*			*k-means*		
Cluster 1	Cluster 2	Cluster 3	Cluster 1	Cluster 2	Cluster 3	Cluster 1	Cluster 2	Cluster 3	Cluster 1	Cluster 2	Cluster 3
M03	M05	M01	M07	M03	M01	M07	M03	M01	M07	M03	M01
M08	M06	M02	M09	M05	M02	M09	M05	M02	M09	M05	M02
M09	M10	M04	M11	M06	M04	M18	M06	M04	M18	M06	M04
M11	M22	M07	M18	M08	M12	M19	M08	M12	M19	M08	M12
M12	M24	M13	M19	M10	M13	M20	M10	M13	M20	M10	M13
M18	M26	M14	M20	M22	M14	M23	M11	M14	M23	M11	M14
M19	M44	M16	M23	M24	M16	M25	M22	M16	M25	M22	M16
M20	M46	M21	M25	M26	M21	M28	M24	M21	M28	M24	M21
M23	M53	M29	M27	M32	M29	M30	M26	M29	M30	M26	M29
M25		M34	M28	M44	M34	M48	M27	M34	M48	M27	M34
M27		M35	M30	M46	M35	M51	M32	M35	M51	M32	M35
M28		M37	M48	M53	M37		M44	M37		M44	M37
M30		M43	M51		M43		M46	M43		M46	M43
M32		M45			M45		M53	M45		M53	M45
M48		M49			M49			M49			M49
M51		M50			M50			M50			M50

other three approaches. Both the *Ward's-Euclidean* and k-means classifications have exactly the same spatial distribution of clusters' elements, whereas the ones from the *Ward's-Manhattan* classification have some differences in the eastern part of the island (M11 and M27), assigning more elements to the northern slope (Cluster 1). However, this classification seems tenable. Moreover, based on the k-means results, the plot of means for each cluster (not shown here) and the distances between the clusters, it was found that Cluster 1 and Cluster 3 are more similar and relatively close to each other (Euclidean distance = 0.35) compared to the distances of the Cluster 2 from the clusters 1 and 3 (Euclidean distance $\approx$ 0.48). It should be noted that the implemented clustering techniques only account for the smoothed SPI series regardless of the rain gauge's location. Although clustering may be somewhat subjective, these results were the basis of the drought regionalisation based on PCA, as described in the next section.

5.4.3 Homogeneous regions of the rotated principal components

The smoothed SPI6 series of moderate or worse droughts were organised into a matrix $\boldsymbol{X}$ with $n = 951$ rows (length of the SPI series) and $p = 41$ columns (number of rain gauges, i.e., number of variables). The principal components analysis (PCA) was applied to the dataset $\boldsymbol{X}$ to transform each variable into a principal component (PC) by means of simple linear transformations.

It is expected that the first few components from the PCA account for meaningful amounts of variance. The scree plot was used as the criterion to choose the number of PCs to retain [169] — Figure 5-9. It shows an abrupt change in slope at the second eigenvalue and a smaller change at the third eigenvalue. By using the eigenvalues, information about the contribution to the data variance of each PC can be extracted, individually and cumulatively. The percentages of the total variance explained by the principal components are 75.62% (PC1), 5.61% (PC2), and 3.02% (PC3), respectively accounting for 84.25% of cumulative variance. Up from the fourth PC, the variance contribution of each new variable or dimension is meaningless. Based on this analysis and supported by the clustering results, only the first three principal components were retained for Varimax rotation in order to identify three homogeneous regions of SPI6. It is expected that after rotation the variance explained by PC1 decreases, and by PC2 and

PC3 increase. By this way, the original 41-dimensional problem, was transformed into a 3-dimensional one. Nevertheless, it is acknowledged that there are other standard *rules of thumb* to detect the number of principal components to retain in a study [50].

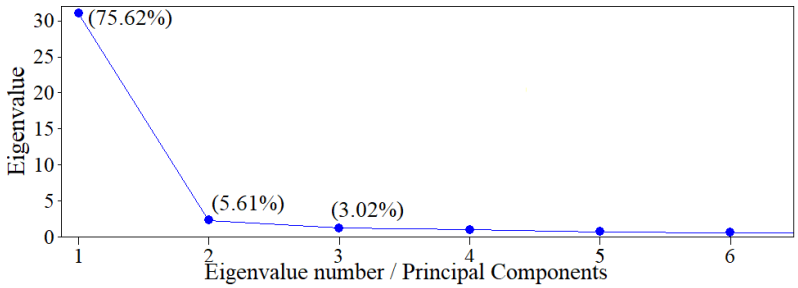

Figure 5-9: First six (out of 41) eigenvalues for the unrotated principal components of the SPI6.

As shown in the left panels of Figure 5-10 (a, b, c), the orthogonal rotation (Varimax) used to the identified spatial patterns provides a more precise delineation of the regions with different drought temporal variability. The IDW interpolation technique (with an exponent of 2 as well) was applied specifically to the component loadings, after rotation, aiming at obtaining smooth and gradual patterns of the SPI6 field. The variance of the retained rotated principal components (RPC1, RPC2, RPC3) account for 23.96%, 32.08%, and 28.21% of the total variance respectively, although the cumulative variance (84.25%) remains unchanged. The component loading of RPC1 has positive and strong correlations with 11 rain gauges located in the northern slope of Madeira Island. The second component loading (RPC2) has positive high correlations mainly in the southern slope (14 rain gauges) of the study area (characterised by low mean annual rainfall, e.g., M05-Funchal Observatório and M53-Lido-Cais do Carvão — Figure 5-8). The remaining 16 rain gauges located in the central area of the island have high correlations with the component loading of RPC3. This spatial pattern is mostly influenced by data from the rain gauges located in the mountainous ridge of the island (with the highest mean annual rainfalls, e.g., M01-Areeiro and M12-Caramujo). Thus, the rotated component loadings seem to well delimit three homogeneous regions, regarding the temporal pattern of SPI6.

According to the left panel of Figure 5-10, the three identified homogeneous regions, namely, the RPC1-RG1 (northern slope), RPC2-RG2 (southern slope), and RPC3-RG3 (central region), are contiguous and do not overlap. They are physically reasonable, and intuitively in accordance to the topography and climatology of the area (Figures 5-1 and 5-8). The regions are also hydrologically quite different regarding the wind and rainfall regimes (as mentioned in section 5.2). The identification of the rain gauges that belong to each homogeneous region is included in Table 5.1. The regionalisation enabled a dimensionality reduction to three relatively manageable regions on the basis of a spatially and temporally varying parameter such as SPI6 after applying a 5-month running-length. The results of PCA using alternate lengths (2, 3, 4 and 6 months, not shown here), presented less interpretability of the spatial distribution of the component loadings, that is, of the homogeneous regions.

In similar studies of regionalisation of temporal drought patterns, [384] considering mainland Portugal (which is approximately 120 times the size of Madeira Island), identified three homogeneous regions as well, with rotated component loading values higher than 0.7 for 144 rain gauges covering the period

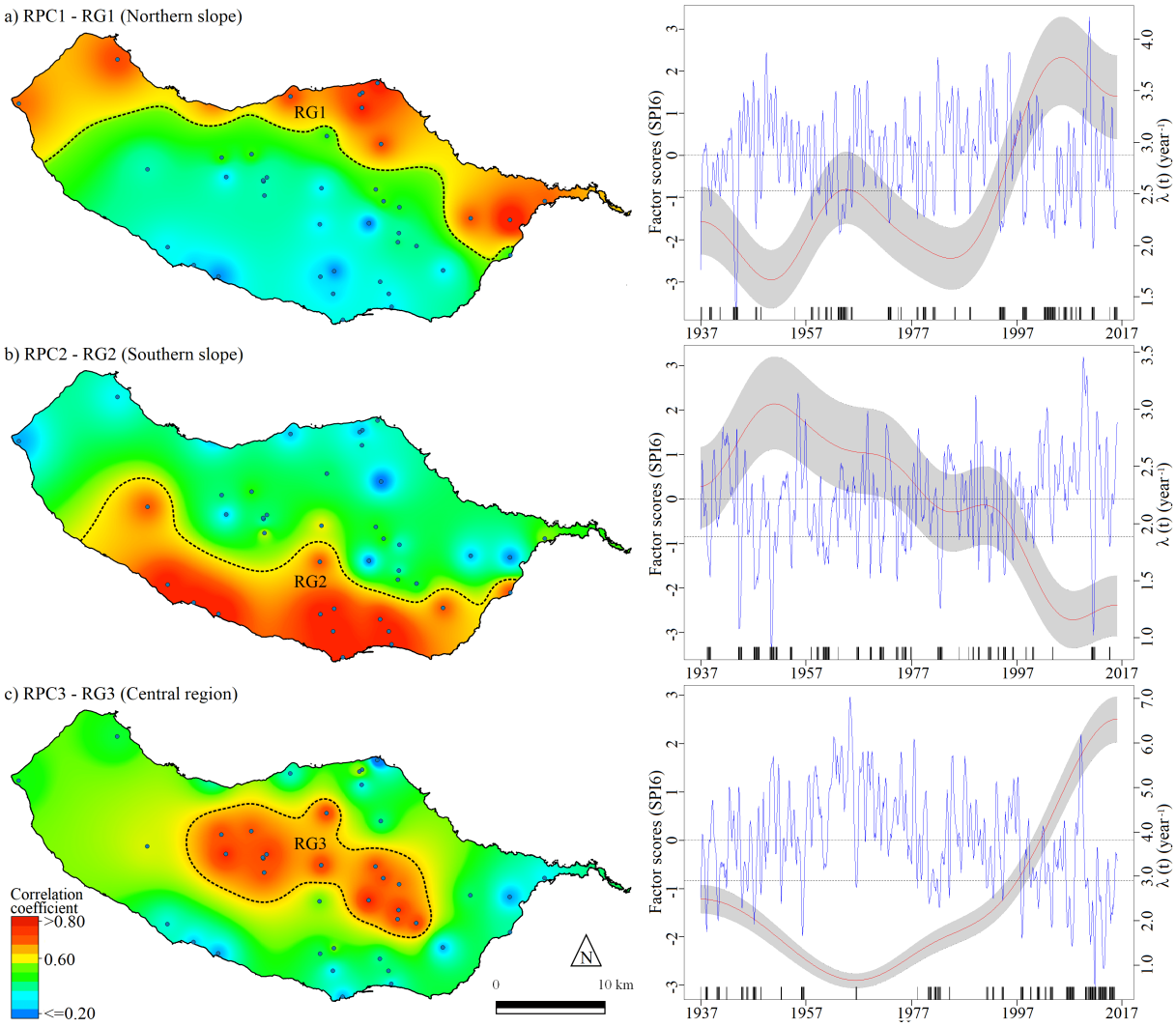

Figure 5-10: Left panel: spatial distribution of component loading (correlation coefficient) of the first 3 rotated principal components — **a**) RPC1, **b**) RPC2, **c**) RPC3 — of the SPI6 signal in Madeira Island and their corresponding homogeneous regions (RG1, RG2, and RG3). Dashed lines identify the areas with correlation coefficients higher than 0.65, used as boundaries between the regions. The bullets represent the location of the 41 selected rain gauges. Right panel: the corresponding standardised RPC scores (regionalised SPI6). Time-dependent occurrence rates, $\lambda(t)$, (*red line*) and confidence band (*shaded area*) of the moderate drought for SPI6 at the 3 identified homogeneous regions, northern slope (RG1), southern slope (RG2), and central part (RG3) of Madeira Island. The horizontal dashed lines represent the adopted drought threshold ($u = -0.84$ for moderate droughts) and vertical ticks indicate the points in time (first month of the 6-consecutive months' period) with SPI6 below this threshold.

1910–2004. This highlights the considerable heterogeneity of drought variability in Madeira Island in comparison to a continental territory.

5.4.4 Duration, magnitude and frequency of moderate droughts

The characterisation of the duration, *Dd*, and magnitude, *Dm* (see Figure 5-4), of the moderate or worse droughts (i.e., for SPI values less than the threshold of $u = -0.84$) was done based on the smoothed SPI6 series at each rain gauge, and also on the RPC scores for the three homogeneous regions shown in Figure 5-10 and Table 5.1 (RG1, RG2, and RG3). In fact, each score is basically a linear combination of

the SPI6 values at the 41 rain gauges, however, with contributions mainly from those at the rain gauges located within its respective homogeneous region, i.e., the rain gauges with high correlation coefficients for each RPC and meaningless contributions from those rain gauges with low correlations (component loadings).

Aiming at validating the three identified homogeneous regions, the characterisation of the drought events from the RPC scores was compared to the one derived from the rain gauges located inside the region to which the scores relates to, as shown in Figure 5-11. In the figure, the SPI6 value for each consecutive period of 6-month was assigned to the beginning month of that period (e.g., a SPI6 value from March to August of the year 2000 was assigned to March 2000).

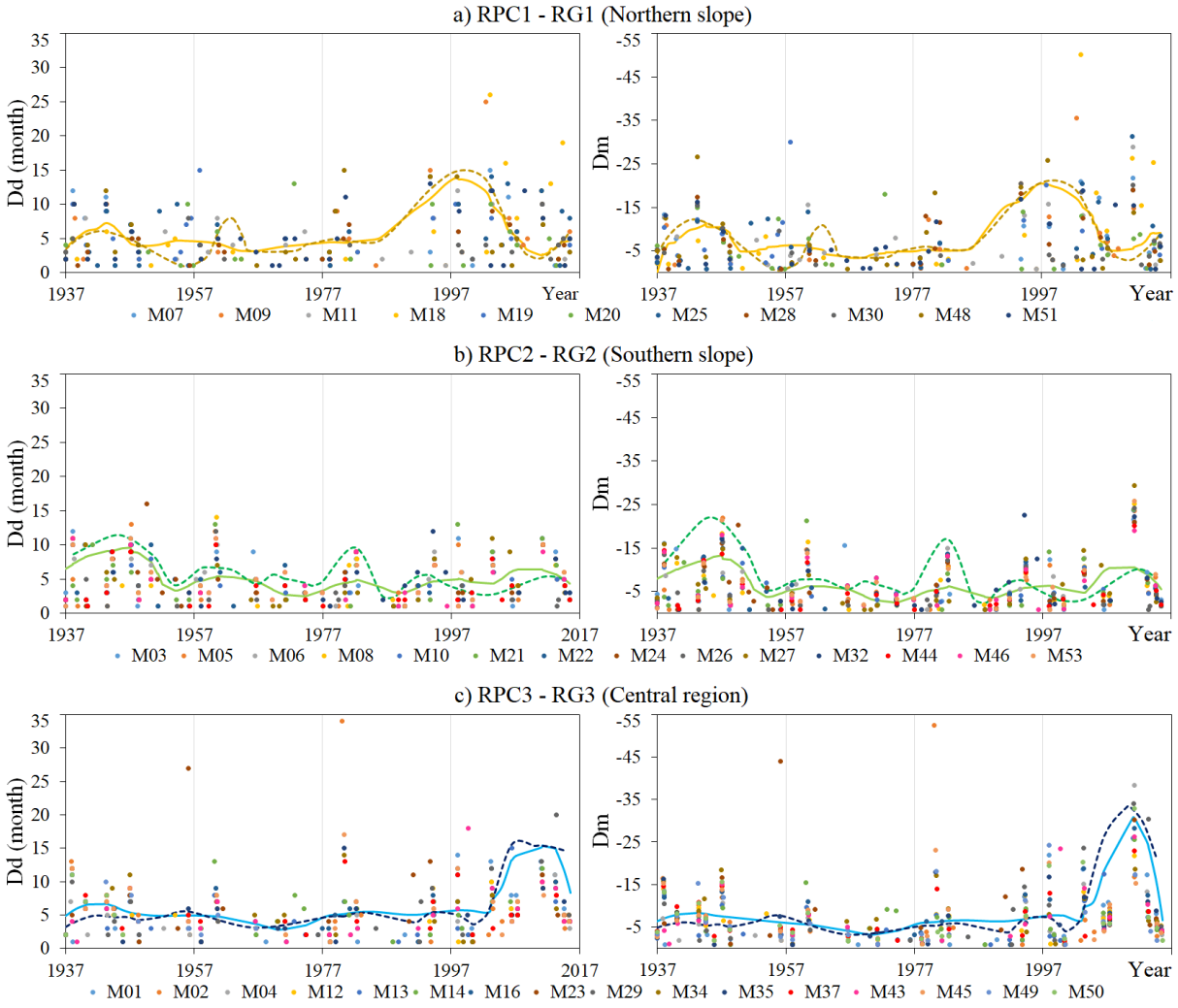

Figure 5-11: The drought duration (Dd) and magnitude (Dm) for SPI6 and $u = -0.84$ in each homogeneous region; values for the rain gauges included in each region (*dots*) and fitted into LOWESS curves (*solid line*); values from the RPCs also fitted into LOWESS curves (*dashed line*).

Figure 5-11 depicts the duration and magnitude of the droughts for each homogeneous region based on the RPC scores smoothed by a Locally Weighted Scatterplot Smoothing (LOWESS) curve with a span factor $f = 0.20$ [14] (*dashed lines*), and the Dd and Dm for the rain gauges located inside the region, in the former, as discrete values (*dots*) and also fitted into LOWESS curves (*solid lines*). In each region, the time series to which the LOWESS model was applied were discontinuous, either univariate (Dd or Dm

identified based on the RPC, with only one value in a given month) or multivariate (Dd or Dm derived from the rain gauges included in the region, with one or more values in a given month).

In Figure 5-11a — RPC1-RG1, there are two observations that diverge from the overall pattern of the solid line (LOWESS curve), both for Dd and Dm. These two observations refer to the rain gauges of M09-Santana and M18-Ponta do Pargo, starting respectively in June 2002 ($Dd = 25$ month, $Dm = -35$), and March 2003 ($Dd = 26$ month, $Dm = -50$). It is noteworthy that M18 is located in the most western part of the island. Its SPI6 series differs from the other rain gauges' SPI6 series, located in the same region in recent years (2001–2016) with more sustained negative values. The latter suggests the presence of different drought patterns for shorter recent periods. According to Figure 5-11c — RPC3-RG3, a major drought event occurred in February 1980, in M02-Bica da Cana, lasting for 34 months and with a magnitude of $Dm = -52$, which is the most severe event among the 41 analysed rain gauges. The end of the event in November 1982 was followed by one of the most widespread and meteorologically catastrophic the El Niño event in December 1982 [53]. In the same figure, the LOWESS curves have a peak for Dd and Dm, between the end of 2010 and the beginning of 2011. In the RPC3-RG3, the droughts of 2010–2011 are by no means exceptional in terms of their Dd and Dm. An inspection of the results of the mean annual rainfall points out that from 2011 onward, the annual rainfalls of the 16 rain gauges located in the RPC3-RG3 region (such as M01-Areeiro, M02-Bica da Cana, and M23-Ribeiro Frio) are all below their corresponding mean annual values, previously shown in Figure 5-8. In contrast, the most severe drought events in the RPC2-RG2 occurred in the mid-1940s and since then there has been no presence of sudden disruptive changes, or apparent trends' changes, to the Dd and Dm of LOWESS curves (Figure 5-11b).

Despite the dispersion shown by the duration and magnitude among the rain gauges included in a given region, there is a general good agreement (RPC2-RG2) or even very good agreement (RPC1-RG1 and RPC3-RG3) between LOWESS curves directly supported by those rain gauges and resulting from the RPCs, which reinforces the proposed regionalisation.

The right panels of Figure 5-10 (a, b, c) present the results from the KORE applied to the times of occurrence of the moderate or worse droughts, as identified for the RPC scores for SPI6 at the three homogeneous regions of Madeira Island. It should be stressed that the analysis considered each 6-month's period under the drought conditions as a discrete data point (vertical ticks), even if that period is a part of a longer one related to the same drought event. Consequently, the KORE characterises the annual frequency of 6-month's periods under the drought conditions rather than the frequency of the drought events.

Figure 5-10a (right panel) shows that the frequency of the periods under the drought conditions in the northern region (RPC1), which exhibit significant inter-annual variability. Compared to the other two homogeneous regions, the northern slope presents clearly two peaks for the studied period: 1) in 1965 with $\lambda(t) = 2.5$ year^{-1}, and 2) in 2004 with $\lambda(t) = 3.8$ year^{-1}. These two peaks are also present in the same years for both duration (Dd) and magnitude (Dm) curves of Figure 5-11a. Regarding the southern slope (RPC2 - Figure 5-10b, right panel), a weak long-term linear trend, towards low $\lambda(t)$ values, is detectable from the year 1950 with $\lambda(t) = 3.0$ year^{-1}, to 2007 with $\lambda(t) = 1.2$ year^{-1}; beyond this

year, it seems to occur in an increasing tendency. This tendency apparently is driven by an exceptionally extreme drought event occurred in 2012 [235], with the highest intensity in the analysed period. However, this trend occurs only during a relatively short period from 2007 to 2016. In general terms, the southern slope's drought occurrence rate curve does not have a considerable development as the other two regions' results, i.e., RPC2 has the lowest $\lambda(t)$ range among the three identified homogeneous regions. In right panel of Figure 5-10c (RPC3), there is a peak in 1937 followed by a decrease in $\lambda(t)$ until a minimum is reached in 1967; up from this year the occurrence rate curve exhibits a positive trend. The same figure shows that the frequency of the periods under the drought conditions in the central region denotes an increase from 2004 onwards, with a high concentration of periods under drought conditions from 2011 on. By combining these results with those of Figure 5-11c, one can conclude that it indicates not an increase in the frequency of the drought events (as it could result from a preliminary analysis), but an increase in the duration of the drought, meaning longer consecutive periods under drought conditions.

The results from the KORE frequency estimator combined to the characterisation of the drought events, suggest that in the northern slope and the central regions of Madeira Island, there seem to occur a significant increase in the number of the periods under drought conditions and in the magnitude of drought events, while in the southern region, those periods had been more frequent in the past. An increase of the drought occurrences in region RPC3-RG3 may alter the natural recharge of groundwater (for which the high central areas are crucial, as mentioned in section 5.2), resulting in a decreased runoff, which is likely to exacerbate the already existing water scarcity problems [104] jeopardising the water security in the island.

5.4.5 Climatic drivers teleconnected to drought events

Aiming at ascertaining whether there is or not an influence of the ENSO and NAO phases on the properties of the droughts at the identified homogeneous regions, as well as a possible ENSO-NAO relationship, different periods were considered based on the long term-term trends and breaking points of the cumulative SOI-6 and NAOI-6.

By visually comparing the cumulative SOI-6 and cumulative NAOI-6 series (Figure 5-12), it is apparent that from 2001–2016, they denote a more pronounced increase and decrease, respectively, than in the past. In the same figure, two breakpoints were visually identified in each series and confirmed by applying the Sequential Mann-Kendall (SQMK) test for change-point detection [343] with a 95% confidence interval, namely in the years 1976–1977 and 1999–2000. These two breakpoints agree with two of the most severe droughts that affected north-eastern South America, the Caribbean (mostly the Lesser Antilles), and regions of Central America [181].

Figure 5-12 suggests a strong relationship between the climate anomalies accompanying the ENSO and NAO (based on the aggregator transformation of SOI and NAOI data) with a distinct seasonal dependence in both observations, similar to Mueller and Roeckner [280] who predict a strengthened negative correlation between the two climatic drivers' indices in the future. In general terms according to the figure, the negative dominant phases occur during La Niña dominance, and the positive NAO phases in El Niño dominance. The model output exhibits a 3-month delay in the emergence of the NAOI

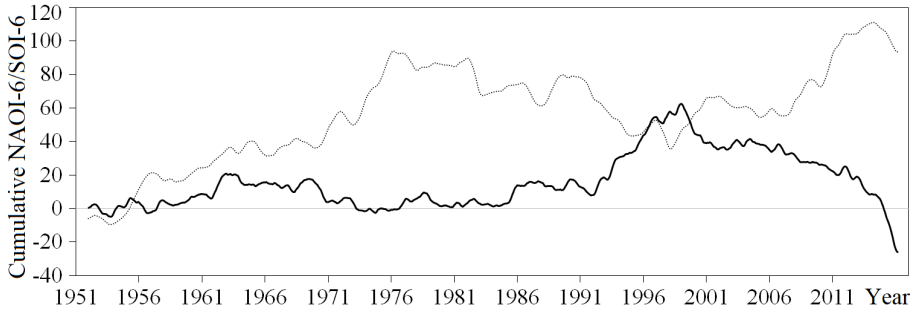

Figure 5-12: The cumulative 6-month running-length SOI (*dashed line*) and NAOI (*solid line*).

signals, i.e., the identified breakpoints occurred first on the cumulative SOI-6 signal, and later on the cumulative NAOI-6. This long-term comparison was performed because some earlier studies stated that the association between ENSO and NAO is weak and difficult to detect in short observational records [139].

According to Mayuening et al. [253] La Niña dominance period shows extreme upward slopes (positive SOI) with dry conditions, and its counterpart El Niño dominance period (negative SOI with extreme downward slopes) generally linked to wet conditions. In contrast, the strong positive phases of the NAOI tend to be associated with dry conditions across northern Europe and wet conditions in southern Europe (Figure 5-6); opposite patterns, i.e., wet conditions in the North and dry conditions in the South, are typically observed during downward slopes of the NAOI [264]. Thus, three subperiods of the entire span of data (1952-2016) were analysed based on the detected change-points in the cumulative series, namely: a) 25 years, from 1952–1976 with upward slopes of the cumulative SOI-6 and downward slopes of the cumulative NAOI-6; b) 24 years, from 1977–2000 with downward slopes of the cumulative SOI-6 and upward slopes of the cumulative NAOI-6; and c) 16 years, from 2001–2016 with extreme upward slopes of the cumulative SOI-6 and extreme downward slopes of the cumulative NAOI-6. The question to address is how these dominant periods affect the droughts. It is expected that the drought characteristics during the positive and negative dominance phases of both cumulative NAOI-6 and SOI-6 would differ.

The duration, magnitude and maximum intensity of the droughts at each identified homogeneous region and subperiods are shown based on combined violin plots [186] aiming at recognising changes in the corresponding density functions. Figure 5-13 shows that in all cases, the distributions are right skewed with absolute values of the sample means always higher than those of the medians. In the first subperiod (Figure 5-13a), the interquartile range (IQR) of the properties in any of the three regions are relatively small and with similar density traces presenting just a few values outside the 95% intervals. From the first subperiod to the second one (25-year and 24-year long, respectively) the number of drought events and of periods under drought conditions increased; although the sample means do not significantly differ among regions, the shapes of the distributions are quite different (Figure 5-13b).

The distribution for the southern slope (RG2) in the second subperiod changed to a "multimodal" distribution with two peaks (Figure 5-13b) while for the other two regions there is a considerable increase in the confidence interval boundaries (length of the whiskers). Despite the subperiods 1977-2000 and 2001-2016 have almost the same IQR — Figures 5-13b and 5-13c — the sample means were pulled up by

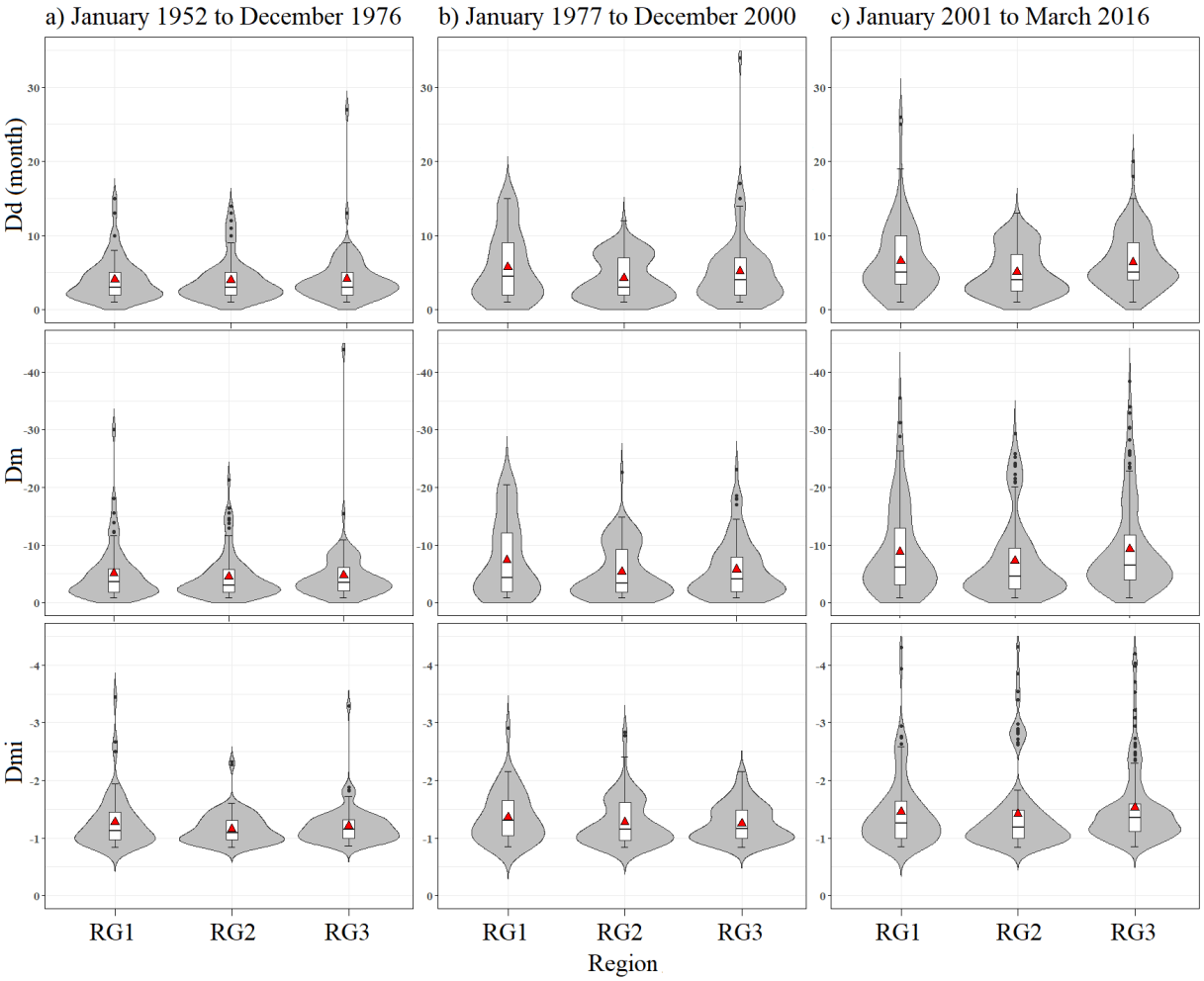

Figure 5-13: Violin plots combining rotated density traces on each side of the drought properties and box plots of the identified moderate or worse droughts of the 41 rain gauges at each homogeneous region for three defined periods, based on both the SOI and NAOI dominant positive/negative phases: **a**) January 1952–December 1976 (228 drought events — 938 periods under drought conditions), **b**) January 1977–December 2000 (306 drought events — 1451 periods under drought conditions), and **c**) January 2001 – March 2016 (266 drought events — 1748 periods under drought conditions). The whiskers indicate the boundaries of a 95% confidence interval, median is the horizontal line in each box or interquartile range (IQR), sample mean (*red triangles*), and the outside the 95% confidence boundaries (*black bullets*).

a considerable high number of large values of *Dm* and *Dmi* in the more recent period.

Although these results are in accordance with the ones from the KORE frequency estimator (obviously with some differences because the KORE is applied only to the periods under drought conditions), it was not possible to establish a clear relationship between ENSO/NAO and drought occurrence. In fact, although the violin plots of the first and third subperiods differ from those of the second subperiod, they are not as similar as the same dominance phase would indicate. Nevertheless, the results from both methods (the KORE and violin plots) confirmed an increase of drought occurrence. It is expected that these increases will be sustained in the island, because the dominance of the climatic drivers' phases over the most recent period (2001-2016) apparently has not ended yet.

The climatic signals — SOI-6 and NAOI-6 — were compared to the three regionalised SPI6 series (derived from the PCA) considering the entire span of data and the same three subperiods mentioned

at the beginning of this section. For the northern slope, the correlations between the SOI-6 and the SPI6 of RPC1-RG1 are very low, as shown in Figure 5-14a (about 64 years from January 1952 to March 2016), and Figure 5-14b (24 years from January 1977 to December 2000). The results for the period, with 25 years, from January 1952 to December 1976, are not included in the figure, because no significant correlations were found.

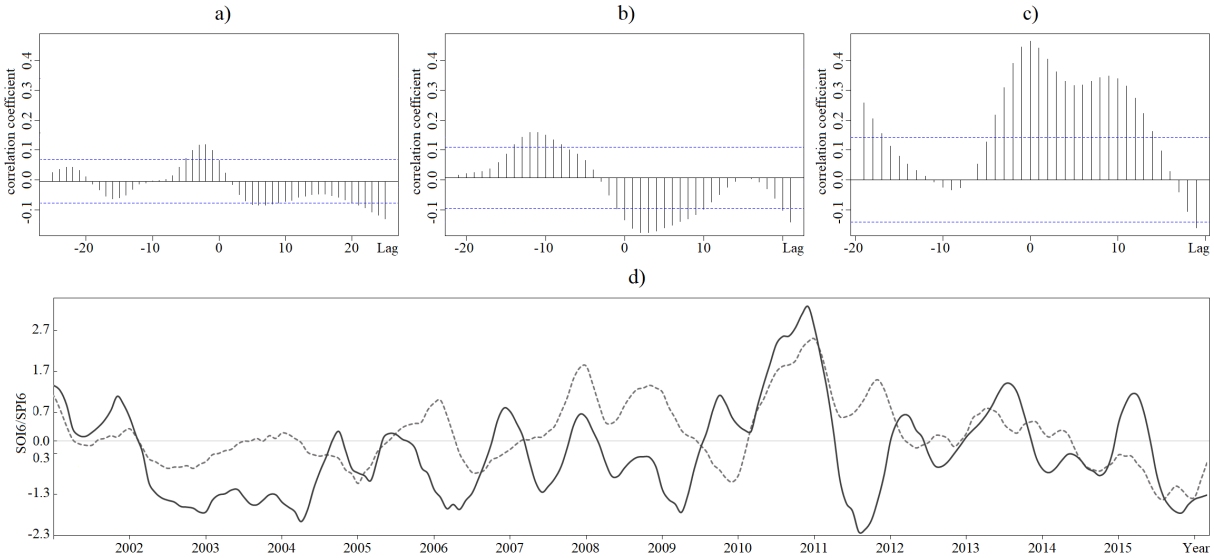

Figure 5-14: Cross-correlation (with a 95% confidence band, *dashed blue line*) between the 6-month running-length SOI (SOI-6) and the of RPC1-RG1: **a**) 1952–2016, **b**) 1977–2000, and **c**) 2001–2016. **d**) SOI-6 signal (*dashed line*) and the SPI6 of RPC1-RG1 (*solid line*).

In contrast, the correlation considering the shortest and most recent 16-year period, from January 2001 to December 2016 is significant, with a correlation coefficient of $r = 0.47$ and a p-value of 9.22e-10 (Figure 5-14c). As shown in Figure 5-14d, the shorter subperiod included the strongest La Niña event (positive SOI in December 2010), followed by the worst drought intensity ($Dmi = -2.2$ in August 2011). A similar behaviour was observed at a larger scale in the cumulative SOI-6 signal, previously described, in which the strongest La Niña dominant periods were followed by very intense droughts. The correlations between the SOI-6 and the SPI6 time series at the southern slope (RPC2-RG2), and at the central region (RPC3-RG3) are very low (correlation coefficients r ranging from -0.15 to 0.47), regardless the considered periods.

The same procedures were repeated for the NAOI-6 signal with surprisingly very poor correlations (e.g., correlation coefficients r ranging from -0.15 to 0.21 at the northern slope). These results may be improved if the definition of NAOI was based, not in Azores, but instead in a station located at latitude lower than the one of Madeira (Figure 5-6) which, however, was not possible as mentioned before.

According to the results obtained, there is not a clear evidence for a teleconnection between ENSO/-NAO phenomena and the identified droughts in Madeira Island in the long-term based on the adopted methodology. Nevertheless, there are subperiods when such correspondence is achieved between La Niña phases and the negative SPI6 phases but only for the RPC1-RG1 and RPC3-RG3 which was an unexpected result. This suggests that in the most recent period (2001–2016) the short-term La Niña phases could have somewhat an influence over the drought occurrences in these two regions. This influence is

more consistent than that in the case of El Niño phases with meaningless correlation. For instance, the positive SOI-6 phases and the negative SPI6 phases of the RPC3-RG3 from January 2010 to December 2011, have a significant correlation of $r = -0.56$ for 5-month lag (not shown here), which could be interpreted as the number of months that it takes for this regionalised SPI6 to react to any changes in the SOI-6 signal. Furthermore, this teleconnection result is in agreement with the analysis of droughts tendency for the same 2-year period of Figure 5-11c described in the previous section. Given that these findings are based on an index merely using precipitation data (the SPI) and a limited number of time windows (the total period with 65 years and three shorter sub periods), the results here described should therefore be treated with caution.

A few remarks must be added, namely related to the SOI capacity to address the droughts. In this sense, the association between La Niña/El Niño phases and droughts, identified in the present work, appears to be consistent with previous results, despite the different methodologies applied and the studied areas. Vicente-Serrano et al. [464], by utilising a Standardized Precipitation Evapotranspiration index (SPEI), concludes that La Niña phases in the Eastern Pacific causes droughts in the Western plains of Ecuador. By analysing a timescale of 12-month SPI (SPI12), from 56 meteorological stations in Southern South America through the 1961–2008 period, Penalba and Rivera [313] found that there is an evident response on the SPI12 to La Niña phases for 12-month lag, whereas there is no evidence of El Niño influence on SPI12 time series. In contrast, Nguyen et al. [288] applied SPI with a 3-month timescale at a Vietnamese river basin, which is three times the area of Madeira Island; the author argues that when El Niño occurs, meteorological drought occurrence in the studied river basin is very likely. Therefore, La Niña could be associated to droughts in longer timescales of SPI (SPI6, SPI12, etc.), whereas El Niño might be related to droughts in shorter timescales (e.g., SPI3) of the same index.

Finally, the results shown in this study mostly represent averages over several episodes of shorter duration. It is hence of interest to further explore individual drought events teleconnected with ENSO/-NAO dynamical processes. The early stage teleconnection assessment presented in this paper aimed at understating possible impacts of climate change on the droughts evolution in Madeira Island.

5.5 Conclusions

The paper presents the first long-term and high-resolution spatio-temporal characterisation of the droughts in Madeira Island by using rainfall data from a dense network comprising of 41 rain gauges, considering a time span of 80 years, from January 1937 to December 2016. To fill the data, a specific procedure, which is often applied to other scientific fields as previously discussed — the MICE algorithm — was used with very encouraging results. In fact, MICE proved to be able to preserve the long-term observed rainfall data structure after filling, even though some rain gauges had a relatively high percentage of missing data. This is quite relevant for small islands which have constraints in data availability. Moderate drought conditions were assessed based on the SPI computed on 6-month timescale (SPI6, related to agricultural droughts).

To analyse the variability of the moderate drought conditions, as identified by the SPI6, clustering

techniques and PCA were used. By applying the Varimax rotation to the first three component loadings, three non-overlapping homogeneous regions denoting different temporal variability were identified, namely, the RPC1-RG1 (northern slope), RPC2-RG2 (southern slope), and RPC3-RG3 (central region). These results support the idea that there are three representative drought variability regions based on SPI6. It should be stressed that because of the location, shape, and relief of Madeira Island, these regions also present quite different climate constraints. The comparison between the regionalisation obtained by using the PCA and clusters derived from different clustering techniques, would seem to suggest a satisfactory agreement regarding the rain gauges located in each homogeneous region. These three regions have also different drought time-dependent occurrence rates in recent years, as described by the KORE. Thus, they should be considered separately for an improved water resources management under drought conditions in Madeira Island for a better understanding, prevention, and mitigation of the consequences of future drought events.

Finally, a comparison between the SPI6 time series at the identified homogeneous regions and the El Niño-Southern Oscillation and North Atlantic Oscillation signals for the period 1952–2016 was made aiming at identifying possible dependencies between the drought events and extreme phases of the cumulative SOI-6 and NAOI-6. The analysis showed that the long-term SPI6 series and the NAOI-6 had no correspondence whatsoever. Although the correlations r between the positive phases of SOI-6 (La Niña phases) and negative values of SPI6 are relatively strong for some short recent periods in the northern slope and central regions, it is not possible to establish a cause-and-effect relationship, because such association sometimes fails. Thus, further work needs to be performed with more recent data and from different stations, not just the Reykjavik-Azores stations, to establish whether the periods under drought conditions are influenced by climatic signals such as ENSO and NAO.

In general, this study has gone some way towards enhancing the understanding about regional drought monitoring in Madeira Island in a changing environment. Moreover, it showed that, in recent years, specifically the central region is suffering a considerable increase in the number of drought events and in their duration, magnitude and maximum intensity. Due to the importance of this region in terms of groundwater recharge, such information is of utmost importance regarding the planning of actions aiming at improving the water security in the island.

THIS PAGE INTENTIONALLY LEFT BLANK

Chapter 6

Droughts Modelling With Regionalised Standardised Precipitation Index

This chapter has been published as: Espinosa, L. A., Portela, M. M., Pontes Filho, J. D., Studart, T. M. D. C., Santos, J. F., and Rodrigues, R. (2019). Jointly modeling drought characteristics with smoothed regionalized SPI series for a small island. *Water*, 11(12), 2489, https://doi.org/10.3390/w11122489

Abstract

The paper refers to a study on droughts in a small Portuguese Atlantic island, namely Madeira Island. The study aimed at addressing the problem of dependent drought events and at developing a copula-based bivariate cumulative distribution function for coupling drought duration and magnitude. The droughts were identified based on the Standardized Precipitation index (SPI) computed at three and six-month timescales at 41 rain gauges distributed over the island and with rainfall data from January 1937 to December 2016. To remove the spurious and short duration dependent droughts a moving average filter (MA) was used. The run theory was applied to the smoothed SPI series to extract the drought duration, magnitude, and interarrival time for each drought category. The smoothed series were also used to identify homogeneous regions based on principal components analysis (PCA). The study showed that MA is necessary for an improved probabilistic interpretation of drought analysis in Madeira Island. It also showed that, despite the small area of the island, three distinct regions with different drought temporal patterns can be identified. The copulas approach proved that the return period of droughts events can differ significantly depending on the way the relationship between drought duration and magnitude is accounted for.

Keywords:

Standardized Precipitation index; drought; Madeira Island; moving average; principal components analysis; copulas.

6.1 Introduction

Droughts, perceived as prolonged and regionally extensive occurrences of below average natural water availability, are amongst the most destructive hazards and can arise virtually everywhere in the Globe [435]. In island environments, where freshwater is often a limiting factor and people strongly rely on precipitation to refill the surface and underground water reservoirs and to support activities, like rain-fed

agriculture, droughts have frequently led to water insecurity — ranging from chronic water scarcity, lack of access to safe drinking water and sanitation services, to hydrological uncertainty [182, 28, 372]. As stated by the Intergovernmental Panel on Climate Change, IPCC, in its periodical assessment reports [255, 310, 31], compared to continental areas, islands are specifically more vulnerable to natural hazards due to their lower adaptive capacity, and are more often affected by extreme hydrological events (e.g., floods and droughts) and climate change, especially the so-called small islands with areas between 100 km^2 and 5000 km^2 [123]. Although small islands are not a homogeneous group, they share many common features, that distinguish them from larger islands [297], which make more challenging their adaptation to the projected climate change risks — such as the increase in the probability of drought and rainfall deficits [250].

The pronounced hydrological temporal but also spatial variability in some of the small islands makes drought complex to analyse and simultaneously a poorly understood extreme hydrological events (e.g., compared to floods) [435]. Examples are Madeira Island with a very pronounced wet season and with notable differences in rainfall between northern and southern slopes; the nearby Porto Santo Island, with some signs of aridity and relatively low rainfall concentrated in a few days [235]; the Azores archipelago with very wet high regions and drier coastal areas [380]; and the Canary Islands, located in a dry belt with very low rainfall near the coast specially in the flat islands [123]. These particular features have contributed to the absence of comprehensive drought assessment methods for small islands.

From a hydrological perspective, droughts are mainly characterised into three major types, with their own specific spatio-temporal characteristics [433], according to their duration and type of freshwater reservoir they affect: meteorological, agricultural, and hydrological droughts [238, 478, 457]. Meteorological droughts are characterised by a prolonged deficit of rainfall from its long-term average. Triggered by longer rainfall deficits, agricultural droughts are characterised by reduced soil moisture. Hydrological droughts are related to the impacts of persistent shortage of rainfall on lakes and reservoirs, rivers, surface water, and groundwater. Droughts can develop from over short periods (a few months) to longer periods (seasons, years, or even decades) [478, 432].

The monitoring of drought employs widely used drought indices, such as the Palmer Drought Severity index (PDSI) [305, 178], the Standardized Precipitation Evapotranspiration index (SPEI) [466, 35], or the Standardized Precipitation index (SPI) [258]. The PDSI uses precipitation and temperature data in a water balance model to compare meteorological and hydrological droughts across space and time, the SPEI considers precipitation and potential evapotranspiration, whereas the SPI only uses precipitation as state variable. Different authors have recommended that droughts should be studied within a regional context [432], because the results of individual case studies may not be comparable [93]. To make the drought analyses results comparable, regardless of the studied region, the drought indexes should be standardised [238] which is precisely one of the most important characteristic of the Standardized Precipitation index. The SPI is likely to be the most frequently used drought indicator worldwide, because it is applicable in all climate regimes [461, 463, 385, 238].

At given location, the SPI quantifies the observed rainfall as a standardised departure from a selected probability distribution function that models the raw rainfall data for the timescale of interest, from 1 to

48-month or longer (1, 3, 6, 9, and 12-month are the most common timescales [427]). The rainfall data are fitted to a probability distribution function, which is then transformed into a normal distribution so that the mean SPI for the location and desired timescale is zero [258]. Negative SPI values represent rainfall deficit, whereas positive SPI values indicate rainfall surplus.

By applying the run theory [504] to the SPI series at a given timescale, the following characteristics of the droughts can be determined (Figure 6-1): drought duration (Dd), during which the SPI is continuously below an adopted critical level or threshold (u); magnitude (Dm) indicating the cumulative absolute deficit due to a drought event below the threshold; drought maximum intensity (Dmi) indicating the minimum value of the drought index below the critical level, and interarrival time (L), which is the time range between the initiation of two consequent drought events.

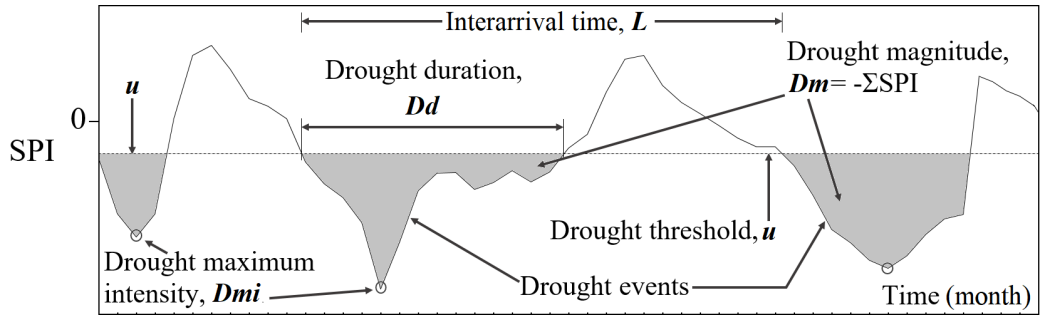

Figure 6-1: Run theory and definition of drought characteristics — Dd, Dm, Dmi, L for SPI values below an adopted threshold, u. Adapted from Santos et al. [384].

However, drought characterisation based on SPI requires a particular attention, due to the possible presence of minor droughts and of mutually dependent droughts [241, 136]. In fact, it is possible that a long SPI run below the threshold u turns out to be split into a number of shorter events due to the occurrence of sporadic and anomalous rainfalls [91] either for very short periods and with little hydrological importance, or for longer periods but unable to counterbalance the rainfall deficit. These smaller drought events cannot be considered mutually independent, and it is advisable to group them into a single large event to capture the true severity of the longer drought they portrait [241]. Filtering techniques can be applied for this purpose [416].

Another specific feature of the droughts is that, although they are regional phenomena, the data required to characterise them are measurements acquired at discrete networks. Therefore special clustering techniques need to be applied to enable a regional characterisation based on pointwise data. Multivariate and geostatistical techniques are commonly used to analyse the spatial and temporal variability of climate variables — such as rainfall, temperature, and air relative humidity [24]. Principal components analysis (PCA) is a multivariate technique that has been relevant in these types of analyses, specially in climate regionalisation [486, 45, 67, 451]. It allows a field to be decomposed into spatial-temporal terms, such as in the analysis of the spatial and temporal variability of droughts characterised based on the SPI [462, 463, 385, 354].

The last challenge when addressing the droughts relates to the capability of the models to describe the dependency among their different characteristics, which, as in many other hydrological phenomena, are presumably highly correlated and should be addressed from a multivariate perspective [59]. However,

droughts have been traditionally studied in a univariate context [407], mostly aiming at recognising their occurrences. Since a univariate approach ignores the dependence structure among the drought characteristics, it may result in a poorer representation of the phenomenon. The analysis of the association among those characteristics based on multivariate approaches although relevant, is still an insufficiently studied issue, namely in small islands.

In the scope briefly mentioned, this paper aims at presenting a pioneering study, particularly in its application to a small island, on drought characterisation. For that purpose, Madeira Island (741 km^2) was selected as case study and the SPI at different timescales was computed based on 80 years of the monthly rainfalls at a large set of rain gauges distributed over the island. The mutually dependent droughts were assessed based on a digital filter, namely the moving average, MA, with different running lengths. By applying principal component analysis, PCA, to the original unfiltered SPI series, but also to the smoothed SPI series given by the MA, homogeneous regions were identified regarding the temporal pattern of the droughts. For each region, representative unsmoothed and smoothed regionalised SPI series were obtained and compared aiming at understanding the effect of the MA and at identifying the running length that should be adopted. Bivariate copulas were then applied to model the dependency structure between some of the drought characteristics extracted from the regionalised smoothed SPI series, namely drought duration, Dd, and drought magnitude, Dm. Finally, different return periods (univariate, bivariate and conditional) were assigned to the drought events.

The study provides a continuous and comprehensive temporal, but also spatial, characterisation of the droughts in Madeira Island enabling to understand the susceptibility of the different regions to the phenomenon, as well as how it has changed along time.

6.2 Study region and data

Madeira is a volcanic island located in the North Atlantic Ocean with an area of 741 km^2, a length of 57 km and a maximum width of 22 km. Centered at 32º 44.34' N and 16º 57.91' W, approximately 600 km northwest of the Western African coast, Madeira Island has a steep topography consisting of an enormous central E-W oriented mountainous system (Pico Ruivo, the highest peak with 1862 m.a.s.l.; Pico do Areeiro, in the island's eastern part with 1818 m.a.s.l.; and Paúl da Serra region above 1400 m.a.s.l. on the west) which divides the island mainly into north and south from an orographical perspective. According to the Koppen's classification [58], the climate is predominantly temperate with dry and warm to hot summers as approaching the coastal zones of Madeira.

Due to the strong topography influence, the rainfall falls predominantly in the north facing slope because of the prevailing N-E trade winds [235]. The rainfall regime, which is remarkably variable between the northern and southern slopes, is not only affected by the local circulation, but also by synoptic systems which are typical in mid-latitudes, such as fronts and extratropical cyclones, and the Azores Anticyclone in the summer season [140]. Rainfall in Madeira is concentrated in the period from October to mid-April, while in summer (from June to August) the rainfalls are very low [58].

The average annual rainfall in Madeira Island presents a very uneven distribution — Figure 6-2 and Table 6.1. The highest average annual values, exceeding 2200.0 mm, are observed in the northern slope and specially in the central highland region of the island (e.g., the rain gauges of M01 with 2592.2 mm, and M02 in the Paúl da Serra region with 2605.7 mm), which is the critical one for the island's water security because it is where most of the natural groundwater recharge areas are located [333, 104]. The smallest rainfalls, less than 650.0 mm, occur in the lowland areas of the southern slope (e.g., the rain gauge of M05 in the city of Funchal with only 608.4 mm).

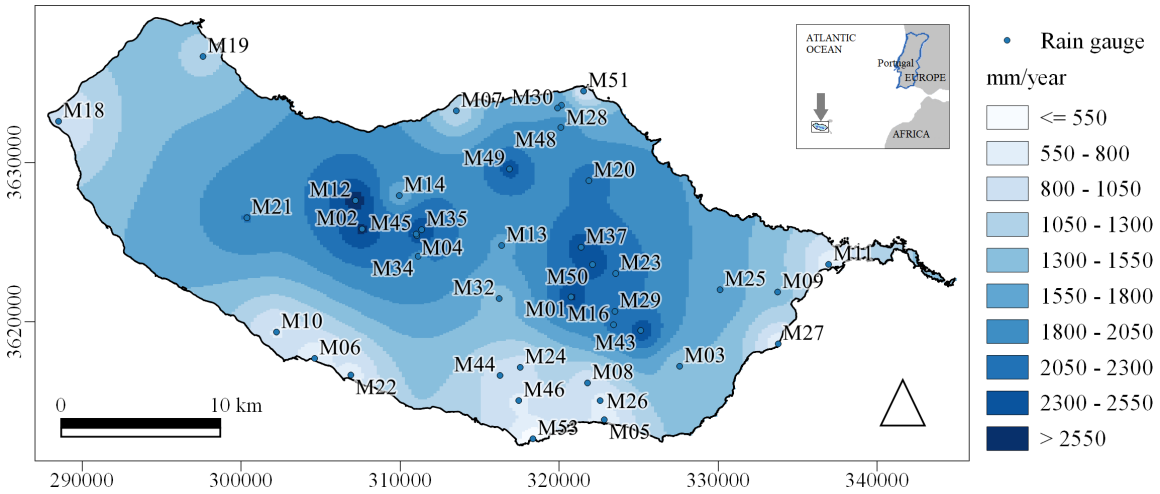

Figure 6-2: Location of the 41 rain gauges of Table 6.1 over the surface of the average rainfall referred to the hydrological year, HDY. Adapted from Espinosa et al. [118].

The drought characterisation in Madeira Island utilised the daily rainfalls, from January 1937 to December 2016 (80 years), at the 41 rain gauges of Figure 6-2 and Table 6.1. The records were provided by the Portuguese Institute for Sea and Atmosphere (IPMA), which has high data quality standards and is one of the main sources of Portuguese hydrometeorological data. The series had a few missing values that were filled in using a gap-filling procedure tested for Madeira Island, namely the Multivariate Imputation by Chained Equations (MICE) [454, 118]. The monthly and annual rainfall series were obtained from the complete daily series.

6.3 Methods

6.3.1 Standardized Precipitation index (SPI) calculation and drought recognition

As previously mentioned, the drought characterisation utilised the SPI, developed by McKee et al. [258], and described in detail by Edwards and McKee [108]. Such index measures the rainfall anomalies at a given location, based on the comparison of the rainfall for a timescale of interest, with the average rainfall in the same period. The historic records are fitted to a probability distribution, which is then transformed into a normal distribution such that the mean SPI value for that location and timescale is zero. The *Pearson Type III* distribution with parameters given by the *L*-moments was applied to describe both the

Table 6.1: The 41 rain gauges adopted in the study. Identification (code and name), WGSM84 coordinates, elevation, average annual rainfalls from October 1937 to September 2016 (hydrological years) (HDY), areal-influence (ATP) according to the Thiessen polygons method, and homogeneous regions (RG1, RG2, RG3) to which they belong. Adapted from Espinosa et al. [118].

Code	**Name**	**Lat-N**	**Lon-W**	**Elev.** (m.a.s.l.)	**HDY** (mm)	**ATP** (km^2)	**Region**
M01	Areeiro	32.7200	-16.9170	1610.00	2592.20	13.67	RG3
M02	Bica da Cana	32.7562	-17.0554	1560.00	2605.70	22.06	RG3
M03	Camacha-Valparaiso	32.6763	-16.8421	675.00	1406.80	28.58	RG2
M04	Encumeada de São Vicente	32.7503	-17.0169	900.00	2410.50	1.12	RG3
M05	Funchal Observatório	32.6476	-16.8924	58.00	608.40	7.08	RG2
M06	Lugar de Baixo	32.6790	-17.0832	15.00	597.70	10.94	RG2
M07	Ponta Delgada	32.8213	-16.9920	123.00	1070.20	17.27	RG1
M08	Sanatório	32.6687	-16.9006	384.00	809.70	11.76	RG2
M09	Santana	32.7220	-16.7742	80.00	1338.90	16.47	RG1
M10	Canhas	32.6942	-17.1098	400.00	779.20	25.20	RG2
M11	Caniçal	32.7374	-16.7387	15.00	674.60	11.35	RG1
M12	Caramujo	32.7694	-17.0585	1214.00	2653.00	30.43	RG3
M13	Curral das Freiras	32.7456	-16.9599	787.00	1754.70	20.09	RG3
M14	Loural	32.7727	-17.0292	368.00	1600.60	19.38	RG3
M16	Montado do Pereiro	32.7019	-16.8839	1260.00	2080.40	6.54	RG3
M18	Ponta do Pargo	32.8108	-17.2589	339.00	817.80	40.68	RG1
M19	Porto do Moniz	32.8492	-17.1628	64.00	1234.20	52.22	RG1
M20	Queimadas	32.7831	-16.9022	881.00	2207.30	34.68	RG1
M21	Rabaçal	32.7585	-17.1311	1233.00	2005.30	88.95	RG2
M22	Ribeira Brava	32.6740	-17.0630	25.00	703.10	24.14	RG2
M23	Ribeiro Frio	32.7309	-16.8830	1167.00	2276.10	19.08	RG3
M24	Santo António	32.6768	-16.9459	525.00	929.80	10.83	RG2
M25	Santo da Serra	32.7260	-16.8170	660.00	1790.10	36.10	RG1
M26	Bom Sucesso	32.6620	-16.8960	291.00	719.60	6.98	RG2
M27	Santa Catarina	32.6936	-16.7731	49.00	660.30	7.75	RG2
M28	Cascalho	32.8290	-16.9250	430.00	1537.80	1.83	RG1
M29	Poiso e Posto Florestal	32.7130	-16.8870	1360.00	2134.50	4.60	RG3
M30	Vale da Lapa	32.8270	-16.9280	346.00	1882.30	5.32	RG1
M32	Lapa Branca-Curral das Freiras	32.7190	-16.9650	610.00	1360.00	22.46	RG2
M34	Serra de Água	32.7420	-17.0200	573.00	1971.00	24.35	RG3
M35	Chão dos Louros E.	32.7570	-17.0180	895.00	2509.70	9.55	RG3
M37	Lombo Furão	32.7490	-16.9110	994.00	2416.20	13.62	RG3
M43	Meia Serra	32.7020	-16.8700	115.00	2444.00	12.48	RG3
M44	Covão ETA	32.6750	-16.9630	510.00	930.30	22.46	RG2
M45	Encumeadas Casa EEM	32.7540	-17.0210	1010.00	2202.40	2.32	RG3
M46	Santa Quitéria ETA	32.6610	-16.9510	320.00	726.50	9.20	RG2
M48	ETA São Jorge	32.8160	-16.9260	500.00	2093.70	10.43	RG1
M49	Fajã Penedo	32.7920	-16.9600	620.00	2378.80	23.84	RG3
M50	Cabeço do Meio-Nogueira	32.7357	-16.8987	995.00	2477.90	4.08	RG3
M51	Ponta de São Jorge	32.8337	-16.9067	266.00	779.30	6.15	RG1
M53	Lido-Cais do Carvão	32.6366	-16.9365	20.00	340.10	4.99	RG2

monthly rainfalls and the cumulative rainfalls at Madeira Island [385, 118].

The drought events were assessed based on the SPI computed at 3 (SPI3) and 6 (SPI6) months for the period of 80 years (960 months of rainfall data) and for the 41 selected rain gauges. These two timescales are usually related to meteorological and agricultural droughts [176], and, the latter, also to early signs of streamflow shortfalls [427]. Such sustained shortfalls are very important for the management of water resources in Madeira Island due to its high dependence on rainfall for groundwater recharge — which is the main source of freshwater in the island [104, 118].

The drought categories for SPI were those proposed by Agnew [9], presented in Table 6.2. According to this classification, there is a drought whenever the SPI falls below the threshold $u < -0.84$. Furthermore, the droughts were characterised based on run theory as depicted in Figure 6-1. It is noteworthy that drought duration (Dd) and magnitude (Dm) are necessarily mutually dependent, because the longer Dd is, the higher Dm should be.

Table 6.2: Drought categories and associated non-exceedance probability based on SPI. Adapted from Agnew [9].

Category	Probability	SPI
No drought	0.60	≥ -0.84 and < 0.84
Moderate drought	0.20	< -0.84
Severe drought	0.10	< -1.28
Extreme drought	0.05	< -1.65

6.3.2 Moving average filter (MA)

Relatively few studies have addressed the run theory applied to the recognition of the droughts characteristics (Figure 6-1) to cope with the possible dependence of the periods under drought conditions. Tallaksen et al. [434], Fleig et al. [136], Van Loon et al. [457] have applied moving average (MA), with different running lengths and at different SPI timescales, to smooth out short-term fluctuations and highlight possible longer drought events. Similar procedures have been carried out by López-Moreno et al. [241], although applied to drought analysis based on streamflow series, Zelenhasić and Salvai [508], Byzedi and Saghafian [48], Li et al. [232], Shin et al. [409]. However, criteria about the running length to adopt, also taking into account the different timescales of SPI, are missing.

The moving average (MA) is the most common filter in digital signal processing, mainly because it is the easiest to understand and use [416]. The MA is a convolution using a very simple filter kernel. This makes it the premier filter for encoded signals in the time domain in which samples are usually created by sampling at regular intervals of time containing information that is interpretable without reference to any other sample [154]. In the present paper, the MA operates by averaging a number of points from the input signal symmetrically chosen around each point in the output signal, according to:

$$y_i = \frac{1}{M} \sum_{j=-(M-1)/2}^{(M-1)/2} x_{i+j} \tag{6.1}$$

where x_i is the input signal, y_i is the output signal, and M is the number of points in the average (running length). For $M = 1$, the output coincides with the original or unsmoothed series.

For the smoothing of SPI3 and SPI6 at the adopted 41 rain gauges, Equation 6.1 was applied aiming at reducing the random noise, i.e., the spurious short droughts and drought interruptions, while maintaining a sharp step response (e.g., Dm, Dmi). Different M were tested and assessed for each SPI timescale, namely, for SPI3, 2 and 3, and for SPI6, 3 and 5. The SPI output series for M equal to 1, have obviously the same values as the input series and were also analysed for both timescales (unsmoothed series). Symmetrical averaging usually requires that M be an odd number. However, for the case of SPI3, because only two values could be adopted for M, they were both tested, despite one being an even number. It is acknowledged that the higher M, the greater the noise reduction, but also the greater the possibility that the signal would be distorted by the smoothing operation. A key issue in SPI series smoothing is the choice of M. In the Madeira case study, the selection of its value for each timescale was assessed based on the regionalised SPI series derived from the unsmoothed and smoothed SPI series at the 41 rain for different values of M, as discussed in Section 6.4.1.

6.3.3 Regionalised Standardized Precipitation index (SPI) series based on principal components analysis (PCA)

Principal components analysis is a statistical procedure that transforms a number of (possibly) correlated variables into a (smaller) number of uncorrelated variables called principal components (PC) [169]. When applied to the Standardized Precipitation index (SPI) values from a set of rain gauges, the analysis allows their regrouping and consequently, the delimitation of climatic regions in relation to synoptic situations, i.e., a regionalised SPI series.

Examples of regionalised climatic series are the three distinct areas having coherent climatic variability identified by Bonaccorso et al. [40] in Sicily from 1926 to 1996, the three homogeneous regions adopted for the drought characterisation in mainland Portugal (which is approximately 120 times the size of Madeira Island) Santos et al. [384], or the two climatic sub-regions in the western Iran by Raziei et al. [355], all of them based on the SPI field. In the case of Madeira Island, the PCA was applied to the unsmoothed and smoothed (with different M) SPI time series at the timescales of 3 and 6 months.

The PCA consists in computing the covariance matrix of the SPI series with the corresponding eigenvalues (λ) and eigenvectors ($\mathbf{v}$). The main applications of the PCA, specifically the principal factor analysis (PFA), are: (1) to reduce the number of variables; (2) to detect structures in the relationship between variables; (4) to reduce the system's information entropy, i.e., the information not directly available about a system due to the uncertainty or randomness of data flow [94, 399]; and (3) to combine correlated variables into factors [207]. As for Madeira Island, the variables are the SPI series at the rain gauges and the factors, the regionalised SPI. Henceforth, the term factor analysis will be used generically to encompass both PCA and PFA.

The determination of the number of components or factors to retain was based on the Kaiser's rule [207], according to which the factors whose eigenvalues are greater than 1 must be retained. The spatial patterns of the eigenvectors (factor loadings) represent the correlation between the original data and the corresponding factor time series. More localised patterns are obtained by applying the Varimax rotation technique to selected factor loadings [3]. The projection of the SPI fields onto the orthonormal eigenfunctions provides the factor score time series [357]. Factor scores are estimates of the actual values of individual cases (observations) or linear combinations of the observed variables which consider what is shared between the item and the factor (i.e., shared variance) and what is not measured (i.e., error term variance) [99]. For instance, the estimated factor score (regionalised SPI) on factor j for observation, or month, i, F_{ji}, can be represented as follows:

$$\mathrm{F}_{ji} = w_{j1}z_{i1} + w_{j2}z_{i2} + ... + w_{jk}z_{ik} \tag{6.2}$$

where w_j is the regression weight, multidimensional value referred to as factor score coefficient; and z_i is the variable, i.e., the SPI series at a single rain gauge. For any single common factor, an infinite number of sets of scores can be derived that would be consistent with the same factor loadings [164]. The factor scores are particularly useful to perform further regional analyses that have been identified in the factor analysis, such as fitting drought characteristics with copulas, as will be mentioned in the next subsections.

6.3.4 Univariate analysis of drought duration and magnitude; selection of probability distribution functions

The univariate analysis of drought duration, Dd, and magnitude, Dm, has not yet established a consensus on the marginal distribution to be used. Shiau [407] suggested the use of Exponential and Gamma distributions to model separately Dd and Dm, respectively. The advisable practice, however, is to test different families to achieve the best fitted model for each region and drought characteristic [21, 272]. Thus, in this study, Exponential, Gamma, Logistic, Lognormal, Normal, and Weibull were inspected — based on the most relevant factor scores for the smoothed regionalised SPI3 and SPI6 series — to determine the most suitable distribution function for drought duration and magnitude values. The Akaike Information Criterion (AIC) was used as a goodness of fit test to define the best fitted distribution and the parameters were estimated using the Maximum Likelihood Estimation (MLE) [509].

6.3.5 Bivariate analysis of drought duration and magnitude

Few researchers have been devoted to the multivariate modelling of extreme events due to the considerably more data requirements, sophisticated mathematical treatment and models required, and complex interpretation of the outputs. A bivariate probabilistic distribution is thus more common, provided it proves to be able to account for the relevant correlations under analysis, mostly because it is easier to apply. One of the drawbacks of using bivariate distributions is that the same family is needed for each marginal distribution [e.g. 153, 406, 23]. Several methods have been proposed to investigate the bivariate characteristic of droughts, such as the product of the conditional distribution of drought severity for a given drought duration and the marginal distribution of drought duration to construct the joint distribution of drought duration and magnitude used by Salas et al. [373] and González and Valdés [156], with complex mathematical derivation involved. Nevertheless, multivariate distributions using copulas, whose applications in hydrology have been increasing in recent years with several and different utilisations [209, 500, 55, 21, 125, 325, 402], can overcome such issues.

Copulas, introduced by Sklar [415], are functions that can be used to separate the marginal distributions from the dependency structure of a given multivariate distribution. According to Nelsen [287], to model n random correlated variables $(x_1, x_2, ..., x_n)$ with respective marginal distributions $F_1(x_1), F_2(x_2), ..., F_n(x_n)$, the joint distribution function $H(x_1, x_2, ..., x_n)$ is given by the copula function $C(u_1, u_2, ..., u_n)$ according to Equation 6.3:

$$H(x_1, x_2, ..., x_n) = C[F_1(x_1), F_2(x_2), ..., F_n(x_n)] = C(u_1, u_2, ..., u_n) \tag{6.3}$$

where $F_k(x_k) = u_k$ for $k = 1, ..., n$, with $u_k \sim u(0, 1)$. The two major classes of copula families are the Meta-elliptic copulas and Archimedean copulas. Meta-elliptic copulas are directly obtained by inverting Sklar's Theorem [415].

Given a bivariate distribution function F with invertible margins F_1 and F_2, a bivariate copula $C(u_1, u_2)$ for $u_1, u_2 \in [0, 1]$ is given by Equation 6.4. Meta-elliptic copulas are symmetric and hence lower and upper tail dependence coefficients are the same.

$$C(u_1, u_2) = F(F_1^{-1}(u_1), F_2^{-1}(u_2)) \tag{6.4}$$

The Archimedean copulas are more flexible than Meta-elliptic and can present lower or upper tail dependence. They are defined by Equation 6.5:

$$(u_1, u_2) = \varphi^{[-1]}(\varphi(u_1) + \varphi(u_2)) \tag{6.5}$$

where φ is the generator function of the copula C and $\varphi[0,1] \rightarrow [0,\infty]$ is a continuous and factually reducing function. The Meta-elliptic Gaussian and t-Student, and the Archimedean Clayton, Frank, and Gumbel, were tested to verify best fit. Table 6.3 presents the formulations of the candidate copula families. When the Archimedean copula is rotated 180^{o} it is called survival copula and can invert the predefined tail dependence to best fit the data.

Table 6.3: Copula candidate family and mathematical formulation.

	Copula Family	**Mathematical Formulation**
Meta-elliptic	Gaussian	$\phi_\rho(\phi^{-1}(u_1), \phi^{-1}(u_2))$
	t-Student	$\mathrm{T}_{\rho,v}(\mathrm{T}_v^{-1}(u_1), \mathrm{T}_v^{-1}(u_2))$
Archimedean	Clayton	$(u_1^{-\theta} + u_2^{-\theta} - 1)^{\frac{-1}{\theta}}$
	Frank	$-\theta^{-1}\log\left\{1 + \frac{(e^{\theta u_1}-1)(e^{\theta u_2}-1)}{(e^{\theta}-1)}\right\}$
	Gumbel	$\exp(-[(-\ln u_1)^{-\theta} + (-\ln u_2)^{\theta}]^{\frac{1}{\theta}})$

Copula parameters estimation

The parameters for the families of the candidate copula were estimated considering the maximum likelihood MLE method, by choosing the Inference Functions from Margins (IFM) method [202]. The use of IFM method requires previous fitting of marginal distributions functions to transform its values into the $(0,1)$ interval.

Best fitted copula

To compare the bivariate copula models from a number of families and choose the best fitted model, the fit statistic AIC was used. First, all the candidate copulas, Gaussian, t-Student, Clayton, Frank, and Gumbel, are fitted using maximum likelihood estimation, MLE. Then the AIC is computed for all copula families and the one with the minimum AIC is chosen. According to Brechmann and Schepsmeier [43], for observations $u_{i,j}$ with $i = 1, ..., N$ and $j = 1, 2$, the AIC of a bivariate copula family c with θ parameter(s) is defined by Equation 6.6:

$$\mathrm{AIC} = -2\sum_{i=1}^{N} \ln[c(u_{i,1}, u_{i,2} \mid \theta)] + 2k \tag{6.6}$$

where one parameter copulas have $k = 1$ and the two parameter t-student has $k = 2$. The two parameter copula is penalised in the minimisation of AIC value to reduce overfitting possibility due to parsimony

principle.

6.3.6 Drought return periods

Univariate return period

A common approach used in hydraulic and hydrological design is based on frequency analysis of the recurrence interval or return period (T) of a given hydrological event. Shiau and Shen [408] define the return period as the average elapsed time between occurrences of the event with a certain magnitude or greater. The highest the return period the more exceptional the event is. The univariate return period of droughts, based on the concept of stochastic processes, is derived as follows. The return period of drought duration (T_{Dd}) or magnitude (T_{Dm}), is described as function of the expected interarrival time $E(L)$ and of the cumulative distribution functions (CDF) of the drought characteristic marginal distributions $F_{Dd}(d)$ or $F_{Dm}(m)$, as defined in Equations 6.7 and 6.8, where both return periods and $E(L)$ are expressed in years [406, 408, 227]. The $E(L)$ is calculated by adjusting a distribution function to interarrival time and deriving its mean value.

$$\mathrm{T}_{Dd} = \frac{E(L)}{P(Dd \geq d)} = \frac{E(L)}{1 - F_{Dd}(d)} \tag{6.7}$$

$$\mathrm{T}_{Dm} = \frac{E(L)}{P(Dm \geq m)} = \frac{E(L)}{1 - F_{Dm}(m)} \tag{6.8}$$

Bivariate drought return periods

Due to the multivariate nature of droughts, Shiau [407] proposed a methodology that categorises the return periods of bivariate distributed hydrological events as joint and conditional return periods. The joint drought duration and magnitude return periods can be defined in two cases: return period for $Dd \geq d$ or $Dm \geq m$ and return period for $Dd \geq d$ and $Dm \geq m$, as described by Equations 6.9 and 6.10, respectively:

$$\mathrm{T}_{Dd\,\mathrm{or}\,Dm} = \frac{E(L)}{P(Dd \geq d\,\mathrm{or}\,Dm \geq m)} = \frac{E(L)}{1 - F_{DdDm}(d,m)} = \frac{E(L)}{1 - C(F_{Dd}(d), F_{Dm}(m))} \tag{6.9}$$

$$\mathrm{T}_{Dd\,\&\,Dm} = \frac{E(L)}{P(Dd \geq d, Dm \geq m)} = \frac{E(L)}{1 - F_{Dd}(d) - F_{Dm}(m) + C(F_{Dd}(d), F_{Dm}(m))} \tag{6.10}$$

where $\mathrm{T}_{Dd\,\mathrm{or}\,Dm}$ is the return period for $Dd \geq d$ or $Dm \geq m$; $\mathrm{T}_{Dd\,\&\,Dm}$ is the return period for $Dd \geq d$ and $Dm \geq m$.

Conditional drought return periods

Similarly, the conditional return periods can be defined for two cases: the return period of drought duration given drought magnitude exceeding a certain threshold ($\mathrm{T}_{Dd|Dm\geq m}$), and the return period of

drought magnitude given drought duration exceeding a certain threshold ($T_{Dm|Dd\geq d}$). These conditional return periods are calculated by Equations 6.11 and 6.12:

$$T_{Dd|Dm\geq m} = \frac{T_{Dm}}{P(Dd \geq d, Dm \geq m)} \tag{6.11}$$

$$T_{Dm|Dd\geq d} = \frac{T_{Dd}}{P(Dd \geq d, Dm \geq m)} \tag{6.12}$$

Detailed discussions on the relationships between univariate, bivariate, and conditional return periods can be found in Shiau [407] and have been applied worldwide [509, 61, 227, 444, 21, 272].

6.4 Results

6.4.1 Smoothed regionalised SPI3 and SPI6

At each of the 41 rain gauges, the SPI series were computed based on 80 years (960 months) of rainfall data, as described in Section 6.3.1, and then smoothed by applying the MA technique, mentioned in Section 6.3.2. The SPI series have different lengths according to the timescale and running length: e.g., the length of the unsmoothed SPI3 is $n = 960 - 2 = 958$ while for $M = 3$ is $n = 960 - 2 - 2 = 956$; the unsmoothed SPI6 series has $n = 960 - 5 = 955$ elements, and the smoothed series with M of 5, $n = 960 - 5 - 4 = 951$ elements. The smoothed SPI series were organised into matrices, $\boldsymbol{X}$, with different number of rows (cases or observations) but with the same number of columns (the 41 rain gauges, i.e., 41 variables), namely, for SPI3, $\boldsymbol{X}_{958\times41}$, $\boldsymbol{X}_{957\times41}$, $\boldsymbol{X}_{956\times41}$, for M equal to 1, 2 and 3, respectively, and for SPI6, $\boldsymbol{X}_{955\times41}$, $\boldsymbol{X}_{953\times41}$, $\boldsymbol{X}_{951\times41}$, for M equal to 1, 3 and 5, also respectively.

The factor analysis was applied to the dataset to transform the 41 variables into the same number of factors — extracted by the PC method — by means of simple linear transformations. The first factors are expected to account for meaningful amounts of variance. By using the eigenvalues (λ), information about the number of factors to retain and the contribution to the data variance of each factor (F) can be extracted individually and cumulative. The Kaiser's rule [207], with threshold of $\lambda > 1.00$, was used as the criterion to choose the number of F to retain (Section 6.3.3). According to the results of Table 6.4, this rule suggests a three-factor solution regardless the timescale of SPI and running length, with explained cumulative variance (Σ%Var) higher than 80.00% (Tables 6.4 and 6.5 for the unrotated and rotated cases, respectively).

By retaining the first three F, the cumulative %Var is in any case higher than 84.00% of the original dataset. Up from the fourth F (F4), the individually explained variance is relatively meaningless. Based on the Kaiser rule, only the first three F were retained for a Varimax maximising rotation (Varimax normalised) of the original variable space. The rotation aims at best fitting the SPI series to the axes that represent the factors, and redistributing the explained variance of each F in the most unequal way. By this way, the original problem of 41 dimensions, was transformed into a three-dimensional problem. The same number of F was retained in a previous study by Espinosa et al. [118] but with different factor retention criteria — based on the scree plot and on some clustering techniques [169].

Table 6.4: Eigenvalues (λ) of each factor (F) from the factor analysis associated with the unrotated solution for different timescale of SPI and running length (M). %Var represents the explained variance calculated by dividing λ by the number of variables, i.e., 41.

Factor	SPI3 unsmoothed			SPI3 with $M=2$			SPI3 with $M=3$			SPI6 unsmoothed			SPI6 with $M=3$			SPI6 with $M=5$		
	λ	%Var	Σ%Var	λ	%Var	Σ%Var	λ	%Var	Σ%Var	λ	%Var	Σ%Var	λ	%Var	Σ%Var	λ	%Var	Σ%Var
1	31.47	76.76	76.76	31.48	76.77	76.77	31.28	76.29	76.29	31.69	77.30	77.30	31.40	76.58	76.58	31.00	75.62	75.62
2	2.42	5.91	82.67	2.41	5.87	82.64	2.39	5.84	82.13	2.23	5.43	82.73	2.26	5.51	82.09	2.30	5.61	81.23
3	1.06	2.59	85.26	1.07	2.61	85.25	1.10	2.69	84.82	1.13	2.77	85.50	1.18	2.89	84.98	1.24	3.02	84.25
4	0.65	1.59	86.85	0.68	1.67	86.92	0.74	1.80	86.62	0.81	1.97	87.47	0.90	2.19	87.17	1.00	2.43	86.68
5	0.58	1.42	88.27	0.59	1.45	88.37	0.60	1.47	88.09	0.63	1.54	89.01	0.66	1.61	88.78	0.72	1.75	88.43
⋮	⋮	⋮	⋮	⋮	⋮	⋮	⋮	⋮	⋮	⋮	⋮	⋮	⋮	⋮	⋮	⋮	⋮	⋮
39	0.02	0.05	85.17	0.02	0.04	85.18	0.02	0.04	84.76	0.02	0.05	85.42	0.01	0.02	84.94	0.01	0.02	84.22
40	0.02	0.05	85.22	0.02	0.04	85.22	0.01	0.03	84.80	0.01	0.02	85.47	0.01	0.02	84.96	0.01	0.02	84.24
41	0.02	0.04	85.26	0.01	0.03	85.25	0.01	0.02	84.82	0.01	0.02	85.49	0.01	0.01	84.97	0.00	0.01	84.25

Factor loadings are part of the output from factor analysis. They explain the correlations between the observed variables and the underlying factors. According to the three-dimensional solution (after Varimax maximising rotation), for the first factor (F1) and regardless of the timescale and M, there are relatively strong factor loadings (correlation coefficients of 0.56 or higher) on the SPI series at the eleven rain gauges located in the northern slope of Madeira and small loadings at the rain gauges located in the southern slope and in central region, as reported in Table 6.5.

Table 6.5: Factor loadings (correlation coefficients) from the factor analysis associated with the rotated solution for different timescales of SPI and running lengths (M). Correlations equal or higher than 0.60 are marked with an asterisk. Smaller factor loadings were assumed to be uncorrelated with their respective F. The rain gauges are sorted in terms of the proposed regionalisation.

Region	**Code**	**SPI3 unsmoothed**			**SPI3 with $M=2$**			**SPI3 with $M=3$**			**SPI6 unsmoothed**			**SPI6 with $M=3$**			**SPI6 with $M=5$**		
		F1	F2	**F3**	F1	F2	**F3**	F1	F2	**F3**	F1	F2	**F3**	F1	F2	**F3**	F1	F2	**F3**
RG1	M07	*0.75	0.41	0.39	*0.75	0.41	0.39	*0.74	0.40	0.41	*0.73	0.41	0.43	*0.71	0.40	0.45	*0.70	0.40	0.47
	M09	*0.88	0.26	0.22	*0.88	0.26	0.22	*0.88	0.26	0.23	*0.87	0.27	0.24	*0.87	0.26	0.25	*0.87	0.25	0.27
	M11	*0.65	0.54	0.28	*0.65	0.55	0.28	*0.64	0.55	0.29	*0.62	0.52	0.31	*0.60	0.53	0.32	*0.61	0.52	0.33
	M18	*0.61	0.45	0.38	*0.60	0.44	0.39	*0.70	0.42	0.40	*0.62	0.34	0.45	*0.70	0.30	0.46	*0.60	0.27	0.48
	M19	*0.61	0.38	0.39	*0.60	0.36	0.40	*0.63	0.35	0.42	*0.61	0.35	0.42	*0.61	0.34	0.44	*0.62	0.33	0.46
	M20	*0.76	0.24	0.39	*0.75	0.24	0.40	*0.74	0.24	0.41	*0.72	0.24	0.40	*0.71	0.23	0.41	*0.69	0.22	0.42
	M25	*0.70	0.31	0.40	*0.68	0.31	0.42	*0.67	0.31	0.43	*0.66	0.30	0.43	*0.64	0.30	0.43	*0.62	0.29	0.44
	M28	*0.80	0.28	0.43	*0.79	0.28	0.44	*0.77	0.28	0.46	*0.77	0.30	0.46	*0.75	0.30	0.49	*0.72	0.30	0.51
	M30	*0.76	0.32	0.49	*0.76	0.31	0.50	*0.74	0.31	0.51	*0.74	0.31	0.51	*0.72	0.30	0.53	*0.70	0.29	0.52
	M48	*0.83	0.32	0.33	*0.82	0.33	0.34	*0.81	0.33	0.34	*0.80	0.35	0.33	*0.79	0.36	0.33	*0.78	0.37	0.33
	M51	*0.80	0.41	0.19	*0.81	0.41	0.18	*0.81	0.41	0.17	*0.81	0.41	0.18	*0.82	0.40	0.17	*0.82	0.39	0.16
RG2	M03	0.38	*0.65	0.48	0.37	*0.65	0.48	0.36	*0.64	0.48	0.38	*0.64	0.50	0.37	*0.64	0.49	0.37	*0.64	0.48
	M05	0.35	*0.85	0.27	0.35	*0.85	0.28	0.35	*0.85	0.29	0.35	*0.84	0.33	0.33	*0.85	0.33	0.32	*0.85	0.33
	M06	0.28	*0.84	0.27	0.28	*0.84	0.27	0.29	*0.84	0.28	0.30	*0.83	0.29	0.30	*0.83	0.29	0.30	*0.83	0.30
	M08	0.36	*0.77	0.37	0.37	*0.77	0.37	0.36	*0.76	0.38	0.36	*0.76	0.40	0.35	*0.76	0.41	0.34	*0.76	0.41
	M10	0.32	*0.81	0.38	0.32	*0.81	0.38	0.32	*0.81	0.38	0.33	*0.80	0.40	0.33	*0.80	0.40	0.33	*0.80	0.40
	M21	0.39	*0.63	0.55	0.39	*0.64	0.56	0.39	*0.63	0.56	0.39	*0.64	0.52	0.39	*0.63	0.52	0.38	*0.62	0.52
	M22	0.28	*0.85	0.30	0.27	*0.85	0.29	0.27	*0.86	0.29	0.29	*0.85	0.29	0.27	*0.86	0.28	0.25	*0.86	0.27
	M24	0.27	*0.79	0.45	0.27	*0.79	0.45	0.26	*0.79	0.46	0.29	*0.78	0.49	0.27	*0.77	0.50	0.25	*0.77	0.50
	M26	0.37	*0.80	0.36	0.37	*0.81	0.37	0.36	*0.81	0.38	0.35	*0.81	0.41	0.34	*0.81	0.42	0.33	*0.81	0.43
	M27	0.54	*0.61	0.36	0.55	*0.60	0.36	0.55	*0.60	0.36	0.53	*0.62	0.40	0.52	*0.63	0.40	0.51	*0.64	0.40
	M32	0.36	*0.68	0.46	0.36	*0.68	0.46	0.35	*0.68	0.47	0.34	*0.68	0.49	0.33	*0.68	0.50	0.31	*0.67	0.50
	M44	0.31	*0.82	0.40	0.31	*0.82	0.40	0.31	*0.82	0.41	0.32	*0.81	0.44	0.31	*0.81	0.44	0.31	*0.81	0.44
	M46	0.33	*0.86	0.32	0.32	*0.86	0.32	0.32	*0.86	0.32	0.33	*0.86	0.33	0.32	*0.87	0.33	0.31	*0.87	0.32
	M53	0.38	*0.84	0.27	0.38	*0.85	0.27	0.37	*0.85	0.27	0.36	*0.86	0.28	0.35	*0.86	0.28	0.34	*0.87	0.28
RG3	M01	0.42	0.45	*0.68	0.41	0.44	*0.69	0.39	0.42	*0.71	0.39	0.38	*0.73	0.37	0.36	*0.75	0.34	0.34	*0.76
	M02	0.44	0.37	*0.71	0.44	0.37	*0.71	0.42	0.37	*0.72	0.39	0.38	*0.73	0.37	0.37	*0.75	0.35	0.37	*0.75
	M04	0.47	0.50	*0.62	0.47	0.50	*0.63	0.46	0.50	*0.64	0.44	0.51	*0.65	0.43	0.51	*0.67	0.41	0.50	*0.69
	M12	0.50	0.46	*0.62	0.50	0.46	*0.62	0.49	0.46	*0.62	0.47	0.46	*0.63	0.47	0.44	*0.63	0.46	0.43	*0.64
	M13	0.30	0.53	*0.62	0.30	0.59	*0.62	0.29	0.52	*0.63	0.33	0.53	*0.68	0.33	0.53	*0.69	0.32	0.55	*0.70
	M14	0.50	0.51	*0.61	0.51	0.51	*0.64	0.50	0.51	*0.66	0.52	0.50	*0.62	0.51	0.49	*0.62	0.50	0.49	*0.63
	M16	0.46	0.50	*0.64	0.46	0.50	*0.64	0.45	0.50	*0.65	0.46	0.50	*0.66	0.44	0.49	*0.67	0.42	0.49	*0.68
	M23	0.52	0.33	*0.63	0.54	0.32	*0.69	0.52	0.32	*0.70	0.51	0.36	*0.66	0.49	0.36	*0.60	0.46	0.36	*0.60
	M29	0.48	0.41	*0.67	0.47	0.40	*0.68	0.45	0.38	*0.70	0.45	0.39	*0.70	0.42	0.38	*0.72	0.40	0.38	*0.74
	M34	0.42	0.55	*0.61	0.42	0.55	*0.64	0.41	0.55	*0.67	0.40	0.53	*0.68	0.39	0.53	*0.68	0.38	0.53	*0.68
	M35	0.44	0.47	*0.71	0.44	0.47	*0.71	0.43	0.46	*0.71	0.41	0.46	*0.73	0.40	0.45	*0.74	0.39	0.45	*0.75
	M37	0.54	0.43	*0.64	0.54	0.44	*0.64	0.53	0.44	*0.64	0.52	0.47	*0.63	0.50	0.47	*0.64	0.48	0.48	*0.64
	M43	0.46	0.47	*0.67	0.46	0.48	*0.67	0.44	0.47	*0.68	0.45	0.47	*0.69	0.43	0.47	*0.70	0.41	0.46	*0.71
	M45	0.45	0.51	*0.65	0.45	0.51	*0.65	0.44	0.50	*0.66	0.43	0.51	*0.68	0.42	0.51	*0.68	0.41	0.51	*0.68
	M49	0.57	0.40	*0.64	0.57	0.41	*0.64	0.58	0.41	*0.63	0.52	0.42	*0.61	0.55	0.43	*0.62	0.53	0.43	*0.62
	M50	0.55	0.49	*0.60	0.55	0.49	*0.61	0.53	0.49	*0.63	0.54	0.49	*0.62	0.53	0.49	*0.63	0.51	0.49	*0.64
Rotated λ =		11.48	13.48	9.99	11.38	13.49	10.09	11.00	13.37	10.42	10.82	13.33	10.90	10.40	13.22	11.22	9.83	13.15	11.56
Σ%Var=			85.26			85.25			84.82			85.49			84.97			84.25	

It is clear from Table 6.5 that, the rain gauges with SPI series with the strongest association to the underlying latent variable factor 2 (F2), are the fourteen located in the southern slope, with factor loadings of 0.60 or higher. The SPI series at the sixteen rain gauges of the central highlands region are associated with factor 3 (F3) — factor loadings of 0.61 or higher. The foregoing suggests that individual factors are modelled by different individual SPI series (provided they are relevant). Note that among comparable unrotated and rotated solutions, the %Var of each F changes but the Σ%Var remains constant (Table 6.4 and Table 6.5). Factor loadings smaller than 0.60 were assumed to be uncorrelated with their respective F. Table 6.5 shows that the cumulative variance, Σ%Var, decreases as the running length increases, but this is just an effect of the decreasing length of the series.

Figure 6-3 depicts the spatial distribution of the rotated factor loadings over Madeira Island, suggesting that the island encompasses three distinct regions characterised by different SPI temporal variability. The factor loading patterns for all the SPI timescales and running lengths are similar, delineating three regions that include all the rain gauges, nearly cover the whole study area and do not overlap, namely: the northern slope or RG1 (11 rain gauges), the southern slope or RG2 (14 rain gauges), and the central region or RG3 (16 rain gauges) (column Region of Table 6.1). Each map of the figure was obtained by cropping and joining the three regions with factor loadings approximately higher than 0.6. Each one of these regions was delimited by applying the inverse distance weighting (IDW) with an exponent of 2 [47] to the corresponding factor loadings. The regions are related to the regionalised SPI, i.e., to the factor scores of F1, F2, and F3 — SPI-RG1, SPI-RG2 and SPI-RG3, respectively — as shown in Figure 6-4. The similar spatial (Figure 6-3) and temporal (Figure 6-4) patterns suggests that the application of MA did not have an effect on the drought regionalisation.

However, the factor loadings shown in Table 6.5 give rise to some considerations that support the choice of the M values. In any region and SPI timescale, when selecting a value for M it is important to ensure that the corresponding factor loadings for the rain gauges there located are the highest, i.e., for that M, those rain gauges should be highly positively correlated to the F of the region but uncorrelated, as much as possible, to the F of the other regions.

Due to the importance of the central region, RG3, on the availability and management of Madeira freshwater resources, special attention was given to the same when applying the previous criteria. Accordingly, based on the values of Table 6.5, $M = 3$ was selected for SPI3, and of $M = 5$ for SPI6. These running lengths are also valid for RG2 while for RG1 there are not preferable ones. However, in any region the highest correlations for different M are always very close and do not compromise the chosen M values.

For the central region, RG3, Figure 6-5 presents the temporal evolution for the period from 2000 to 2016, adopted as example, of the regionalised SPI (SPI-RG3) from the factor analysis based on the unsmoothed and smoothed series with different running lengths. The figure shows that the application of MA to the original SPI series prior to the factor analysis, eliminates spurious and short duration events for both regionalised SPI3 and SPI6, and that the value of the running length determines the smoothness of the factor score time series. Although the SPI series with M of 2, 3, and 5, are smoother than those computed based on the unsmoothed data, the general pattern for the different time series is the same.

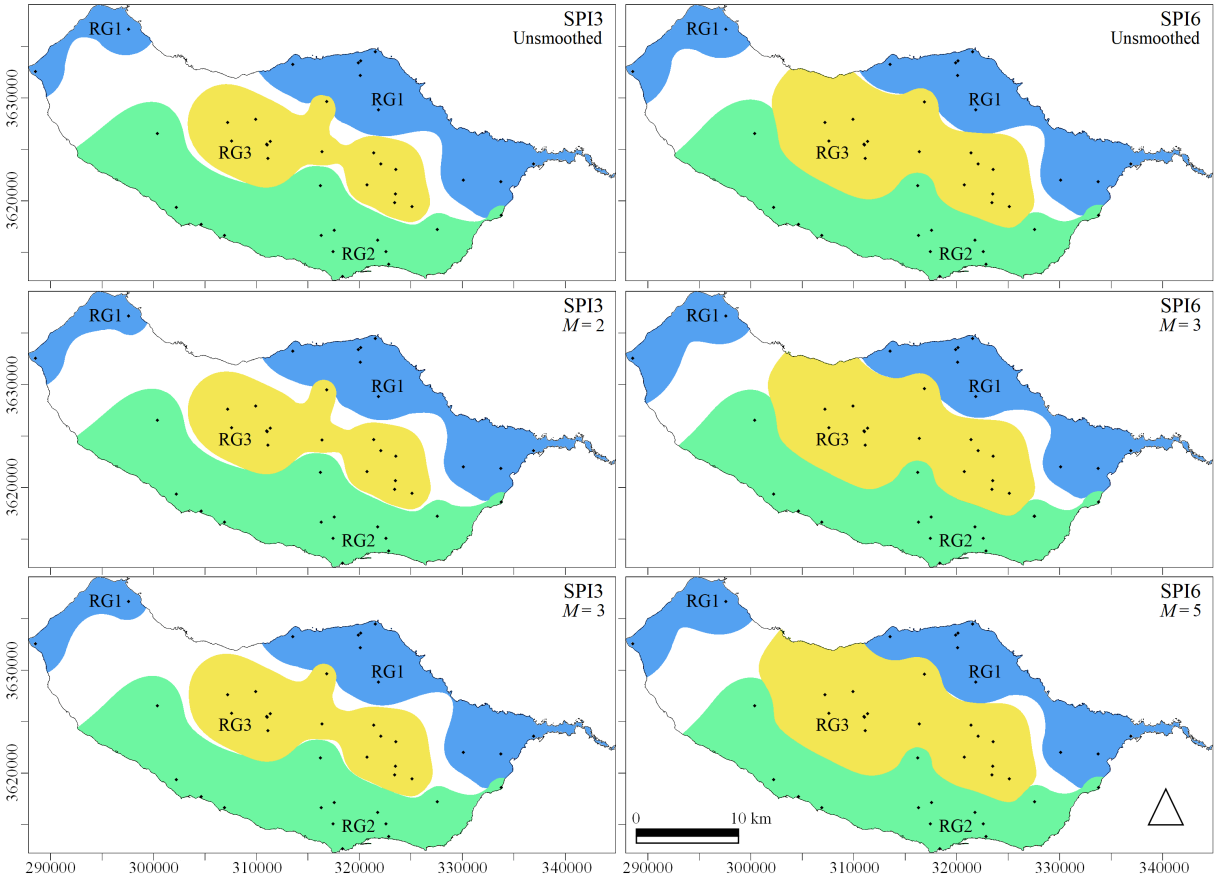

Figure 6-3: Spatial distribution of the homogeneous regions based on the factor loadings (correlation coefficients) higher than 0.60. The regions RG1, RG2, and RG3, are related to F1, F2, and F3, respectively.

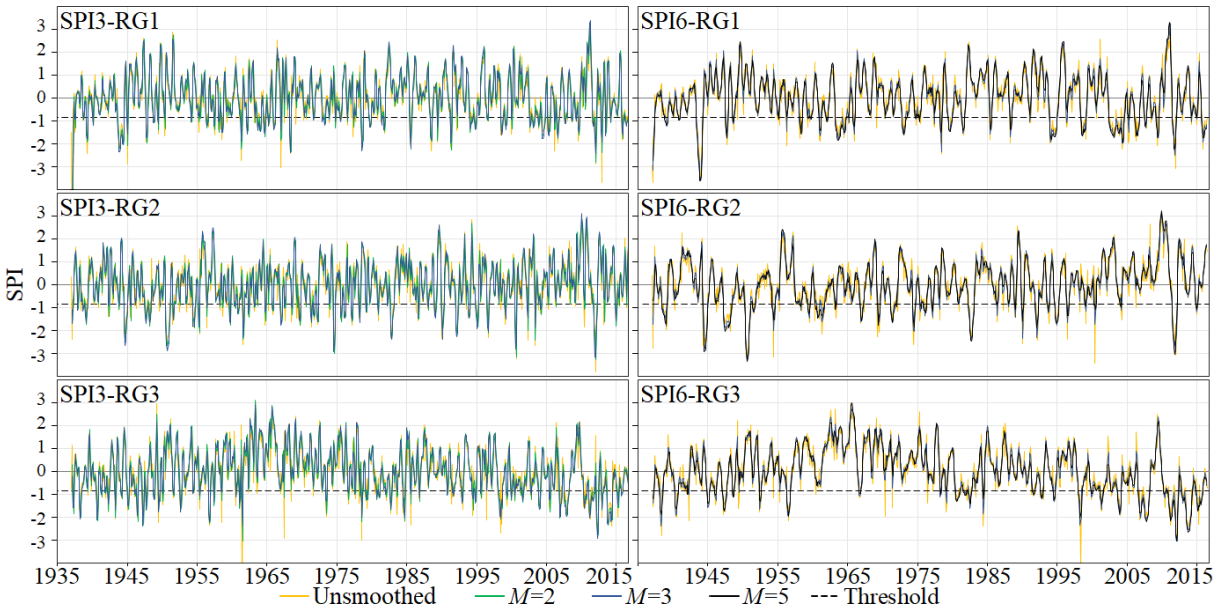

Figure 6-4: January 1937 to December 2016. F1 (RG1-northern slope), F2 (RG2-southern slope) and F3 (RG3-central region) from the series of SPI3 (left figures with unsmoothed series and with running lengths, M, of 2 and 3) and of SPI6 (right figures with also unsmoothed series and with M of 3 and 5).

To support the choice of the values of the running lengths, the yearly number of months under moderate or worse drought conditions (Table 6.2) given by SPI3-RG3 and SPI6-RG3, for the last 16

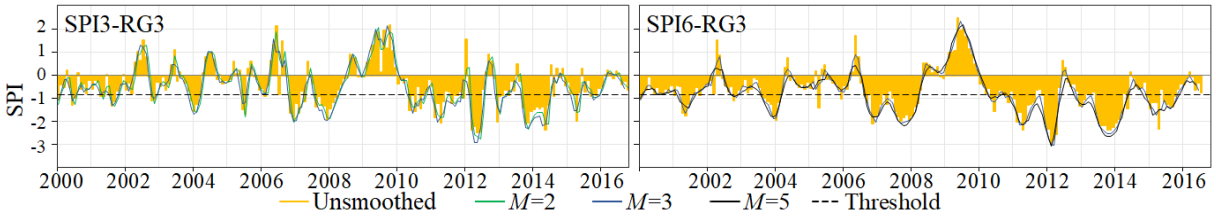

Figure 6-5: January 2000 to December 2016. F3 (RG3-central region) from the SPI3 (left for unsmoothed series and M of 2 and 3) and the SPI6 series (right for unsmoothed series and M of 3 and 5).

years with data, were obtained as a function of M, as shown in Figure 6-6. According to the figure, the regionalised unsmoothed SPI3 indicates 65 months with $u < -0.84$, whereas for $M = 2$, and $M = 3$, there are 68, and 72 months, respectively. The equivalent numbers for SPI6 are 77, 88, and 94 for the unsmoothed and for the smoothed series with $M = 3$, $M = 5$, respectively. The number of months with moderate or worse droughts from the unsmoothed and smoothed SPI3 series is similar. For the SPI6 series it increases, especially due to the increase in the number of months with severe and extreme droughts (e.g., the year of 2011 or 2015).

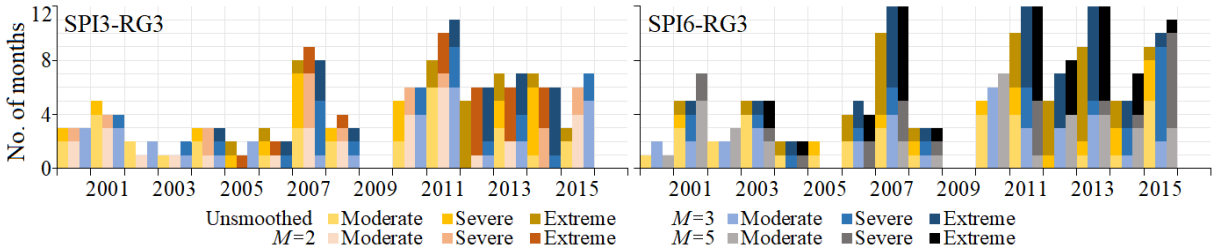

Figure 6-6: Number of months under drought conditions from January 2000 to December 2016 for the regionalised SPI3 (left figures) and SPI6 (right figures) at the central region.

Also for RG3, Figure 6-7 enables a closer look at the drought characteristics. For both SPI timescales, it shows that for the unsmoothed SPI series there is a higher number of 1-month droughts, however with smaller magnitude which can make the drought analysis biased and, therefore, less representative. As the running length increases, the number of drought events decreases, while Dd and Dm increase. The smoothed regionalised series always allow to recognise the more severe droughts with longer duration and higher magnitude. On the basis of these findings and of those from the factor analysis, the smoothed SPI series, whether at the rain gauges (non-regionalised) or regionalised based on $M = 3$, for SPI3, and on $M = 5$, for SPI6, have been selected in pursuing the study based on copulas.

6.4.2 Estimation of drought characteristics and univariate analysis

The understanding of the relationship among drought duration and magnitude is essential to better comprehend the phenomenon and its impacts. For this purpose, the Dd and Dm values were obtained for the 80-year period by applying the run theory (section 6.3.1) to the smoothed SPI3 and SPI6 series ($M = 3$ and $M = 5$, respectively), as shown in Figure 6-8. The resulting descriptive statistics are presented in Table 6.6.

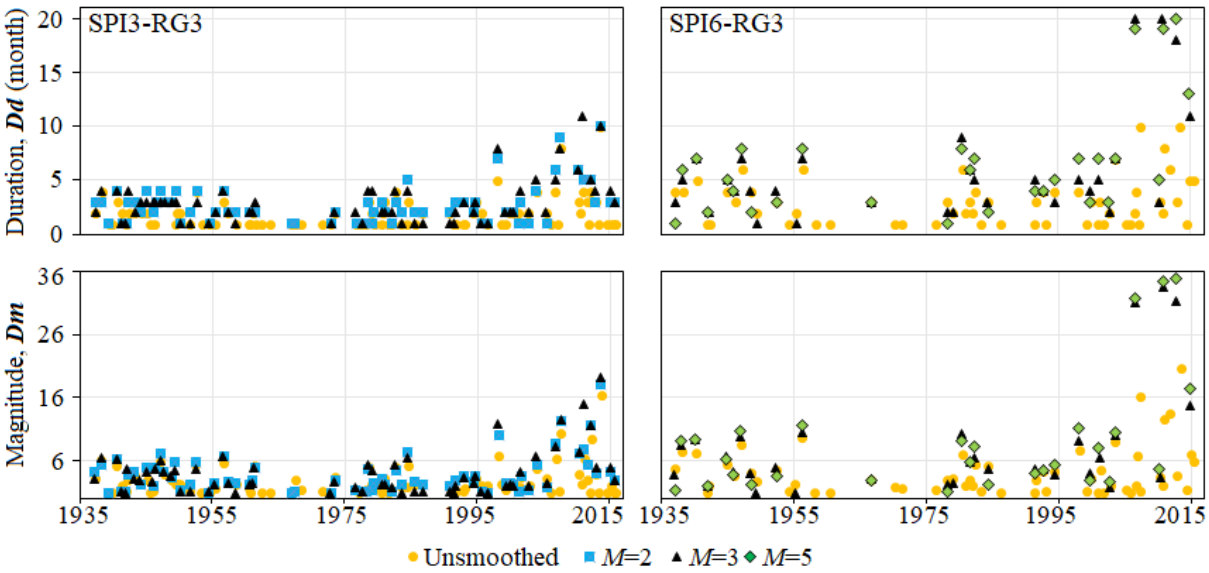

Figure 6-7: *Dd* and *Dm* of the drought events for the regionalised unsmoothed and smoothed series with different running lengths for SPI3 (left figures) and SPI6 (right figures) series in the central region (RG3).

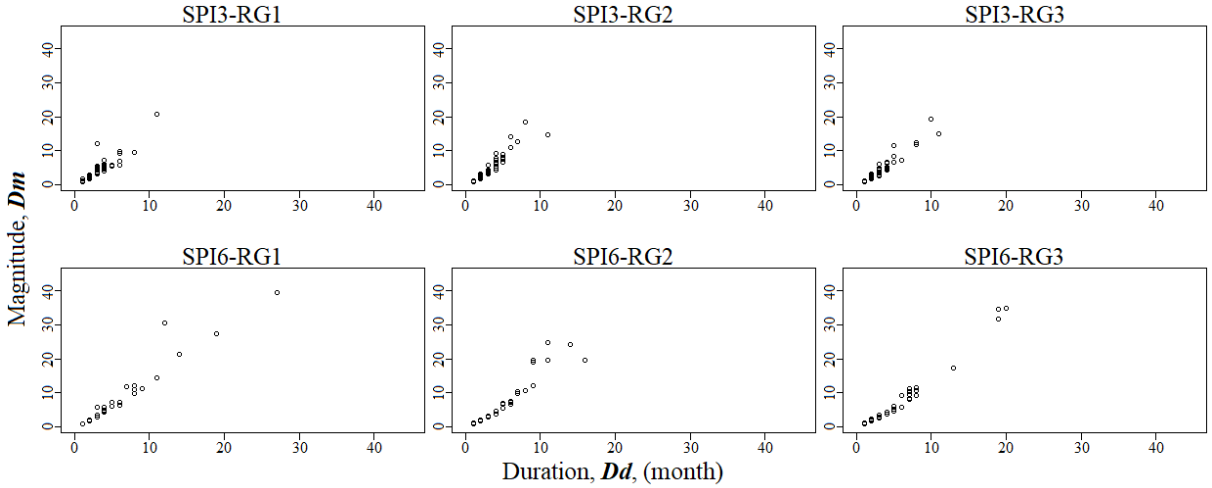

Figure 6-8: Scatter plots between *Dd* and *Dm* obtained from the regionalised SPI3 (with $M = 3$) and SPI6 (with $M = 5$) series, for the different regions.

The number of events that occurred in the different regions of Madeira Islands during 1937–2016 ranged from 58 to 65, for SPI3, and from 29 to 35, for SPI6. Despite the smaller number of events for SPI6 comparatively to SPI3 (which resulted in larger interarrival times), the *Dd* and *Dm* values indicate worse drought conditions. The Kendall's τ correlation coefficient presents very high values (higher than 0.80) which are in accordance with dependence visible in the scatter plots of Figure 6-8. However, such coefficient measures only the overall strength of the association between *Dd* and *Dm*, but does not give information about how such association varies across the distribution [459]. The higher Kendall's τ for SPI6 denotes a stronger correlation between *Dd* and *Dm*. The mean values of *Dd* and *Dm* suggest, for SPI3, regions with similar characteristics, while for SPI6, the values for RG3 are higher. However, these findings are quite vague because they are based on a univariate appraisal which justifies a copula-based characterisation of the dependency structure between *Dd* and *Dm*, presented in the next sections.

Table 6.6: For each region, drought events statistics for $u < -0.84$ based on the regionalised SPI3 (with $M = 3$) and SPI6 (with $M = 5$). $E(L)$ is the expected drought interarrival time. Kendall's τ is the correlation between Dd (in month) and Dm.

Time series	**No. events**	**Average** $E(L)$		**Kendall's** τ	Dd (month)				Dm			
		(month)	(year)		**Mean**	**Max**	**SD**	**CV**	**Mean**	**Max**	**SD**	**CV**
SPI3-RG1	63	15.17	1.26	0.83	3.00	11	1.89	0.63	4.06	20.85	3.29	0.81
SPI3-RG2	58	16.48	1.37	0.89	3.07	11	1.88	0.61	4.43	18.57	3.78	0.85
SPI3-RG3	65	14.71	1.23	0.87	2.95	11	2.06	0.70	3.98	19.33	3.57	0.90
SPI6-RG1	35	27.17	2.26	0.91	5.63	27	5.55	0.99	7.87	39.49	9.07	1.15
SPI6-RG2	32	29.72	2.48	0.93	5.53	16	3.77	0.68	7.95	24.93	7.18	0.90
SPI6-RG3	29	32.79	2.73	0.92	6.52	20	5.15	0.79	9.00	34.90	9.39	1.04

6.4.3 Estimation of bivariate joint distributions

The bivariate copulas of Table 6.7 were used to determine the best-fitted copula for modelling bivariate joint distribution between drought duration and magnitude aiming at obtaining the corresponding joint return periods, which are essential for evaluating and predicting the regional drought risks. According to Sections 6.3.4 and 6.3.5, one copula function was selected for each homogeneous region and timescale. The estimated parameters and values of the goodness-of-fit test AIC for the best-fitted copula are listed in the same table. For SPI3, for example, the Survival Gumbel was chosen for all the three regions. On the other hand, for SPI6, a specific copula family was assigned to each region, meaning that the drought characteristics and their dependence are more distinct among regions.

Table 6.7: Selected copula families, Kendall tau (τ), marginal distributions and parameters of the models. Par stands for the copula parameter and Par1 and Par2 for the marginal distribution parameters.

Time series	**Copula**				**Drought duration,** Dd				**Magnitude,** Dm			
	Selected family	**Par**	**Kendall's** τ	**AIC**	**Marginal**	**Par1**	**Par2**	**AIC**	**Marginal**	**Par1**	**Par2**	**AIC**
SPI3-RG1	Survival Gumbel	5.78	0.82	-166.77	log-normal	0.91	0.62	238.06	log-normal	1.12	0.77	290.57
SPI3-RG2	Survival Gumbel	6.67	0.85	-171.54	log-normal	0.96	0.58	216.12	log-normal	1.18	0.79	278.28
SPI3-RG3	Survival Gumbel	7.57	0.86	-210.22	log-normal	0.88	0.62	242.15	log-normal	1.06	0.80	296.83
SPI6-RG1	Survival Gumbel	12.40	0.91	-143.60	log-normal	1.34	0.88	188.58	log-normal	1.50	1.09	214.26
SPI6-RG2	Clayton	16.47	0.89	-121.63	Gamma	2.22	0.40	168.00	log-normal	1.66	0.96	197.97
SPI6-RG3	Gaussian	0.98	0.89	-104.17	log-normal	1.60	0.76	163.02	log-normal	1.78	0.91	184.06

Figure 6-9 presents the copulas that best describe the observed dependence patterns between normalised values of Dd and Dm. The normalisation was performed to allow direct comparisons among multivariate normal shapes and to bring out specific features, such as sharp corners indicating tail dependence [43]. Only SPI6 in region RG3 (SPI6-RG3) presented a copula without tail dependence, i.e., a Gaussian one. On the other hand, SPI6-RG2 presented the greatest lower tail dependence. This result indicates that with the increase in drought duration and magnitude values, the linear correlation between the variables tends to decrease. Although the copulas for SPI6-RG1 and SPI6-RG2 are of the same class (Archimedean copulas, Table 6.3), the dependence structure of the former is closer to SPI6-RG3 (Meta-elliptic copula). This result indicates the existence of a lower tail dependence for SPI6-RG1 less pronounced than the one for SPI6-RG2.

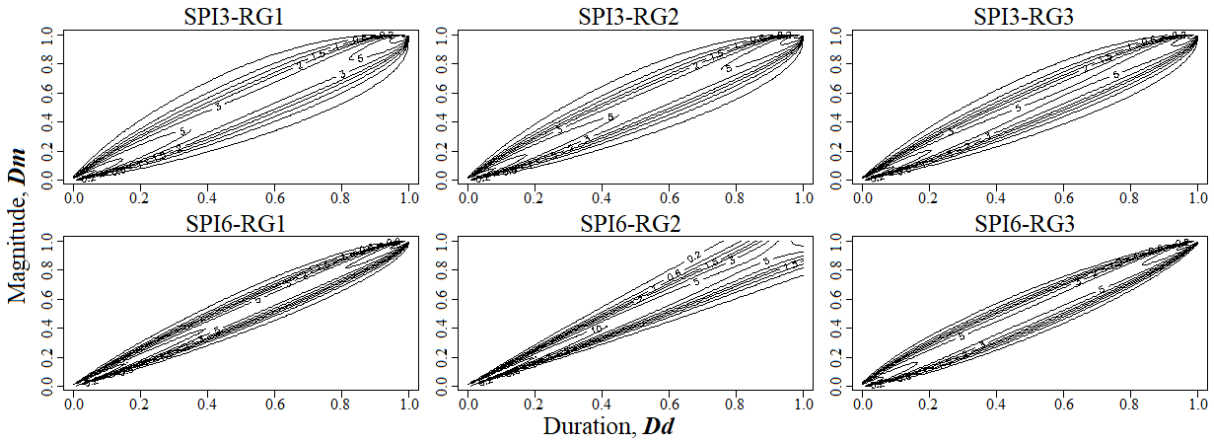

Figure 6-9: Joint cumulative distribution functions of the best-fitted copula of normalised drought duration and magnitude for each region and timescale of SPI.

6.4.4 Regional bivariate return period of drought events

Since various Dd and Dm combinations can result in the same return period, the joint return periods defined by Equations 6.9 and 6.10 ($T_{Dd\,or\,Dm}$ and $T_{Dd\,\&\,Dm}$, respectively) were obtained and represented in the form of the contours lines shown in Figure 6-10. Different patterns can be observed. In fact, for $T_{Dd\,or\,Dm}$ there are not bounds (meaning that the contour lines do not cross the axes) while the contour lines for $T_{Dd\,\&\,Dm}$ are bounded by the axes. Based on the figure and as an example, a combination of $Dd = 20$ months and $Dm = 10$ for SPI6 results in $T_{Dd\,or\,Dm} = 10$ years for all the three regions, while for $T_{Dd\,\&\,Dm}$ equals to 74, 588 and 84 years, in RG1, RG2, RG3 respectively.

For each region and SPI timescale, Table 6.8 identifies the five drought events with the highest return periods according to the different approaches. Just for the sake of systematising, the start dates of the droughts were identified based on the events to which correspond the return periods $T_{Dd\,\&\,Dm}$.

A numerical example shows that, for SPI6-RG1, regardless the approach, the worst drought, wiht $Dd = 27$ months and $Dm = 39.49$, occurred in June 2002. According to the univariate approach (Equations 6.7 and 6.8), the return periods are 167.5 and 99.7 years. As for the bivariate approach, the return periods $T_{Dd\,or\,Dm}$ and $T_{Dd\,\&\,Dm}$ are 96.1 and 178.7 years (Equations 6.9 and 6.10). Finally, the conditional return periods are $T_{Dd|Dm\geq m} = 7867.7$ years and $T_{Dm|Dd\geq d} = 13218.2$ years (Equations 6.11 and 6.12, respectively). The univariate return periods were computed based on the best fitted distribution for each region and drought characteristic (Section 6.3.4), and are also identified in Table 6.7.

Table 6.8 shows that for RG1 and RG2 the ranking of the exceptionality of the drought events for each SPI timescale seldom coincides. RG3 is an exception, with only the event beginning in September 2013, according to SPI3, out of order. This coherence among results may indicate a better performance of the models due to the more homogeneous behaviour of the region. The table also stresses that the conditional return periods are always much higher because they are restricted to smaller sample spaces due to the conditional constraints (drought magnitude or duration exceeding certain thresholds).

Figures 6-11 and 6-12 represent the conditional return periods although only for SPI6, in order to

shorten the paper, but also because the results for SPI3 are similar. Note that, due to the adopted scale of the axes some of the more exceptional drought events of Table 6.8 are not represented.

Table 6.8: For each region and SPI timescale, start dates and characteristics of the five droughts with the highest return period $T_{Dd\,\&\,Dm}$ and their corresponding univariate, bivariate, and conditional return periods.

Time series	**Start date** $\mathbf{T}_{Dd\,\&\,Dm}$	*Dd* (month)	*Dm*	**Univariate** (year)		**Bivariate** (year)		**Conditional** (year)	
				$\mathbf{T}_{Dd}$	$\mathbf{T}_{Dm}$	$\mathbf{T}_{Dd\,\mathbf{or}\,Dm}$	$\mathbf{T}_{Dd\,\&\,Dm}$	$\mathbf{T}_{Dd\|Dm\geq m}$	$\mathbf{T}_{Dm\|Dd\geq d}$
SPI3-RG1	Sep 1943	11	20.85	148.5	201.7	115.7	327.9	52293.8	38496.1
	Aug 1963	8	9.64	41.5	18.7	17.8	47.0	694.3	1544.0
	Feb 1937	3	12.14	3.3	34.6	3.3	34.7	948.8	90.6
	Sep 2011	6	9.66	16.0	18.8	13.4	24.4	361.6	308.6
	May 2004	6	9.25	16.0	16.9	12.8	22.8	303.5	288.6
SPI3-RG2	Jul 1947	11	14.63	215.5	47.7	47.0	230.8	8014.6	36215.6
	Jul 1950	8	18.57	52.5	98.8	48.0	119.9	8630.8	4582.3
	Oct 2011	6	14.25	18.4	44.3	17.9	47.5	1531.7	637.7
	Jul 1944	7	12.58	31.4	31.4	24.4	44.3	1011.6	1013.1
	Sep 1982	6	10.89	18.4	21.6	15.8	27.0	424.6	361.9
SPI3-RG3	Sep 2013	10	19.33	106.3	144.6	89.0	196.4	23167.7	17033.1
	Jan 2010	11	14.85	160.2	61.7	59.2	179.5	9034.1	23459.4
	Aug 2007	8	12.48	44.2	37.0	31.2	57.0	1721.7	2052.5
	Feb 1998	8	11.79	44.2	31.6	28.2	53.4	1377.4	1922.3
	Mar 2012	5	11.55	10.0	29.9	9.9	30.5	744.1	248.3
SPI6-RG1	Jun 2002	27	39.49	167.5	99.7	96.1	178.7	7867.7	13218.2
	Apr 1963	19	27.46	64.9	47.3	45.1	69.7	1456.5	1997.2
	May 1943	12	30.54	23.1	58.3	23.1	58.5	1505.9	597.8
	Dec 1993	14	21.46	31.9	30.2	27.2	36.1	481.6	508.4
	May 1998	11	14.55	19.5	16.2	15.6	20.5	147.0	176.9
SPI6-RG2	Jun 1960	16	19.52	147.3	29.3	28.0	193.6	2290.6	11515.8
	Apr 1947	14	24.27	75.8	45.5	35.9	136.2	2500.7	4166.6
	May 1950	11	24.93	29.0	48.2	24.6	68.4	1329.3	799.6
	Apr 1982	11	19.66	29.0	29.7	21.4	46.4	556.2	542.7
	Jun 2011	9	19.75	15.8	30.0	14.9	33.5	405.1	213.1
SPI6-RG3	Oct 2012	20	34.90	83.6	105.4	79.5	112.8	4353.9	3452.8
	Nov 2010	19	34.57	72.0	102.9	70.2	106.8	4020.8	2814.0
	Sep 2006	19	31.74	72.0	83.2	67.0	91.1	2772.6	2399.7
	Nov 2014	13	17.43	26.9	23.2	22.1	28.5	241.3	280.6
	Apr 1956	8	11.56	10.4	11.8	10.1	12.3	53.0	46.4

Figure 6-13 summarises the results from the univariate and bivariate analysis based on the representation of the return periods of all the drought events from 1937 to 2016. Although the return period is a discontinuous variable, in the figure the different points were connected just to improve its readability, thus allowing to easily detect the most exceptional drought events (i.e., with the highest return periods) in Madeira Island.

The results for SPI3 show that the period from January 1937 to December 1999 has been characterised by numerous drought events (represented by the black bullets), that were particularly intense in RG1 and RG2 in the earlier years. In RG1, the first and long-term drought event took place from September 1943 to July 1944 with $T_{Dd\,\&\,Dm} = 327.9$ years (Table 6.8)[1]. Approximately three years after its end (that is, in July 1947), two considerable events occurred, also spaced of three years ($T_{Dd\,\&\,Dm}$ of 230.8 and 119.9 years), but this time in RG2. After the end of these events there were not very exceptional droughts in any region until November 2003. From this year on, several events with sustained high return periods took place, namely in RG3, the most important region in terms of freshwater sources. As for SPI6,

[1]Not depicted in Figure 6-13 due to the vertical scale adopted for improving the legibility of the figure.

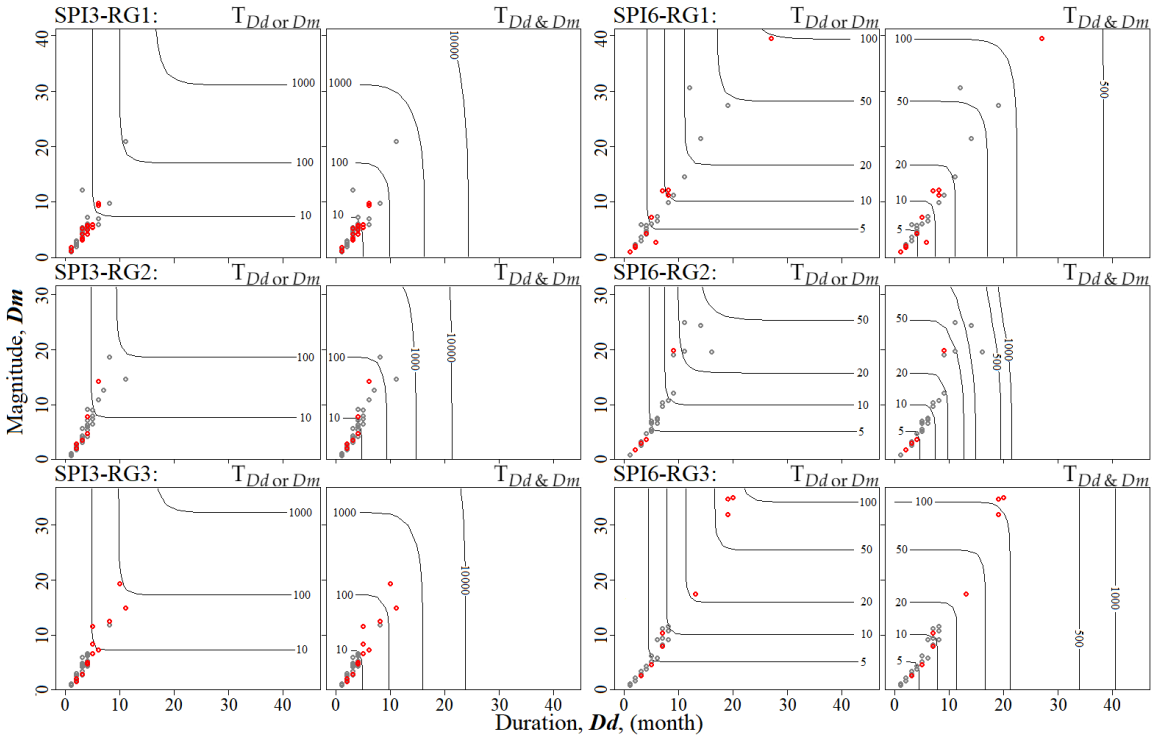

Figure 6-10: Joint return periods, $T_{Dd\,or\,Dm}$, $T_{Dd\,\&\,Dm}$ for each region and SPI timescale. The drought events that started between January 1937 and December 1999 are represented by grey circles, and those with start from January 2000 on, by red circles.

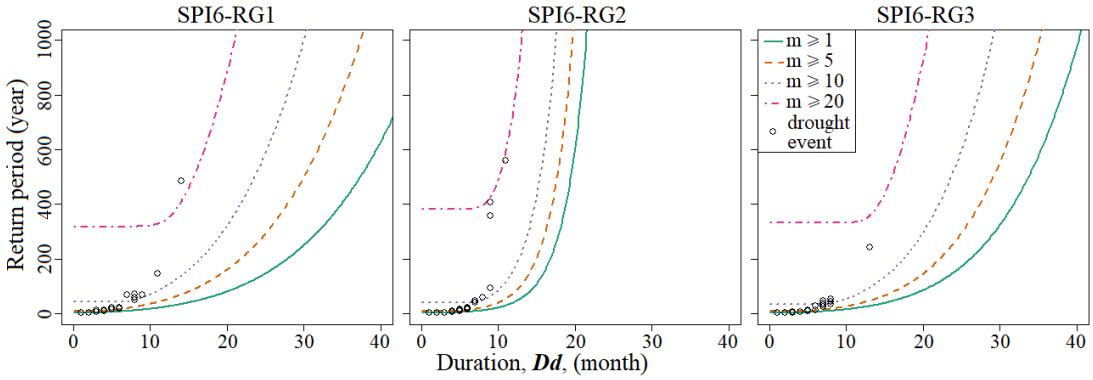

Figure 6-11: Conditional return period $T_{Dd|Dm\geq m}$ for different drought magnitudes (denoted by m) for SPI6 in the three regions.

RG1 discloses a performance opposite to that of SPI3, with more exceptional droughts in more recent years. The results for RG2 and RG3 are similar to those based on SPI3, with a higher concentration of important droughts in the past and more considerable events in recent times, respectively. These results are in line with the study about time-dependent occurrence rates of droughts also in Madeira Island by Espinosa et al. [118].

6.5 Discussion and conclusions

This work presents a systematic analysis of the effect of the moving average filter on drought assessment based on the SPI series (SPI3 and SPI6) from 1936 to 2016, and of the jointly modelling of drought

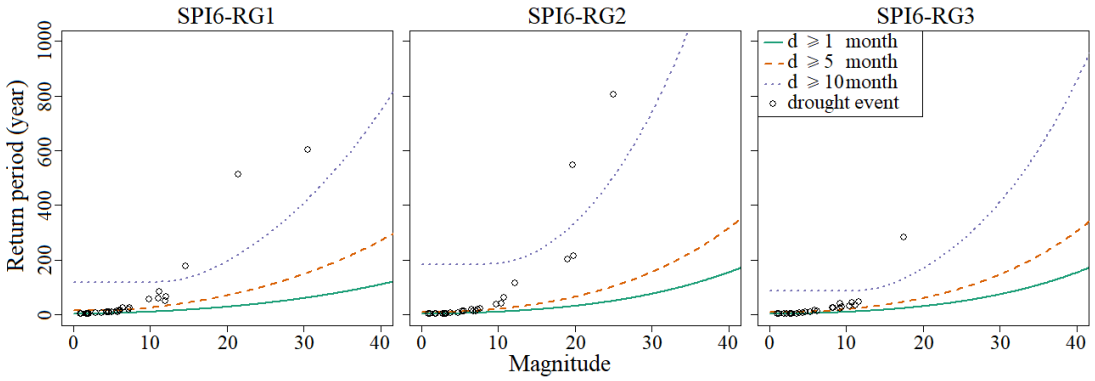

Figure 6-12: Conditional return period $T_{Dm|Dd \geq d}$ for different drought duration (denoted by d) for SPI6 in the three regions.

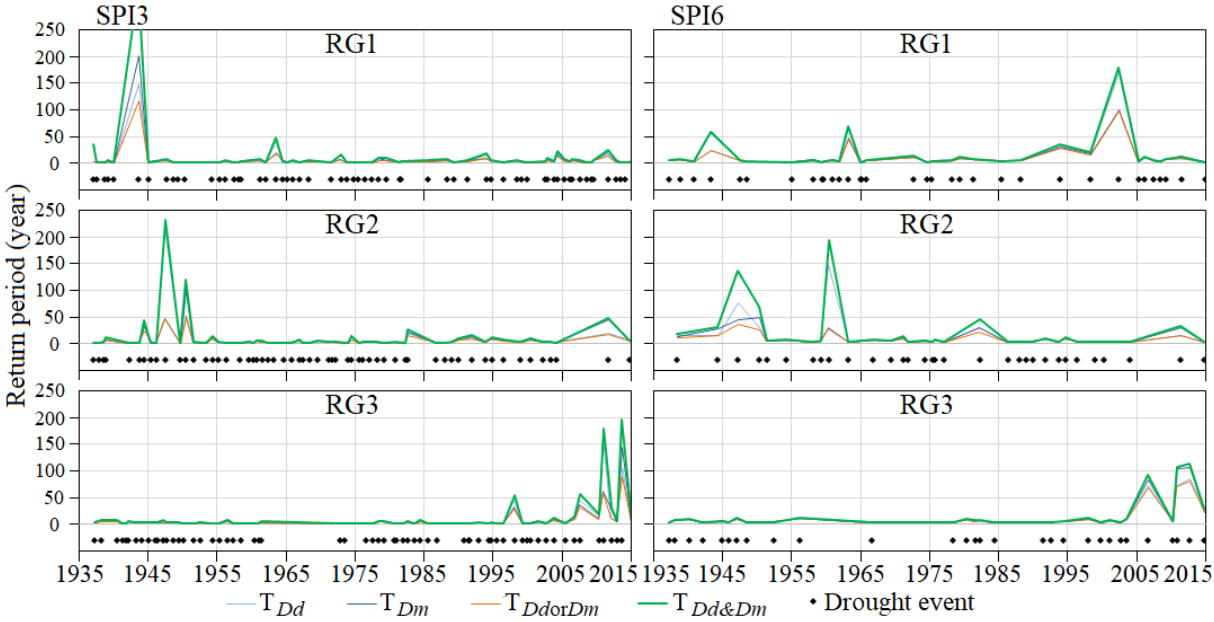

Figure 6-13: Univariate, and bivariate return period ($T_{Dd}, T_{Dm}, T_{Dd\,\text{or}\,Dm}, T_{Dd\,\&\,Dm}$) for SPI3 (left figures with $M = 3$) and SPI6 (right figures with $M = 5$). The start date of each drought event is represented by the location of the black bullet.

characteristics with bivariate copulas for Madeira Island. The factor loadings from the factor analysis applied to unsmoothed and smoothed SPI series identified three distinct regions with different temporal patterns of the droughts: northern slope (RG1), southern slope (RG2) and central region (RG3). RG1 denotes exceptional droughts both in earlier years and at present, RG2 suffered the worst droughts in the past, while RG3 has featured more exceptional drought events from the year 2000 onwards. Special attention was given to this last region due to its relevance for the island's water security, as main region for the recharge of the groundwater reservoirs.

Planning and management of water resources systems under drought conditions often require the estimation of return periods of the exceptional drought events [408, 40]. However, droughts are defined by multiple characteristics, some of them, presumably highly correlated. Based on the regionalised SPI series, two drought characteristics, namely, drought duration (Dd) and magnitude (Dm) were analysed and bivariate copulas were implemented to construct their joint distributions aiming at estimating return

periods. The drought maximum intensity (Dmi, Figure 6-1) was not considered to avoid possible redundant information, since it is already part of the Dm data, and also due to its poorly correlation with Dd as stated by Sharma [404], Dracup et al. [102] and Chen et al. [61].

The bivariate approach enabled the generation of the joint return periods return periods between Dd and Dm of Figure 6-10. The figure shows that the events that took place more recently, namely, after January 2000 (red circles), present higher or even the highest return periods, meaning that the drought events they represent were more exceptional. This is particularly evident in RG3, regardless the SPI timescale, but also in RG1, in this case only for SPI6. Table 6.8 also stresses the critical situation of RG3. In fact, from the five more exceptional drought events, regardless the SPI timescale, four took place after 2000 (more specifically after 2006). The table also shows the poorer performance of the univariate approach: in fact, for a same region and SPI timescales, all the droughts with the same duration would have the same return period, regardless the drought magnitude, and vice versa.

Aiming at discussing the information gained with the application of factor analysis and copulas, the results presented in Figure 6-13 will be compared to those from a drought characterisation considering the 41 original SPI series. For that purpose, for the entire island and for each of the homogeneous regions, the yearly areas affected by moderate, severe and extreme drought were computed, based on the non-regionalised and unsmoothed SPI for wettest months of the rainy season and for the entire season itself, $SPI3_{Nov-Jan}$ and $SPI6_{Oct-Mar}$, respectively, as shown in Figures 6-14 and 6-15. The Thiessen polygon method [441] was applied to assign an areal-influence (ATP from Table 6.1) to each rain gauge. The area attributed in each year to a specified drought category was given by the cumulative areas of the rain gauges with values of SPI within the limits of that category (Table 6.2). The total areas thus achieved for each year were made dimensionless by division by the Madeira area or by the area assigned to each region, in this last case, computed based on the rain gauges located in the region.

Figures 6-14 and 6-15 show that, generally, the island and each of its three regions have been similarly affected in terms of percentage of the area under drought conditions. Most of the same driest spells occurred in the three regions — such as exceptionally extreme droughts of 1947, 1995, and 2011 [235] — but sometimes with different distribution of the areas assigned to the three drought categories. Figure 6-15 suggests that the distribution of the years with moderate, severe and extreme droughts is similar among regions for $SPI3_{Nov-Jan}$. However, in the case of $SPI6_{Oct-Mar}$, regardless the affected area, for RG1 and RG3 the concentration of years with severe and extreme droughts is higher in recent years (2000–2016), whereas RG2 exhibits an opposite behavior, i.e., a higher concentration of years with severe and extreme events in the past. Even though Figure 6-15 refers to annual series and Figure 6-13 to continuous series there is a certain similarity between sub periods with more severe and extreme droughts and with the highest return periods, denoting coherence among different characterisations.

Finally, the same copula approach was applied to the regionalised unsmoothed SPI. The results for $T_{Dd\,\&\,Dm}$ based on SPI6-RG3 are presented in Figure 6-16 which also includes the ones from the smoothed series with a running length of $M = 5$. The figure confirms that smoothing the SPI series prior to factor analysis allows the elimination of the spurious droughts events and/or their clustering, thus improving the visibility of the more exceptional droughts, as it happened in November 2010 and October 2012. It

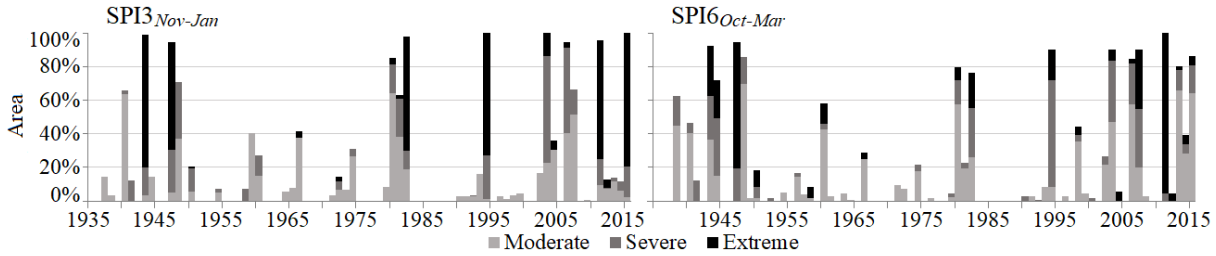

Figure 6-14: $SPI3_{Nov-Jan}$ (left figure) and $SPI6_{Oct-Mar}$ (right figure) series. Yearly area of Madeira Island affected by the different drought categories (740.63 km^2 — 41 rain gauges).

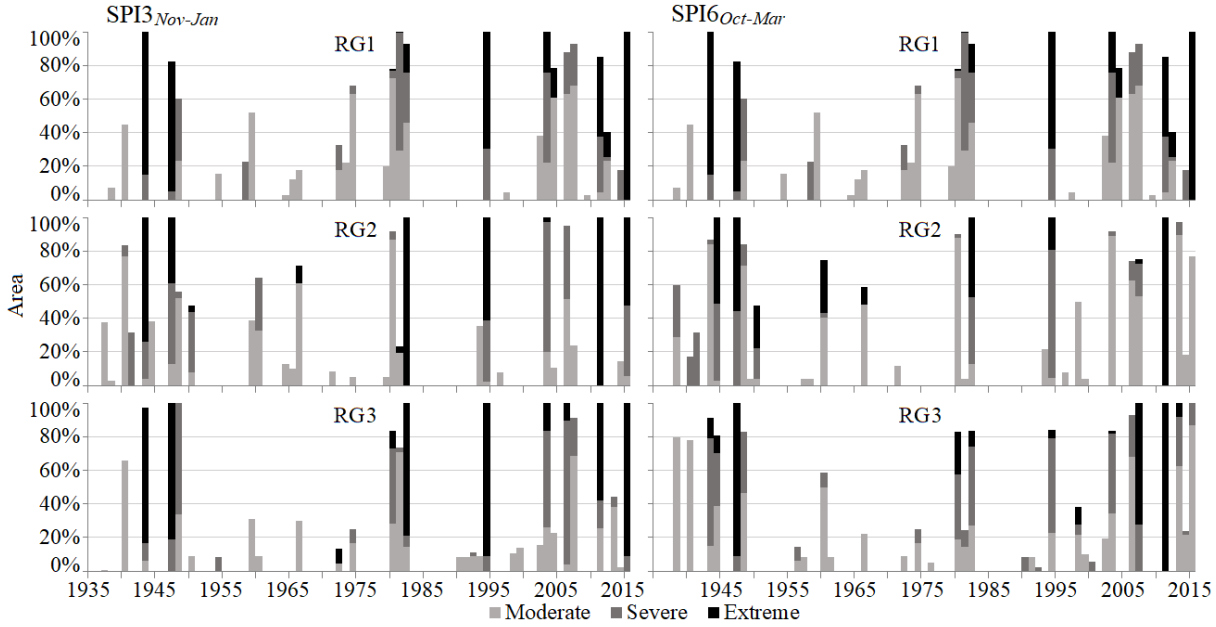

Figure 6-15: $SPI3_{Nov-Jan}$ (left figures) and $SPI6_{Oct-Mar}$ (right figures) series. For each region, yearly area affected by the different drought categories (RG1 with 232.35 km^2 — 11 rain gauges, RG2 with 281.18 km^2 — 14 rain gauges, and RG3 with 227.10 km^2 — 16 rain gauges).

should be stressed that the return periods that result from the unsmoothed SPI series may be much higher than those from the smoothed series due to the higher temporal variability of the unsmoothed SPI series. The less steep response of the smoothed series compared to the one from the unsmoothed series may be because the MA filter has a good performance in the time domain (as mentioned in Section 6.3.2), but has a poor performance in the frequency domain [416]. Since in the present study, the response that describes how the information in the time domain (the SPI series) is being modified by the system is the important parameter and the frequency response is of little concern, this makes the MA filter applicable. In other fields of Hydrology, such as in flood frequency analysis Halbert et al. [170], Archer et al. [19], the response in the frequency domain is all important, while the one in the time domain does not matter. Consequently, a frequency-domain filter may be more appropriate, e.g., the Fourier transforms [41]. Therefore, the selection of a digital filter should consider the features of the studied phenomenon.

Advances were made in the study of drought analysis based on regionalised smoothed series including on the criteria to selected the running length, M, and on the consequences of different M values. The copula approach showed that the drought events may have completely different return periods, depending

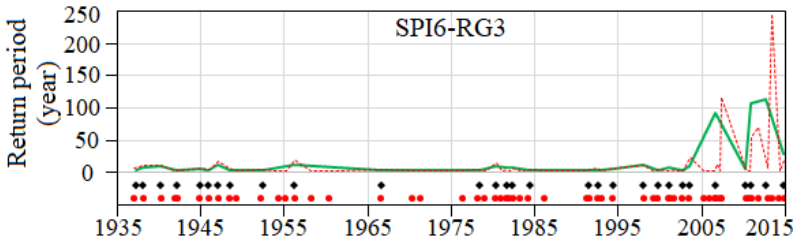

Figure 6-16: The central region. The start of drought events and their associated bivariate return period $T_{Dd\,\&\,Dm}$ for SPI6 series without smoothing (dashed line and red bullets) and with $M = 5$ (solid line and black bullets).

on how the relationship between Dd and Dm is accounted for. In any case, the univariate approach only provides part of the information, often underestimating the exceptionality of the events. The use of bivariate approaches, namely based on copulas, can easily overcome such constraint.

THIS PAGE INTENTIONALLY LEFT BLANK

Chapter 7

Extremal Dependence of a Daily North Atlantic Oscillation Index and Regionalised Rainfall

This chapter has been published as: Espinosa, L. A., Portela, M. M., and Rodrigues, R. (2020). Significant Extremal Dependence of a Daily North Atlantic Oscillation Index (NAOI) and Weighted Regionalised Rainfall in a Small Island Using the Extremogram. *Water*, 12(11): 2989, https://doi.org/10.3390/w12112989

Abstract

Extremal dependence or independence may occur among the components of univariate or bivariate random vectors. Assessing which asymptotic regime occurs and also its extent are crucial tasks when such vectors are used as statistical models for risk assessment in the field of Climatology under climate change conditions. Motivated by the poor resolution of current global climate models in North Atlantic Small Islands, the extremal dependence between a North Atlantic Oscillation index (NAOI) and rainfall was considered at multi-year dominance of negative and positive NAOI, i.e., –NAOI and +NAOI dominance subperiods, respectively. The datasets used (from 1948–2017) were daily NAOI, and three daily weighted regionalised rainfall series computed based on factor analysis and the Voronoi polygons method from 40 rain gauges in the small island of Madeira (∼740 km^2), Portugal. The extremogram technique was applied for measuring the extremal dependence within the NAOI univariate series. The cross-extremogram determined the dependence between the upper tail of the weighted regionalised rainfalls, and the upper and lower tails of daily NAOI. Throughout the 70-year period, the results suggest systematic evidence of statistical dependence over Madeira between exceptionally –NAOI records and extreme rainfalls, which is stronger in the –NAOI dominance subperiods. The extremal dependence for +NAOI records is only significant in recent years, however, with a still unclear +NAOI dominance.

Keywords:

Extremal dependence; climate change; extremogram, cross-extremogram; extreme rainfall; NAOI; small island; Madeira Island.

7.1 Introduction

In the framework of climate research, problems related to the teleconnection between extreme rainfall and extreme phases of climatic drivers are still debatable issues [39]. Such challenges are even more pronounced in small island environments particularly those with orographic complexity which are often more vulnerable to extreme events [255]. So, adequate knowledge of the extremal dependence of rainfall and of oscillation prominent modes in the climate system — such as the North Atlantic Oscillation (NAO) — is necessary. This is of great concern given the impacts of the more frequent and intense occurrence of extreme rainfall in recent years [129, 304, 376, 429], and, at the same time, the increased interannual variability of the winter NAO [172].

In this context, the present work describes and discusses a historical overview of the extreme rainfall changes in a North Atlantic small island and their probable dependence on the NAO positive and negative phases based on concepts of extremal dependence. In this regard, quantitative tools for measuring different kinds of dependence were used, i.e., the extremogram and its extension the cross-extremogram developed by Davis and Mikosch [79].

Extreme events are natural phenomena with very rare frequencies associated with disasters or events that result in damage — e.g., floods, heat and cold waves, wildfires, earthquakes, and tsunamis [417]. Modelling and prediction of extreme events have been the focus of research in disaster prevention and mitigation efforts. Rainfall is one of the most frequent factor related to widespread severe weather hazards when its intensity far exceeds the average value, i.e., when extreme rainfall occurs. There are some studies on extreme rainfall for mainland Portugal such as Costa and Soares [68], Soares et al. [421], and Santos and Fragoso [386]. For Madeira — a Portuguese small island situated in the North Atlantic Ocean, southwest of Portugal — researchers have focused on other meteorological aspects (e.g., fog precipitation) or on isolated case studies of extreme rainfall events such as in Luna et al. [244], Fragoso et al. [140], Levizzani et al. [231], Teixeira et al. [438], and Gouveia-Reis et al. [158]. Particularly for Madeira Island, any of these relatively few studies have measured the possible time dependencies of extreme regionalised rainfall events and extreme phases of climatic drivers.

The concepts of extremal dependence are defined by requiring that all the components of a random vector have a similar behaviour. The word extremal refers to dependence structures leading to extremal values under certain criteria — e.g., extreme quantiles and probabilities of rare events, peaks over threshold (POT) method, generalised pareto distribution and maximum likelihood estimation approaches, among others [458], [124], [4]. Extremal dependence can be interpreted as the ordinary perception of an extreme or rare natural event whereby the higher the magnitude, the higher the damage for all the individuals involved can be. Analogously, in a small island all rainfalls, especially the extreme ones, might be influenced by a weather phenomenon, or a combination of phenomena, and react similarly [460]. Weather phenomena (e.g., the NAO, frontal structures, and low-pressure systems) can be defined as natural events that occur as a result of one or a combination of the water cycle and pressure systems effects.

The Autocorrelation Function (ACF) is commonly used to measure dependencies in Gaussian time series and linear models [490]. Nevertheless, the estimation of the extreme values' ACF — such as of

extreme daily rainfalls — can be rather imprecise and even misleading since the asymptotic confidence bands are typically larger than the estimated autocorrelation [79]. Due to the tail-heaviness of daily rainfall time series, as well as of other climate time series, the normal distribution is inadequate for modelling the marginal distribution of extreme events. This tail-heaviness is normally characterised by excess kurtosis, i.e., the higher the kurtosis coefficient is above the normal level (greater than 3), the more likely that future daily rainfall will be extremely large. To overcome the limitations of the ACF and to capture the extremal dependence in time series data, Davis and Mikosch [79] introduced the extremogram. The extremogram is an alternative to the ACF to measure dependencies between events in the upper tail or in the lower tail of a single time series, or of a univariate random vector, that comply with an adopted threshold. The cross-extremogram which is analogous to the Cross-correlation Function (CCF), allows for measuring the extremal dependence — in the upper tails, the lower tails or a combination of both tails — for a bivariate random vector. The presentation of extremograms as well of cross-extremograms in the form of graphs can provide information about the time trend dependency patterns for extreme events.

NAO is a weather phenomenon defined as fluctuations in the difference of atmospheric pressure at sea level (SLP) between two points over a specified period of time across the North Atlantic. The mathematical description of the NAO phase, i.e., the NAO index (NAOI) is traditionally defined by the Icelandic Low and the Azores High, although there are other definitions which consider the pressure observations of the Lisbon High, or the Gibraltar High instead as described in Osborn et al. [301] and Hurrell and Deser [195]. This phenomenon is a major mode of climate variability that influence the likelihood of extreme rainfall of the North Atlantic. Therefore, different NAO phases — positive and negative which sometimes correspond to the upper tail and lower tails in the NAOI time series, respectively — can be can be associated with increases or decreases in natural disaster risk [271].

Climate variability in continental Europe is highly controlled by variability in the atmospheric circulation [452]. Different studies have provided a clear framework of the strong influence of the NAO on the continental European rainfall. Tabari and Willems [431] have shown that the NAO signal in winter has a controlling influence not only on continental European extreme rainfall anomaly in winter, but also in a delayed way on the extreme rainfall events in the following seasons. For central Portugal, Trigo et al. [448] have assessed the impact of the NAO on the winter rainfall and the timing of associated landslide events due to extreme rainfall. However, there is less recognition of the role of the atmospheric circulation variability in the form of the NAO in Madeira Island extreme rainfall.

Generally, investigations into the possible effects of the NAO on extreme rainfall have been performed using indices at monthly or seasonal scale — e.g., the winter, from December through March, station-based NAOI as defined by Osborn et al. [301]. Besides this, the rarely detailed presence of small islands in global climate models is very common making this research relevant. Here, a more detailed study is conducted using time series, from 1st January 1948 to 30th September 2017, of the daily NAOI — constructed by projecting the daily anomalies over the Northern Hemisphere onto the loading pattern of the NAO [74] — and of the regionalised daily rainfall records from a dense network of ground-based rain gauges over Madeira Island.

The main objectives are i) "clustering" of the daily rainfall series at 40 rain gauges based on regionalisation techniques (Figure 7-1 and Table 7.1), ii) identifying subperiods of sustained phases of the NAOI attributable to its extreme daily events, i.e., negative (–NAOI) and positive (+NAOI) dominance subperiods, and iii) exploring the extremal dependence between regionalised rainfall in Madeira and the NAOI during the dominance subperiods. Throughout this work, the term “extreme” for rainfall refers to values in the upper tail whereas for the NAOI to both lower and upper tails. The probable dependence in the univariate and bivariate time series are ascertained via the extremogram and the cross-extremogram, respectively. This work focuses on the application of extremal dependence methods firstly, to a univariate climatic driver dataset, and secondly to the bivariate case (the regionalised rainfall and climatic driver), rather than on statistical methods for extremal dependence.

7.2 Study area

Located in European Macaronesia, Madeira is the largest island of the Madeira Archipelago with an area of $\backsim$740 km^2, a maximum width of 22.5 km and a length of 57.3 km. Based on its size and topography, Madeira can be categorised as a mountainous small island [123]. Centred at N 32°44’30” and W 16°57’58”, and about 610 km northwest of the Western African coast, the island has a very complex orography and is completely formed by volcanic materials (Figure 7-1), consisting of a central mountainous system EW oriented (close to ST12 rain gauge, Pico Ruivo with 1862.0 m.a.s.l.; near ST01 rain gauge, Pico do Areeiro with 1818.0 m.a.s.l.; and in the vicinity of ST02 rain gauge the region of Paúl da Serra which lies above 1400.0 m.a.s.l.) cut by deep valleys. The differences between the winter and summer temperatures are generally small.

According to the Koppen’s classification, the island’s climate is predominantly temperate with dry and warm to hot summers as approaching the coastal lowland zones of Madeira [58]. The distribution of rainfall presents an evident seasonal pattern, thoroughly different between the rainy season, that extends from November to March (or sometimes to mid-April), and the dry season, with insignificant rainfall amounts during July and August. The rainfall in the island has a wide variation determined by the elevation with higher amounts in the north ($\sim$1500 mm year^{-1}) and central highlands ($\sim$2300 mm year^{-1}) than in the south ($\sim$600 mm year^{-1}), as previously characterised [118].

7.3 Rainfall and NAO data

7.3.1 Daily rainfall data

The hydrological data used in the present study were daily rainfalls during almost 70 years, from 1st January 1948 to 30th September 2017, at forty rain gauges evenly spaced over Madeira, except for the most western part of the island which is much less monitored (Figure 7-1). The rainfall data was obtained via the procedure implemented by [118] to the daily records made available by the competent authority, the Portuguese Institute for Sea and Atmosphere, IPMA (https://www.ipma.pt) which is one of the main sources of hydrometeorological data for Portugal.

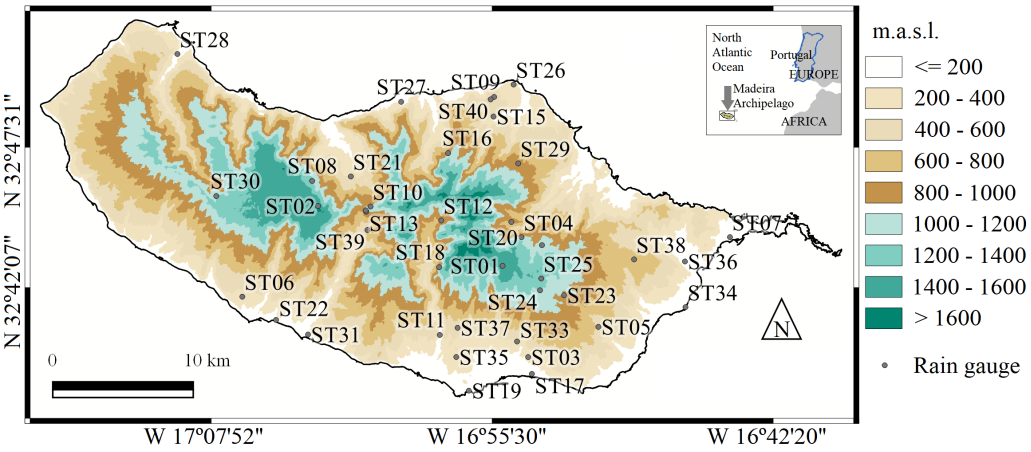

Figure 7-1: Location (WGS84 coordinates) and relief of Madeira Island. Spatial distribution of the forty rain gauges considered in this study depicted by bullets and their respective identification codes from ST01–ST40 (Table 7.1).

7.3.2 North Atlantic Oscillation index (NAOI) daily data

The NAOI represents a pattern of low-frequency tropospheric height variability. This pressure difference measure is based on centres-of-action of 500 millibars constant pressure (mb) height patterns. Note that these height fields are spectrally truncated to total wavenumber 10 in order to emphasise large-scale aspects of the teleconnections. The calculation of this teleconnection index utilises the ESRL/PSD Global Ensemble Forecasting System Reforecast2 (GEFS/R) ensemble forecasts from the averaged region N 55°–70°; W 70°–10° which in turn is subtracted from N 35°–45°; W 70°–10°, retrieved from the NOAA Physical Sciences Laboratory, NOAA PSL portal [292]. The daily NAOI dataset which does not present missing data was utilised for the same period as in the case of daily rainfall (from 1948 through 2017).

7.4 Methods

7.4.1 Regionalisation of the daily rainfall series

Notwithstanding Madeira is a small island, it exhibits some significant microclimatic or localised features [58]. Therefore, when analysing the rainfall, it is necessary to identify homogeneous regions or regions with similar regimes and put them together in space [245]. In order to achieve this, a two-steps process was implemented based, firstly, on the principal components analysis (PCA), specifically the principal factors analysis (PFA) to group the rain gauges, followed by the Voronoi polygons method, also known as Thiessen, to spatial average the forty daily rainfall series for the nearly 70-year reference period. The former analysis has been widely used for reducing the number of dimensions or variables by finding uncorrelated linear combinations of the original data, and documenting the homogeneity or detecting structures in the relationship among climatic variables (e.g., Abatzoglou et al. [2], Espinosa et al. [116], Ferrelli et al. [132], Pomee and Hertig [324]). Such analysis has been also applied to rainfall (e.g., Baeriswyl and Rebetez [24], Álvarez-Rodríguez et al. [16], Santos et al. [387], Fazel et al. [128], Raja and Aydin [345]). The Thiessen intends to assign areal significance [122] to analyse spatially distributed data

Table 7.1: The forty rain gauges utilised. Identification (code and name), coordinates (WGS84), elevation, areal influence according to the Voronoi polygons method, and the region to which they belong from the factor analysis.

Code	Name	Coordinate		Elevation	Areal influence	Factor-Region
		Latitude N	Longitude W	(m.a.s.l.)	(km^2)	
ST01	Areeiro	32°43'11"	16°55'01"	1610.1	13.67	F2-CEN
ST02	Bica da Cana	32°45'22"	17°03'19"	1560.2	22.05	F2-CEN
ST03	Bom Sucesso	32°39'43"	16°53'45"	292.0	6.98	F1-SOU
ST04	Cabeço do Meio-Nogueira	32°44'08"	16°53'55"	995.3	4.07	F2-CEN
ST05	Camacha-Valparaiso	32°40'34"	16°50'31"	675.2	28.57	F1-SOU
ST06	Canhas	32°41'39"	17°06'35"	400.4	25.19	F1-SOU
ST07	Caniçal	32°44'14"	16°44'19"	16.2	11.34	F3-NOR
ST08	Caramujo	32°46'09"	17°03'30"	1214.5	30.41	F2-CEN
ST09	Cascalho	32°49'44"	16°55'30"	430.4	1.83	F3-NOR
ST10	Chão dos Louros Encumeadas	32°45'25"	17°01'04"	895.2	9.54	F2-CEN
ST11	Covão ETA	32°40'29"	16°57'46"	510.1	22.45	F1-SOU
ST12	Curral das Freiras	32°44'44"	16°57'35"	787.4	20.08	F2-CEN
ST13	Encumeada de São Vicente	32°45'01"	17°01'00"	900.2	1.12	F2-CEN
ST14	Encumeadas Casa EEM	32°45'14"	17°01'15"	1010.5	2.32	F2-CEN
ST15	ETA São Jorge	32°48'57"	16°55'33"	500.5	10.42	F3-NOR
ST16	Fajã Penedo	32°47'31"	16°57'36"	620.5	23.83	F3-NOR
ST17	Funchal Observatório	32°38'51"	16°53'32"	58.2	7.08	F1-SOU
ST18	Lapa Branca-Curral das Freiras	32°43'08"	16°57'53"	610.2	22.45	F2-CEN
ST19	Lido-Cais do Carvão	32°38'11"	16°56'11"	20.5	4.98	F1-SOU
ST20	Lombo Furão	32°44'56"	16°54'39"	994.5	13.61	F2-CEN
ST21	Loural	32°46'21"	17°01'45"	368.1	19.37	F2-CEN
ST22	Lugar de Baixo	32°40'44"	17°04'59"	15.1	10.94	F1-SOU
ST23	Meia Serra	32°42'07"	16°52'12"	115.3	12.47	F2-CEN
ST24	Montado do Pereiro	32°42'06"	16°53'02"	1261.0	6.53	F2-CEN
ST25	Poiso-Posto Florestal	32°42'46"	16°53'13"	1360.2	4.60	F2-CEN
ST26	Ponta de São Jorge	32°50'01"	16°54'24"	266.5	6.15	F3-NOR
ST27	Ponta Delgada	32°49'16"	16°59'31"	123.3	17.26	F3-NOR
ST28	Porto do Moniz	32°50'57"	17°09'46"	64.3	80.65	F3-NOR
ST29	Queimadas	32°46'59"	16°54'07"	881.4	34.66	F3-NOR
ST30	Rabaçal	32°45'30"	17°07'51"	1233.4	101.10	F2-CEN
ST31	Ribeira Brava	32°40'26"	17°03'46"	25.4	24.13	F1-SOU
ST32	Ribeiro Frio	32°43'51"	16°52'58"	1167.1	19.07	F2-CEN
ST33	Sanatório	32°40'07"	16°54'02"	384.1	11.75	F1-SOU
ST34	Santa Catarina	32°41'36"	16°46'23"	49.2	7.74	F1-SOU
ST35	Santa Quitéria ETA	32°39'39"	16°57'03"	321.0	9.20	F1-SOU
ST36	Santana	32°43'19"	16°46'27"	80.4	16.46	F3-NOR
ST37	Santo António	32°40'36"	16°56'45"	525.3	10.82	F1-SOU
ST38	Santo da Serra	32°43'33"	16°49'01"	660.2	36.08	F3-NOR
ST39	Serra de Água	32°44'31"	17°01'11"	573.2	24.34	F2-CEN
ST40	Vale da Lapa	32°49'37"	16°55'40"	347.0	5.31	F3-NOR

(e.g., rainfall measurements) and to estimate regionalised rainfall values.

In this work, the factor analysis, taking into account both PCA and PFA, consisted of computing both the covariance and correlation matrices of the daily rainfalls (1948-2017) at the forty rain gauges of Table 7.1, i.e., the forty variables for the 40-dimension problem with their corresponding eigenvalues and principal factor loadings after varimax rotation [3]. The selection of a possible correct number of principal components or principal factors to retain was determined based on the "elbow" of the scree plot [210] and on the Kaiser's criterion (K1 rule), according to which the factors whose eigenvalues overweight 1.0 are the ones to be retained [207, 210]. The final step of the regionalisation process corresponded to the Voronoi method applied to the daily rainfall at the rain gauges located in each homogeneous region to spatially average the daily series. The homogeneous regions were delimited based on the rotated factor

loadings of rain gauges with correlations higher than +0.60 [118, 116]. The number of regionalised rainfall series depended on the number of the retained factors (i.e., of homogeneous regions) in accordance with the previously specified criteria.

7.4.2 Dominant negative and positive NAO phases

The influence of the NAO mode on the continental European climatic conditions has been widely studied and well-recognised from a number of studies' findings, such as those by Trigo et al. [448] and Hurrell and Deser [195], with generalised wet conditions in southern Europe, and increased precipitation affecting northern Europe during the NAO negative phases — contrary circumstances occur during the NAO positive phases. However, such anomalies influence on the extreme rainfall over Madeira has not been addressed in detail, as previously mentioned.

In order to obtain relevant information from the extreme NAOI events and to ascertain how the dominant negative and positive NAO phases throughout the fairly large reference period affect Madeira extreme rainfall at daily scale, a LOWESS (locally weighted regression) was applied to the NAOI series with a typical smoothing parameter value of $f = 3$ [64]. This was done to build up a function that describes point by point the deterministic part of the variation in the extreme NAOI data (lower and upper tails), and to obtain adequate –NAOI or +NAOI dominance subperiods.

For the established NAOI dominance subperiods, both the NAOI and rainfall data were analysed from an extremal dependence perspective by applying firstly the extremogram solely to the daily NAOI, and secondly the cross-extremogram to the bivariate series of daily NAOI and rainfall. Such methods (implemented in R https://cran.r-project.org/), as well as some necessary concepts, are mathematically described in the following subsections.

7.4.3 Strictly stationary and regularly varying

A time series $\{X_t\}_{t=1,2,...}$, is said to be strictly stationary [229] if for all k, all τ, all t_1, ..., t_k

$$F_X(x_{t_1+\tau}, ..., x_{t_k+\tau}) \stackrel{d}{=} F_X(x_{t_1+\tau}, ..., x_{t_k+\tau}) \tag{7.1}$$

where $\stackrel{d}{=}$ denotes equality in distribution. Considering a d-dimensional process, i.e., $(\mathbf{X}_t)$ and defining $\mathbf{Y}_h := (X_1, ..., X_1)$, the process $(\mathbf{X}_t)$ is said to be regularly varying with tail index α if:

$$\frac{P(x^{-1}\mathbf{Y}_h \in \cdot)}{P(\parallel \mathbf{Y}_h \parallel > x} \xrightarrow{\nu}, \qquad x \to \infty \tag{7.2}$$

for some non-null Radon measure μ_h on the Borel σ-field $\mathfrak{B}\overline{\mathbb{R}}_0^{hd}$ of $\overline{\mathbb{R}}_0^{hd} = \overline{\mathbb{R}}_0^{hd} \backslash \{0\}$ (that is an extended hd-dimensional real number bounded away from zero) with the property:

$$\mu_h(tC) = t^{-\alpha}\mu_h(C), \quad t > 0 \text{ for any Borel set } C \subset \overline{\mathbb{R}}_0^{hd} \tag{7.3}$$

In Expression (7.2), $\|\cdot\|$ is any norm in $\overline{\mathbb{R}}_0^{hd}$ and $\xrightarrow{\nu}$ refers to vague convergence on $\mathfrak{B}\overline{\mathbb{R}}_0^{hd}$, $x \in \mathbb{R}_0^{hd}$. If the process is $(\mathbf{X}_t)$ regularly varying, then there exists a sequence such that:

$$nP(a_m^{-1}\mathbf{Y}_h \in \cdot) \xrightarrow{\nu} \nu_h(\cdot) \tag{7.4}$$

where ν_h is another measure. Also, ν_h and μ_h are only differed by a non-zero proportional constant, c_h say (i.e., $\nu_h = c_h\mu_h$, $c_h > 0$).

7.4.4 Tail-dependence

The concepts of tail-dependence are standard tools to describe the amount of extremal dependence between random variables. A tail-dependence coefficient (TDC) roughly measures the probability of occurring extreme values, i.e., exceeding an upper or lower threshold, for one random variable given that another assumes an extreme value as well [229]. The upper TDC is defined for a two-dimensional random variable (X_0, X_h) as the limit, provided it does exist, of

$$\lambda_U = \lim_{x\to\infty} P(X_h > x | X_0 > x) \tag{7.5}$$

where X_h and X_0 are one-dimensional strictly stationary series. Given the limit exists, Equation (7.5) can be rearranged into the following expression:

$$\lambda_U = \lim_{x\to\infty} P(x^{-1}X_h \in (1,\infty) | x^{-1}X_0 \in (1,\infty)) \tag{7.6}$$

The lower TDC is defined analogously as:

$$\lambda_L = \lim_{x\to\infty} P(X_h \leqslant x | X_0 \leqslant x) \tag{7.7}$$

7.4.5 Extremogram

Davis and Mikosch [79] developed the extremogram using the upper TDC from $(1,\infty)$ in Equation (7.6) to a general Borel sets, and from one-dimensional vector X_t in Equation (7.6) to a d-dimensional vector $\mathbf{X}_t$. The extremogram is defined as follows:

$$\rho_{AB}(h) = P(a_m^{-1}\mathbf{X}_h \in B | a_m^{-1}\mathbf{X}_0 \in A), \quad h \in \mathbb{Z} \tag{7.8}$$

$$= \frac{P(a_m^{-1}\mathbf{X}_0 \in A, a_m^{-1}\mathbf{X}_h \in B}{P(a_m^{-1}\mathbf{X}_0 \in A)} \tag{7.9}$$

where A and B are Borel sets, a_n is a sequence $\to \infty$ such that $P(|\mathbf{X}_t| > a_m \sim n^{-1}$. Since A and B are bounded away from zero, the events $\{a_m^{-1}X_0 \in A\}$ and $\{a_m^{-1}X_h \in B\}$ are becoming extreme in the sense their probabilities are converging to zero, h is the value of the time lag.

The extremogram is estimated by:

$$\mathbb{E}\rho_{AB}(h) = \frac{\sum_{t=1}^{n-h} I_{\{a_m^{-1}X_t \in A, a_m^{-1}X_{t+h} \in B\}}}{\sum_{t=1}^{n} I_{\{a_m^{-1}X_t \in A}} \tag{7.10}$$

and the numerator in Equation (7.10) can be expressed as follows:

$$\sum_{t=1}^{n-h} I_{\{a_m^{-1}X_t \in (1,\infty), a_m^{-1}X_{t+h} \in (1,\infty)\}} = \sum_{t=1}^{n-h} I_{\{X_t \in (a_m,\infty), X_{t+h} \in (a_m,\infty)\}} \tag{7.11}$$

which counts the total number of pairs (X_t, X_{t+h}) when both values are greater or lower than a_m (normally a chosen percentile rank). It represents the total number of pairs of extreme values which are h-lags apart. Analogously, the denominator in Equation (7.10) can be expressed as:

$$\sum_{t=1}^{n} I_{\{a_m^{-1}X_t \in (1,\infty)\}} = \sum_{t=1}^{n} I_{\{X_t \in (a_m,\infty)\}} \tag{7.12}$$

accounting for the total number of realisations of the random variables $\{X_t\}$ whose values are greater than the adopted a_m regarded as extreme values. The extremogram is analogue of the ACF as mentioned and depends only on the extreme values in the sequence. Overall, the extremogram can be interpreted as the conditional probability of occurrence of extreme event in time $(t+h)$ given that there is an exceedance at time t. This function was used for the univariate case, i.e., applied to the daily time series X (NAOI).

7.4.6 Cross-extremogram

The cross-extremogram is the right method to measure the extremal dependence of bivariate time series the — in this case, the bivariate daily time series X (NAOI) and Y (rainfall) — and to see how far another time series may affect the one that is being analysed. The cross extremogram is defined as:

$$\rho_{AB}(h) = P(a_m^{-1}\mathbf{Y}_h \in B | a_m^{-1}\mathbf{X}_0 \in A), \quad h \in \mathbb{Z} \tag{7.13}$$

and it is calculated as follows:

$$\mathbb{E}\rho_{AB}(h) = \frac{\sum_{t=1}^{n-h} I_{\{a_m^{-1}Y_{t+h} \in B, a_m^{-1}X_t \in A\}}}{\sum_{t=1}^{n} I_{\{a_m^{-1}X_t \in A}} \tag{7.14}$$

where a_m is $(1 - 1/m)$-quantile that indicates extreme events in time series X_t and Y_t. Please refer to Davis and Mikosch [79] for the proofs of Equations (7.10) and (7.14).

In this application, daily rainfalls above the 99^{th} empirical percentile rank, i.e., an empirical quantile value relative to 100 [228], in the computed weighted regionalised series have been considered as extreme wet days or extreme rainfall events (upper tail) on the basis of the recommendation by the Expert Team on Climate Change Detection, Monitoring and Indices (ETCCDMI) [224]. In a similar way, extreme events for the daily NAOI series have been identified for both, below 1^{st} and above 99^{th} percentiles' ranks, i.e., the lower tail and upper tail, respectively.

7.5 Results

7.5.1 Weighted regionalised daily rainfall series

Based on the "elbow" of the curve in the scree plot from Figure 7-2 coupled with the K1 rule, the first three principal factors were retained. Varimax rotation was computed to maximise the variances of each individual record for the various retained factors [3] and to optimise the interpretation of the derived variables found by factor analysis, especially the loadings or correlations. Collectively, the three retained factors explain about 82% of the total variance — F1 30%, F2 28%, and F3 24%.

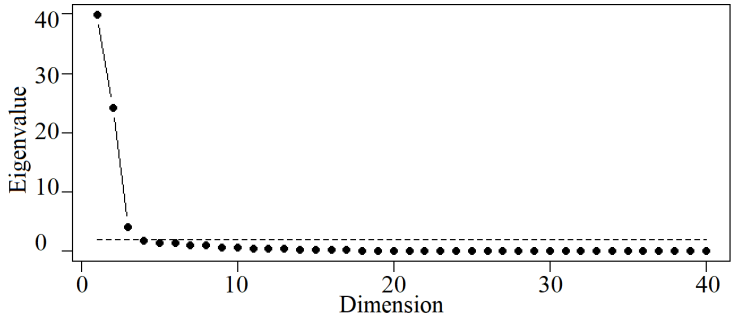

Figure 7-2: Scree plot from the sample covariance matrix obtained via the factor analysis based on the daily rainfall from 1st January 1948 to 30th September 2017 at the 40 rain gauges (the unrotated solution of the 40-dimensions problem). Horizontal dashed line shows the 1.0 eigenvalue.

Since the loadings mapping, or correlation mapping, has been considered as one the most effective representation for climatological pattern classification [502], the principal factor loadings (after rotation) from the correlation matrix were used as the main tool for regionalisation. The rotated correlations were interpolated by applying the inverse distance weighting (IDW) interpolation method with an exponent of 2 [47] and then plotted altogether superimposing the three retained factors (Figure 7-3), although only highlighting those regions higher than the threshold set at +0.60 [116].

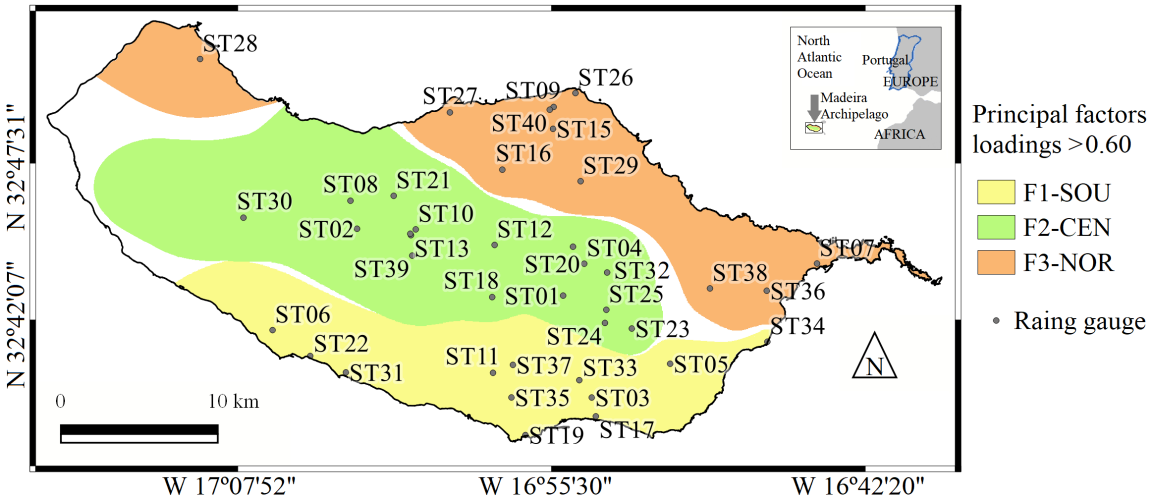

Figure 7-3: Spatial distribution of the principal factor loadings after rotation (varimax) higher than 0.60 from the factor analysis based on daily rainfall records (1948–2017) at the 40 rain gauges (WGS84). The region F1-SOU is related to the first factor, F2-CEN to the second factor, and F3-NOR to the third factor.

On this basis, the spatial distribution of the principal factor loadings is displayed in Figure 7-3 (see also Factor-Region column of Table 7.1). Rotation enabled the rainfall field to be divided into coherent homogeneous regions that do not overlap, although the Madeira western part is not fully included in any of the factors due to the lack of rain gauges located there. Even so, this clearly discriminates the island from south to north into three distinctive homogeneous regions: the southern slope (F1-SOU with 12 rain gauges), the central region (F2-CEN with 17 rain gauges), and the northern slope (F3-NOR with 11 rain gauges). Through the factor analysis, it was possible to establish a mature climatic regionalisation in terms of daily rainfalls that encompassed all the rain gauges. This step served only to group the rain gauges and, thus, to spatially average the original daily rainfall series by applying the Voronoi polygons.

To facilitate the calculations of the spatially weighted rainfall data required by the extremal dependence analysis, every rain gauge was assigned to a homogeneous region. This was based on the proximity of the Voronoi polygons' sides and the limits of the homogeneous regions of Figure 7-3 — columns identified in Table 7.1 by Areal influence and Factor-Region.

Figure 7-4 presents the temporal evolution of daily rainfall series resulting from the Voronoi method, for the period of 1948–2017 in the representative F1-SOU (169.82 km^2), F2-CEN (326.80 km^2), and F3-NOR (243.98 km^2) homogeneous regions. The coastal southern slope F1-SOU, located at lower elevations (Figure 7-1), is the driest region with weighted mean daily rainfall of 2.40 mm. The equivalent value for F2-CEN, located inland on the central highlands and plateau (Paúl da Serra, close to ST02 rain gauge), is 5.98 mm, which makes it the wettest region, whereas the coastal northern slope F3-NOR has intermediate characteristics, both regarding the weighted mean daily rainfall (4.37 mm) and elevation.

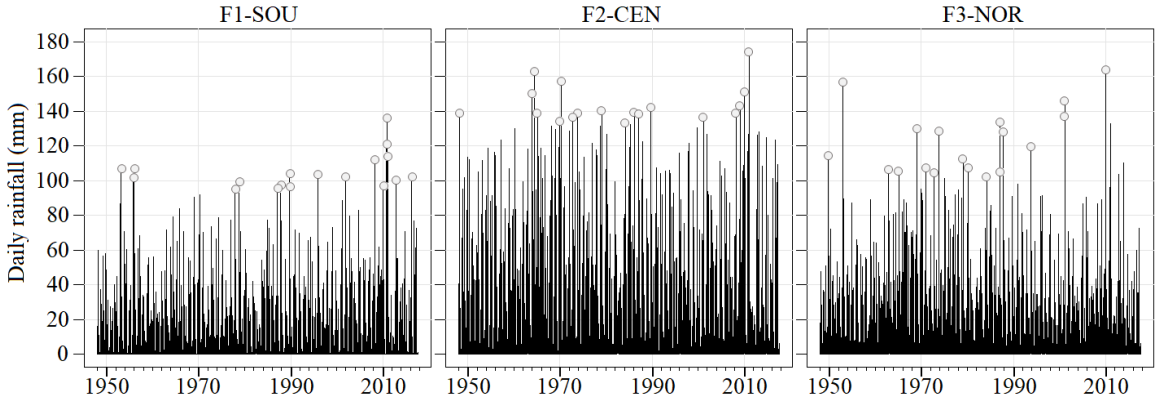

Figure 7-4: Weighted regionalised daily rainfall series spanning from 1st January 1948 to 30th September 2017 from the Voronoi polygons method for the identified regions via the factor analysis, F1-SOU (southern slope — 12 rain gauges), F2-CEN (central region — 17 rain gauges), and F3-NOR (northern slope — 11 rain gauges). Daily rainfalls exceeding the 90% quantile of the upper tail 99th percentile of the corresponding time series are depicted by circles.

The occurrence of rainfall events identified as extremes is particularly pronounced in the island for the analysed 70-year reference period. Those events occurred during the rainy season from end of October to mid-April, although with a very reduced number of extremes happening in June and September. Though the rainfall seasonal distribution among regions is very much alike, the extreme rainfall quantities are quite contrasting. For instance, the upper tail 99th percentile ranges from 37.2–135.5 mm for F1-SOU, from 75.5–174.2 mm for F2-CEN, and from 46.4–163.5 mm for F3-NOR. Moreover, the temporal occurrence

of extremes shows some important differences depending on the region.

As an example, the rainfalls pointed out in Figure 7-4 by circles correspond to daily values exceeding 81.4, 128.2, 94.8 mm for F1-SOU, F2-CEN, F3-NOR, respectively, i.e., exceeding the 90% quantile of the upper tail 99$^{\text{th}}$ percentile in each time series. For F1-SOU, the five highest extremes occurred on 21$^{\text{st}}$ January 1952, 8$^{\text{th}}$ April 2008, 22$^{\text{nd}}$ October and 26$^{\text{th}}$ November 2010, and 26$^{\text{th}}$ January 2011; additionally, the figure clearly shows that such events are more concentrated in recent years, expressly after the year 2001. In fact, this is the only region with a very recent circled extreme (22$^{\text{nd}}$ April 2016). F2-CEN and F3-NOR differ from the extremal occurrence pattern in F1-SOU. Considering the temporal distribution of the circled extremes, the central and northern regions seem to have similar distribution, both with a dense agglomeration of circled extremes between the years 1964 and 1990 — in addition, F2-CEN has a second-high concentration of extremes from 2004 to 2012. A number of temporal dissimilarities between F2-CEN and F3-NOR arise when comparing their respective highest events. The five highest extremes for F2-CEN are pinpointed on 8$^{\text{th}}$ November 1963, 21$^{\text{st}}$ June 1964, 26$^{\text{th}}$ March 1970, 21$^{\text{st}}$ February 2010, and 26$^{\text{th}}$ January 2011; whereas for F3-NOR on 19$^{\text{th}}$ November 1952, 23$^{\text{th}}$ January 1987, 5$^{\text{th}}$ March 2001, 6$^{\text{th}}$ March 2001, and 2$^{\text{nd}}$ February 2010.

Despite the temporal distribution differences, the worst rainfall extremes in the three regions took place throughout the hydrological years of 2009/10 and 2010/11 (starting on 1$^{\text{st}}$ October). Actually, it has been well-documented that numerous intense rainfall events, resulting in debris flow and flash floods, occurred in Madeira Island in those years such as the events that happened on 2$^{\text{nd}}$ February 2010 and 20$^{\text{th}}$ February which in some areas triggered a sudden rise of the river flows causing debris flows, and thus 47 casualties [239]. Although those documented extremes are mostly based on single rain gauges' data, their importance coincide with the ones identified in the computed regionalised daily rainfall series, which reinforces the practical use of the latter.

7.5.2 Dominant extremal NAOI subperiods and their extremograms

Figure 7-5 was obtained based on the 26,280 NAOI records from the NOAA PSL — spectrally truncated as mentioned in Section 7.3.2 — for the period 1948 to 2017 (with a sample daily mean of –4.90). In the figure, the records below the 1$^{\text{st}}$ and above the 99$^{\text{th}}$ empirical percentiles' ranks are represented by triangles. The dominance subperiods are denoted by solid vertical bars overlapping the original daily data, however not related to extreme events. About 45 years were pinpointed as having –NAOI dominance, and 25 years as having +NAOI dominance. According to the fitted LOWESS curve in Figure 7-5, the series started markedly with a –NAOI dominance, reaching the negative peak around the year 1963. The negative NAO throughout the winter 1962/63 is also mentioned by Greatbatch et al. [161]. Thereafter, the observations became less negative apparently with an upward trend, which led the signal to switch to a +NAOI dominance in 1980. The first positive dominance with its peak around the year 1990, and also the highest record in the entire period, lasted for almost 19 years. Then, a –NAOI dominated subperiod occurred for 12 years with a close succession or high concentration of very extreme NAOI events in the lower tail during the end of December and the months of January and February 2010. From the year 2012 to the very end of the time series, the signal was positively dominated, although with a seemingly

unfinished dominance. It should be noted that the most negative NAOI observations have been registered from November through March, and the highest positive observations from December through April.

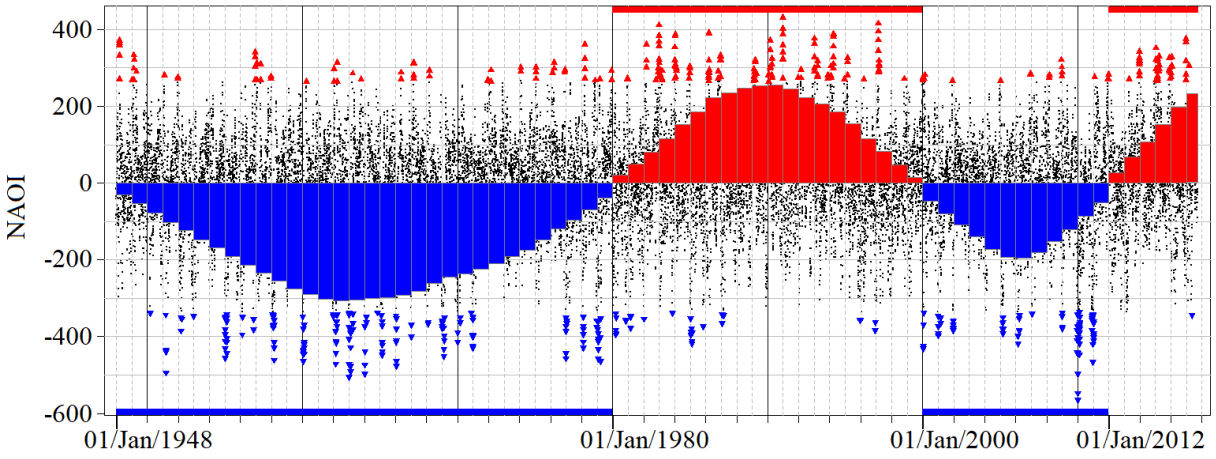

Figure 7-5: Daily records of NAOI from 1st January 1948 to 30th September 2017. The lower and upper tails' daily observations are identified by blue and red triangles, respectively; and fitted into a LOWESS curve: the –NAOI dominance subperiods from January 1948 to December 1979, and from January 2000 to December 2011 (blue vertical and horizontal bars); and the +NAOI ones from January 1980 to December 1999, and from 2012 on (red vertical and horizontal bars).

In this perspective, the 70-year reference period was divided into NAOI dominance subperiods, namely: the first, from 1st January 1948 to 31st December 1979; the second, from 1st January 1980 to 31st December 1999; the third, from 1st January 2000 to 31st December 2011; and the fourth, from 1st January 2012 to 30th September 2017. This subdivision was done to determine possible temporal changes in the influence of the extremal NAOI on extreme rainfalls during the NAOI dominance (the –NAOI and +NAOI dominance) based on the adopted techniques for extremal dependence, i.e., the extremogram and its extension the cross-extremogram.

The NAOI series in Figure 7-5 has the property that is heavy-tailed, i.e., the extreme negative and positive values are rather pronounced and occur in clustered days (e.g., the clustered blue triangles in January 2010). It is expected that the NAOI lower and upper tails would exhibit different dependence subject to each dominance subperiod. Thus, the extremogram was applied to the univariate daily NAOI series to quantify its conditional extremal serial dependence — that is, to measure the persistence of extremal daily NAOI with rare event probabilities at future instants of time (i.e., future days) for the upper and lower tails which in this cases refer to +NAOI and –NAOI, respectively. This in turn, supported the decision made to subdivide the reference period into subperiods to be further analysed. The extremograms for the lower and upper tails of the daily NAOI, assessed by Equation (7.10), are shown in Figure 7-6 providing a non-parametric estimate at large of extremal dependence as a function of time-lag in days.

In the first subperiod (–NAOI dominated), it is evident from the faster decay of the vertical lines for the upper tail in the top graph of Figure 7-6 that these extremes lack of clustering while the slower decay and somewhat periodicity shown for the lower tail (bottom graph) indicate the opposite — extremal clustering. Nevertheless, it is virtually impossible to make any inferences whether dependence or independence may occur among the extremal components of the daily NAOI series without a sense for the asymptotic distribution [103]. Under the assumption of no serial dependence (H_0, extremes are

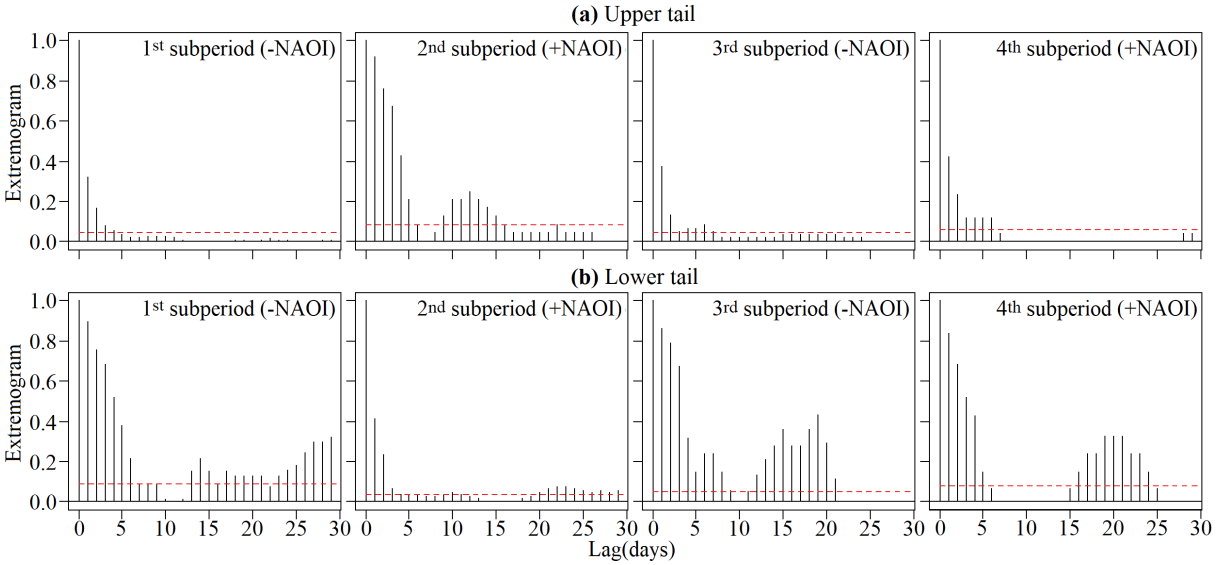

Figure 7-6: Extremograms of the univariate daily time series X (NAOI) for (**a**) the upper tail, and (**b**) the lower tail, for the dominance subperiods: 1st one (1948–1979), 2nd one (1980–1999), 3rd one (2000–2011), and 4th one (2012–2017). Horizontal red dashed lines indicate the upper 97.5% empirical confidence bands (for an α of 5%) for independent data, obtained via $m = 10,000$ permutations.

independent), empirical confidence bands for an α of 5% were computed by using $m = 10,000$ random permutations of the data for testing significant serial extremal dependence, although only the upper 97.5% confidence bands are shown in the figure.

Clearly, the extremogram for the lower tail in the first subperiod (Figure 7-6 bottom graph) is significantly greater than the upper limit of the confidence band (dashed line) in most of its realisations with enough evidence to reject H_0 compared with the upper tail extremogram which tails off after lag 4 and obviously fails to reject the null hypothesis of serial dependence. This behaviour is mirrored in the following subperiod, i.e., in the +NAOI dominated subperiod from 1980–1999 in which the extremal positive NAOI events (upper tail) seem to denote serial dependence (H_1, extremes are dependent) whereas for the extremal negative NAOI events, this is not the case. Conversely, the third subperiod (–NAOI dominated) displays a strong structure in the plot for the lower tail values themselves, similar to that of the first subperiod, with high probabilities (e.g., higher than 0.2) of given an extreme event at time t to observe another in the next 2 to 4, 6 to 7, and 13 to 20 days. This alternating character of the lower and upper tails throughout each NAOI dominance subperiod is not consistent with that of the most recent period from 2012–2017 which is +NAOI dominated and with higher extremogram values for the lower tail events. This behaviour may be due to the incompleteness of the dominance, as mentioned and shown in the last section of the fitted LOWESS curve of Figure 7-5.

7.5.3 Extremal dependence of the regionalised rainfall and NAOI via the Cross-Extremogram

The multivariate extension of the extremogram — that is, the cross-extremogram — was used in this case for teleconnection, to the bivariate daily time series X (NAOI) and Y (rainfall) at the four NAOI dominance subperiods, whether –NAOI or +NAOI, as was mentioned previously. The cross-extremogram

application provided insightful information about the conditional dependence between the daily NAOI and regionalised rainfall (F1-SOU, F2-CEN, F3-NOR) firstly, in their upper tails, and secondly, in the rainfall upper tail and NAOI lower tail, i.e., $P(Y > y, X > x)$ and $P(Y > y, X < x)$, respectively.

Equation (7.14) was utilised in order to determine the degree of influence of daily NAOI over rainfall. Simply put, it allowed to estimate the dependence and probability of occurrence of rainfall extreme events at lagged time, expressed in days, $(t + h)$ provided that a NAOI extreme event occurs in day t. The cross-extremograms for values above the rainfall and NAOI thresholds $a_{m(upper)Y}$, $a_{m(upper)X}$ (99^{th} percentiles' ranks); and below the NAOI threshold $a_{m(lower)X}$ (1^{st} percentile rank) with confidence bands (for $m = 10,000$ permutations) for lag 1 to 30 days (horizontal axis) and the probabilities of the extremal dependence (vertical axis) are shown in Figures from 7-7 to 7-10, respectively, for the four NAOI dominance subperiods.

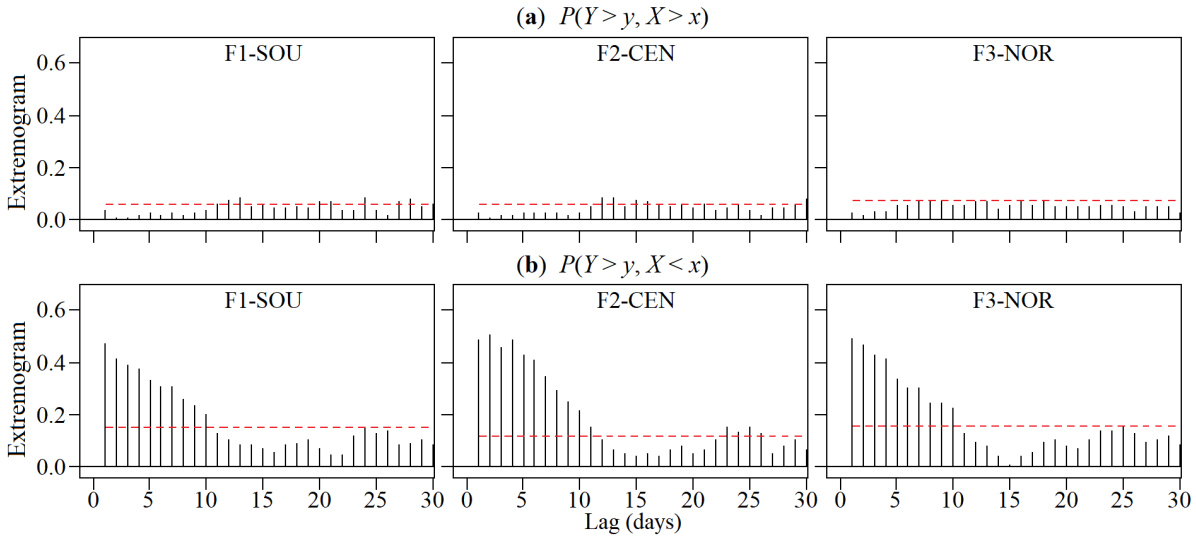

Figure 7-7: Cross-extremograms for the 1^{st} subperiod (1948–1979, –NAOI) of the bivariate daily time series X (NAOI) and Y (rainfall) for (**a**) X and Y upper tails, and for (**b**) the lower tail in X and the upper tail in Y (vertical axes cut off at 0.60). Horizontal red dashed lines indicate the upper 97.5% empirical confidence bands (α of 5%).

The cross-extremograms in the longest subperiod from the year 1948–1979 (–NAOI dominated) are illustrated in Figure 7-7. A spike in the figure can be regarded as the probability of obtaining a rainfall extreme in the region given that there was a NAOI extreme event (either positive or negative) in t days before. It is worth noting that after lag 30, there are no significant spikes in any of the generated extremograms and cross-extremograms (here not shown). For this 32-year subperiod as well as the other subperiods, the NAOI lower tail events ($X < x$) are highly negative NAOI records, whereas those of the NAOI upper tail ($X > x$) are highly positive records (as illustrated in Figure 7-5 by blue and red triangles, respectively). For the upper tails (top graphs), the cross-extremograms give little significance of dependence between the NAOI and rainfall extremes. Specifically, in southern slope (F1-SOU series), there are some signs of extremal dependence of the NAOI at some lags (e.g., at lags 12, 13, and 15 days), however, their probabilities are very low and marginally above the permutation generated confidence band. In the F2-CEN series (central region), the cross-extremogram exhibits a similar pattern as seen in the F1-SOU series with a few extremal dependence indications. Although the cross-extremogram for the

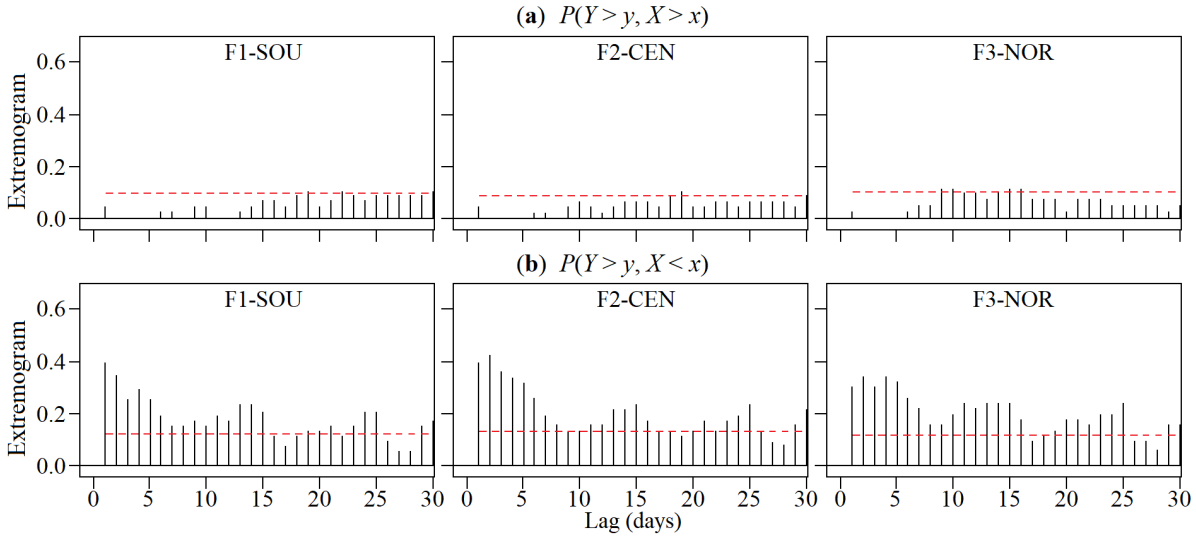

Figure 7-8: Cross-extremograms for the 2nd subperiod (1980–1999, +NAOI) of the bivariate daily time series X (NAOI) and Y (rainfall) for (**a**) X and Y upper tails, and for (**b**) the lower tail in X and the upper tail in Y (vertical axes cut off at 0.60). Horizontal red dashed lines indicate the upper 97.5% empirical confidence bands (α of 5%).

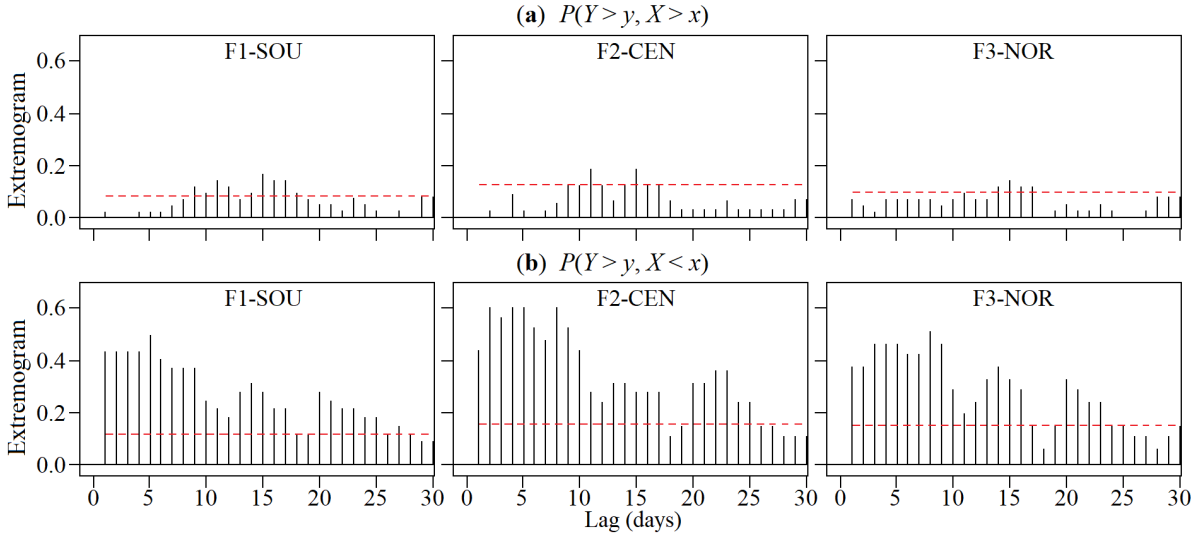

Figure 7-9: Cross-extremograms for the 3rd subperiod (2000–2011, –NAOI) of the bivariate daily time series X (NAOI) and Y (rainfall) for (**a**) X and Y upper tails, and for (**b**) the lower tail in X and the upper tail in Y (vertical axes cut off at 0.60). Horizontal red dashed lines indicate the upper 97.5% empirical confidence bands (α of 5%).

F3-NOR series has also a very alike development, any of the clustered events surpasses the correspondent dashed line, meaning that there is not enough evidence to reject H_0. In contrast with the upper tails results, the cross-extremograms between Y upper tail and X lower tail point at some general strong and significant extremal dependence with a slow decay from lag 1 through 10 days for the three identified regions, as shown in the bottom graphs of Figure 7-7. This somehow shows that given the –NAOI dominance for this subperiod, there are apparently stronger effects of the NAOI lower tail on rainfall extremes than those of the NAOI upper tail.

Figure 7-8 shows the cross-extremograms corresponding to the second subperiod from 1980–1999 with a +NAOI dominance. There is again little structure in the $P(Y > y, X > x)$ plots (top graphs) for the

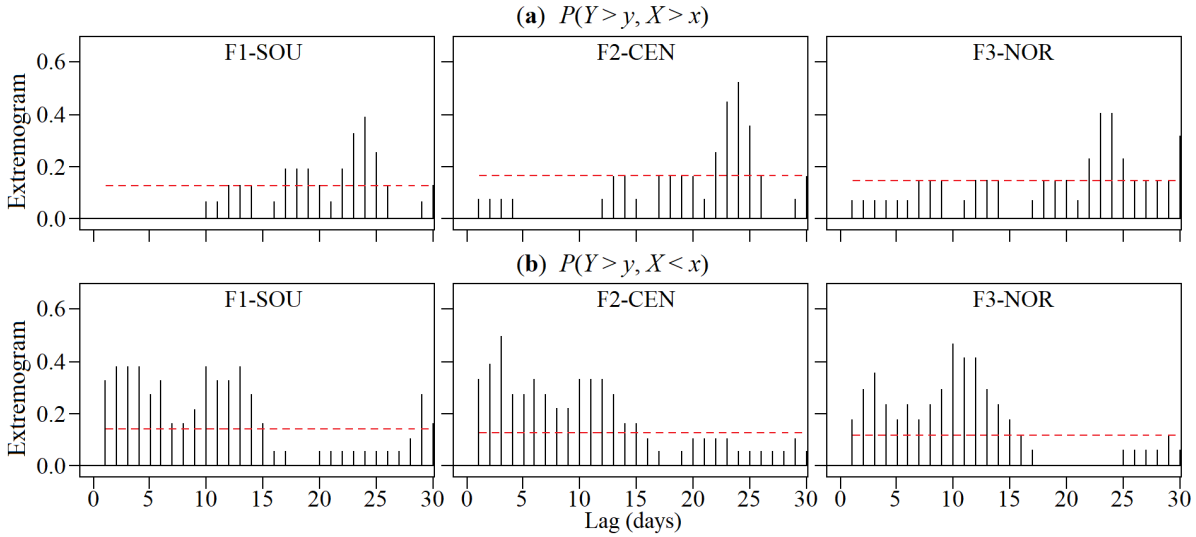

Figure 7-10: Cross-extremograms for the 4$^{\text{th}}$ subperiod (2012–2017, +NAOI) of the bivariate daily time series X (NAOI) and Y (rainfall) for (**a**) X and Y upper tails, and for (**b**) the lower tail in X and the upper tail in Y (vertical axes cut off at 0.60). Horizontal red dashed lines indicate the upper 97.5% empirical confidence bands (α of 5%).

three regions — only a few spikes in the F3-NOR cross-extremogram are slightly exceeding the confidence band. On the other hand, the $P(Y > y, X < x)$ plots (bottom graphs) have almost identical development with a higher clustering of extremes and significant extremal dependence during three lags around lag 1 to 7, 11 to 15, and 23 to 25 days. However, the degree of dependence is dissimilar at some extent among regions. As an example, the dependence of extremes is greater during the first lags in F2-CEN than in the other regions, whilst F3-NOR denotes a much more delayed response based on its smother high and low levels. In comparison to the results for the first subperiod, the ones for the second subperiod did not meet the expectations of having stronger effects of the NAOI upper tail on rainfall extremes than those of the NAOI lower tail given the +NAOI dominance.

The recognised cross-extremogram pattern in the two previous dominance subperiods coincides with that shown in Figure 7-9 from 2000–2011 (–NAOI dominated). Despite this, the $P(Y > y, X < x)$ plots for the third subperiod (bottom graphs) denote fuzzier decay with significantly greater probabilities of extremal dependence and an increased number of clustered events overweighting the band for independence, and therefore, accepting H_1 — extremes are dependent.

Following the negligible dependence for the bivariate daily series' upper tails in the third subperiod, the most recent 6-year (2012–2017) subperiod — with an unfinished NAOI dominance as was mentioned — presents a distinct pattern. It is clear from Figure 7-10 that the upper tails (top graphs) show more significantly dependent events in this subperiod than in the previous ones. Nevertheless, the $P(Y > y, X < x)$ plots (bottom graphs) have large spikes and dependence from lag 1–15 days.

Overall, these results suggest a sustained influence all over Madeira Island — at different levels — of extremely negative daily NAOI observations throughout the 70-year reference period than the extremely positive daily NAOI on the localised extreme daily rainfall events. This deserves further discussion.

7.5.4 Discussion and conclusions

For Madeira Island, the extremal dependence between local climate and large-scale forcings — such as the North Atlantic Oscillation — was established by incorporating the concepts of rainfall "clustering" by means of regionalisation and the tails dependencies, i.e., the extremogram and cross-extremogram. In understanding the relationship between the large-scale circulation and rainfall extremes, which is increasingly essential in vulnerability and impact assessment studies due to climate change, rainfall regionalisation is useful. The daily rainfall regionalisation of the forty rain gauges' complete series from 1st January 1948 to 30th September 2017 has been realistically aimed at not only setting up the most ideal of climatic regions of Madeira, but as well at producing an acceptable categorisation scheme based on rainfall variability, and not just on rainfall quantities, for further studies such as for climate change impact analyses. The methodology applied in this work firstly integrated the use of both principal factors based classification of rain gauges' time series and the Voronoi polygons method applied to those time series.

Climate regionalisation is not a seamless process that removes all elements of discrepancies. Uncertainty of this process has been the focus for a long time of discussion and debate among classic some other modern classifications — e.g., Ackerman [6], Thornthwaite [442], and MacLeod and Korycinska [246]. Such examples reflect the long history of discussing changes in regionalisation, some of them, also as a result of climate change. In this paper, the aim was not obtaining factor scores [99] based on the daily rainfalls series but rather computing factor loadings to use them, after rotation, to group the rain gauges into different regions. Therefore, the factor analysis approach in this work was purposely made simpler using rainfall as single variable of the 40 rain gauges with a common period of complete data. Rotation is more usually used in factor analysis than in PCA, and its importance depends much more on the interest of the analysis. The unrotated solution has not been spatially presented but the scree plot (Figure 7-2) since most of its explained variability is concentrated in the first factor with 71% which would mean that a single region could be acceptable. As an attempt to clarify the relationship among factors or regions, varimax rotation was applied as was performed in climate regionalisation, but using a different climatic variable [118, 116]. Principal factors obtained with other rotation techniques like quartimax, equimax, direct-oblimini, and promax [218] were also tested (here not shown) denoting almost the same results as those obtained via the varimax application, i.e., three factors retained explaining about 82% of the variability. Hence variability and, in some cases, the number of retained factors vary from technique to technique. Moreover, the factor loadings obtained using different rotated factors indicate that retaining three factors do not compromise prime information (explained cumulative variabilities higher than 80%).

Although the correlations mapping using different rotation techniques recognises almost the same regions (southern slope, central region, and northern region), the results of the homogeneous regions differ slightly for some rain gauges within the limits of the spatial distribution of factors (F1, F2, and F3). For instance, ST30 rain gauge is included in F2-CEN homogeneous region (Figure 7-3) with a correlation of 0.57 for F1, 0.62 for F2, and 0.35 for F3. However, quartimax results are 0.63, 0.56, and 0.33, respectively, making this rain gauge part of F1-SOU instead. Though factor analysis, including both PCA and PFA, is a robust mathematical procedure, its application in climate regionalisation requires

subjective decisions to some extent such as the choice of the correlation or covariance matrices, the optimal number of retained factors, and the rotation method [3, 210].

The here achieved regionalisation based on daily rainfall data — southern slope, central region, and northern slope — is consistent with previous spatial drought characterisations [118, 116], but using monthly data and PFA transformed into Standardized Precipitation index (SPI) and factor scores instead. The small differences among the limits of the homogeneous regions in these characterisations are due to the fact that the regionalised variables are different — though the drought indices SPI were also derived from the rainfall data. Although climate egionalisation is somewhat a subjective process which does not produce a definitive arrangement and that there are several approaches in the literature (e.g., Johannessen et al. [203], Parracho et al. [309], Wu et al. [496]), the regionalisation obtained in this work succeeded in explaining the daily rainfall climatology of Madeira Island with strong spatio-temporal variations.

In evaluating whether the computed regionalised rainfall series (after applying the Voronoi method) have been able to capture the seasonality, long-term fluctuation, and particularly daily rainfall extreme events, the extremes and the mean annual rainfall per region (from October to September) were compared to documented individual station's records and to the official reports, respectively. As mentioned at the end of Section 7.5.3, there is a fairly good correspondence between the occurrence of rainfall extremes from the regionalised and single rain gauges' series (e.g., the extreme events that occurred between the years 2009/10 and 2010/11). Overall, the value of 1669 mm for the weighted mean annual rainfall over Madeira is quite close to the one from the river basin management plan of Madeira, of 1628 $\mathrm{mm\,year^{-1}}$ [336, 100], although referred to different periods — in the present study 69 years, from October 1948 to September 2017, and 50 years, from October 1941 to September 1991, in [336, 100]. The mean annual rainfall of 873 $\mathrm{mm\,year^{-1}}$ now obtained for FI-SOU is remarkably below average, for F2-CEN is notably above with 24142 $\mathrm{mm\,year^{-1}}$, and for F3-NOR is marginally below with 1590 $\mathrm{mm\,year^{-1}}$, which are as well in accordance to the spatial pattern shown in [336].

The rainfall in Madeira is seen to be affected by the local topography coupled with the large-scale forcing interactions. F2-CEN and F3-NOR generally receive more rainfall than F1-SOU. This is due to the influence of the prevailing NE trade winds, from the northeast to southwest, on the climate of the small island [235]. This results in an increasing gradient in rainfall between southern and northern slopes. Due to the elevation differences (Figure 7-1), the windward-facing regions, namely, F2-CEN and F3-NOR experience orographic rainfall [244], as a result of adiabatic air expansion [123]. This increases the rainfall, particularly in F2-CEN which is one of the most favourable regions out of the three in terms of higher rainfall and water resources availability both surface and groundwater such as the Paúl da Serra plateau [333], ST02 in Figure 7-1. In contrast, F1-SOU lies in the leeward rain shadow and at lowest elevations which results in a much drier region. This indicates the ability of the rainfall regionalisation to recognise the unique characteristics and contribution of each homogeneous region to total rainfall in the small island. The regionalised daily rainfall series were crucial for the extremal dependence analysis between heavy rainfall events and the large-scale forcing of the NAO with regard to extremely positive and negative NAOI values.

Despite the winter NAO from December through March (the so-called NAOI DJFM in terms of

index) shows the strongest influence of the NAO on the surface climate — as stated by Hurrell et al. [196], López-Moreno and Vicente-Serrano [240], Hurrell and Deser [195] — all-year-long daily NAOI records (from 1948–2017) from the NOAA PSL have been considered. Either way, the lower and upper tails' NAOI events (blue and red triangles in Figure 7-5) were pointed out almost entirely during the first half of the hydrological year (from October through March) neglecting equally important extremes out of this period. Different approaches have been used to define an NAOI such as the station-based method [74] given by the normalised SLP between high pressure, i.e., a southern station located in Iberian Peninsula or the Azores (**C** and **B** in Figure 7-11, respectively) and a northern station (low pressure), usually making use of a southwest Icelandic station (**F** in Figure 7-11). As an alternative, NAOI can be obtained from gridded climate datasets utilising orthogonal analysis or PCA. Similar methods like ensembles of simulations from a general circulation model can produce climatic datasets as the one here analysed which extends a daily NAOI back to the year 1948 and consistently updated by the NOAA PSL (Section 7.3.2). Because all indices from shorter to longer time scales show similar temporal evolutions and are highly correlated at interannual and interdecadal time scales, an exact NAOI definition is of less importance. However, the same time scale and length of both rainfall and NAOI have been reckoned with as determining factors in this study.

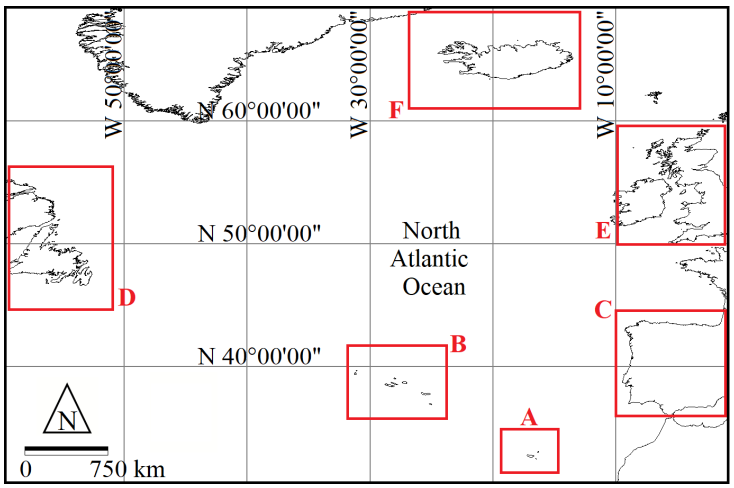

Figure 7-11: Location of: (**A**) Madeira Archipelago, (**B**) The Azores, (**C**) Iberian Peninsula (mostly formed by continental Portugal and Spain), (**D**) Newfoundland and Labrador (the easternmost province of Canada), (**E**) The British Isles, and (**F**) Iceland. Projection: Geographic Latitude-Longitude; datum: WGS84; planar unit: arc degrees.

The results of the negative (–NAOI) and positive (+NAOI) dominance of NAOI (Figure 7-5) demonstrate the interannual, but more importantly, the multi-year and interdecadal variability of daily NAOI extreme events. Beyond the generalised spatio-temporal variations of the NAO influencing rainfall throughout the North Atlantic Ocean and over some continental regions (e.g., the Azores, the eastern Canada, U.S., Europe) this work highlights the outstanding influence of –NAOI and +NAOI dominance on the extreme rainfall for Madeira Island (**A** in Figure 7-11) during the four multi-year subperiods. Thus, the fitted LOWESS curve of Figure 7-5 was compared to an earlier characterisation from the year 1870–2090 by Osborn et al. [301] of a filtered NAOI DJFM single realisation obtained from ensembles means of four greenhouse gases (GSa) experiments. Only the patterns were the focus due to the resolution differences

and also because absolute spectrally truncated daily NAOI and NAOI DJFM values are not comparable. Although not shown, the comparison stresses that both signals' patterns exhibit a prevalence of negative NAOI dominance from the 1950s to 1980s, followed by a reduction of the total NAOI, or integrated area above or under the signal, of alternating sign anomalies, namely, +NAOI, –NAOI, and +NAOI. It is also apparent, that in some recent years there is an increase of more consecutive and more extremes negative NAOI observations (e.g., daily NAOI values from 2009/10 to 2011/12). Additionally, the apparent upward trend in the LOWESS curve from 1960's to 1990's is also in accordance with that based on real data by Osborn et al. [301], and also linked to quickly climatic variables changes (e.g., the rapidly temperatures rise) in the North Atlantic Ocean region [499]. These remarks and some others through the extremogram application to the univariate daily NAOI series as mentioned in Section 7.5.2, strengthen the justification to follow through the extremal dependence analysis adopting subperiods, i.e., from 1948–1979 (1^{st} subperiod), 1980–1999 (2^{nd} subperiod), 2000–2011 (3^{rd} subperiod), and 2012–2017 (4^{th} subperiod).

The statistics of the three weighted regionalised rainfall series indicate that the response of maximum daily rainfall to the NAOI dominance has an alternating structure. For instance, the maximum daily rainfalls for F2-CEN are 162.9 mm for 1^{st} subperiod (–NAOI dominance), 142.0 mm for 2^{nd} subperiod (+NAOI dominance), 174.2 mm for 3^{rd} subperiod (–NAOI dominance), and 128.0 mm for 4^{th} subperiod (+NAOI dominance). In the same way, for F1-SOU the values are 107.1 mm, 104.1 mm, 135.5 mm, and 101.5 mm; and for F3-NOR 156.1 mm, 133.0 mm, 163.5 mm, and 110.3 mm. These figures show that the higher maximum rainfall occurred in the –NAOI dominance periods. The fact that this alternating behaviour is found in the three regions in Madeira is indicative of the important effect of the NAOI lower tail (regarded as –NAOI) rather than the NAOI upper tail (+NAOI) on extreme rainfall events. Additionally, the same cross-extremogram approach was applied for teleconnection between extreme rainfall and extreme NAOI, although considering the complete 70-year reference period instead of the subperiods as done for Figures 7-7 to 7-10. The plots of Figure 7-12 are virtually identical, but with lower spikes smoother than those displayed in Figures 7-7 to 7-9, i.e., with a significant extremal dependence between the rainfall extremes and extremely negative NAOI, and an almost non-existent dependence as for the upper tails. This suggests that particularly attention should be given to the negative NAOI and its effects on the extreme rainfall development in Madeira.

To support the aforementioned findings, a simplified analysis (adopting the same rainfall threshold as for the extremogram analysis, i.e., the 99^{th} percentile rank) between the dimensionless number of exceedances of daily rainfalls and NAOI DJFM, as defined by Hurrell and Deser [195], was carried out for the 69 hydrological years, from October 1948 to September 2017. Figure 7-13 depicts, for each homogeneous region, the number of rainfalls above $a_{m(upper)Y}$, in each hydrological year divided by their corresponding mean annual number (dimensionless number of exceedances in the horizontal axis) plotted against NAOI DJFM in the same year (vertical axis). The station-based winter NAOI DJFM data was retrieved from National Center for Atmospheric Research (NCAR) [285], for the stations located in Lisbon and Stykkisholmur (**C** and **F**, respectively, in Figure 7-11). Boxplots were constructed to represent the NAOI DJFM samples dispersion for three exceedances categories, i) values lower than the mean, ii) between one and two times the mean, and iii) higher than two times the mean. Figure 7-13 evidences

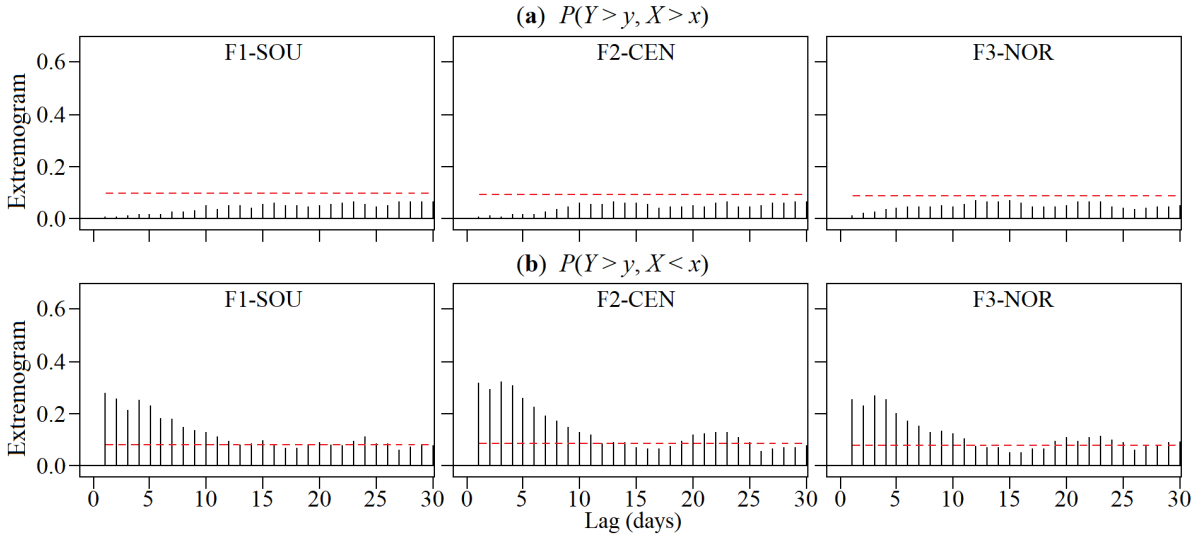

Figure 7-12: Cross-extremograms for the reference period from 1948 to 2017 of the bivariate daily time series X (NAOI) and Y (rainfall) for (**a**) X and Y upper tails, and for (**b**) the lower tail in X and the upper tail in Y (vertical axes cut off at 0.60). Horizontal red dashed lines indicate the upper 97.5% empirical confidence bands (α of 5%).

that regardless the region, most of the "weaker" extreme rainfall years, with below average number of exceedances, are associated to positive NAOI DJFM values, and the "very extreme" rainfall years, with more than twice the average number of occurrences, to negative NAOI DJFM. This is in agreement with the detected alternating character of the maximum daily rainfalls for each NAOI dominance subperiod.

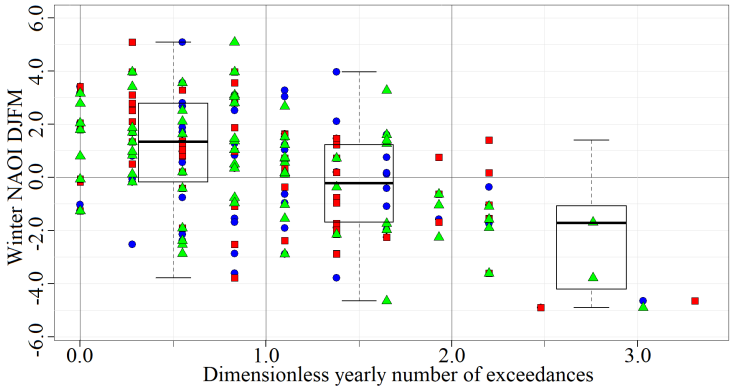

Figure 7-13: Dimensionless yearly number of exceedances (horizontal axis) in each hydrological year, from 1948/49 to 2016/17, for each of the weighted regionalised daily rainfall series (F1-SOU, blue circles; F2-CEN, red squares; F3-NOR, green triangles) and their corresponding NAOI DJFM (vertical axis). Boxplots constructed based on the NAOI DJFM on an annual basis for three exceedances categories: less than one exceedance per year, from one to two exceedances per year, and more than two exceedances per year.

Besides the statistical interpretation of i) the –NAOI and +NAOI dominance subperiods here identified, ii) the alternating daily maximum structure in the multi-year subperiods, iii) the teleconnection insights from the extremal dependence analysis (via the extremogram and cross-extremogram), and iv) the straightforward rainfall exceedances results; an explanation can be drawn from a meteorological perspective. For instance, +NAOI values are associated with stronger westerlies (prevailing anti-trade winds from the west headed for the east) over latitudes N 30°–60° (Figure 7-11), and with milder weather over

western mainland Europe [195]. Generally, extreme or heavy and frequent rainfall are due to long-distance air streams whose origin may be as NE trade winds [254].

On top of the NE trade winds, Madeira's climate is influenced as well by the Azores anticyclone [334] mostly bringing drier conditions. This anticyclone is stronger-than-average during the high +NAOI. Conversely, very low –NAOI indicates weakening of the Azores anticyclone [449] as occurred in the 2009/10, a year characterised by record persistence of the negative phase of the NAO [52], and with the lowest daily –NAOI ever registered as already shown in Figure 7-5. Furthermore, –NAOI strengthens the NE trade winds allowing cold air to build up over the small island and may result in wetter conditions [134] favourable for the extreme rainfall occurrence.

The association of disturbances of the atmosphere or storms, usually accompanied by rainfall or snow, with the NAO activity is well known for continental areas and large islands, as has been mentioned, except for some small islands. Serreze et al. [398] developed an algorithm to realistically track storms via the NAO activity in winter. According to the authors –NAOI has less storms in Iceland, more in a band stretching from the British Isles to Newfoundland and Labrador, and even more notably over Iberian Peninsula (**F**, **E**, **D**, **C**, in Figure 7-11 respectively). This suggests that the –NAOI effect may shift south-eastwards from Iberian Peninsula with increased storms characterised by substantial heavy rainfalls in Madeira Island, with a somewhat symmetrical +NAOI effect but to a lesser degree. These claims are supported by the statistically significant evidence found and discussed in this extremal serial dependence analysis between the weighted regionalised rainfalls and daily NAOI compared with previous studies though focused on single rain gauges' and on monthly and seasonal NAOI data.

It is important to point out that a NAOI definition only indicates the most probable pressure set-up over a period of time, which in turn can give strong clues as to the types of storms and their related intensity. Recent studies have shown that weather models have very good performance at predicting winter NAOI [388] and daily NAOI [77]. Such capability coupled with the results here shown gives the possibility of forecasting extreme rainfalls and consequently implementing anticipatory risk reduction measures. Thus, modelling extremal dependence between rainfall and predictable major climatic drivers may play a crucial role in water resources and risk management in Madeira but also in other North Atlantic small islands, namely under a changing climate.

THIS PAGE INTENTIONALLY LEFT BLANK

Chapter 8

Bivariate Modelling of a Teleconnection Index and Extreme Rainfall

This chapter has been published as: Espinosa, L. A., Portela, M. M., Pontes Filho, J. D., and Zelenakova, M. (2021a). Bivariate Modelling of a Teleconnection Index and Extreme Rainfall in a Small North Atlantic Island. *Climate*, 9(5): 86, https://doi.org/10.3390/cli9050086

Abstract

This paper explores practical applications of bivariate modelling via copulas of two likely dependent random variables, i.e., of the North Atlantic Oscillation (NAO) coupled with extreme rainfall on the small island of Madeira, Portugal. Madeira, due to its small size ($\sim$740 km^2), very pronounced mountain landscape, and location in the North Atlantic, spans a wide range of rainfall regimes, or microclimates, which hamper the analyses of extreme rainfall. Previous studies showed that the influence of the North Atlantic Oscillation (NAO) on extreme rainfall is largest in the North Atlantic sector with the likelihood of increased rainfall events from December through February particularly during negative NAO phases. Thus, a copula-based approach was adopted for teleconnection aiming at assigning return periods of daily values of a NAO index (NAOI) coupled with extreme daily rainfalls — for the period from December 1967 to February 2017 — at six representative rain gauges of the island. Results show that (i) bivariate copulas describing the dependence characteristics of the underlying joint distributions may provide useful analytical expressions of the return periods of the coupled previous NAOI and extreme rainfall, and that (ii) recent years show signs of increasing climate variability with more anomalous daily negative NAOI along with higher extreme rainfall events. These findings highlight the importance of multivariate modelling for teleconnections of prominent pattern of climate variability, such as the NAO, to extreme rainfall in North Atlantic regions, especially in small islands which are highly vulnerable to the effects of abrupt climate variability.

Keywords:

North Atlantic Oscillation; winter extreme rainfall; Madeira Island; copulas; teleconnection; climate variability.

8.1 Introduction

Climate tends to change at a slow pace, however, this does not mean that climate is not prone to experience short-term fluctuations or anomalies at seasonal or longer timescales [137, 76]. For instance,

being the rainfall an essential meteorological variable subject to climate system components (e.g., to the atmosphere), it can fluctuate around the average without causing the long-term rainfall average itself to change [506]. This phenomenon is a clear example of climate variability which refers to variations in the mean state and in other statistics on spatio-temporal scales [198] — such as extreme hydrological events withdrawing too far away from long-term values. These variations result from atmospheric and oceanic circulation which in turn is caused mostly by differential heating of the sun on Earth. Globally, atmosphere-ocean circulations may spawn extreme rainfall events or even exacerbate local and regional rainfalls from season to season or year to year time periods [177, 389].

Furthermore, it is acknowledged that higher global surface temperature (GTS) increases the intensity of extreme rainfall events more greatly than of average rainfalls [215, 410, 411, 314]. For the North Atlantic sector, a substantial portion of the GTS variability is associated with the North Atlantic Oscillation (NAO), a hemispheric meridional oscillation with one centre of action over the subtropical Atlantic and the other near Iceland. The NAO refers to large-scale changes in atmospheric pressure at sea level (SLP), and thus, changes in GTS and rainfall [470]. The NAO-related impacts on climate, particularly in winter, extend from eastern North America to Greenland and from northwestern Africa over Europe [131]. Despite this large-scale circulation pattern is non-linear in how it reacts, it has been shown that it has largely influenced the occurrence of extreme rainfalls during its negative and positive phases leading to stronger climate responses depending on the location in the North Atlantic or the proximity to the Atlantic Ocean [e.g. 448, 56, 431]. For instance, when the NAO is in its negative phase, pressure anomalies are not so noticeable producing stronger-than-average easterlies. Throughout the same negative NAO phase, warmer and wetter conditions characterise the northwestern Atlantic and southern European regions, whereas colder and drier than average conditions in Northern Europe [240]. Contrasting patterns occur during the NAO positive phases with generalised opposite conditions.

A remarkable feature of the NAO is the upward seasonal and annual trend shown since the late 1980s, with high positive records [171]. However, this period has been also characterised by persistent negative NAO index (NAOI) values that seem to be unprecedented in the daily observational record [119]. Some of these persistent negative anomalies have occurred since the 2009/2010 winter. In this period, the NAO swung into an extreme negative phase, escaping the long-term upward trend, fostering unusually wet conditions and apparently promoting extreme rainfall events in some North Atlantic regions, most notably in the European Macaronesia — e.g., in the Canary Islands, and the Madeira Archipelago [72]. Thus, monitoring the state of the NAO at shorter timescales (e.g., at daily scale) can improve the understanding of the climate variability on rainfall extremes — as performed in this research work for a small island of the Madeira Archipelago, namely, Madeira Island — and be crucial for better short-term water resources management and planning.

Although the effects of the NAO persist for some months, the closest relationships are shown in the winter period accounting for more than one-third of the total rainfall variance from December through February [473, 474]. The formulae for the relationships between NAO and extreme rainfalls in this research work are therefore based on rainfalls above a quantile threshold occurring in those months and on previous NAOI to such events, i.e., on the occurrence of unprecedented NAOI values and extreme

rainfalls with a time lag.

In this study, statistical models are developed to assess (i) how persistent NAO conditions alone can model extreme daily rainfall, and (ii) if considering a multivariate approach — specifically a bivariate one between NAO and rainfall — improves the assessment of climate variability in the small Portuguese island of Madeira. This island is the appropriate setting for this analysis as it shows an overall mild climate but different microclimates due to its geographical location, sharped topography, and effect of the mountain ridge and of the North Atlantic Ocean. In the mountain region of Madeira, particularly during the winter season, heavy rainfall have triggered flash floods, landslides and debris flows (the so-called "*aluviões*") [140], in periods which coincide with perturbation of Earth's energy balance. In addition, during the winter of 2009/2010 the most negative NAO records were registered for the last 160 years clearly outside of the long-term averages or trends [205] along with extreme rainfall which in turn led to numerous hazards and causalities for the same winter period. Although rare, hydrological extreme events, such as extreme rainfall, have cost losses of lives and had negative economic and social impacts in the island. Therefore, the need for appropriate statistical models of extreme hydro-meteorological events linked to large-scale atmospheric phenomena, i.e., teleconnection, becomes clear, particularly in the current context of a more recent pronounced climate variability.

Extreme rainfall events have often been linked to the strong climatic conditions and climate variability in the North Atlantic and adjacent land areas. For instance, Wilby et al. [489] investigates correlations between British Isles extreme rainfall and other climatic variables in relation to decadal variations in the atmospheric circulations — in terms of the NAOI — during winter. Tramblay et al. [445], provides a regional assessment of trends and variability in extreme rainfall over Maghreb countries — the western and northern African countries of Morocco, Tunisia, Algeria, and Lybia — showing that extreme rainfalls exhibit a strong spatial variability and are moderately correlated with large-scale atmospheric patterns such as the NAO — but also with the El Niño Southern Oscillation (ENSO) as described in [475]. Further, the NAO has also been found to affect the intensity and frequency of extreme rainfall. Queralt et al. [341] analyse 102 rain gauges with daily records over Spain and the Balearic Islands from 1997 through 2006, arguing that NAO exerts a clear effect on the increasing intensity of total and extreme rainfall rates in northern and westernmost Spanish regions, and on the increasing rainfall frequency in central and southwestern areas. Specifically for Madeira Island, very few studies have been undertaken to understand the influence of the NAO on extreme rainfall. As an example, Espinosa et al. [119] focus on short-term climatic fluctuations in the NAO (e.g., daily NAOI) and claim the existence of systematic evidence of statistical dependence over Madeira between exceptionally daily negative NAOI ($-$NAOI) records and extreme regionalised rainfalls, based on a bivariate extremal dependence analysis, which is stronger in sustained $-$NAOI year-long periods. And it is in this context that the relevance of this study comes up by assessing some of the climate variability aspects.

Such assessment was conducted with the use of copulas [112] to model the bivariate dependence between daily NAOI and extreme daily rainfall in Madeira, from 1967/1968 to 2016/2017, assuming both variables exhibit different marginal behaviour. Copulas have been recently used to determine the conditional probabilities and return periods of multivariate problems. Wong et al. [495] fit a trivariate

copula to drought characteristics, i.e., drought magnitude, duration and intensity, for some Australian rainfall districts. André and de Zea Bermudez [18] analyse and characterise the dependence using copulas between daily maximum wind speeds observed in mainland Portugal and simulate daily maximum wind speeds produced by a numerical physical model. Gouveia-Reis et al. [158] investigate the dependence of Madeira's rainfall data and spatial variables (altitude, slope orientation, distance between rain gauges, and distance to the sea) within an extreme value copula approach through an analysis of maximum annual data. To the knowledge of the authors, a more complex framework with at least one large-scale atmospheric pattern as predictor — in this research work, the state of daily NAO — and extreme rainfall as response variable has not yet been addressed.

The present paper is structured as follows. A brief description of the study area, the data used, and copula is given with a focus on bivariate return periods. The winter extreme daily rainfalls at six rain gauges in the island are first selected based on an empirical percentile as threshold. A low-pass filter is applied to the daily NAOI series. The correlation between extreme rainfalls and previous smoothed NAOI, i.e., with a lag in between, is assessed. The bivariate observations for marginals selection and copula modelling are determined. Bivariate copula models for NAOI and extreme rainfalls are developed and compared. The selected copulas are then used to determine the bivariate joint and conditional return periods, besides univariate return periods, to assess the climate variability of the NAO and rainfall for Madeira Island from a multivariate perspective. The marginal and copula selection, and the climate variability assessment are also discussed.

8.2 Physical features of the study area

Madeira is the largest island of the Madeira Archipelago with an area of approximately 740 km^2, a length of 58 km and 23 km width. Centred at 32°75' N and 17°00' W, the small island of Madeira — according to its size [123] — is completely shaped by volcanic materials, consisting of an enormous east–to-west (EW) oriented mass that is cut by deep valleys [332]. Madeira has a mountain ridge that extends mainly along the central part of the island with the highest peaks in the eastern part, Pico Ruivo (1862 m.a.s.l.) and Pico do Areeiro (1818 m.a.s.l.), while the Paúl da Serra plateau (with approx. 24 km^2 above 1400 m.a.s.l.) is located in the western part, as shown in Figure 8-1. The abrupt orography of peaks and valleys, together with the North Atlantic effect, provide the island with a great variety of microclimates, mostly with mild summer and winter, except for the highlands where the lowest temperatures are registered [380].

The rainfall regime over the Madeira is affected by local circulation and also by synoptic systems such as fronts and extratropical cyclones [140]. The distribution of rainfall presents an evident seasonal pattern, thoroughly different between the rainy season, that extends from November to March, and the dry season, with insignificant rainfall amounts during July and August [58]. The pronounced spatial variability of the rainfall in Madeira is determined mostly by the topography and the trade winds or easterlies — the permanent EW prevailing winds that flow in the Earth's equatorial region [38] — with higher amounts in the north-east (∼1600 $mm\,year^{-1}$) and central highlands (∼2300 $mm\,year^{-1}$) than in

the western (~800 mm year^{-1}) and southern regions (~600 mm year^{-1}), as previously characterised by Espinosa and Portela [115].

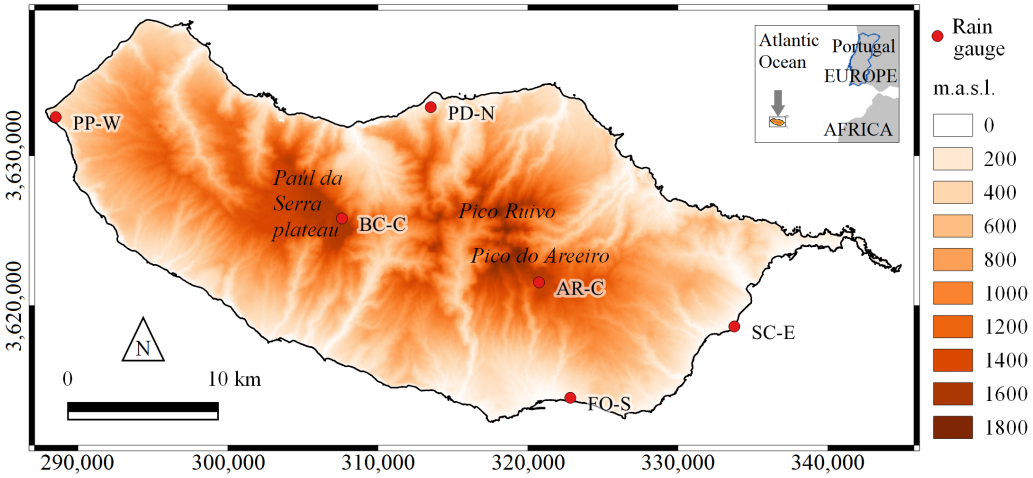

Figure 8-1: Coordinates WGS84 (UTM zone 28N) and relief of Madeira Island, Portugal. Spatial distribution of the six rain gauges used in this study depicted by bullets and their identification codes (description in Table 8.1).

8.3 Materials and methods

To assess the climate variability from 1 December 1967 to 28 February 2017, it was vital to derive some connected schemes of relationship or teleconnections to the NAO from extreme daily rainfall events. On this end, the rainfall daily data from December to February (DJF) of the following year were considered at six rain gauges of the island, with the expectation that different rainfall regimes would be identified due to their location: in the northern, southern, eastern and western slopes, and in the central ridge and plateau. The rainfalls above the 99$^{\text{th}}$ empirical percentile rank were considered as extreme rainfall events — following the recommendation of the Expert Team on Climate Change Detection, Monitoring and Indices (ETCCDMI) [224]. Based on the considered period, the number of selected rainfalls is 90 consecutive days during 50 years. Out of the 4,500 days of winter DJF rainfall at each rain gauge, the highest 45 rainfalls, i.e., 1%, were chosen as extreme rainfall events.

Different smoothed NAOI series were considered — by simple averages — relating to their running length, m, and to the lag between the ending day of the smoothed series and the day of occurrence of each extreme rainfall event, l. The Pearson linear correlation [169] was applied to analyse the relationship between the smoothed and lagged values of NAOI and the selected extreme rainfalls events. Based on this correlation analysis, (i) the smoothing factor or low-pass filter [154] of m NAOI daily values and (ii) the number of lagged days, l, between the end of the smoothed NAOI values and the occurrence of extreme rainfalls were selected. This analysis was based on the rainfall data at Areeiro rain gauge (AR-C in Figure 8-1). This rain gauge is located at the central highlands — an area that highly contributes to the island's fresh water availability and aquifers recharge due to the high rainfall and geological conditions prone for infiltration [58]. The previous NAOI values (smoothed and lagged NAOI) based on the preceding correlation analysis were assigned to the extreme rainfalls. The m and l achieved based on AR-C were

applied to the other five stations so that the final dataset for copulas modelling could be assembled.

Subsequently, the Wald-Wolfowitz runs test [492] was used to test the null hypothesis H_0 of independence for the observations of the final dataset (either NAOI values or extreme rainfalls). The second part of the methodology consisted of the bivariate analysis of NAOI as the "cause" of extreme rainfall using copulas by modelling such teleconnection. Finally, the concept of bivariate return period was applied for the events defined by the joint behaviour of pairs of the random variables adopted, i.e., daily NAOI and extreme daily rainfall. This was the core of the climate variability assessment for the island of Madeira.

8.3.1 Rain gauge data

The daily rainfall data at six representative rain gauges located at the central highlands (AR-C and BC-C), southern (FO-S), northern (PD-N), western (PP-W), and eastern (SC-E) slopes, were used — Table 8.1 and Figure 8-1. The data for the time-frame from December 1967 to February 2017 were made available by IPMA — Portuguese Institute for the Ocean and Atmosphere (https://www.ipma.pt/en/). The data had some gaps that were filled, as described in Espinosa et al. [120]. IPMA is the national authority in the fields of meteorology, aeronautical meteorology, climate, seismology, and geomagnetism, and an institution of reference at international level also devoted to the promotion and coordination of scientific research. For each of the rain gauges, 4,500 winter daily rainfall data were retrieved, i.e., 90 DJF daily values for 50 years (excluding leap year days).

Table 8.1: The six rain gauges adopted in the study. Identification (code and name), coordinates WGS84 (UTM zone 28N), and elevation. In the code, the character after the hyphen indicates the location of the gauge, i.e., C for centre and S, N, W, and E for southern, northern, western, and eastern coastal areas, respectively.

Code	Name	UTM-X Easting (m)	UTM-Y Northing (m)	Elevation (m.a.s.l.)
AR-C	Areeiro	320,746.000	3,621,552.000	1,610.0
BC-C	Bica da Cana	307,604.000	3,625,815.000	1,560.0
FO-S	Funchal Observatório	322,831.000	3,613,854.000	58.0
PD-N	Ponta Delgada	313,525.801	3,633,232.797	123.0
PP-W	Ponta do Pargo	288,512.995	3,632,569.609	339.0
SC-E	Santa Catarina	333,770.000	3,618,611.000	49.0

8.3.2 North Atlantic Oscillation index (NAOI) data

The large-scale atmospheric characteristics were identified through the analysis of a synoptic meteorological index for the North Atlantic Oscillation, i.e., NAOI, at daily scale retrieved from portal of the NOAA Physical Sciences Laboratory, NOAA PSL [293]. The NAOI represents a pattern of low-frequency tropospheric height variability. This measure of pressure difference is based on centres-of-action of 500 millibars constant pressure (mb) height patterns. Note that these height fields are spectrally truncated to total wave number 10 in order to emphasise large-scale aspects of teleconnection. The calculation of this teleconnection index utilises the ESRL/PSD Global Ensemble Forecasting System Reforecast2 (GEFS/R) ensemble forecasts from the averaged region 55°–70° N; 70°–10° W which in turn is subtracted from 35°–45° N; 70°–10° W. The NAOI daily records were utilised for the same period as in the case of

daily rainfall (DJF, from 1967/1968 through 2016/2017), but including also the months of September, October, and November prior each December.

8.3.3 Bivariate copula

The problem of specifying a probability model for dependent bivariate observations can be greatly simplified by expressing the corresponding joint distribution F_{XY} in terms of its marginals, F_X and F_Y, and an associated dependence function copula $\mathbf{C}$ — introduced by Sklar [415] — completely defined through the functional identity $F_{XY} = \mathbf{C}(F_X, F_Y)$. $\mathbf{C}$ is a bivariate copula, hereafter copula. It is precisely the copula that captures the features of a joint distribution. Moreover, copulas measure the association and dependence structure properties connecting random variables. In this research work, a possible way of analysing bivariate data (NAOI, X; and extreme rainfall, Y) consisted of investigating the dependence function and the marginals separately. This approach was convenient for the climate variability assessment, because this allowed studying the dependence structure independently of any marginal effect. Regardless of the marginal laws involved, the analysis of this research work was focused on practical applications of copulas modelling for teleconnection and not on the equations involved. Nevertheless, the main mathematical descriptions related to the copula concept [415], are next presented.

Definition 1. Let $\mathbb{I} = [0, 1]$; a copula is a bivariate function $\mathbf{C} : \mathbb{I} \times \mathbb{I} \to \mathbb{I}$ such that (1) uniform marginals: for all u, $v \in \mathbb{I}$ it holds that $\mathbf{C}(u, 0) = 0, \mathbf{C}(u, 1) = u, \mathbf{C}(0, v) = 0$, and $\mathbf{C}(1, v) = v$; and (2) two-increasing: for all $u_1, u_2, v_1, v_2 \in \mathbb{I}$ such that $u_1 \leq u_2$ and $v_1 \leq v_2$ it holds that $\mathbf{C}(u_2, v_2) - \mathbf{C}(u_2, v_1) - \mathbf{C}(u_1, v_2) + \mathbf{C}(u_1, v_1) \geq 0$; where $\mathbf{C}$ is uniformly continuous on $\mathbb{I}^2$. Hereafter F_X, F_Y (respectively, F_U, F_V will denote the marginal distribution functions of the random variables X, Y (respectively U, V).

Theorem 1. *(Sklar). Let F_{XY} be a joint distribution function with marginals F_X and F_Y. Then there exists a copula $\mathbf{C}$ such that*

$$F_{XY}(x, y) = \mathbf{C}(F_X(x), F_Y(y)) \tag{8.1}$$

for all reals x, y. If F_X, F_Y are continuous, then $\mathbf{C}$ is unique; otherwise, $\mathbf{C}$ is uniquely defined on Range $(F_X) \times$ Range (F_Y). *Conversely, if $\mathbf{C}$ is a copula and F_X, F_Y are distribution functions, then F_{XY} given by Equation* 8.1 *is a joint distribution function with marginals F_X and F_Y.* The detailed proof of Sklar's Theorem can be found in Schweizer and Sklar [394].

In addition, since $\mathbf{C}_{X,Y}$ is invariant under strictly increasing transformation of X and Y, by virtue of the Probability Integral Transform, the pair of random variables can be expressed as (U, V), where

$$\begin{cases} U = F_X(X) \\ V = F_Y(Y), \end{cases} \tag{8.2}$$

with $(U, V) \sim \mathbf{C}_{U,V} = \mathbf{C}_{X,Y}$. Being U and V non-exceedance probabilities given by the marginal distribution functions, they are uniform on $\mathbb{I}$, i.e. $U \sim \mathcal{U}(0, 1)$ and $V \sim \mathcal{U}(0, 1)$ [286]. Hereafter (X, Y) is considered as the pair of NAOI and extreme rainfall variables — and also the pair (U, V) respectively — having a direct practical meaning.

Given a bivariate distribution function F with invertible margins F_X and F_Y, a bivariate copula $\mathbf{C}(u, v)$ for $u, v \in [0, 1]$ is given by the following Equation 8.3. Meta-elliptic copulas are symmetric and hence lower and upper tail dependence coefficients are the same.

$$\mathbf{C}(u, v) = F(F_X^{-1}(u), F_Y^{-1}(v)) \tag{8.3}$$

The Archimedean copulas are more flexible than Meta-elliptic and can present lower or upper tail dependence which are defined by Equation 8.4:

$$\mathbf{C}(u, v) = \varphi(\varphi^{-1}(u) + \varphi^{-1}(v)) \tag{8.4}$$

where φ is the generator function of the copula $\mathbf{C}$ and $\varphi[0, 1] \rightarrow [0, \infty]$ is a continuous and factually reducing function. The Meta-elliptic Gaussian and Student's t, and the Archimedean Clayton, Frank, and Gumbel, were tested to verify best fit. Table 8.2 presents the formulations of the candidate copula families. When the Archimedean copula is rotated 180° it is called survival copula and can invert the predefined tail dependence to best fit the data.

Table 8.2: Copula candidate family and mathematical formulation.

Copula class	Copula family	Mathematical formulation
Meta-elliptic	Gaussian	$\phi_\rho(\phi^{-1}(u), \phi^{-1}(v))$
	Student's t	$\mathrm{T}_{\rho,v}(\mathrm{T}_v^{-1}(u), \mathrm{T}_v^{-1}(v))$
Archimedean	Clayton	$(u^{-\theta} + v^{-\theta} - 1)^{\frac{-1}{\theta}}$
	Frank	$-\theta^{-1}\log\left[1 + \frac{(e^{\theta u}-1)(e^{\theta v}-1)}{(e^{\theta}-1)}\right]$
	Gumbel	$\exp\{-[(-\ln u)^{-\theta} + (-\ln v)^{\theta}]^{\frac{1}{\theta}}\}$

Copula parameters estimation

The parameters for the candidate copula families were estimated considering the Maximum Likelihood Estimation (MLE) method, by choosing the Inference Functions from Margins (IFM) method [202]. The use of IFM method requires previous fitting of marginal distributions functions to transform the variables' values into the $(0, 1)$ interval.

Best fitted copula

To compare the bivariate copula models from a number of families and choose the best fitted model, the fit statistic AIC was used. First, all the candidate copulas, Gaussian, Student's t, Clayton, Frank, and Gumbel, are fitted using maximum likelihood estimation, MLE. Then the AIC is computed for all copula families and the one with the minimum AIC is chosen. According to Brechmann and Schepsmeier [43], for observations u_j and v_j with $j = 1, ..., N$, the AIC of a bivariate copula family $\mathbf{C}$ with θ parameter(s) is defined by Equation 8.5:

$$\text{AIC} = -2\sum_{i=1}^{N} \ln[\mathbf{C}(u_j, v_j \mid \theta)] + 2k \tag{8.5}$$

where one parameter copulas has $k = 1$ and the two parameter Student's t has $k = 2$. The two parameter copula is penalised in the minimisation of AIC value to reduce possibility of overfitting due to parsimony principle.

Bivariate return periods

In this subsection the concept of return period for events defined by their joint behaviour of pairs of random variables is introduced. This concept was applied to emphasise the particular facets of the dynamics of the considered NAOI — with particular emphasis on the negative phase of the NAO — and extreme rainfall phenomenon in Madeira Island. But first, some necessary concepts are mathematically described as follows.

Among the several definitions of return period, Shiau and Shen [408] describes it as the average elapsed time between occurrences of the event with a certain magnitude or greater than a threshold. The highest the return period the more exceptional the event is. The univariate return periods of NAOI and extreme rainfall, based on the concept of stochastic processes, are derived as follows. The return period — adapted from Shiau and Shen [408], Shiau [406], Kwon and Lall [227] — of the NAOI (T_{NI}) or extreme rainfall (T_{RN}), is expressed as function of the expected interarrival time $E(L)$ and of the cumulative distribution functions (CDF) of the NAOI, $F_{NI}(ni)$, and the extreme rainfalls, $F_{RN}(rn)$, as defined in Equations 8.6 and 8.7, respectively (marginal distributions). Note that in this case T and $E(L)$ are expressed in years. The $E(L)$ was obtained by dividing the 45 bivariate events (based on the chosen extreme rainfalls) by the 50 analysed years resulting in 0.9 year for each of the six rain gauges.

$$\text{T}_{NI} = \frac{E(L)}{P(NI \geq ni)} = \frac{E(L)}{1 - F_{NI}(ni)} \tag{8.6}$$

$$\text{T}_{RN} = \frac{E(L)}{P(RN \geq rn)} = \frac{E(L)}{1 - F_{RN}(rn)} \tag{8.7}$$

Assuming that the phenomenon here studied has a multivariate nature, the return periods of the bivariate distributed NAOI and extreme rainfall events were computed as joint and conditional return periods based on the works by Shiau [407] — but for drought analysis from a multivariate perspective in that case. Thus, the joint NAOI and extreme rainfall return period can be defined for $NI \geq ni$ and $RN \geq rn$, as described in Equation 8.8:

$$\text{T}_{NI\,\&\,RN} = \frac{E(L)}{P(NI \geq ni, RN \geq rn)} = \frac{E(L)}{1 - F_{NI}(ni) - F_{RN}(rn) + \mathbf{C}(F_{NI}(ni), F_{RN}(rn))} \tag{8.8}$$

where $\text{T}_{NI\,\&\,RN}$ is the return period for $NI \geq ni$ (NAOI) and $RN \geq rn$ (extreme rainfall).

Analogously, the conditional return period was calculated for the case when NAOI is the cause of extreme rainfall, i.e., the return period of extreme rainfall given that the previous NAOI is lower than a

certain threshold ($T_{RN|NI\geq ni}$). This conditional return period is calculated by Equation 8.9:

$$T_{RN|NI\geq ni} = \frac{T_{NI}}{P(RN \geq rn, NI \geq ni)} = \frac{E(L)}{[1 - F_{NI}(ni)][1 - F_{NI}(ni) - F_{RN}(rn) + \mathbf{C}(F_{NI}(ni), F_{RN}(rn))]} \tag{8.9}$$

Further discussion on the calculations and relationships between univariate, bivariate, and conditional return periods is out of the scope of this paper. However, this can be found in Shiau [407].

8.4 Results

The results are structured as follows. In Section 8.4.1, the characteristics and temporal distribution of the 45 winter extreme daily rainfalls, from 1 December to 28 February of the following year (DJF) during the considered 50 years (1967/1968–2016/2017), are shown at each of the six adopted rain gauges in Madeira Island. Then, in Section 8.4.2, the correlations between both, the non-smoothed ($m = 0$) and smoothed daily NAOI series (after applying a low-pass filter $m \geq 0$), and extreme daily rainfall events at AR-C (Areeiro rain gauge) are presented under the assumption that the NAO is the major stressor of extreme rainfall. Different running lengths, m, and time lags, l, are tested for the NAOI aiming at identifying the coupled series of previous NAOI and extreme rainfalls with maximum correlation. The m and l based on AR-C are then applied to the other five rain gauges, thus ensembling the final dataset with 45 bivariate observations at the six rain gauges in total. Subsequently, the overall strength of the association between previous NAOI and extreme rainfall is described. In Section 8.4.3, the estimation of the bivariate joint distributions along with the copulas' construction are shown. Finally, in Section 8.4.4, the results of the bivariate return periods based on the chosen copulas for the NAO and extreme rainfall phenomena are presented.

8.4.1 Extreme daily rainfall distribution analysis

The analysis of the winter from December to February (DJF) extreme daily rainfalls from 1967/1968 through 2016/2017 at the representative rain gauges indicates a particularly differentiated distribution of extreme events over Madeira. The highest daily rainfall values ($\geq$ 200 mm) are systematically recorded at the island's central highlands and plateau, i.e., at the AR-C (Areeiro) and BC-C (Bica da Cana) rain gauges (Figure 8-2**a**). The lowest extreme daily rainfalls ($\leq$ 50 mm) occur in the coastal southern, eastern, and western areas (approximately 60.0 m.a.s.l.), namely, at FO-S (Funchal Observatório), SC-E (Santa Catarina), and PP-W (Ponta do Pargo). The remaining rain gauge, i.e., PD-N (Ponta Delgada) in the northern slope displays a mixed distribution (50–150 mm). Furthermore, Figure 8-2**a** shows a concentration of highly extreme rainfalls from all the six rain gauges — including their corresponding maximum historic records in most cases — during the years 2010 and 2011. From the same figure, the comparison between the maximum values and the lowest ones, suggests that the sharp topography of the island has a major role in the extreme rainfall distribution. However, when making the extreme rainfalls dimensionless, by dividing by the corresponding averages, as represented in Figure 8-2**b**, the different

series show a similar behaviour, i.e., a similar temporal variability around the average, with the most extreme occurrences also concentrated in the winter of 2009/2010 and 2010/2011.

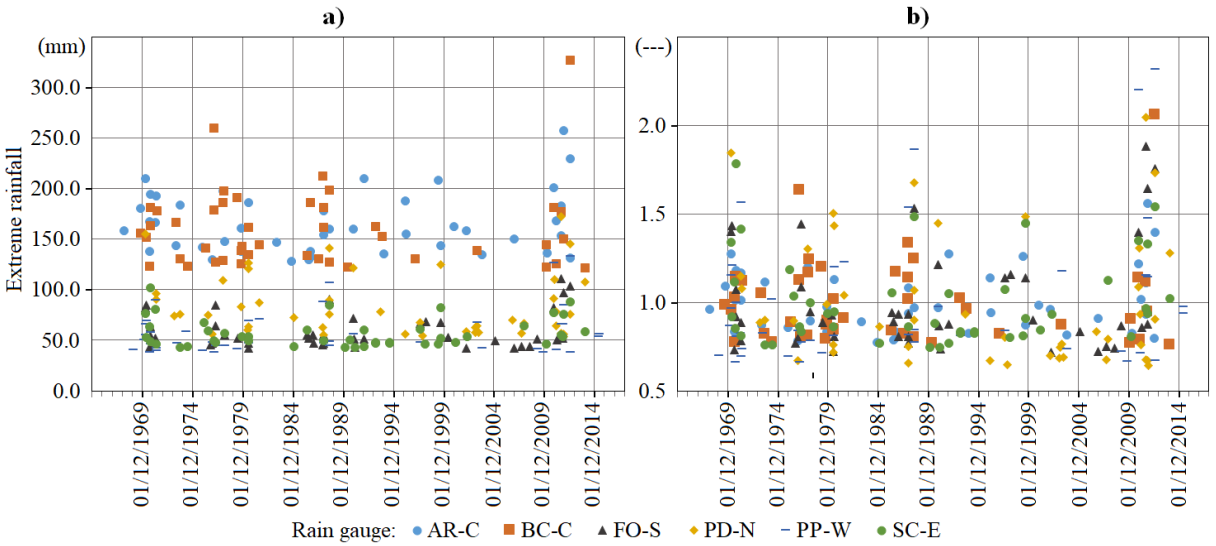

Figure 8-2: The winter (DJF) extreme daily rainfalls, i.e., the highest 45 rainfalls or 1% of the retrieved 4,500 daily data at each rain gauge from 1967/1968 through 2016/2017, in absolute (**a**) and dimensionless (**b**) terms.

8.4.2 Alignment of the NAOI and extreme rainfall series

The analysis between (i) smoothed and lagged NAOI values and (ii) extreme rainfall events was inspired by the extreme rainfall event of 20 February 2010 that triggered deadly debris flow occurrences in Madeira [140]. The daily rainfall records of that event were assigned to 9:00 am of the next day. A preliminary analysis of the NAOI suggested that such event could be teleconnected to the persistence of strongly negative values in previous days. Figure 8-3 exemplifies an extract of the non-smoothed (1d) and smoothed NAOI values — from 2 days (2d) to 30 days (30d), i.e., low-pass filter m from 2 to 30, respectively — from December 2009 to February 2010. In the figure, consecutive negative NAOI values can be observed in the first days of January 2010.

As mentioned, the effect of smoothed previous NAOI values on extreme rainfall events was assessed for the candidate rain gauge of Areeiro (AR-C) aiming at developing a criterion to align the bivariate series which was then applied to the other rain gauges. AR-C has almost complete historic daily data and some of the island's heaviest rainfall records, such as those that triggered the "*aluviões*" (debris flows) on 20 February 2010. This assessment ascertained an alignment or cause-effect between the X (smoothed and lagged NAOI) and Y (extreme rainfall) series by maximising the Pearson correlation applied to the 45 selected extreme rainfall events at AR-C (depicted in Figure 8-2**a**). This made possible to identify (i) the running length, m, of the low-pass filter of daily NAOI records, and (ii) the lag in days, l, between the end of the smoothed NAOI series and the extreme rainfalls that occurred after that end.

As a result of the previous analysis, a maximum value of $r = -0.84$ for the Pearson correlation coefficient was obtained based on the low-pass filter of $m = 14$ (14d) averaged NAOI values, ending 39 days prior to the extreme rainfalls events — depicted in Figure 8-4. For m values lower and higher than

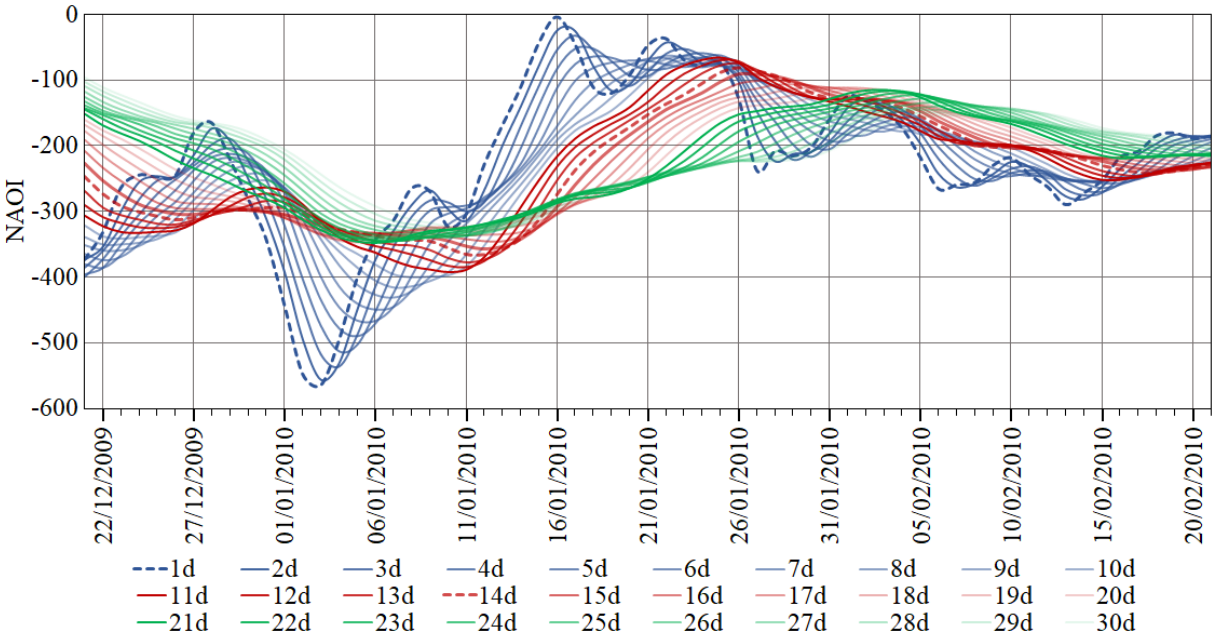

Figure 8-3: Example of the non-smoothed (1d) and smoothed daily NAOI series in a period prior to the 20 February 2010 flash floods, landslides and debris. The smoothed NAOI values were computed by a low-pass filter, or moving average, from the previous 2 days (2d, $m = 2$) to previous 30 days (30d, $m = 30$) and assigned to the most recent record date.

14, but also for l shorter and longer than 39 days, the correlations between coupled NAOI values and extreme rainfalls yielded no statistically significant improvement.

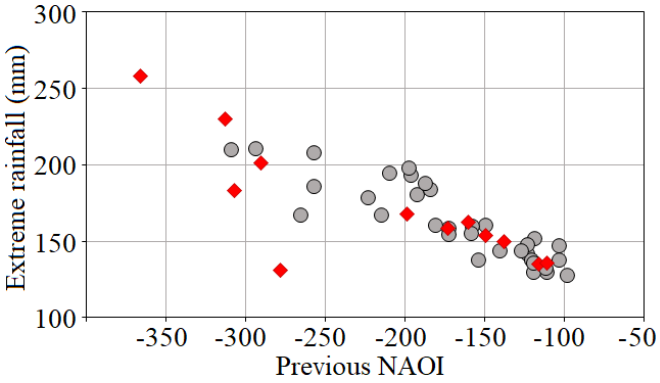

Figure 8-4: Scatter plot of previous smoothed NAOI and extreme rainfalls, both at daily scale, for $m = 14$ and $l = 39$ days. The 45 bivariate observations (1967/1968–2016/2017) at the AR-C rain gauge are depicted by bullets and red diamonds, being the latter the events occurred between December 2000 and the end of the reference period. The correlation (r) between previous NAOI and extreme rainfalls is -0.84.

In order to establish the final dataset for teleconnection via copulas, the same $m = 14$ and l=39 days for NAOI — hereafter previous NAOI — were adopted at the other rain gauges, rather than repeating the analysis for each of them. The main purpose of this was to conclude to what extent the results obtained based on AR-C could be adopted over the island, thus simplifying further analysis on the effect of the NAO persistence over the rainfall regime in Madeira. Albeit based on the same m and l, the previous NAOI values assigned to the extreme rainfalls may differ among rain gauges because of the different dates of occurrence of those events.

The copulas modelled in this research work corresponded to *all the variables being independent* [374]. This is the copula type of any random vector established by independent variables. The elements of the extreme rainfall series may, in practice, be assumed to be independent [492]. In some cases, however, there may be significant dependence among extreme values although they are random in a series. Conversely, independence implies that no observation in the data series has any influence on any following observations. In this regard, the independence of the univariate vectors of previous NAOI and extreme rainfalls was evaluated via the Wald-Wolfowitz runs test having the null hypothesis H_0 of independence with 0.05 as critical value. The null hypothesis was tested at the six stations resulting in $p-$values ranging from 0.31 to 0.97, for previous NAOI, and from 0.11 to 0.79, for extreme rainfall. Being these results greater than the critical value, it was not possible to reject the H_0 of independence in any case.

8.4.3 Bivariate joint distributions and constructed copulas

Before showing the dependence modelling of the two random variables via copulas, the resulting descriptive statistics of the bivariate series are presented in Table 8.3. Because the values of the previous NAOI are always negative, in the copulas models, NI refers to their opposites. Additionally, given that the number of extreme rainfalls events and of analysed years are the same for the six rain gauges, the resulting $E(L)$ is also the same (0.90). The Kendall's τ correlation coefficient presents a high negative value for AR-C which is in accordance with the visible dependence in the scatter plot set out in Figure 8-4, and with the Pearson correlation (r). Still, Kendall's τ measures only the overall strength of the association between previous NAOI and extreme rainfall, but does not provide with accurate information about how this association varies across the distribution [459]. The mean values of extreme rainfall suggest similar characteristics at the central highlands (AR-C and BC-C) with higher values than on the lowlands (e.g., FO-S and PP-W) as previously identified (Section 8.4.1). Concerning the mean of previous NAOI, values are homogeneous in the six series. Note that the most negative previous NAOI (Min of -366.03) always appears in the coupled series. Such value resulted from consecutive strongly negative NAOI in the first days of January 2010 (Figure 8-3) that were assigned to the rainfalls on 20 February 2010. The previous assessment is somewhat unclear since it is based on a univariate perspective which justifies a copula-based characterisation of the bivariate dependency structure.

Table 8.3: Statistics of the bivariate observations (previous NAOI and extreme rainfall) at each rain gauge from 1967/1968–2016/2017. $E(L)$ is the expected interarrival time, and Kendall tau (τ) correlates the two variables.

Rain gauge	Number of observations	$E(L)$ (year)	Kendall tau (τ)	Previous NAOI, $-NI$				Extreme rainfall (mm), RN			
				Mean	Min	SD	CV	Mean	Max	SD	CV
AR-C	45	0.90	-0.71	-183.31	-366.03	69.42	-0.38	165.00	257.60	29.64	0.18
BC-C	45	0.90	-0.51	-185.08	-366.03	58.52	-0.32	159.03	327.30	39.19	0.25
FO-S	45	0.90	-0.50	-174.85	-366.03	78.25	-0.45	58.94	111.00	17.65	0.30
PD-N	45	0.90	-0.29	-177.44	-366.03	70.70	-0.40	84.03	172.10	30.37	0.36
PP-W	45	0.90	-0.27	-173.34	-366.03	80.92	-0.47	57.53	133.30	22.20	0.39
SC-E	45	0.90	-0.42	-180.94	-366.03	72.98	-0.40	57.16	101.90	14.21	0.25

The bivariate joint distributions between previous NAOI and extreme rainfall were determined to

model copulas for teleconnection aiming at obtaining the corresponding return periods. One copula function was selected for each rain gauge as indicated in Section 8.3.3. Table 8.4 reports the selected copulas for the bivariate series based on the marginal distributions of previous NAOI and extreme rainfall. The estimated parameters and values of the goodness-of-fit test (AIC) for the best-fitted copulas and marginal distributions are listed in the same. The selection of marginals for the individual variables (log-normal in most cases) allowed to model the dependence structure via copulas. Only AR-C and SC-E have the same selected copula family, i.e., Survival Gumbel, whether different copulas were assigned to the other four rain gauges. This means that the joint bivariate characteristics and their dependence are distinct among the regions of the island, thus, need specific copulas to be modelled.

Table 8.4: Selected copula families, Kendall tau (τ), univariate distributions used for candidate of marginal distributions of NI and RN, and parameters of the models at each rain gauge. Par stands for the copula parameter, and Par1 and Par2 for the marginal distribution parameters.

Rain gauge	Copula				Opposite previous NAOI, NI				Extreme rainfall, RN			
	Family	Par	τ	AIC	Univariate dist.	Par1	Par2	AIC	Univariate dist.	Par1	Par2	AIC
AR-C	Survival Gumbel	3.28	0.70	-66.61	log-normal	5.15	0.36	502.09	log-normal	5.09	0.17	429.61
BC-C	Frank	4.90	0.45	-18.91	log-normal	5.17	0.30	490.18	log-normal	5.05	0.21	445.14
FO-S	Student's t	0.63	0.44	-27.18	log-normal	5.07	0.42	509.67	log-normal	4.04	0.26	374.56
PD-N	Gumbel	1.38	0.28	-9.53	log-normal	5.10	0.39	506.36	log-normal	4.38	0.32	423.23
PP-W	Gaussian	0.50	0.33	-10.79	Weibull	2.32	196.04	522.39	log-normal	4.00	0.31	387.31
SC-E	Survival Gumbel	1.69	0.41	-16.43	log-normal	5.12	0.39	508.15	log-normal	4.02	0.22	357.72

The copula $\mathbf{C}_{U,V}$ that best describe the observed dependence patterns between normalised values of previous NAOI, U, and of extreme rainfall, V, are presented as contour lines in Figure 8-5. The normalisation of values was done for allowing direct comparisons among the multivariate normal shapes of the rain gauges' observations and bringing out specific features, such as the dependence measure of tail dependence [43]. This allowed to determine the level of association among extreme events in the lower and upper tails for previous NAOI and extreme rainfall, respectively. In this case, the previous NAOI lower tail corresponds to strongly negative previous NAOI values and the importance of this association lies in the fact that negative NAOI values have been connected to impacts on regional climate variability during winter [e.g. 191].

Figure 8-5 shows that Survival Gumbel copula (the rotated Gumbel copula) best-fitted the bivariate series at AR-C and SC-E rain gauges with a stronger dependency in the lower tail of previous NAOI and in the upper tail of extreme rainfall. On the other hand, the PD-N series presented a Gumbel copula with an inverted dependence structure. The copulas for FO-S and PP-W are of the same class, i.e., meta-elliptic copulas (Table 8.2), although with different dependence structure. The joint distribution at FO-S was modelled with Student's t copula by generating joint symmetric tail dependence, hence allowing an increased probability of joint extreme events. For the series at PP-W the Gaussian copula was used by generating joint symmetric dependence, and, according to the copula's characteristics, with no tail dependence, i.e., no joint extreme events. For BC-C, the goodness-of-fit test resulted in well-fitted Frank copula being symmetric and with more probability concentrated in the tails, however, without neither lower nor upper tail dependence. Rather than from just a linear correlation analysis, these results robustly evidence different dependence structures between previous NAOI and extreme rainfall across the island.

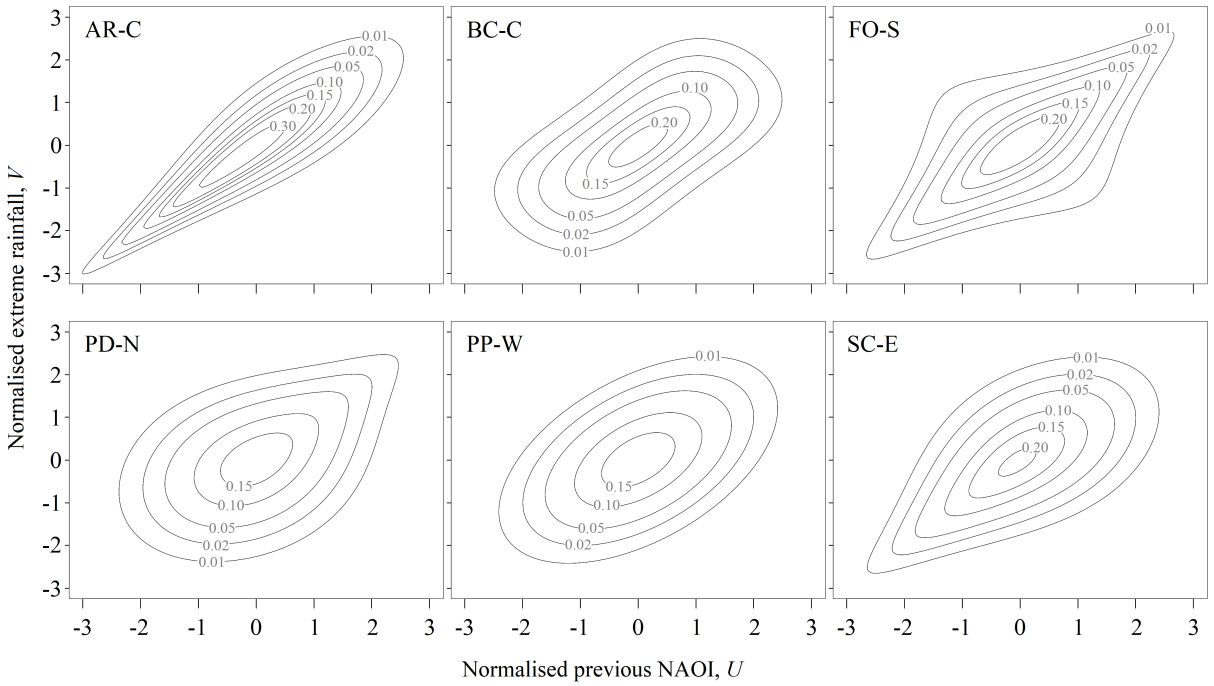

Figure 8-5: Normalised contour plots of the selected bivariate copulas, namely of: Survival Gumbel (AR-C and SC-E), Frank (BC-C), Student's t (FO-S), Gumbel (PD-N), and Gaussian (PP-W).

8.4.4 Bivariate return periods of the previous NAOI and extreme rainfall events

The return periods $\mathrm{T}_{NI\,\&\,RN}$, defined by Equation 8.8, of the 45 coupled events depending upon the modelled joint behaviour of the two random variables at each rain gauge are shown in Figure 8-6. Those with the highest return periods $\mathrm{T}_{NI\,\&\,RN}$ are reported in Table 8.5. Since various combinations of previous NAOI and extreme rainfall can result in the same $\mathrm{T}_{NI\,\&\,RN}$, the return periods are presented as contour lines in the figure. These lines are bounded by the axes and denote different patterns regarding the location of the rain gauge on the island. As an illustrative example, a combination of previous NAOI of -200 and a daily rainfall of 100 mm results in $\mathrm{T}_{NI\,\&\,RN} \approx 3$ years at the central highlands (AR-C and BC-C), $\mathrm{T}_{NI\,\&\,RN} \approx 90$ years on the southern lowland (FO-S), $\mathrm{T}_{NI\,\&\,RN} \approx 9$ years on the northern slope (PD-N), $\mathrm{T}_{NI\,\&\,RN} \approx 25$ years in the western area (PP-W), and $\mathrm{T}_{NI\,\&\,RN} \approx 450$ years in the eastern region of the island (SC-E).

Figure 8-6 also presents the bivariate events differentiating those from the initial 33-year subperiod, from December 1967 to February 2000, to the ones from the final 17-year subperiod, from December 2000 to February 2017. For the initial subperiod, this differentiation resulted in 33, 36, 32, 26, 32, and 35 extreme events for AR-C, BC-C, FO-S, PD-N, PP-W, and SC-E, respectively; and consequently for the final subperiod in 12, 9, 13, 19, 13, and 10 events. By dividing the number of events by the number of years of their respective subperiod, interarrival times different to the one used to construct copulas were obtained. A comparison of the $E(L)$ between the two subperiods revealed that for all the rain gauges, except for PD-N, $E(L)$ decreased, meaning less frequent extreme rainfall events in the last 17 years.

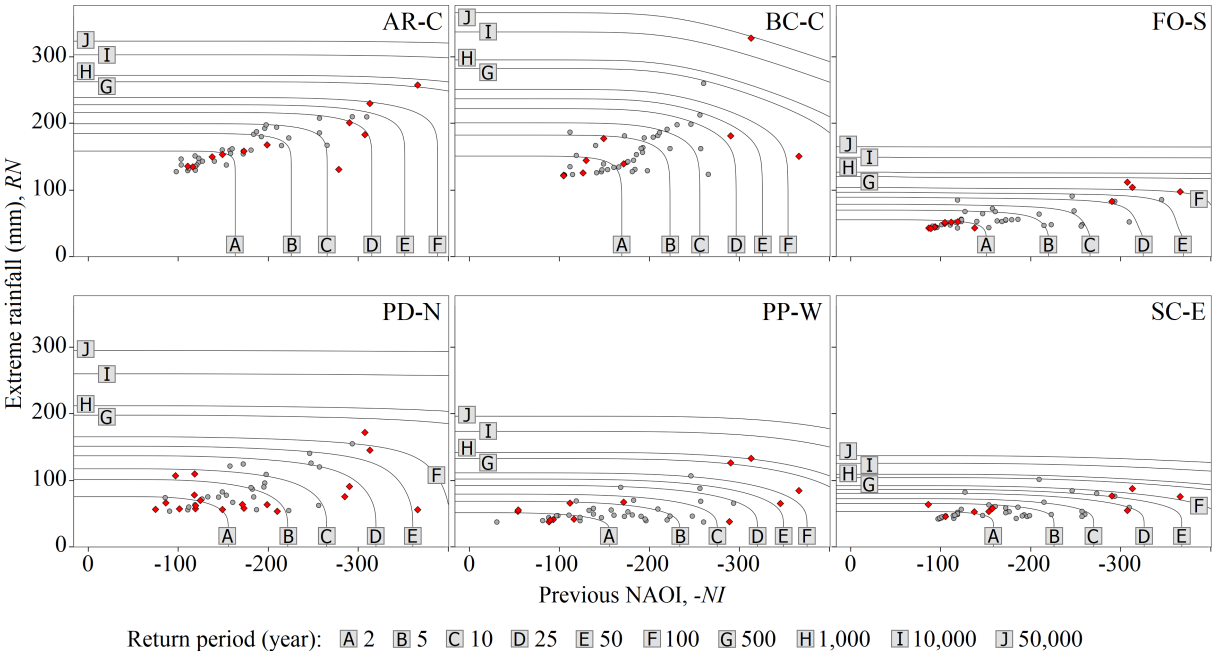

Figure 8-6: Contour lines of the joint return periods $T_{NI\,\&\,RN}$ of the 45 bivariate events in each rain gauge. The letters from A to J, stand for the different return periods between 2 and 50,000 years. The events occurring from 1967/1968 to 1999/2000 are depicted by grey bullets, and those from 2000/2001 and 2016/2017 by red diamonds.

However, the figure shows that the most extreme bivariate events with higher return periods, except for SC-E, always took place in the more recent subperiod.

Figure 8-7 depicts the conditional return periods i.e., the return period of extreme rainfall given that the previous NAOI is lower than a certain threshold. Note that, the horizontal axes are always the same but the vertical axes are not. Moreover, some of the more exceptional bivariate events of Table 8.5 are not depicted in the figure due to the adopted vertical scales. For uniformity purposes, the reported events are those with the highest return periods associated to $T_{NI\,\&\,RN}$ as previously mentioned. By way of example, for AR-C, regardless the return period approach, the most unusual event occurred in February 2010 with previous NAOI of -366.0 and extreme rainfall of 257.6 mm. The univariate analysis, based on the best fitted marginal distribution and Equations 8.6 to 8.7, resulted in return periods of 491 and 2,646 years, respectively. From the multivariate analysis, the joint return period (Equation 8.8) is 4,407 years whereas the conditional one (Equation 8.9) corresponds to 259,894 years.

In general terms, the achieved univariate and bivariate return periods from December 1967 to February 2017 show that the island has been characterised by numerous events with an unsteady chronological development particularly with highly negative previous NAOI and more intense extreme rainfalls in earlier years. Based on the results shown in Figure 8-6 coupled with those reported in Table 8.5, from December 2010 to February 2011 the persistently negative phase of the NAO (in this case previous NAOI) is according to the assumptions made for the bivariate problem in generating highly winter daily extreme rainfalls across Madeira. These observed extreme rainfall patterns can be attributed — among other atmospheric processes — to the leading pattern of climate variability over the Northern Hemisphere, i.e., to the NAO variability, however.

Table 8.5: At each of the six rain gauges, dates and characteristics of the three bivariate observations (previous NAOI and extreme daily rainfalls) with the highest return periods $T_{NI\,\&\,RN}$ and their corresponding univariate, bivariate, and conditional return periods rounded to the nearest integer in years.

Rain gauge	Date $T_{NI\,\&\,RN}$	Previous NAOI, $-NI$	Extreme rainfall (mm), RN	T_{NI} (year)	T_{RN} (year)	$T_{NI\,\&\,RN}$ (year)	$T_{RN\|NI\geq ni}$ (year)
AR-C	21/02/2010	-366.0	257.6	491	2,646	4,407	259,844
	26/01/2011	-313.0	230.0	180	422	674	14,560
	05/12/1991	-309.4	210.0	169	129	293	5,922
BC-C	26/01/2011	-313.0	327.3	278	44,618	324,643	10,843,673
	15/12/1976	-260.2	259.6	82	1,175	3,010	29,683
	21/02/2010	-366.0	150.4	1,009	15	1,072	129,742
FO-S	02/02/2010	-307.4	111.0	143	1,600	1,991	34,109
	26/01/2011	-313.0	103.4	156	758	1,011	18,887
	21/02/2010	-366.0	96.8	355	401	787	33,537
PD-N	02/02/2010	-307.4	172.1	152	1,034	1,525	27,882
	01/01/1969	-293.4	155.2	120	449	742	10,721
	26/01/2011	-313.0	145.5	167	279	598	12,010
PP-W	26/01/2011	-313.0	133.3	160	3,794	7,975	153,443
	27/02/2009	-290.3	126.6	100	2,295	4,157	49,821
	21/02/2010	-366.0	85.0	585	107	1,348	94,663
SC-E	10/02/1969	-209.4	101.9	29	2,642	3,420	12,027
	26/01/2011	-313.0	88.0	151	432	1,517	27,517
	21/02/2010	-366.0	76.0	364	104	1,031	45,060

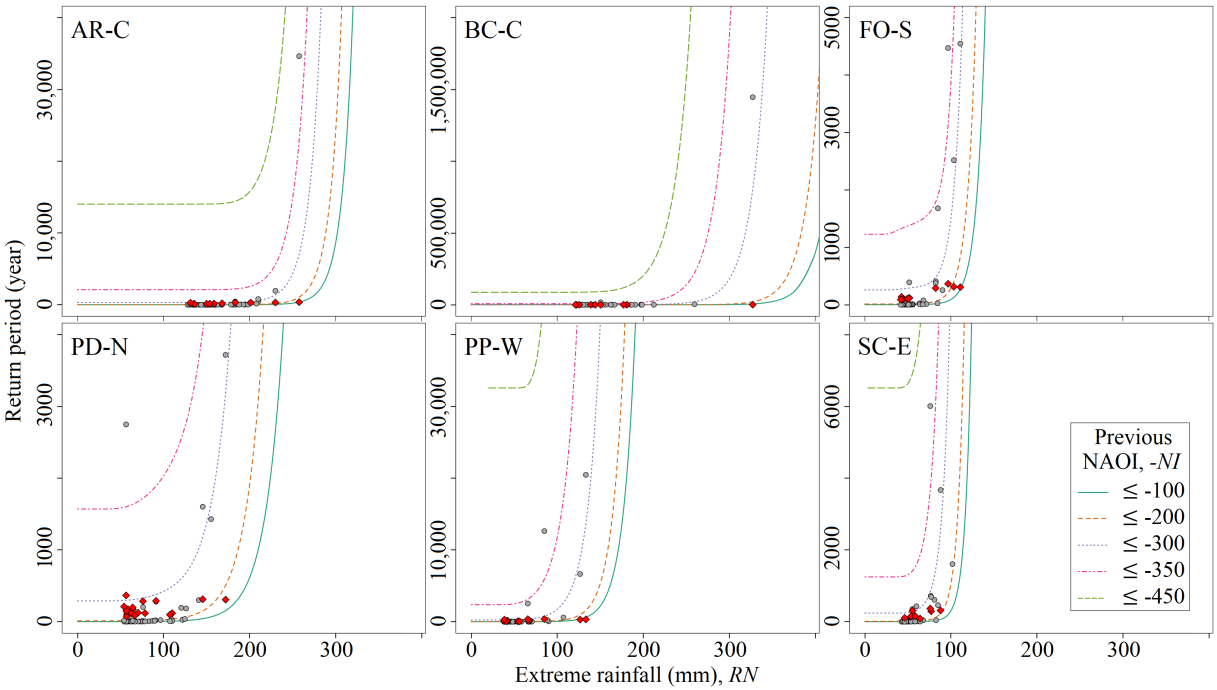

Figure 8-7: Conditional return periods $T_{RN|NI\geq ni}$ for different previous NAOI values. The bivariate observations from 1967/1968 to 1999/2000 are depicted by grey bullets, and from 2000/2001 and 2016/2017 by red diamonds.

8.5 Discussion and conclusions

The influence of the NAO large-circulation pattern on 45 winter (DJF) extreme rainfalls (from December 1967 to February 2017) was examined at daily scale for six rain gauges with apparently distinct micro-climates and rainfall variability due to their location in Madeira Island, i.e., in the northern, southern, eastern and western coastal zones, and in the central highlands. This influence was addressed by using an index, selected among others [201], capturing representative daily spatio-temporal-dependent features associated with the pattern in SLP over the North Atlantic sector or with the NAO pattern, i.e., daily NAOI, coupled with daily rainfall records. Accordingly, this research work delineates a systematic analysis of the jointly modelling of NAOI for the same day or prior to the occurrence of extreme rainfall events via bivariate copulas. To do so, in the initial stage of this research work, the cause-effect degree between (i) non-smoothed and smoothed NAOI values and (ii) extreme daily rainfall events was measured. This process enabled the ensemble of the final dataset representing the core for copula modelling describing the dependence characteristics of the analysed bivariate problem. The copula modelling also ascertained long-distance relationships between random events of previous NAOI and extreme rainfall on the island, i.e., teleconnections, specifically used for the calculation of bivariate return periods, and thus making a climate variability assessment.

8.5.1 Negative NAO persistence and climate variability

Despite the shifts in the NAO do not necessarily create simultaneous, symmetrical rainfall imbalances or anomalies, this research work ascertained an atmospheric configuration resulting in strongly negative Pearson correlation (r) for the bivariate coupled events for the Areeiro rain gauge. Note that all the previous NAOI values associated to the 45 extreme rainfalls at each rain gauge were negative (plotted in Figure 8-6) and part of negative NAO phases, i.e., of weaker than usual differences in pressure [131]. This reinforces the hypothesis that during winter — the time when the NAO pattern is very strong and broadly extended [201] — the impacts on climate variability are produced mainly by persistent figures of negative NAO.

The correlation (r) between previous NAOI and extreme rainfall is consistently below than -0.50, except for the northern slope, namely, -0.84 (AR-C), -0.58 (BC-C), -0.69 (FO-S), -0.48 (PD-N), -0.52 (PP-W), and -0.52 (SC-E). Although the correlation always portraits a symmetrical association, it differs among rain gauges, suggesting different extremal rainfall behaviour. Additionally, a comparison was done between the ratios of long-term rainfall average of the 4,500 daily rainfalls (11.36, 11.68, 3.04, 4.67, 3.44, and 3.21 mm, respectively for AR-C, BC-C, FO-S, PD-N, PP-W, and SC-E) and their respective mean extreme values (reported in Table 8.3). Accordingly, this revealed that greater ratios characterised the coastal zones highlighting their greater vulnerability to extreme rainfall events from 1967/1968 through 2016/2017 than the central highlands which, however, experienced high heavy rainfall. This indicated — and confirmed later with the copula modelling — that the studied bivariate phenomenon or climate variability in the assembled dataset has marked inter-island variation.

8.5.2 Copula-based modelling of NAO teleconnection in extreme rainfall

The preliminary results indicated that the inter-annual variability of extreme winter rainfall — which is often high on small islands as on Madeira [123] — was largely modulated by the NAO mode. Such noticeable influence on extreme events required a multidimensional analysis of the random variables. The modelling of dependence structure conventionally assumes directly or indirectly linear correlation given through the Pearson correlation coefficient, r [217]. However, as mentioned, the studied NAO phenomena is particularly complex and a combination of different stochastic processes. Thus, a bivariate approach [415] using copulas was used in each of the rain gauges to skirt these constraints by allowing the independently modelling of univariate marginals and of non-linear dependence structure between two vectors. Additionally, the copulas were adopted due to their flexibility and the various types of dependence that they allow for, and because they do not depend on the marginal distributions F_X and F_Y [113, 1]. To measure the association among the random variables, the Kendall's τ correlation coefficient was used instead to overcome the shortcoming of the r coefficient. The τ coefficient varied from strong (at AR-C) to moderate for the bivariate observations (see Table 8.3). The difference in τ correlation may be due to the model establishment (based on a single rain gauge, AR-C) but also to internal climate variability or other sources of rainfall variability across the island. In any case, to build a copula, the degree of association in some way must be assessed [63] but keeping in mind that the resulting copulas are conditional upon to the array used. Note that negative correlations affect the types of copulas that can be employed in this study, as some copulas exist only in the positive dependence space. To circumvent this hurdle and not double the number of copulas in the analysis (e.g., by including rotated versions of Archimedean copula families), the copulas were modelled with opposite previous NAOI series (NI), instead of the negative series.

8.5.3 Climate variability assessment based on the bivariate return periods

The return periods achieved using copulas highlight the importance of modelling the joint behaviour of previous NAOI and extreme rainfall. The bivariate modelling may simplify the calculations, and unveil the mechanism of structure-dependent behaviour of the phenomena of interest. From the analysed joint events, well-defined marginal probability distributions were established which in turn, allowed calculating the joint probability and thus estimate contour lines of the return period. This adopted bivariate approach contrasts with those traditionally implemented for assessing bivariate return periods of specific extreme hydrological events. As an example, Kim et al. [222] assess the hydrological risk based on univariate and multivariate density functions, although the authors state that the joint density is not mathematically manageable. Additionally, a comparison of the joint and conditional return periods to those separately calculated (Table 8.5), shows that univariate approaches may underestimate the risk related to specific events. Therefore, the multivariate analysis seem to have advantages over univariate applications by defining a more complex dependence structure closer to reality. Nevertheless, it is acknowledged that future work should quantitatively investigate the integration of another large-scale circulation pattern — such as El Niño Southern Oscillation (ENSO) [425] — to the climate variability assessment for a more

dynamical analysis [e.g. 217, 192], and for addressing the remarkable transition toward a warmer winter climate regime, i.e., sustained higher GTS [436, 215].

Detecting variations in extreme rainfall series and the large-scale modes that generate those variations are crucial to identify climate variability which is generally characterised by anomalous extreme events. Such anomalies clearly outnumber the bivariate long-term average as demonstrated in the current analysis. Figure 8-6 (and also Figure 8-7, although with truncated vertical axes) covers most of the results obtained with coherent response and relationships at different degrees between extreme rainfall patterns with respect to the previous NAOI. These also show that as the previous NAOI gets more negative, the return period curves are more dependent on the development of this index. That is, for a given extreme rainfall, its return period is constant or almost constant for the higher NAOI values. As the previous NAOI values become more negative, the return period can increase substantially as a result of the exceptionality of the bivariate event. This strongly suggests that previous NAOI (i) is the main trigger of the winter (DJF) extreme daily rainfalls, and that (ii) contains information regarding the antecedent atmospheric conditions. These results clearly show that the identified DJF extreme rainfalls can be associated with changes in the previous NAOI signal — further reading on the dynamic mechanisms of extreme rainfall and the negative phase of NAO in Madeira can be found in [119]. Moreover, the same figures depict the noticeable increase in intensity in the joint behaviour of previous NAOI (highly negative) and extreme rainfall in earlier years. These results are corroborative evidences of increased climate variability in Madeira accompanied by remarkable increase in variability in the NAO, specifically toward the persistence of a negative winter NAO, from ca. early 2000's on — as identified by Taws et al. [436], Hanna et al. [172], Hanna and Cropper [171].

8.5.4 Challenges and advances related to extreme rainfall analyses

The remarkable identified bivariate events of winter 2009/2010 and 2010/2011 (some of the most intense events ever recorded) further emphasise the challenges for climate variability assessment for the small island of Madeira. Note that small island environments are highly vulnerable to natural disasters such as cyclones and storm surges. They are also susceptible to flash floods, landslides and debris flows as a result of extreme rainfall [123]. It is therefore, essential to study variability of extreme rainfall at shorter time scales along with atmospheric observations from a multivariate perspective. This in turn may help to understand the atmospheric physics and the mechanisms that can shift a heavy rain event into one producing floods on the island. Even though the teleconnection based on copulas is not well-established for all the analysed rain gauges, it is still essential for planning water-related activities considering the vulnerability of the island to large-scale climatic variations.

Chapter 9

Conclusions and Further Developments

This thesis addresses the problem of climate-induced changes in hydrological extremes, long-term variability and trends in terms of magnitude and frequency. The core of the research — whose results are here summarised — is presented in Chapters 3 to 8 and includes variable selection, rainfall data preparation, gap-filling techniques, rainfall trend analysis, drought characterisation, heavy rainfall modelling, and teleconnection in the Portuguese small island of Madeira. The analysed period spans from 1937/1938 to 2016/2017. Besides rainfall data, other climatological data are utilised, namely, the mathematical definitions of the North Atlantic Oscillation (NAO) and of the El Niño Southern Oscillation (ENSO). Additionally, to tackle the issue of long-term trend in a continental scale, i.e., in mainland Portugal, a study on rainfall trends assessment, from 1913/1914 to 2018/2019, is presented in Appendix A.

9.1 Summary of results

Six peer-reviewed studies looking at the climate-induced changes in Madeira Island — from rainfall trends to hydrological extremes such as droughts and heavy rainfall — have been published during the preparation of this doctoral thesis. The result is mounting evidence that current rainfall trends are raising the risk of some types of hydrological extremes, especially those linked to sustained decreasing conditions such as droughts. On the other hand, extreme rainfall events as heavy rainfall, rather than becoming more frequent they are growing more intense.

The considered timescales and reference periods aim at highlighting extreme events from a particular period or season. Note that most of the results regarding Madeira Island, when possible, are compared to other authors' published material, despite the latter are not as comprehensive — to the best of the author's knowledge — as the results achieved in this thesis. In addition, the mapping of results includes different types of studies from rainfall to conceptually correlated climate variables. Different rainfall maps are available in Chapters 3, 4, and 5. Climate regionalisation based on factor analysis applied to the Standardized Precipitation index (SPI) for drought characterisation is shown in Chapters 5 and 6, and to the rainfall field in Chapter 7 — suggesting that there are three representative climatic homogeneous regions in the island, i.e., the northern and southern slopes, and central region. Novel representations of

the relationship between seasonal and annual trends of the NAO and rainfall are covered in Chapters 3 and 4. Finally, the seemingly abstract concept of changes in the NAO and climate variability linked to heavy rainfall measurements is addressed in Chapters 7 and 8 based on proposed teleconnections.

9.2 Overarching conclusions

Combining the previous results with the published studies over the past sixty years, provides evidences that in Madeira Island (1) seasonal rainfall — e.g., winter and annual rainfall — has shown a gradual decrease since the late 1960's with the uncertainty regarding to whether rainfall will continue to decrease or it will counterbalance the already experienced rainfall deficits; (2) the variability of seasonal and annual rainfall is highly correlated with the large-scale atmospheric circulation pattern of NAO; (3) droughts in the island have become worse and more linked to ENSO than in the past; and that (4) heavy rainfall is clearly intensified by the persistent changes in the NAO mainly during negative NAO phases. The previous aspects are detailed in the next sub sections.

9.2.1 Rainfall trends and change-point detection

A comprehensive characterisation of the rainfall trends at different time-spans in Madeira Island, from short durations to the year, to identify shifts in the temporal patterns of the rainfall series has been done based on rainfall data at 41 rain gauges. In general, from the 1970's on, Madeira's climate is becoming drier with well-established decrease of the rainfall in the central region and northern slope. Only a narrow coastal strip of the southern slope presented upward trends. It should be noted that although the rainfall amounts vary widely from one rain gauge to another, the rainfall trends denote a spatial regularity. These findings are in line with numerous studies based on outputs of Global Climate Models (GCMs) in other latitudinal locations suggesting seasonal and annual rainfall decreases under global warming.

Rainfall variability is an active process, thus, to more accurately characterise the rainfall regime and detect its changes, it is necessary to have long and updated rainfall data — as systematically addressed for Madeira Island. Despite the statistical significant results obtained, it is uncertain whether the pronounced decreasing rainfall trends in recent years can be considered as lasting or not.

9.2.2 Regional rainfall response to the North Atlantic Oscillation

The NAO is one of the most important large-scale modes of atmospheric circulation in the Northern Hemisphere and particularly associated with rainfall variability [195]. Significant associations have been ascertained with strong negative correlations between changes in the rainfall and in the NAO index (NAOI) displayed for Madeira in all the trimesters of the wet semester [73]. A strong relationship between NAOI and rainfall changes has been also observed at annual scale. Thus, changes in NAO seem to be inextricably linked to those observed in rainfall of the small island. This may be attributable to NAO impacts on trade winds [147] corresponding to higher rainfall amounts on windward slopes when such winds are stronger. Consequently, the spatial variation in rainfall trends of Madeira may be explained by its high dependence on the dynamic interaction of the trade winds with the island's morphology. Recently,

strong positive NAOI phases have been associated with weaker trade winds [183] and drier conditions, specifically with the downward rainfall trends of Madeira's wet season. This teleconnection represents a solid basis to explain the climate change effects on the island's rainfall, suggesting that changes of the NAO climatic driver can be directly linked to the rainfall trends[1].

9.2.3 Spatio-temporal characterisation of droughts

Accordingly, the northern slope and particularly the central region currently denote recent higher number of periods under drought conditions, while the southern slope featured more frequent droughts in the past. Additionally, the study of bivariate copulas for drought characterisation revealed that — based on the SPI related to early signs of streamflow shortfalls, i.e., on the SPI6 — the northern slope and central region have experienced in recent years more exceptional drought episodes according to the joint distribution of drought duration and drought magnitude while the southern slope denoted more exceptional events in the past. Combining the results from the KORE and bivariate copulas shows strong evidence that the island, especially its central part, is currently in the midst of the worst drought ever registered which started around the year 2010–2011. Special attention is given to the previous region due to its relevance for the island's water security, as main region for the replenishment of the groundwater reservoirs. This highlights the fact that the three identified regions should be considered separately for an improved water resources management under drought conditions in Madeira, and for a better understanding, prevention, and mitigation of the consequences of future drought events.

9.2.4 Effects of the North Atlantic Oscillation on extreme rainfall

The cross-extremogram determined the dependence between the upper tail of the weighted regionalised rainfalls, and the upper and lower tails of daily NAOI. The statistics of the three weighted regionalised rainfall series indicate that the response of maximum daily rainfall to the NAOI dominance has an alternating structure. The fact that this alternating behaviour is found in the three regions in Madeira is indicative of the important effect of the NAOI lower tail (with negative figures regarded as –NAOI) rather than the NAOI upper tail (with positive values regarded as +NAOI) on extreme rainfall events. This suggests that particularly attention should be given to the negative NAOI and its effects on the extreme rainfall development in Madeira. This suggests systematic evidence of statistical dependence over Madeira between exceptionally –NAOI records and extreme rainfall which is stronger in the –NAOI dominance subperiods. The extremal dependence for +NAOI records is only significant in recent years, however, with a still unclear +NAOI dominance.

This is reinforced by the bivariate joint distribution analysis of daily rainfall series and NAOI, strongly suggesting that previous –NAOI (i) is the main trigger of the winter (DJF) extreme daily rainfall, and that (ii) it contains information regarding the antecedent atmospheric conditions. For instance, in the central region of the island, DJF rainfall in 2010 and 2011 broke records, with an average of 270 mm falling over in 24 hours along with extreme previous –NAOI. Note that small island environments are highly vulnerable

[1] A work presented at the Annual Conference of MIT Portugal 2019 summarising these results was granted the first place by the *Fundação Luso-Americana para o Desenvolvimento* (FLAD) in the PhD poster session.

to natural disasters such as cyclones and storm surges. They are also susceptible to flash floods, landslides and debris flows as a result of extreme rainfall [123]. It is therefore, essential to study variability of extreme rainfall at shorter time scales along with atmospheric observations from a multivariate perspective. This in turn may help to understand the atmospheric physics and the mechanisms that can shift an extreme rainfall event into one producing floods, including debris-flows and flash-floods, on the island.

9.3 Further developments

Different aspects related to the effects of climate change and abrupt climate variability on hydrological variables have been studied in this thesis. However, such effects are separated from anthropogenic causes of climate change or the impact of human activities. Therefore, some of these changes can be studied more profoundly or even new ones could be raised for the small island. Further research may include:

- Assignment of uncertainties to the detected trends (Chapters 3 and 4) which were addressed from a deterministic perspective, although based on commonly used statistical models.
- Evaluation of uncertainties of the return periods associated to the analysed hydrological extremes should be performed. This is based on the fact that the further away from the data one has to extrapolate, the larger the uncertainties of the resulting estimates will be — as in the case of the obtained bivariate return periods computed via copulas in Chapters 6 and 8.
- Attribution research should be implemented to the extreme rainfall events in order to identify the signal of human influence in general indicators of climate change, such as increasing global mean temperature. While it may seem contradictory, increases in temperature may be contributing to more extreme winter conditions in the island — i.e., as the warming atmosphere traps more water vapour later and later into the year, that vapour amounts leads to heavier rainfall events when the temperatures do drop. Thus, impact assessment must done based on well-established links between the change in the extreme and the impact in question. Addressing these issues will help identify the vulnerable regions to climate change in the small island.

Finally, a brief reflection about the role of the ground-based hydrological data. To address past and current changes in hydrological variables, namely in small environments with well-differentiated microclimates (as it is the case of Madeira Island) it is fundamental the use of numerous and long enough series of such data given that the spatial resolution of the GCMs is still a major constraint. Ensuring the continuity of the ground-based measuring networks and maintaining the quality of the data they provide is, therefore, a major issue, also towards bridging techniques between methodologies based on such data and GCMs. The final goal is always to understand current and, more importantly, future water-related issues in small island environments. Such understanding will contribute to the basis for future water resources assessment and modelling and provide new insights into how hydrological variables will be affected by global climate variability and change. This in turn should be aimed at developing strategic adaptation and risk management measures towards water and society security.

Bibliography

[1] Abadi, M. S. E. (2015). *Analysis of new techniques for risk aggregation and dependence modelling.* PhD thesis, Instituto Superior de Economia e Gestão.

[2] Abatzoglou, J. T., Redmond, K. T., and Edwards, L. M. (2009). Classification of regional climate variability in the state of California. *Journal of Applied Meteorology and Climatology*, 48(8):1527–1541.

[3] Abdi, H. (2003). Factor rotations in factor analyses. *Encyclopedia for Research Methods for the Social Sciences. Sage: Thousand Oaks, CA*, pages 792–795.

[4] Acero, F. J., García, J. A., and Gallego, M. C. (2011). Peaks-over-threshold study of trends in extreme rainfall over the Iberian Peninsula. *Journal of Climate*, 24(4):1089–1105.

[5] Achour, K., Meddi, M., Zeroual, A., Bouabdelli, S., Maccioni, P., and Moramarco, T. (2020). Spatio-temporal analysis and forecasting of drought in the plains of northwestern Algeria using the Standardized Precipitation Index. *Journal of Earth System Science*, 129(1):1–22.

[6] Ackerman, E. A. (1941). The Köppen classification of climates in North America. *Geographical Review*, pages 105–111.

[7] Adarsh, S. and Janga Reddy, M. (2015). Trend analysis of rainfall in four meteorological subdivisions of southern India using nonparametric methods and discrete wavelet transforms. *International Journal of Climatology*, 35(6):1107–1124.

[8] Adeloye, A. J. and Rustum, R. (2012). Self-organising map rainfall-runoff multivariate modelling for runoff reconstruction in inadequately gauged basins. *Hydrology Research*, 43(5):603–617.

[9] Agnew, C. (2000). Using the SPI to identify drought. *Drought Network News*, 12(1).

[10] Aissia, M.-A. B., Chebana, F., and Ouarda, T. B. (2017). Multivariate missing data in hydrology–Review and applications. *Advances in water resources*, 110:299–309.

[11] Akritas, M. G., Murphy, S. A., and Lavalley, M. P. (1995). The Theil-Sen estimator with doubly censored data and applications to astronomy. *Journal of the American Statistical Association*, 90(429):170–177.

[12] Albergel, C., Dutra, E., Bonan, B., Zheng, Y., Munier, S., Balsamo, G., de Rosnay, P., Munoz-Sabater, J., and Calvet, J. C. (2019). Monitoring and forecasting the impact of the 2018 summer heatwave on vegetation. *Remote Sensing*, 11(5):520.

[13] Aleryani, A., Wang, W., and De La Iglesia, B. (2018). Dealing with missing data and uncertainty in the context of data mining. In *International Conference on Hybrid Artificial Intelligence Systems*, pages 289–301. Springer.

[14] Alexandridis, A. K. and Zapranis, A. D. (2013). Handling the Data. In *Weather Derivatives*, pages 37–54. Springer.

[15] Allan, R. J., Nicholls, N., Jones, P. D., and Butterworth, I. J. (1991). A further extension of the Tahiti-Darwin SOI, early ENSO events and Darwin pressure. *Journal of Climate*, 4(7):743–749.

[16] Álvarez-Rodríguez, J., Llasat, M., and Estrela, T. (2017). Analysis of geographic and orographic influence in Spanish monthly precipitation. *International Journal of Climatology*, 37:350–362.

[17] Andrade, C. and Belo-Pereira, M. (2015). Assessment of droughts in the Iberian Peninsula using the WASP-Index. *Atmospheric Science Letters*, 16(3):208–218.

[18] André, L. and de Zea Bermudez, P. (2020). Modelling dependence between observed and simulated wind speed data using copulas. *Stochastic Environmental Research and Risk Assessment*, 34(11):1725–1753.

[19] Archer, D. R., Parkin, G., and Fowler, H. J. (2016). Assessing long term flash flooding frequency using historical information. *Hydrology Research*, 48(1):1–16.

[20] Awange, J. L., Kuhn, M., Anyah, R., and Forootan, E. (2017). Changes and variability of precipitation and temperature in the Ganges–Brahmaputra–Meghna River Basin based on global high-resolution reanalyses. *International Journal of Climatology*, 37(4):2141–2159.

[21] Ayantobo, O. O., Li, Y., and Song, S. (2018). Multivariate drought frequency analysis using four-variate symmetric and asymmetric Archimedean copula functions. *Water resources management*, 33(1):103–127.

[22] Azur, M., Stuart, E., Frangakis, C., and Leaf, P. (2011). Multiple imputation by chained equations: what is it and how does it work? *International journal of methods in psychiatric research*, 20(1):40–49.

[23] Bacchi, B., Becciu, G., and Kottegoda, N. T. (1994). Bivariate exponential model applied to intensities and durations of extreme rainfall. *Journal of hydrology*, 155(1-2):225–236.

[24] Baeriswyl, P.-A. and Rebetez, M. (1997). Regionalization of precipitation in Switzerland by means of principal component analysis. *Theoretical and Applied Climatology*, 58(1-2):31–41.

[25] Baines, P. G. and Folland, C. K. (2007). Evidence for a rapid global climate shift across the late 1960s. *Journal of Climate*, 20(12):2721–2744.

[26] Baioni, D., Castaldini, D., and Cencetti, C. (2011). Human activity and damaging landslides and floods on Madeira Island. *Natural Hazards & Earth System Sciences*, 11(11).

[27] Barnett, J. (2011). Dangerous climate change in the Pacific Islands: food production and food security. *Regional Environmental Change*, 11(1):229–237.

[28] Barnett, J. and Waters, E. (2016). Rethinking the vulnerability of small island states: climate change and development in the Pacific Islands. In *The palgrave handbook of international development*, pages 731–748. Springer.

[29] Barnston, A. G. and Livezey, R. E. (1987). Classification, seasonality and persistence of low-frequency atmospheric circulation patterns. *Monthly weather review*, 115(6):1083–1126.

[30] Bärring, L. (1988). Reginalization of daily rainfall in Kenya by means of common factor analysis. *Journal of climatology*, 8(4):371–389.

[31] Barros, V., Field, C., Dokke, D., Mastrandrea, M., Mach, K., Bilir, T. E., Chatterjee, M., Ebi, K., Estrada, Y., Genova, R., et al. (2014). *Climate change 2014: impacts, adaptation, and vulnerability-Part B: regional aspects-Contribution of Working Group II to the Fifth Assessment Report of the Intergovernmental Panel on Climate Change*. Cambridge University Press.

[32] Bartier, P. M. and Keller, C. P. (1996). Multivariate interpolation to incorporate thematic surface data using inverse distance weighting (IDW). *Computers & Geosciences*, 22(7):795–799.

[33] Bates, B., Kundzewicz, Z., and Wu, S. (2008). *Climate change and water*. Intergovernmental Panel on Climate Change Secretariat.

[34] Beck, H. E., Van Dijk, A. I., Levizzani, V., Schellekens, J., Gonzalez Miralles, D., Martens, B., and De Roo, A. (2017). MSWEP: 3-hourly 0.25 global gridded precipitation (1979-2015) by merging gauge, satellite, and reanalysis data. *Hydrology and Earth System Sciences*, 21(1):589–615.

[35] Beguería, S., Vicente-Serrano, S. M., Reig, F., and Latorre, B. (2014). Standardized precipitation evapotranspiration index (SPEI) revisited: parameter fitting, evapotranspiration models, tools, datasets and drought monitoring. *International Journal of Climatology*, 34(10):3001–3023.

[36] Belo-Pereira, M., Dutra, E., and Viterbo, P. (2011). Evaluation of global precipitation data sets over the Iberian Peninsula. *Journal of Geophysical Research: Atmospheres*, 116(D20).

[37] Berchin, I. I., Valduga, I. B., Garcia, J., de Andrade, J. B. S. O., et al. (2017). Climate change and forced migrations: An effort towards recognizing climate refugees. *Geoforum*, 84:147–150.

[38] Black, D. E., Peterson, L. C., Overpeck, J. T., Kaplan, A., Evans, M. N., and Kashgarian, M. (1999). Eight centuries of North Atlantic Ocean atmosphere variability. *Science*, 286(5445):1709–1713.

[39] Boers, N., Goswami, B., Rheinwalt, A., Bookhagen, B., Hoskins, B., and Kurths, J. (2019). Complex networks reveal global pattern of extreme-rainfall teleconnections. *Nature*, 566(7744):373–377.

[40] Bonaccorso, B., Bordi, I., Cancelliere, A., Rossi, G., and Sutera, A. (2003). Spatial variability of drought: an analysis of the SPI in Sicily. *Water resources management*, 17(4):273–296.

[41] Bracewell, R. N. and Bracewell, R. N. (1986). *The Fourier transform and its applications*, volume 31999. McGraw-Hill New York.

[42] Braconnot, P., Harrison, S. P., Kageyama, M., Bartlein, P. J., Masson-Delmotte, V., Abe-Ouchi, A., Otto-Bliesner, B., and Zhao, Y. (2012). Evaluation of climate models using palaeoclimatic data. *Nature Climate Change*, 2(6):417–424.

[43] Brechmann, E. and Schepsmeier, U. (2013). Cdvine: Modeling dependence with c-and d-vine copulas in R. *Journal of Statistical Software*, 52(3):1–27.

[44] Briffa, K., Van Der Schrier, G., and Jones, P. (2009). Wet and dry summers in Europe since 1750: evidence of increasing drought. *International Journal of Climatology: A Journal of the Royal Meteorological Society*, 29(13):1894–1905.

[45] Briggs, R. and Lemin, J. (1992). Delineation of climatic regions in Maine. *Canadian Journal of Forest Research*, 22(6):801–811.

[46] Browne, M. W. (2001). An overview of analytic rotation in exploratory factor analysis. *Multivariate behavioral research*, 36(1):111–150.

[47] Burrough, P. and McDonnell, R. (1998). Spatial Information Systems and Geostatistics. *P. Burrough, & R. McDonnell, Principles of Geographical Information Systems*, 333.

[48] Byzedi, M. and Saghafian, B. (2010). Analysis of hydrological drought based on daily flow series. *Proc. World Acad. Sci. Eng. Technol*, 70:249–252.

[49] Campozano, L., Sánchez, E., Aviles, A., Samaniego, E., et al. (2014). Evaluation of infilling methods for time series of daily precipitation and temperature: The case of the Ecuadorian Andes. *Revista Maskana*.

[50] Cangelosi, R. and Goriely, A. (2007). Component retention in principal component analysis with application to cDNA microarray data. *Biology direct*, 2(1):2.

[51] Carvalho, A., Schmidt, L., Santos, F. D., and Delicado, A. (2014). Climate change research and policy in Portugal. *Wiley Interdisciplinary Reviews: Climate Change*, 5(2):199–217.

[52] Cattiaux, J., Vautard, R., Cassou, C., Yiou, P., Masson-Delmotte, V., and Codron, F. (2010). Winter 2010 in Europe: A cold extreme in a warming climate. *Geophysical Research Letters*, 37(20).

[53] Caviedes, C. N. (1984). El Nino 1982-83. *Geographical Review*, 74(3):267–290.

[54] Chakraborty, D., Saha, S., Singh, R., Sethy, B., Kumar, A., Saikia, U., Das, S., Makdoh, B., Borah, T. R., Chanu, A. N., et al. (2017). Trend analysis and change point detection of mean air temperature: A spatio-temporal perspective of North-Eastern India. *Environmental Processes*, 4(4):937–957.

[55] Chang, J., Li, Y., Wang, Y., and Yuan, M. (2016). Copula-based drought risk assessment combined with an integrated index in the Wei River Basin, China. *Journal of Hydrology*, 540:824–834.

[56] Charlery, J., Nurse, L., and Whitehall, K. (2006). Exploring the relationship between the North Atlantic oscillation and rainfall patterns in Barbados. *International Journal of Climatology: A Journal of the Royal Meteorological Society*, 26(6):819–827.

[57] Chaudhry, A., Li, W., Basri, A., and Patenaude, F. (2019). A method for improving imputation and prediction accuracy of highly seasonal univariate data with large periods of missingness. *Wireless Communications and Mobile Computing*, 2019.

[58] Chazarra, A., Mestre, A., Pires, V., Cunha, S., Silva, A., Marques, J., Carvalho, F., Mendes, M., Neto, J., Mendes, L., and Filipe Nunes, L. (2011). *Climate Atlas of the Archipelagos of the Canary Islands, Madeira and the Azores: air temperature and precipitation (1971-2000)*. AEMET and IPMA.

[59] Chebana, F. and Ouarda, T. B. (2011). Multivariate quantiles in hydrological frequency analysis. *Environmetrics*, 22(1):63–78.

[60] Chen, F.-W. and Liu, C.-W. (2012). Estimation of the spatial rainfall distribution using inverse distance weighting (IDW) in the middle of Taiwan. *Paddy and Water Environment*, 10(3):209–222.

[61] Chen, L., Singh, V. P., Guo, S., Mishra, A. K., and Guo, J. (2012). Drought analysis using copulas. *Journal of Hydrologic Engineering*, 18(7):797–808.

[62] Clark, I. (1979). *Practical geostatistics*, volume 3. Applied Science Publishers London.

[63] Clemen, R. T. and Reilly, T. (1999). Correlations and copulas for decision and risk analysis. *Management Science*, 45(2):208–224.

[64] Cleveland, W. (1979). Robust locally weighted regression and smoothing scatterplots. *Journal of the American statistical association*, 74(368):829–836.

[65] Collins, M., Knutti, R., Arblaster, J., Dufresne, J.-L., Fichefet, T., Friedlingstein, P., Gao, X., Gutowski, W. J., Johns, T., Krinner, G., et al. (2013). Long-term climate change: projections, commitments and irreversibility. In *Climate Change 2013-The Physical Science Basis: Contribution of Working Group I to the Fifth Assessment Report of the Intergovernmental Panel on Climate Change*, pages 1029–1136. Cambridge University Press.

[66] Comrie, A. C. and Glenn, E. C. (1998). Principal components-based regionalization of precipitation regimes across the southwest United States and northern Mexico, with an application to monsoon precipitation variability. *Climate Research*, 10(3):201–215.

[67] Corte-Real, J., Qian, B., and Xu, H. (1998). Regional climate change in Portugal: precipitation variability associated with large-scale atmospheric circulation. *International journal of climatology*, 18(6):619–635.

[68] Costa, A. C. and Soares, A. (2009). Trends in extreme precipitation indices derived from a daily rainfall database for the South of Portugal. *International Journal of Climatology: A Journal of the Royal Meteorological Society*, 29(13):1956–1975.

[69] Costa, M. A. M., Moors, E. J., and Fraser, E. D. (2011). Socioeconomics, policy, or climate change: what is driving vulnerability in southern Portugal? *Ecology and Society*, 16(1).

[70] Couto, F., Salgado, R., and Costa, M. J. (2012). Analysis of intense rainfall events on Madeira Island during the 2009/2010 winter. *Natural hazards and earth system sciences*, 12(7):2225–2240.

[71] Cowling, A., Hall, P., and Phillips, M. J. (1996). Bootstrap confidence regions for the intensity of a Poisson point process. *Journal of the American Statistical Association*, 91(436):1516–1524.

[72] Cropper, T. (2013). The weather and climate of Macaronesia: past, present and future. *Weather*, 68(11):300–307.

[73] Cropper, T. and Hanna, E. (2014). An analysis of the climate of Macaronesia, 1865–2012. *International Journal of Climatology*, 34(3):604–622.

[74] Cropper, T., Hanna, E., Valente, M. A., and Jónsson, T. (2015). A daily Azores–Iceland North Atlantic Oscillation index back to 1850. *Geoscience Data Journal*, 2(1):12–24.

[75] Cubasch, U., Wuebbles, D., Chen, D., Facchini, M. C., Frame, D., Mahowald, N., and Winther, J.-G. (2013). Introduction. In 'Climate Change 2013: The Physical Science Basis. Contribution of Working Group I to the Fifth Assessment Report of the Intergovernmental Panel on Climate Change'. *(Cambridge, UK, and New York: Cambridge University Press)*.

[76] Cuspilici, A., Monforte, P., and Ragusa, M. (2017). Study of Saharan dust influence on PM10 measures in Sicily from 2013 to 2015. *Ecological Indicators*, 76:297–303.

[77] Dai, G., Mu, M., and Jiang, Z. (2019). Evaluation of the forecast performance for North Atlantic Oscillation onset. *Advances in Atmospheric Sciences*, 36(7):753–765.

[78] Das, P. K., Chakraborty, A., and Seshasai, M. (2014). Spatial analysis of temporal trend of rainfall and rainy days during the Indian Summer Monsoon season using daily gridded (0.5× 0.5) rainfall data for the period of 1971–2005. *Meteorological Applications*, 21(3):481–493.

[79] Davis, R. A. and Mikosch, T. (2009). The extremogram: A correlogram for extreme events. *Bernoulli*, 15(4):977–1009.

[80] Dawood, M. et al. (2017). Spatio-statistical analysis of temperature fluctuation using Mann–Kendall and Sen's slope approach. *Climate dynamics*, 48(3-4):783–797.

[81] de Carvalho, J. R. P., Monteiro, A., Boffinho, J. E., Nakai, A. M., and Assad, E. D. (2017). Model for multiple imputation to estimate daily rainfall data and filling of faults. *Revista Brasileira de Meteorologia*, 32(4):575–583.

[82] De Castro, M., Martín-Vide, J., and Alonso, S. (2005). The climate of Spain: past, present and scenarios for the 21st century. *A preliminary assessment of the impacts in Spain due to the effects of climate change. ECCE Project-Final report. Ministerio de Medio Ambiente, Madrid.*

[83] De Groot, R. S., Fisher, B., Christie, M., Aronson, J., Braat, L., Haines-Young, R., Gowdy, J., Maltby, E., Neuville, A., and Polasky, S. (2010). Integrating the ecological and economic dimensions in biodiversity and ecosystem service valuation. In *The Economics of Ecosystems and Biodiversity (TEEB): Ecological and Economic Foundations*, pages 9–40. Earthscan, Routledge.

[84] De la Barreda, B., Metcalfe, S. E., and Boyd, D. S. (2020). Precipitation regionalization, anomalies and drought occurrence in the Yucatan Peninsula, Mexico. *International Journal of Climatology*, 40(10):4541–4555.

[85] de Lima, M., Carvalho, S., and de Lima, J. (2010a). Investigating annual and monthly trends in precipitation structure: an overview across Portugal. *Natural Hazards and Earth System Sciences*, 10(11):2429.

[86] de Lima, M., Carvalho, S., de Lima, J., and Coelho, M. (2010b). Trends in precipitation: analysis of long annual and monthly time series from mainland Portugal. *Advances in Geosciences*, 25.

[87] de Lima, M. I. P., Marques, A. C., de Lima, J., and Coelho, M. (2007). Precipitation trends in mainland Portugal in the period 1941-2000. *IAHS publication*, 310:94.

[88] de Lima, M. I. P., Santo, F. E., Ramos, A. M., and Trigo, R. M. (2015). Trends and correlations in annual extreme precipitation indices for mainland Portugal, 1941–2007. *Theoretical and Applied Climatology*, 119(1-2):55–75.

[89] De Luca, P., Messori, G., Wilby, R. L., Mazzoleni, M., and Di Baldassarre, G. (2020). Concurrent wet and dry hydrological extremes at the global scale. *Earth System Dynamics*, 11(1):251–266.

[90] De Luis, M., Gonzalez-Hidalgo, J. C., Longares, L. A., and Stepanek, P. (2009). Seasonal precipitation trends in the Mediterranean Iberian Peninsula in second half of 20th century. *Int J Climatol*, 29:1312–1323.

[91] De Michele, C., Salvadori, G., Vezzoli, R., and Pecora, S. (2013). Multivariate assessment of droughts: Frequency analysis and dynamic return period. *Water Resources Research*, 49(10):6985–6994.

[92] Delhomme, J. P. (1978). Kriging in the hydrosciences. *Advances in water resources*, 1(5):251–266.

[93] Demuth, S., Stahl, K., et al. (2001). *Assessment of the Regional. Impact of Droughts in Europe (ARIDE)-Final Report.* University of Freiburg/Institute of Hydrology.

[94] Deng, X. and Tian, X. (2014). Entropy principal component analysis and its application to nonlinear chemical process fault diagnosis. *Asia-Pacific Journal of Chemical Engineering*, 9(5):696–706.

[95] Deser, C., Hurrell, J. W., and Phillips, A. S. (2017). The role of the North Atlantic Oscillation in European climate projections. *Climate dynamics*, 49(9):3141–3157.

[96] Dietz, S. (2011). High impact, low probability? An empirical analysis of risk in the economics of climate change. *Climatic change*, 108(3):519–541.

[97] Diggle, P. (1985). A kernel method for smoothing point process data. *Applied statistics*, pages 138–147.

[98] Dillan, W. and Goldstein, M. (1984). Multivariate Analysis. *Methods and Applications*.

[99] DiStefano, C., Zhu, M., and Mindrila, D. (2009). Understanding and using factor scores: Considerations for the applied researcher. *Practical Assessment, Research, and Evaluation*, 14(1):20.

[100] DLR (2008). Decreto Legislativo Regional 38/2008/M, 2008-08-20.

[101] Donat, M. G., Lowry, A. L., Alexander, L. V., O'Gorman, P. A., and Maher, N. (2016). More extreme precipitation in the world's dry and wet regions. *Nature Climate Change*, 6(5):508–513.

[102] Dracup, J. A., Lee, K. S., and Paulson Jr, E. G. (1980). On the definition of droughts. *Water resources research*, 16(2):297–302.

[103] Draisma, G., Drees, H., Ferreira, A., De Haan, L., et al. (2004). Bivariate tail estimation: dependence in asymptotic independence. *Bernoulli*, 10(2):251–280.

[104] Duarte, R. (1998). Prospecção e captação de águas subterrâneas em terrenos vulcânicos, arquipélago da Madeira. *4º Congresso da Água-A Água como Recurso Estruturante do Desenvolvimento" Coimbra*.

[105] Duarte, R. (2012). Prospecção e captação de águas subterrâneas em terrenos vulcânicos, arquipélago da Madeira. *Acessivel em www. aprh. pt/congressos, consultado em 20.07*.

[106] Duffy, P., Doutriaux, C., Santer, B., and Fodor, I. (2001). Effect of missing data on estimates of near-surface temperature change since 1900. *Journal of Climate*, 14(13):2809–2814.

[107] Earls, J. and Dixon, B. (2007). Spatial interpolation of rainfall data using ArcGIS: A comparative study. In *Proceedings of the 27th Annual ESRI International User Conference*, volume 31.

[108] Edwards, D. C. and McKee, T. (1997). *Characteristics of 20th century drought in the United States at multiple time scales*, volume 2. Dept. of Atmospheric Science, Colorado State University.

[109] Eekhout, J. P., Hunink, J. E., Terink, W., and de Vente, J. (2018). Why increased extreme precipitation under climate change negatively affects water security. *Hydrology & Earth System Sciences*, 22(11).

[110] Ehrendorfer, M. (1987). A regionalization of Austria's precipitation climate using principal component analysis. *Journal of Climatology*, 7(1):71–89.

[111] Eischeid, J., Pasteris, P., Diaz, H., Plantico, M., and Lott, N. (2000). Creating a serially complete, national daily time series of temperature and precipitation for the western United States. *Journal of Applied Meteorology*, 39(9):1580–1591.

[112] Embrechts, P., Lindskog, F., and McNeil, A. (2001). Modelling dependence with copulas. *Rapport technique, Département de mathématiques, Institut Fédéral de Technologie de Zurich, Zurich*, 14.

[113] Embrechts, P., Mcneil, E., and Straumann, D. (1999). Correlation: pitfalls and alternatives. In *Risk Magazine*. Citeseer.

[114] Enders, C. K., Mistler, S. A., and Keller, B. T. (2016). Multilevel multiple imputation: A review and evaluation of joint modeling and chained equations imputation. *Psychological Methods*, 21(2):222.

[115] Espinosa, L. A. and Portela, M. M. (2020). Rainfall trends over a small island teleconnected to the North Atlantic Oscillation – the case of Madeira Island, Portugal. *Water Resources Management*, 34(14):4449–4467.

[116] Espinosa, L. A., Portela, M. M., Pontes Filho, J. D., Studart, T. M. d. C., Santos, J. F., and Rodrigues, R. (2019a). Jointly modeling drought characteristics with smoothed regionalized SPI series for a small island. *Water*, 11(12):2489.

[117] Espinosa, L. A., Portela, M. M., and Rodrigues, R. (2018). Spatiotemporal characterization of droughts in Madeira Island (1937-2016): a preliminary assesment. In del Agua, F. N. C., editor, *Proceedings of the X Iberian Congress of Water Management and Planning (X Congreso Ibérico de Gestión y Planificación del Agua)*.

[118] Espinosa, L. A., Portela, M. M., and Rodrigues, R. (2019b). Spatio-temporal variability of droughts over past 80 years in Madeira Island. *Journal of Hydrology: Regional Studies*, 25:100623.

[119] Espinosa, L. A., Portela, M. M., and Rodrigues, R. (2020). Significant Extremal Dependence of a Daily North Atlantic Oscillation Index (NAOI) and Weighted Regionalised Rainfall in a Small Island Using the Extremogram. *Water*, 12(11):2989.

[120] Espinosa, L. A., Portela, M. M., and Rodrigues, R. (2021). Rainfall trends over a North Atlantic small island in the period 1937/1938–2016/2017 and an early climate teleconnection. *Theoretical and Applied Climatology*, 144(1-2):469–491.

[121] Espinoza, J. C., Ronchail, J., Guyot, J. L., Junquas, C., Vauchel, P., Lavado, W., Drapeau, G., and Pombosa, R. (2011). Climate variability and extreme drought in the upper Solimões River (western Amazon Basin): Understanding the exceptional 2010 drought. *Geophysical Research Letters*, 38(13).

[122] Evans, D. G. and Jones, S. M. (1987). Detecting Voronoi (area-of-influence) polygons. *Mathematical geology*, 19(6):523–537.

[123] Falkland, A., Custodio, E., et al. (1991). *Hydrology and water resources of small islands: A practical guide*, volume No. 49. UNESCO.

[124] Fan, L. and Chen, D. (2016). Trends in extreme precipitation indices across China detected using quantile regression. *Atmospheric Science Letters*, 17(7):400–406.

[125] Fan, L., Wang, H., Liu, Z., and Li, N. (2018). Quantifying the relationship between drought and water scarcity using Copulas: Case study of Beijing–Tianjin–Hebei metropolitan areas in China. *Water*, 10(11):1622.

[126] Faris, P., Ghali, W., Brant, R., Norris, C., Galbraith, D., Knudtson, M., Investigators, A., et al. (2002). Multiple imputation versus data enhancement for dealing with missing data in observational health care outcome analyses. *Journal of clinical epidemiology*, 55(2):184–191.

[127] Fasen, V., Klüppelberg, C., and Schlather, M. (2010). High-level dependence in time series models. *Extremes*, 13(1):1–33.

[128] Fazel, N., Berndtsson, R., Uvo, C. B., Madani, K., and Kløve, B. (2018). Regionalization of precipitation characteristics in Iran's Lake Urmia basin. *Theoretical and applied climatology*, 132(1-2):363–373.

[129] Feng, Z., Leung, L. R., Hagos, S., Houze, R. A., Burleyson, C. D., and Balaguru, K. (2016). More frequent intense and long-lived storms dominate the springtime trend in central US rainfall. *Nature communications*, 7(1):1–8.

[130] Fernández-Montes, S., Rodrigo, F. S., Seubert, S., and Sousa, P. M. (2013). Spring and summer extreme temperatures in Iberia during last century in relation to circulation types. *Atmospheric Research*, 127:154–177.

[131] Ferrari, E., Caloiero, T., and Coscarelli, R. (2013). Influence of the North Atlantic Oscillation on winter rainfall in Calabria (southern Italy). *Theoretical and applied climatology*, 114(3):479–494.

[132] Ferrelli, F., Brendel, A., Aliaga, V. S., Piccolo, M. C., and Perillo, G. M. E. (2019). Climate regionalization and trends based on daily temperature and precipitation extremes in the south of the Pampas (Argentina). *Geographical Research Letters*.

[133] Field, C. B., Barros, V., Stocker, T. F., and Dahe, Q. (2012). *Managing the risks of extreme events and disasters to advance climate change adaptation: special report of the intergovernmental panel on climate change*. Cambridge University Press.

[134] Figueira, C., de Sequeira, M. M., Vasconcelos, R., and Prada, S. (2013). Cloud water interception in the temperate laurel forest of Madeira Island. *Hydrological sciences journal*, 58(1):152–161.

[135] Flato, G., Marotzke, J., Abiodun, B., Braconnot, P., Chou, S. C., Collins, W., Cox, P., Driouech, F., Emori, S., Eyring, V., et al. (2014). Evaluation of climate models. In *Climate change 2013: the physical science basis. Contribution of Working Group I to the Fifth Assessment Report of the Intergovernmental Panel on Climate Change*, pages 741–866. Cambridge University Press.

[136] Fleig, A. K., Tallaksen, L. M., Hisdal, H., and Demuth, S. (2006). A global evaluation of streamflow drought characteristics. *Hydrology and Earth System Sciences Discussions*, 10(4):535–552.

[137] Folland, C. K., Karl, T. R., and Jim Salinger, M. (2002). Observed climate variability and change. *Weather*, 57(8):269–278.

[138] Forster, P. M., Maycock, A. C., McKenna, C. M., and Smith, C. J. (2020). Latest climate models confirm need for urgent mitigation. *Nature Climate Change*, 10(1):7–10.

[139] Fraedrich, K. (1994). An ENSO impact on Europe? *Tellus A*, 46(4):541–552.

[140] Fragoso, M., Trigo, R., Pinto, J., Lopes, S., Lopes, A., Ulbrich, S., and Magro, C. (2012). The 20 February 2010 Madeira flash-floods: synoptic analysis and extreme rainfall assessment. *Natural Hazards and Earth System Science*, 12(3):715–730.

[141] Franzke, C. (2009). Multi-scale analysis of teleconnection indices: climate noise and nonlinear trend analysis. *Nonlinear Processes in Geophysics*, 16(1):65–76.

[142] Gaetani, M., Baldi, M., Dalu, G., and Maracchi, G. (2011). Jetstream and rainfall distribution in the Mediterranean region. *Natural Hazards and Earth System Sciences*, 11(9):2469–2481.

[143] Gamerman, D. and Lopes, H. F. (2006). *Markov chain Monte Carlo: stochastic simulation for Bayesian inference*. Chapman and Hall/CRC.

[144] Gao, Y. (2017). *Dealing with missing data in hydrology: Data analysis of discharge and groundwater time-series in Northeast Germany*. PhD thesis, Freie Universität Berlin.

[145] García-Cueto, O. R., Santillán-Soto, N., López-Velázquez, E., Reyes-López, J., Cruz-Sotelo, S., and Ojeda-Benítez, S. (2019). Trends of climate change indices in some Mexican cities from 1980 to 2010. *Theoretical and Applied Climatology*, 137(1-2):775–790.

[146] Gebrechorkos, S. H., Hülsmann, S., and Bernhofer, C. (2019). Long-term trends in rainfall and temperature using high-resolution climate datasets in East Africa. *Scientific reports*, 9(1):1–9.

[147] George, S. E. and Saunders, M. A. (2001). North Atlantic Oscillation impact on tropical north Atlantic winter atmospheric variability. *Geophysical Research Letters*, 28(6):1015–1018.

[148] Gibelin, A.-L. and Déqué, M. (2003). Anthropogenic climate change over the Mediterranean region simulated by a global variable resolution model. *Climate Dynamics*, 20(4):327–339.

[149] Gilbert, R. O. (1987). *Statistical methods for environmental pollution monitoring*. John Wiley & Sons.

[150] Giorgi, F., Coppola, E., and Raffaele, F. (2014). A consistent picture of the hydroclimatic response to global warming from multiple indices: Models and observations. *Journal of Geophysical Research: Atmospheres*, 119(20):11–695.

[151] Giorgi, F. and Lionello, P. (2008). Climate change projections for the Mediterranean region. *Global and planetary change*, 63(2-3):90–104.

[152] Girons Lopez, M., Wennerström, H., Nordén, L.-Å., and Seibert, J. (2015). Location and density of rain gauges for the estimation of spatial varying precipitation. *Geografiska Annaler: Series A, Physical Geography*, 97(1):167–179.

[153] Goel, N., Seth, S., and Chandra, S. (1998). Multivariate modeling of flood flows. *Journal of Hydraulic Engineering*, 124(2):146–155.

[154] Golestan, S., Ramezani, M., Guerrero, J. M., Freijedo, F. D., and Monfared, M. (2013). Moving average filter based phase-locked loops: Performance analysis and design guidelines. *IEEE Transactions on Power Electronics*, 29(6):2750–2763.

[155] Gommes, R. and Petrassi, F. (1996). Rainfall variability and drought in sub-Saharan Africa. *SD dimensions, FAO*.

[156] González, J. and Valdés, J. B. (2003). Bivariate drought recurrence analysis using tree ring reconstructions. *Journal of Hydrologic Engineering*, 8(5):247–258.

[157] Gottschalk, L. (1985). Hydrological regionalization of Sweden. *Hydrological Sciences Journal*, 30(1):65–83.

[158] Gouveia-Reis, D., Lopes, L. G., and Mendonça, S. (2016). A dependence modelling study of extreme rainfall in Madeira Island. *Physics and Chemistry of the Earth, Parts A/B/C*, 94:85–93.

[159] Graham, J. (2009). Missing data analysis: Making it work in the real world. *Annual review of psychology*, 60:549–576.

[160] Graham, J. W., Olchowski, A. E., and Gilreath, T. D. (2007). How many imputations are really needed? Some practical clarifications of multiple imputation theory. *Prevention science*, 8(3):206–213.

[161] Greatbatch, R. J., Gollan, G., Jung, T., and Kunz, T. (2015). Tropical origin of the severe European winter of 1962/1963. *Quarterly Journal of the Royal Meteorological Society*, 141(686):153–165.

[162] Greenland, S. and Finkle, W. D. (1995). A critical look at methods for handling missing covariates in epidemiologic regression analyses. *American journal of epidemiology*, 142(12):1255–1264.

[163] Greve, P., Orlowsky, B., Mueller, B., Sheffield, J., Reichstein, M., and Seneviratne, S. I. (2014). Global assessment of trends in wetting and drying over land. *Nature geoscience*, 7(10):716–721.

[164] Grice, J. W. (2001). Computing and evaluating factor scores. *Psychological methods*, 6(4):430.

[165] Grimaldi, S., Petroselli, A., Tauro, F., and Porfiri, M. (2012). Time of concentration: a paradox in modern hydrology. *Hydrological Sciences journal*, 57(2):217–228.

[166] Gudendorf, G. and Segers, J. (2010). Extreme-value copulas. In *Copula theory and its applications*, pages 127–145. Springer.

[167] Guttman, N. B. (1999). Accepting the standardized precipitation index: a calculation algorithm 1. *JAWRA Journal of the American Water Resources Association*, 35(2):311–322.

[168] Gutzler, D. and Robbins, T. (2011). Climate variability and projected change in the western United States: regional downscaling and drought statistics. *Climate Dynamics*, 37(5-6):835–849.

[169] Hair, J., Black, W., Babin, B., Anderson, R., and Tatham, R. (1998). *Multivariate data analysis*, volume 5. Prentice hall.

[170] Halbert, K., Nguyen, C. C., Payrastre, O., and Gaume, E. (2016). Reducing uncertainty in flood frequency analyses: A comparison of local and regional approaches involving information on extreme historical floods. *Journal of hydrology*, 541:90–98.

[171] Hanna, E. and Cropper, T. E. (2017). North Atlantic Oscillation. In *Oxford Research Encyclopedia of Climate Science*. Oxford Research Encyclopedias.

[172] Hanna, E., Cropper, T. E., Jones, P. D., Scaife, A. A., and Allan, R. (2015). Recent seasonal asymmetric changes in the NAO (a marked summer decline and increased winter variability) and associated changes in the AO and Greenland Blocking Index. *International Journal of Climatology*, 35(9):2540–2554.

[173] Hannachi, A., Jolliffe, I. T., and Stephenson, D. B. (2007). Empirical orthogonal functions and related techniques in atmospheric science: A review. *International Journal of Climatology: A Journal of the Royal Meteorological Society*, 27(9):1119–1152.

[174] Harris, R. M., Beaumont, L. J., Vance, T. R., Tozer, C. R., Remenyi, T. A., Perkins-Kirkpatrick, S. E., Mitchell, P. J., Nicotra, A., McGregor, S., Andrew, N., et al. (2018). Biological responses to the press and pulse of climate trends and extreme events. *Nature Climate Change*, 8(7):579.

[175] Hashorva, E. (2005). Asymptotics and bounds for multivariate Gaussian tails. *Journal of theoretical probability*, 18(1):79–97.

[176] Hayes, M. J., Svoboda, M. D., Wiihite, D. A., and Vanyarkho, O. V. (1999). Monitoring the 1996 drought using the standardized precipitation index. *Bulletin of the American meteorological society*, 80(3):429–438.

[177] Haylock, M. and Goodess, C. (2004). Interannual variability of European extreme winter rainfall and links with mean large-scale circulation. *International Journal of Climatology: A Journal of the Royal Meteorological Society*, 24(6):759–776.

[178] Heim Jr, R. R. (2002). A review of twentieth-century drought indices used in the United States. *Bulletin of the American Meteorological Society*, 83(8):1149–1165.

[179] Helama, S., Meriläinen, J., and Tuomenvirta, H. (2009). Multicentennial megadrought in northern Europe coincided with a global El Niño–Southern Oscillation drought pattern during the Medieval Climate Anomaly. *Geology*, 37(2):175–178.

[180] Helsel, D. R. and Hirsch, R. M. (2002). *Statistical methods in water resources*, volume 323. US Geological survey Reston, VA.

[181] Herrera, D. and Ault, T. (2017). Insights from a New High-Resolution Drought Atlas for the Caribbean Spanning 1950–2016. *Journal of Climate*, 30(19):7801–7825.

[182] Herrera, D. A., Ault, T. R., Fasullo, J. T., Coats, S. J., Carrillo, C. M., Cook, B. I., and Williams, A. P. (2018). Exacerbation of the 2013–2016 Pan-Caribbean Drought by Anthropogenic Warming. *Geophysical research letters*, 45(19):10–619.

[183] Herrera, R. G., Puyol, D. G., MartÍn, E. H., Presa, L. G., and Rodríguez, P. R. (2001). Influence of the North Atlantic oscillation on the Canary Islands precipitation. *Journal of Climate*, 14(19):3889–3903.

[184] Hersbach, H., Bell, B., Berrisford, P., Hirahara, S., Horányi, A., Muñoz-Sabater, J., Nicolas, J., Peubey, C., Radu, R., Schepers, D., et al. (2020). The ERA5 global reanalysis. *Quarterly Journal of the Royal Meteorological Society*, 146(730):1999–2049.

[185] Hewitson, B., Janetos, A. C., Carter, T. R., Giorgi, F., Jones, R. G., Kwon, W. T., Mearns, L. O., Schipper, E. L. F., and Van Aalst, M. K. (2015). Regional context. In *Climate Change 2014: Impacts, Adaptation and Vulnerability: Part B: Regional Aspects: Working Group II Contribution to the Fifth Assessment Report of the Intergovernmental Panel on Climate Change*, pages 1133–1198. Cambridge University Press.

[186] Hintze, J. L. and Nelson, R. D. (1998). Violin plots: a box plot-density trace synergism. *The American Statistician*, 52(2):181–184.

[187] Hirsch, R. M. and Slack, J. R. (1984). A nonparametric trend test for seasonal data with serial dependence. *Water Resources Research*, 20(6):727–732.

[188] Hoerling, M., Eischeid, J., Perlwitz, J., Quan, X., Zhang, T., and Pegion, P. (2012). On the increased frequency of Mediterranean drought. *Journal of climate*, 25(6):2146–2161.

[189] Hou, A. Y., Kakar, R. K., Neeck, S., Azarbarzin, A. A., Kummerow, C. D., Kojima, M., Oki, R., Nakamura, K., and Iguchi, T. (2014). The global precipitation measurement mission. *Bulletin of the American Meteorological Society*, 95(5):701–722.

[190] Houghton, J., Jenkins, G., and Ephraums, J. (1990). IPCC first assessment report 1990. *Scientific Assessment of Climate Change: Report of Working Group*, 1.

[191] Huang, J., Ji, M., Higuchi, K., and Shabbar, A. (2006). Temporal structures of the North Atlantic Oscillation and its impact on the regional climate variability. *Advances in Atmospheric Sciences*, 23(1):23–32.

[192] Hui-Mean, F., Yusof, F., Yusop, Z., and Suhaila, J. (2019). Trivariate copula in drought analysis: A case study in peninsular Malaysia. *Theoretical and Applied Climatology*, 138(1):657–671.

[193] Hurrell, J. (1995). Decadal trends in the North Atlantic Oscillation: regional temperatures and precipitation. *Science*, 269(5224):676–679.

[194] Hurrell, J. (2018). NCAR Staff (Eds): The Climate Data Guide: Hurrell North Atlantic Oscillation (NAO) Index (station-based).

[195] Hurrell, J. W. and Deser, C. (2010). North Atlantic climate variability: the role of the North Atlantic Oscillation. *Journal of marine systems*, 79(3-4):231–244.

[196] Hurrell, J. W., Kushnir, Y., and Visbeck, M. (2001). The north Atlantic oscillation. *Science*, 291(5504):603–605.

[197] Iles, C. and Hegerl, G. (2017). Role of the North Atlantic Oscillation in decadal temperature trends. *Environmental Research Letters*, 12(11):114010.

[198] Iliopoulou, T. and Koutsoyiannis, D. (2020). Projecting the future of rainfall extremes: better classic than trendy. *Journal of Hydrology*, 588:125005.

[199] INE (2012). *Censos 2011 Resultados Definitivos - Região Autónoma da Madeira*. Periodicidade decenal, Lisboa, Portugal, instituto nacional de estatística, i.p, statistics portugal edition.

[200] Iqbal, M., Hameed, S., and Khan, F. (2013). Influence of Azores high pressure on Middle Eastern rainfall. *Theoretical and applied climatology*, 111(1-2):211–221.

[201] Jianping, L. and Wang, J. X. (2003). A new North Atlantic Oscillation index and its variability. *Advances in Atmospheric Sciences*, 20(5):661–676.

[202] Joe, H. (1997). *Multivariate models and multivariate dependence concepts*. CRC Press.

[203] Johannessen, O. M., Kuzmina, S. I., Bobylev, L. P., and Miles, M. W. (2016). Surface air temperature variability and trends in the Arctic: new amplification assessment and regionalisation. *Tellus A: Dynamic Meteorology and Oceanography*, 68(1):28234.

[204] Jones, P., Jonsson, T., and Wheeler, D. (1997). Extension to the North Atlantic Oscillation using early instrumental pressure observations from Gibraltar and south-west Iceland. *International Journal of Climatology: A Journal of the Royal Meteorological Society*, 17(13):1433–1450.

[205] Jung, T., Vitart, F., Ferranti, L., and Morcrette, J.-J. (2011). Origin and predictability of the extreme negative NAO winter of 2009/10. *Geophysical Research Letters*, 38(7).

[206] Jury, M. R. and Winter, A. (2010). Warming of an elevated layer over the Caribbean. *Climatic Change*, 99(1-2):247–259.

[207] Kaiser, H. F. (1960). The application of electronic computers to factor analysis. *Educational and psychological measurement*, 20(1):141–151.

[208] Kang, H. (2013). The prevention and handling of the missing data. *Korean journal of anesthesiology*, 64(5):402–406.

[209] Kao, S.-C. and Govindaraju, R. S. (2010). A copula-based joint deficit index for droughts. *Journal of Hydrology*, 380(1-2):121–134.

[210] Kaufman, J. D. and Dunlap, W. P. (2000). Determining the number of factors to retain: Q windows-based FORTRAN-IMSL program for parallel analysis. *Behavior Research Methods, Instruments, & Computers*, 32(3):389–395.

[211] Kendall, M. G. (1948). Rank correlation methods. *The British Psychological Society*.

[212] Kenney, J. (1962). Moving averages. *mathematics of statistics*, 1:221–223.

[213] Kenward, M. and Carpenter, J. (2007). Multiple imputation: current perspectives. *Statistical methods in medical research*, 16(3):199–218.

[214] Khan, M. Z. K., Sharma, A., and Mehrotra, R. (2017). Global seasonal precipitation forecasts using improved sea surface temperature predictions. *Journal of Geophysical Research: Atmospheres*, 122(9):4773–4785.

[215] Kharin, V. V., Zwiers, F., Zhang, X., and Wehner, M. (2013). Changes in temperature and precipitation extremes in the CMIP5 ensemble. *Climatic change*, 119(2):345–357.

[216] Kharin, V. V. and Zwiers, F. W. (2005). Estimating extremes in transient climate change simulations. *Journal of Climate*, 18(8):1156–1173.

[217] Khedun, C. P., Mishra, A. K., Singh, V. P., and Giardino, J. R. (2014). A copula-based precipitation forecasting model: Investigating the interdecadal modulation of ENSO's impacts on monthly precipitation. *Water Resources Research*, 50(1):580–600.

[218] Kieffer, K. M. (1998). Orthogonal versus Oblique Factor Rotation: A Review of the Literature regarding the Pros and Cons. In *Practical Assessment, Research, and Evaluation*.

[219] Killick, R., Fearnhead, P., and Eckley, I. A. (2012). Optimal detection of changepoints with a linear computational cost. *Journal of the American Statistical Association*, 107(500):1590–1598.

[220] Kim, J.-M., Sungur, E. A., Choi, T., and Heo, T.-Y. (2011). Generalized bivariate copulas and their properties. *Model Assisted Statistics and Applications*, 6(2):127–136.

[221] Kim, J.-W. and Pachepsky, Y. A. (2010). Reconstructing missing daily precipitation data using regression trees and artificial neural networks for SWAT streamflow simulation. *Journal of hydrology*, 394(3-4):305–314.

[222] Kim, T.-W., Valdés, J. B., and Yoo, C. (2003). Nonparametric approach for estimating return periods of droughts in arid regions. *Journal of Hydrologic Engineering*, 8(5):237–246.

[223] King, R. (2015). *Cluster analysis and data mining : an introduction*. New Delhi : Mercury Learning and Information.

[224] Klein Tank, A., Peterson, T., Quadir, D., Dorji, S., Zou, X., Tang, H., Santhosh, K., Joshi, U., Jaswal, A., Kolli, R., et al. (2006). Changes in daily temperature and precipitation extremes in central and south Asia. *Journal of Geophysical Research: Atmospheres*, 111(D16).

[225] Knippertz, P., Ulbrich, U., Marques, F., and Corte-Real, J. (2003). Decadal changes in the link between El Niño and springtime North Atlantic Oscillation and European–North African rainfall. *International Journal of Climatology: A Journal of the Royal Meteorological Society*, 23(11):1293–1311.

[226] Krishan, R., Nikam, B. R., Pingale, S. M., Chandrakar, A., and Khare, D. (2018). Analysis of trends in rainfall and dry/wet years over a century in the Eastern Ganga Canal command. *Meteorological Applications*, 25(4):561–574.

[227] Kwon, H.-H. and Lall, U. (2016). A copula-based nonstationary frequency analysis for the 2012–2015 drought in California. *Water Resources Research*, 52(7):5662–5675.

[228] Langford, E. (2006). Quartiles in elementary statistics. *Journal of Statistics Education*, 14(3).

[229] Ledford, A. W. and Tawn, J. A. (1997). Modelling dependence within joint tail regions. *Journal of the Royal Statistical Society: Series B (Statistical Methodology)*, 59(2):475–499.

[230] Lee, J. H. and Kim, C. J. (2013). A multimodel assessment of the climate change effect on the drought severity–duration–frequency relationship. *Hydrological Processes*, 27(19):2800–2813.

[231] Levizzani, V., Laviola, S., Cattani, E., and Costa, M. J. (2013). Extreme precipitation on the Island of Madeira on 20 February 2010 as seen by satellite passive microwave sounders. *European Journal of Remote Sensing*, 46(1):475–489.

[232] Li, S., Xiong, L., Dong, L., and Zhang, J. (2013). Effects of the Three Gorges Reservoir on the hydrological droughts at the downstream Yichang station during 2003–2011. *Hydrological Processes*, 27(26):3981–3993.

[233] Li, X., Zhou, W., and Chen, Y. D. (2015). Assessment of regional drought trend and risk over China: A drought climate division perspective. *Journal of Climate*, 28(18):7025–7037.

[234] Li, Y. and Lau, N.-C. (2012). Impact of ENSO on the atmospheric variability over the North Atlantic in late winter—Role of transient eddies. *Journal of Climate*, 25(1):320–342.

[235] Liberato, M., Ramos, A., Gouveia, C., Sousa, P., Russo, A., Trigo, R., and Santo, F. (2017). Exceptionally extreme drought in Madeira Archipelago in 2012: Vegetation impacts and driving conditions. *Agricultural and forest meteorology*, 232:195–209.

[236] Linacre, E. (2003). *Climate data and resources: a reference and guide*. Routledge.

[237] Lionello, P., Abrantes, F., Gacic, M., Planton, S., Trigo, R. M., and Ulbrich, U. (2014). The climate of the Mediterranean region: research progress and climate change impacts.

[238] Lloyd-Hughes, B. and Saunders, M. (2002). A drought climatology for Europe. *International journal of climatology*, 22(13):1571–1592.

[239] Lopes, S., Fragoso, M., and Lopes, A. (2020). Heavy Rainfall Events and Mass Movements in the Funchal Area (Madeira, Portugal): Spatial Analysis and Susceptibility Assessment. *Atmosphere*, 11(1):104.

[240] López-Moreno, J. I. and Vicente-Serrano, S. (2008). Positive and negative phases of the wintertime North Atlantic Oscillation and drought occurrence over Europe: a multitemporal-scale approach. *Journal of Climate*, 21(6):1220–1243.

[241] López-Moreno, J. I., Vicente-Serrano, S. M., Beguería, S., García-Ruiz, J. M., Portela, M. M., and Almeida, A. (2009a). Dam effects on droughts magnitude and duration in a transboundary basin: The Lower River Tagus, Spain and Portugal. *Water Resources Research*, 45(2).

[242] López-Moreno, J. I., Vicente-Serrano, S. M., Gimeno, L., and Nieto, R. (2009b). Stability of the seasonal distribution of precipitation in the Mediterranean region: Observations since 1950 and projections for the 21st century. *Geophysical Research Letters*, 36(10).

[243] Lowry, W. (1972). *Compendium of lecture notes in climatology for class IV meteorological personnel*. Secretariat of the World Meteorological Organization.

[244] Luna, T., Rocha, A., Carvalho, A., Ferreira, J., and Sousa, J. (2011). Modelling the extreme precipitation event over Madeira Island on 20 February 2010. *Natural Hazards and Earth System Sciences*, 11(9):2437–2452.

[245] Lyra, G. B., Oliveira-Júnior, J. F., and Zeri, M. (2014). Cluster analysis applied to the spatial and temporal variability of monthly rainfall in Alagoas state, Northeast of Brazil. *International Journal of Climatology*, 34(13):3546–3558.

[246] MacLeod, A. and Korycinska, A. (2019). Detailing Köppen–Geiger climate zones at sub-national to continental scale: a resource for pest risk analysis. *EPPO Bulletin*, 49(1):73–82.

[247] Mann, H. B. (1945). Nonparametric tests against trend. *Econometrica: Journal of the Econometric Society*, pages 245–259.

[248] Mares, I., Mares, C., and Mihailescu, M. (2002). NAO impact on the summer moisture variability across Europe. *Physics and Chemistry of the Earth, Parts A/B/C*, 27(23):1013–1017.

[249] Marshall, J., Kushnir, Y., Battisti, D., Chang, P., Czaja, A., Dickson, R., Hurrell, J., McCartney, M., Saravanan, R., and Visbeck, M. (2001). North Atlantic climate variability: phenomena, impacts and mechanisms. *International journal of climatology*, 21(15):1863–1898.

[250] Masson-Delmotte, V. (2018). *Global Warming of 1.5 OC: An IPCC Special Report on the Impacts of Global Warming of 1.5° C Above Pre-industrial Levels and Related Global Greenhouse Gas Emission Pathways, in the Context of Strengthening the Global Response to the Threat of Climate Change, Sustainable Development, and Efforts to Eradicate Poverty*. World Meteorological Organization.

[251] Matsui, M. and Mikosch, T. (2015). The extremogram and the cross-extremogram for a bivariate GARCH (1, 1) process. *arXiv preprint arXiv:1505.05385*.

[252] Mayer, P., V. Marzol-Jaén, M., and Parreño-Castellano, J. (2017). Precipitation trends and a daily precipitation concentration index for the mid-Eastern Atlantic (Canary Islands, Spain). *Cuadernos de Investigación Geográfica*, 43.

[253] Mayuening, E., Kuning, M., Green, H., Ueranantasun, A., and Chuai-Aree, S. (2015). The Southern Oscillation Index as a Random Walk. *Walailak Journal of Science and Technology (WJST)*, 13(5):317–327.

[254] McAdie, A. (1922). Monsoon and Trade Winds as Rain Makers and Desert Makers. *Geographical Review*, 12(3):412–419.

[255] McCarthy, J. J., Canziani, O. F., Leary, N. A., Dokken, D. J., and White, K. S. (2001). *Climate change 2001: impacts, adaptation, and vulnerability: contribution of Working Group II to the third assessment report of the Intergovernmental Panel on Climate Change*, volume 2. Cambridge University Press.

[256] McGree, S., Schreider, S., and Kuleshov, Y. (2016). Trends and variability in droughts in the Pacific Islands and Northeast Australia. *Journal of Climate*, 29(23):8377–8397.

[257] McKee, T., Doesken, N., and Kleist, J. (1993a). SPI Drought Index.

[258] McKee, T. B., Doesken, N. J., Kleist, J., et al. (1993b). The relationship of drought frequency and duration to time scales. In *Proceedings of the 8th Conference on Applied Climatology*, volume 17, pages 179–183. American Meteorological Society Boston, MA.

[259] McKinley, S. and Levine, M. (1998). Cubic spline interpolation. *College of the Redwoods*, 45(1):1049–1060.

[260] McMillan, W. (1985). Evaluation of agricultural water supplies in Antigua and Barbuda. *report and map prepared for the Department of Regional Development and Environment, Organization of American States*.

[261] Meghanadh, B., Aravalath, L., Joshi, B., Sathiamoorthy, R., and Kumar, M. (2019). Imputation of Missing Values in the Fundamental Data: Using MICE Framework. *Journal of Quantitative Economics*, 17(3):459–475.

[262] Merabtene, T., Siddique, M., and Shanableh, A. (2016). Assessment of seasonal and annual rainfall trends and variability in Sharjah City, UAE. *Advances in Meteorology*, 2016.

[263] Merkel, U. and Latif, M. (2002). A high resolution AGCM study of the El Nino impact on the North Atlantic/European sector. *Geophysical Research Letters*, 29(9):5–1.

[264] MetOffice (2018). North Atlantic Oscillation.

[265] Meze-Hausken, E. (2004). Contrasting climate variability and meteorological drought with perceived drought and climate change in northern Ethiopia. *Climate research*, 27(1):19–31.

[266] Min, S., Zhang, X., Zwiers, F., Friederichs, P., and Hense, A. (2009). Signal detectability in extreme precipitation changes assessed from twentieth century climate simulations. *Climate Dynamics*, 32(1):95–111.

[267] Miranda, P., Coelho, F., Tomé, A. R., Valente, M. A., Carvalho, A., Pires, C., Pires, H. O., Pires, V. C., and Ramalho, C. (2002). 20th century Portuguese climate and climate scenarios. *Climate Change in Portugal. Scenarios, Impacts and Adaptation Measures—SIAM Project (Santos FD, Forbes K, Moita R, eds). Lisbon: Gradiva Publishers*, pages 23–83.

[268] Miranda, P., Valente, M., Tomé, A., Trigo, R., Coelho, M., Aguiar, A., and Azevedo, E. (2006). O clima de Portugal nos séculos XX e XXI. *Alterações Climáticas em Portugal. Cenários, Impactos e Medidas de Adaptação*, page 45e113.

[269] Miró, J. J., Caselles, V., and Estrela, M. J. (2017). Multiple imputation of rainfall missing data in the Iberian Mediterranean context. *Atmospheric research*, 197:313–330.

[270] Miró, J. J., Estrela, M. J., Caselles, V., and Gómez, I. (2018). Spatial and temporal rainfall changes in the Júcar and Segura basins (1955–2016): Fine-scale trends. *International Journal of Climatology*, 38(13):4699–4722.

[271] Mitchell, D., Davini, P., Harvey, B., Massey, N., Haustein, K., Woollings, T., Jones, R., Otto, F., Guillod, B., and Sparrow, S. (2017). Assessing mid-latitude dynamics in extreme event attribution systems. *Climate Dynamics*, 48(11):3889–3901.

[272] Montaseri, M., Amirataee, B., and Rezaie, H. (2018). New approach in bivariate drought duration and severity analysis. *Journal of hydrology*, 559:166–181.

[273] Morales, J. L., Horta-Rangel, F. A., Segovia-Domínguez, I., Morua, A. R., and Hernández, J. H. (2019). Analysis of a new spatial interpolation weighting method to estimate missing data applied to rainfall records. *Atmósfera*, 32(3):237–259.

[274] Moreira, E., Mexia, J., and Pereira, L. (2012). Are drought occurrence and severity aggravating? A study on SPI drought class transitions using log-linear models and ANOVA-like inference. *Hydrology and Earth System Sciences*, 16:3011–3028.

[275] Moreira, E., Mexia, J. a., Pereira, L., et al. (1993). Análise de clusters com modelos loglineares utilizando testes de razões de verosimelhança na procura de regiões homogéneas visando a gestão de secas. In Colibri, editor, *Gestão do Risco em Secas Métodos, tecnologias e desafios*, pages 91–101. Instituto Superior de Agronomia da Udade Técnica de Lisboa.

[276] Mudelsee, M. (2011). The bootstrap in climate risk analysis. In *In Extremis*, pages 44–58. Springer.

[277] Mudelsee, M., Börngen, M., Tetzlaff, G., and Grünewald, U. (2003). No upward trends in the occurrence of extreme floods in central Europe. *Nature*, 425(6954):166.

[278] Mudelsee, M., Börngen, M., Tetzlaff, G., and Grünewald, U. (2004). Extreme floods in central Europe over the past 500 years: Role of cyclone pathway Zugstrasse Vb. *Journal of Geophysical Research: Atmospheres*, 109(D23).

[279] Mueller, T., Pusuluri, N., Mathias, K., Cornelius, P., Barnhisel, R., and Shearer, S. (2004). Map quality for ordinary kriging and inverse distance weighted interpolation. *Soil Science Society of America Journal*, 68(6):2042–2047.

[280] Mueller, W. A. and Roeckner, E. (2006). ENSO impact on midlatitude circulation patterns in future climate change projections. *Geophysical research letters*, 33(5).

[281] Muñoz, J. M. H. (2015). *Assessing the impact of climate variability on seasonal streamflow forecasting in the Iberian Peninsula*. PhD thesis, Universidad de Granada.

[282] Mwale, F. D., Adeloye, A., and Rustum, R. (2012). Infilling of missing rainfall and streamflow data in the Shire River basin, Malawi–A self organizing map approach. *Physics and Chemistry of the Earth, Parts A/B/C*, 50:34–43.

[283] Mwale, F. D., Adeloye, A., and Rustum, R. (2014). Application of self-organising maps and multi-layer perceptron-artificial neural networks for streamflow and water level forecasting in data-poor catchments: the case of the Lower Shire floodplain, Malawi. *Hydrology Research*, 45(6):838–854.

[284] Nanda, T., Sahoo, B., and Chatterjee, C. (2017). Enhancing the applicability of Kohonen Self-Organizing Map (KSOM) estimator for gap-filling in hydrometeorological timeseries data. *Journal of hydrology*, 549:133–147.

[285] NCAR (2020 (last access on May 15, 2020)). Hurrell North Atlantic Oscillation (NAO) Index (Station Based). https://climatedataguide.ucar.edu/.

[286] Nelsen, R. B. (2006). Methods of constructing copulas. *An introduction to copulas*, pages 51–108.

[287] Nelsen, R. B. (2007). *An introduction to copulas*. Springer Science & Business Media.

[288] Nguyen, L., Li, Q., and Nguyen, V. (2014). Effects of ENSO on SPEI/SPI drought indices in the Vietnam Songcai basin. *Advanced civil, urban and environmental engineering*, 2:453–464.

[289] Nicholls, N. (2010). Local and remote causes of the southern Australian autumn-winter rainfall decline, 1958–2007. *Climate dynamics*, 34(6):835–845.

[290] Nissen, K. M. and Ulbrich, U. (2017). Increasing frequencies and changing characteristics of heavy precipitation events threatening infrastructure in Europe under climate change. *Nat. Hazards Earth Syst. Sci.*, 17:1177–1190.

[291] NOAA (2012). North Atlantic Oscillation (NAO).

[292] NOAA (2020 (last access on February 20, 2020)). Daily Climate Timeseries: NAO: NOAA PSL. https://psl.noaa.gov/data/timeseries/daily/NAO/.

[293] NOAA (2020 (last access on January 2, 2021)). Daily Climate Timeseries: NAO: NOAA PSL. https://psl.noaa.gov/data/timeseries/daily/NAO/.

[294] Nogueira, J., Fernandes, P., and Nascimento, A. (2003). Composition of volatiles of banana cultivars from Madeira Island. *Phytochemical Analysis: An International Journal of Plant Chemical and Biochemical Techniques*, 14(2):87–90.

[295] Norrant, C. and Douguédroit, A. (2006). Monthly and daily precipitation trends in the Mediterranean (1950–2000). *Theoretical and Applied Climatology*, 83(1):89–106.

[296] Nunes, A. and Lourenço, L. (2015). Precipitation variability in Portugal from 1960 to 2011. *Journal of Geographical Sciences*, 25(7):784–800.

[297] Nurse, L. A., Sem, G., Hay, J. E., Suarez, A. G., Wong, P. P., Briguglio, L., and Ragoonaden, S. (2001). Small island states. *Climate change*, pages 843–875.

[298] Ojeda, M. M. d. V. G. V. (2018). *Climate-change projections in the Iberian peninsula: a study of the hydrological impacts*. PhD thesis, Universidad de Granada.

[299] Oliva, M. and Fritz, M. (2018). Permafrost degradation on a warmer Earth: Challenges and perspectives. *Current Opinion in Environmental Science & Health*, 5:14–18.

[300] Oo, H. T., Zin, W. W., and Kyi, C. C. T. (2020). Analysis of streamflow response to changing climate conditions using SWAT model. *Civil Engineering Journal*, 6(2):194–209.

[301] Osborn, T. J., Briffa, K. R., Tett, S. F., Jones, P. D., and Trigo, R. M. (1999). Evaluation of the North Atlantic Oscillation as simulated by a coupled climate model. *Climate Dynamics*, 15(9):685–702.

[302] Ouatiki, H., Boudhar, A., Ouhinou, A., Arioua, A., Hssaisoune, M., Bouamri, H., and Benabdelouahab, T. (2019). Trend analysis of rainfall and drought over the Oum Er-Rbia River Basin in Morocco during 1970–2010. *Arabian Journal of Geosciences*, 12(4):128.

[303] Ourbak, T. and Magnan, A. K. (2018). The Paris Agreement and climate change negotiations: Small Islands, big players. *Regional Environmental Change*, 18(8):2201–2207.

[304] Padilla, F. M., Mommer, L., de Caluwe, H., Smit-Tiekstra, A. E., Visser, E. J., and de Kroon, H. (2019). Effects of extreme rainfall events are independent of plant species richness in an experimental grassland community. *Oecologia*, 191(1):177–190.

[305] Palmer, W. C. (1965). Meteorological drought. Research Paper No. 45. Washington, DC: US Department of Commerce. *Weather Bureau*, page 59.

[306] Panda, A. and Sahu, N. (2019). Trend analysis of seasonal rainfall and temperature pattern in Kalahandi, Bolangir and Koraput districts of Odisha, India. *Atmospheric Science Letters*, 20(10):e932.

[307] Parker, W. S. (2016). Reanalyses and observations: What's the difference? *Bulletin of the American Meteorological Society*, 97(9):1565–1572.

[308] Parr, J. and Rogers, J. (2002). Water-Quality Monitoring in Anguilla. *Water and Environment Journal*, 16(2):96–99.

[309] Parracho, A., Melo-Gonçalves, P., and Rocha, A. (2016). Regionalisation of precipitation for the Iberian Peninsula and climate change. *Physics and Chemistry of the Earth, Parts A/B/C*, 94:146–154.

[310] Parry, M., Parry, M. L., Canziani, O., Palutikof, J., Van der Linden, P., and Hanson, C. (2007). *Climate change 2007: impacts, adaptation and vulnerability: Working group II contribution to the fourth assessment report of the Intergovernmental Panel on Climate Change*, volume 4. Cambridge University Press.

[311] Páscoa, P., Gouveia, C., Russo, A., and Trigo, R. M. (2017). Drought trends in the Iberian Peninsula over the last 112 years. *Advances in Meteorology*, 2017.

[312] Pecl, G. T., Araújo, M. B., Bell, J. D., Blanchard, J., Bonebrake, T. C., Chen, I.-C., Clark, T. D., Colwell, R. K., Danielsen, F., Evengård, B., et al. (2017). Biodiversity redistribution under climate change: Impacts on ecosystems and human well-being. *Science*, 355(6332).

[313] Penalba, O. and Rivera, J. (2016). Precipitation response to El Niño/La Niña events in Southern South America–emphasis in regional drought occurrences. *Advances in Geosciences*, 42:1–14.

[314] Pendergrass, A. G. and Hartmann, D. L. (2014). The atmospheric energy constraint on global-mean precipitation change. *Journal of climate*, 27(2):757–768.

[315] Pereira, L. S., Louro, V., Do Rosário, L., and Almeida, A. (2006). Desertification, territory and people, a holistic approach in the Portuguese context. In *Desertification in the Mediterranean Region. A Security Issue*, pages 269–289. Springer.

[316] Peters, W., Bastos, A., Ciais, P., and Vermeulen, A. (2020). A historical, geographical and ecological perspective on the 2018 European summer drought.

[317] Pfahl, S., O'Gorman, P. A., and Fischer, E. M. (2017). Understanding the regional pattern of projected future changes in extreme precipitation. *Nature Climate Change*, 7(6):423–427.

[318] Pfister, C., Weingartner, R., and Luterbacher, J. (2006). Hydrological winter droughts over the last 450 years in the Upper Rhine basin: a methodological approach. *Hydrological Sciences journal*, 51(5):966–985.

[319] Philandras, C., Nastos, P., Kapsomenakis, J., Douvis, K., Tselioudis, G., and Zerefos, C. (2011). Long term precipitation trends and variability within the Mediterranean region. *Natural Hazards and Earth System Sciences*, 11(12):3235.

[320] Pigott, T. D. (2001). A review of methods for missing data. *Educational research and evaluation*, 7(4):353–383.

[321] Pimenta, M. T., Santos, M. J., and Rodrigues, R. (1997). A proposal of indices to identify desertification prone areas. *Jornadas de reflexión sobre el Anexo IV de aplicatión para el Mediterrâneo Norte–Convenio de Lucha contra la Desertificación, Murcia (Spain)*.

[322] PNA (2015). Relatório n.º 1. Caracterização geral dos recursos hídricos e suas atualizações, enquadramento legal dos Planos e balanço hídricos do 1º ciclo. In *Plano Nacional da Água*. APA - Agência Portuguesa do Ambiente. Portugal.

[323] Polunchenko, A. S. and Tartakovsky, A. G. (2012). State-of-the-art in sequential change-point detection. *Methodology and computing in applied probability*, 14(3):649–684.

[324] Pomee, M. S. and Hertig, E. (2019). Statistical downscaling of temperature over the Euro-Mediterranean region: the role of sea surface temperature and soil moisture as additional predictors. In *Geophysical Research Abstracts*, volume 21.

[325] Pontes Filho, J. D., Portela, M. M., Marinho de Carvalho Studart, T., and Souza Filho, F. d. A. (2019). A Continuous Drought Probability Monitoring System, CDPMS, Based on Copulas. *Water*, 11(9):1925.

[326] Portela, M., Zelenáková, M., Santos, J., Purcz, P., Silva, A., and Hlavatá, H. (2015). Drought analysis in Slovakia: regionalization, frequency analysis and precipitation thresholds. *WIT Transactions on Ecology and the Environment*, 197:237–248.

[327] Portela, M. M. and Carvalho Quintela, A. d. (1998). Indícios de mudança climática em séries de precipitação em Portugal Continental. *Recursos Hídricos*, 19(2):41–74.

[328] Portela, M. M. and Carvalho Quintela, A. d. (2001). A diminuiçào da precipitaçào em épocas do año como indício de mudança climática: casos estudiados em Portugal continental. *Ingeniería del agua*, 8(1):79–92.

[329] Portela, M. M., Espinosa, L. A., Studart, T., and Zelenakova, M. (2019). Rainfall Trends in Southern Portugal at Different Time Scales. In *INCREaSE 2019. International Congress on Engineering and Sustainability in the XXI Century*, pages 3–19. Springer.

[330] Portela, M. M., Santos, J. F., and Silva, A. (2014). Trends in rainfall and streamflow series: Portuguese case studies. *International journal of safety and security engineering*, 4(3):221–248.

[331] Prada, S. (2000). *Geologia e recursos hídricos subterrâneos da ilha da Madeira. Dissertação para obtenção do Grau de Doutor em Geologia*. PhD thesis, Universidade da Madeira, Funchal (Portugal).

[332] Prada, S. and da Silva, M. (2001). Fog precipitation on the Island of Madeira (Portugal). *Environmental Geology*, 41(3):384–389.

[333] Prada, S., Da Silva, M., and Cruz, J. (2005a). Groundwater behaviour in Madeira, volcanic island (Portugal). *Hydrogeology Journal*, 13(5-6):800–812.

[334] Prada, S., da Silva, M. O., Figueira, C., Meneses, M., and Pontes, A. (2007). Fog water collection in Madeira Island (Portugal). In *Proceedings of the 4th International Conference on Fog, Fog Collection and Dew*, pages 22–27.

[335] Prada, S., Perestrelo, M., Nunes, A., Figueira, C., and Cruz, J. (2005b). Disponibilidades hídricas da Ilha da Madeira. *Proyecto AQUAMAC: técnicas y métodos para la gestion sostenible del agua en la Macaronesia*, pages 261–294.

[336] PRAM (2003). Plano Regional da Água da Regiao Autonoma da Madeira, PRAM, Relatorio Tecnico.

[337] Preisendorfer, R. and Mobley, C. (1988). *Principal component analysis in meteorology and oceanography*, volume 425. Elsevier Amsterdam.

[338] Prudhomme, C., Parry, S., Hannaford, J., Clark, D. B., Hagemann, S., and Voss, F. (2011). How well do large-scale models reproduce regional hydrological extremes in Europe? *Journal of Hydrometeorology*, 12(6):1181–1204.

[339] Puccetti, G., Wang, R., et al. (2015). Extremal dependence concepts. *Statistical Science*, 30(4):485–517.

[340] Qian, B., Corte-Real, J., and Xu, H. (2000). Is the North Atlantic Oscillation the most important atmospheric pattern for precipitation in Europe? *Journal of Geophysical Research: Atmospheres*, 105(D9):11901–11910.

[341] Queralt, S., Hernández, E., Barriopedro, D., Gallego, D., Ribera, P., and Casanova, C. (2009). North Atlantic Oscillation influence and weather types associated with winter total and extreme precipitation events in Spain. *Atmospheric Research*, 94(4):675–683.

[342] Radi, N. F. A., Zakaria, R., and Azman, M. A.-z. (2015). Estimation of missing rainfall data using spatial interpolation and imputation methods. In *AIP conference proceedings*, volume 1643, pages 42–48. AIP.

[343] Rahman, M. A., Yunsheng, L., and Sultana, N. (2017). Analysis and prediction of rainfall trends over Bangladesh using Mann–Kendall, Spearman's rho tests and ARIMA model. *Meteorology and Atmospheric Physics*, 129(4):409–424.

[344] Rahmstorf, S. and Coumou, D. (2011). Increase of extreme events in a warming world. *Proceedings of the National Academy of Sciences*, 108(44):17905–17909.

[345] Raja, N. B. and Aydin, O. (2019). Regionalization of precipitation in Mauritius: a statistical approach. *Meteorological Applications*, 26(4):711–719.

[346] Rajczak, J. and Schär, C. (2017). Projections of future precipitation extremes over Europe: a multimodel assessment of climate simulations. *Journal of Geophysical Research: Atmospheres*, 122(20):10–773.

[347] Ramjeawon, T. (1994). Water resources management on the small Island of Mauritius. *International Journal of Water Resources Development*, 10(2):143–155.

[348] Ramos, M. R. and Cordeiro, C. (2013). Trend tests in time series with missing values: A case study with imputation. In *AIP Conference Proceedings*, volume 1558, pages 1909–1912. AIP.

[349] Ramos-Calzado, P., Gómez-Camacho, J., Pérez-Bernal, F., and Pita-López, M. (2008). A novel approach to precipitation series completion in climatological datasets: application to Andalusia. *International Journal of Climatology: A Journal of the Royal Meteorological Society*, 28(11):1525–1534.

[350] Randles, R. (1988). Wilcoxon signed rank test. *Encyclopedia of statistical sciences*.

[351] Rao, G., Uppala, R., Singh, V., and Giridhar, M. (2015). Rainfall Trend Analysis: A Case Study of Godavari Sub Basin–Kadam Water Shed, Adilabad District, Telangana State. *3rd National Conference on Water, Environment and Society*.

[352] Rashid, M., Beecham, S., and Chowdhury, R. K. (2014). Influence of climate drivers on variability and trends in seasonal rainfall in the Onkaparinga catchment in South Australia: a wavelet approach. In *13th International conference on urban drainage (ICUD)*, volume 712.

[353] Rasmusson, E. M. and Wallace, J. M. (1983). Meteorological aspects of the El Nino/southern oscillation. *Science*, 222(4629):1195–1202.

[354] Raziei, T., Martins, D., Bordi, I., Santos, J., Portela, M. M., Pereira, L., and Sutera, A. (2015). SPI Modes of Drought Spatial and Temporal Variability in Portugal: Comparing Observations, PT02 and GPCC Gridded Datasets. *Water Resources Management*, 29(2):487–504.

[355] Raziei, T., Saghafian, B., Paulo, A. A., Pereira, L. S., and Bordi, I. (2009). Spatial patterns and temporal variability of drought in western Iran. *Water Resources Management*, 23(3):439–455.

[356] Renard, B. and Lang, M. (2007). Use of a Gaussian copula for multivariate extreme value analysis: some case studies in hydrology. *Advances in Water Resources*, 30(4):897–912.

[357] Rencher, A. C. (2002). *Methods of multivariate analysis. Second Ed*, volume 492. John Wiley & Sons.

[358] Richman, M. B. (1986). Rotation of principal components. *Journal of climatology*, 6(3):293–335.

[359] Rodrigo, F. and Trigo, R. M. (2007). Trends in daily rainfall in the Iberian Peninsula from 1951 to 2002. *International Journal of Climatology: A Journal of the Royal Meteorological Society*, 27(4):513–529.

[360] Rodrigues, D. and Ayala-Carcedo, F. J. (2003). Rain induced landslides and debris flows in Madeira Island, Portugal. *Landslide News*, 14-15(15):43–45.

[361] Rodríguez-Puebla, C. and Nieto, S. (2010). Trends of precipitation over the Iberian Peninsula and the North Atlantic Oscillation under climate change conditions. *International Journal of Climatology*, 30(12):1807–1815.

[362] Rodwell, M. J., Rowell, D. P., and Folland, C. K. (1999). Oceanic forcing of the wintertime North Atlantic Oscillation and European climate. *Nature*, 398(6725):320–323.

[363] Rossi, G. (2000). Drought Mitigation Measures: A Comprehensive Framework. In *Drought and Drought Mitigation in Europe*, pages 233–246. Springer Netherlands.

[364] Rowe, M. (1984). The freshwater "Central Lens" of Bermuda. *Journal of Hydrology*, 73(1-2):165–176.

[365] Royston, P. et al. (2004). Multiple imputation of missing values. *Stata journal*, 4(3):227–41.

[366] Royston, P. et al. (2009). Multiple imputation of missing values: further update of ice, with an emphasis on categorical variables. *Stata Journal*, 9(3):466.

[367] Rubin, D. (1976). Inference and missing data. *Biometrika*, 63(3):581–592.

[368] Rubin, D. (1987). Multiple imputation for nonresponse in surveys. new york: John wiley & sons inc. *Wiley Series in Probability and Statistics*.

[369] Rubin, D. (2004). *Multiple imputation for nonresponse in surveys*, volume 81. John Wiley & Sons.

[370] Rustum, R., Adeloye, A., and Mwale, F. D. (2017). Spatial and temporal trend analysis of long-term rainfall records in data-poor catchments with missing data, a case study of lower Shire flood plain in Malawi for the period of 1953–2010. *Hydrol Earth Syst Sci. https://doi. org/10.5194/hess-2017-601*.

[371] Rutkowska, A. (2015). Properties of the Cox–Stuart test for trend in application to hydrological series: the simulation study. *Communications in Statistics-Simulation and Computation*, 44(3):565–579.

[372] Sadoff, C. W., Borgomeo, E., and De Waal, D. (2017). *Turbulent Waters: Pursuing Water Security in Fragile Contexts*. World Bank.

[373] Salas, J. D., Fu, C., Cancelliere, A., Dustin, D., Bode, D., Pineda, A., and Vincent, E. (2005). Characterizing the severity and risk of drought in the Poudre River, Colorado. *Journal of Water Resources Planning and Management*, 131(5):383–393.

[374] Salazar, Y. (2011). General multivariate dependence using associated copulas. *Statistical Journal*, 14(1):1–28.

[375] Salvadori, G. and De Michele, C. (2007). On the use of copulas in hydrology: theory and practice. *Journal of Hydrologic Engineering*, 12(4):369–380.

[376] Sanches, F., Verdum, R., Fisch, G., Gass, S. L. B., Rocha, V. M., et al. (2019). Extreme Rainfall Events in the Southwest of Rio Grande do Sul (Brazil) and Its Association with the Sandization Process. *American Journal of Climate Change*, 8(04):441.

[377] Sanson, A. and Goodall, J. (2017). Developmental science's role in responding to the climate crisis. *ISSBD Bulletin*, 1(17):10–15.

[378] Santo, F. E., Ramos, A. M., de Lima, M. I. P., and Trigo, R. M. (2014). Seasonal changes in daily precipitation extremes in mainland Portugal from 1941 to 2007. *Regional environmental change*, 14(5):1765–1788.

[379] Santos, F. and Portela, M. M. (2008). Quantificação de tendências em séries de precipitação mensal e anual em Portugal Continental. *Seminário Ibero-Americano sobre Sistemas de Abastecimento Urbano SEREA*, 8.

[380] Santos, F., Valente, M., Miranda, P., Aguiar, A., Azevedo, E., Tomé, A., and Coelho, F. (2004). Climate change scenarios in the Azores and Madeira islands. *World Resource Review*, 16(4):473–491.

[381] Santos, F. D., Forbes, K., and Moita, R. (2002). *Climate change in Portugal: scenarios, impacts and adaptation measures: SIAM Project*. Gradiva.

[382] Santos, F. D. and Miranda, P. (2006). *Alterações climáticas em Portugal. Cenários, impactos e medidas de adaptação: Projecto SIAM II-1ª edição*, volume 14. Unidade de Silvicultura e Produtos Florestais.

[383] Santos, J., Corte-Real, J., and Leite, S. (2005). Weather regimes and their connection to the winter rainfall in Portugal. *International Journal of Climatology: A Journal of the Royal Meteorological Society*, 25(1):33–50.

[384] Santos, J., Portela, M., and Pulido-Calvo, I. (2011). Regional frequency analysis of droughts in Portugal. *Water Resources Management*, 25(14):3537.

[385] Santos, J., Pulido-Calvo, I., and Portela, M. (2010). Spatial and temporal variability of droughts in Portugal. *Water Resources Research*, 46(3).

[386] Santos, M. and Fragoso, M. (2013). Precipitation variability in Northern Portugal: data homogeneity assessment and trends in extreme precipitation indices. *Atmospheric research*, 131:34–45.

[387] Santos, M., Fragoso, M., and Santos, J. A. (2017). Regionalization and susceptibility assessment to daily precipitation extremes in mainland Portugal. *Applied Geography*, 86:128–138.

[388] Scaife, A., Arribas, A., Blockley, E., Brookshaw, A., Clark, R., Dunstone, N., Eade, R., Fereday, D., Folland, C., Gordon, M., et al. (2014). Skillful long-range prediction of European and North American winters. *Geophysical Research Letters*, 41(7):2514–2519.

[389] Scaife, A. A., Folland, C. K., Alexander, L. V., Moberg, A., and Knight, J. R. (2008). European climate extremes and the North Atlantic Oscillation. *Journal of Climate*, 21(1):72–83.

[390] Schafer, J. (1999). Multiple imputation: a primer. *Statistical methods in medical research*, 8(1):3–15.

[391] Schewe, J., Gosling, S. N., Reyer, C., Zhao, F., Ciais, P., Elliott, J., Francois, L., Huber, V., Lotze, H. K., Seneviratne, S. I., et al. (2019). State-of-the-art global models underestimate impacts from climate extremes. *Nature communications*, 10(1):1–14.

[392] Schlenker, W. and Auffhammer, M. (2018). The cost of a warming climate.

[393] Schneider, T. (2001). Analysis of incomplete climate data: Estimation of mean values and covariance matrices and imputation of missing values. *Journal of climate*, 14(5):853–871.

[394] Schweizer, B. and Sklar, A. (2011). *Probabilistic metric spaces*. Courier Corporation.

[395] Segers, J. (2012). Max-stable models for multivariate extremes. *arXiv preprint arXiv:1204.0332*.

[396] Sen, P. K. (1968). Estimates of the regression coefficient based on Kendall's tau. *Journal of the American statistical association*, 63(324):1379–1389.

[397] Sen, Z. (2016). *Spatial modeling principles in earth sciences*. Springer.

[398] Serreze, M. C., Carse, F., Barry, R. G., and Rogers, J. C. (1997). Icelandic low cyclone activity: Climatological features, linkages with the NAO, and relationships with recent changes in the Northern Hemisphere circulation. *Journal of Climate*, 10(3):453–464.

[399] Shannon, C. E. (1948). A mathematical theory of communication. *Bell system technical journal*, 27(3):379–423.

[400] Shao, W. and Kam, J. (2020). Retrospective and prospective evaluations of drought and flood. *Science of The Total Environment*, 748:141155.

[401] Sharif, M. and Burn, D. H. (2007). Improved k-nearest neighbor weather generating model. *Journal of Hydrologic Engineering*, 12(1):42–51.

[402] Sharifi, E., Saghafian, B., and Steinacker, R. (2019). Copula-based stochastic uncertainty analysis of satellite precipitation products. *Journal of hydrology*, 570:739–754.

[403] Sharma, S., Swayne, D. A., and Obimbo, C. (2016). Trend analysis and change point techniques: a survey. *Energy, Ecology and Environment*, 1(3):123–130.

[404] Sharma, T. (1997). A drought frequency formula. *Hydrological sciences journal*, 42(6):803–814.

[405] Sheffield, J. and Wood, E. F. (2008). Projected changes in drought occurrence under future global warming from multi-model, multi-scenario, IPCC AR4 simulations. *Climate dynamics*, 31(1):79–105.

[406] Shiau, J.-T. (2003). Return period of bivariate distributed extreme hydrological events. *Stochastic environmental research and risk assessment*, 17(1-2):42–57.

[407] Shiau, J.-T. (2006). Fitting drought duration and severity with two-dimensional copulas. *Water resources management*, 20(5):795–815.

[408] Shiau, J.-T. and Shen, H. W. (2001). Recurrence analysis of hydrologic droughts of differing severity. *Journal of Water Resources Planning and Management*, 127(1):30–40.

[409] Shin, J. Y., Chen, S., Lee, J.-H., and Kim, T.-W. (2018). Investigation of drought propagation in South Korea using drought index and conditional probability. *Terrestrial, Atmospheric & Oceanic Sciences*, 29(2).

[410] Sillmann, J., Kharin, V., Zhang, X., Zwiers, F., and Bronaugh, D. (2013a). Climate extremes indices in the CMIP5 multimodel ensemble: Part 1. Model evaluation in the present climate. *Journal of Geophysical Research: Atmospheres*, 118(4):1716–1733.

[411] Sillmann, J., Kharin, V. V., Zwiers, F., Zhang, X., and Bronaugh, D. (2013b). Climate extremes indices in the CMIP5 multimodel ensemble: Part 2. Future climate projections. *Journal of Geophysical Research: Atmospheres*, 118(6):2473–2493.

[412] Silva, A. (2017). *Nonstationarity and uncertainty of extreme hydrological events*. PhD dissertation, IST/UTL, Lisbon.

[413] Silva, A., Portela, M., and Naghettini, M. (2012). Nonstationarities in the occurrence rates of flood events in Portuguese watersheds. *Hydrology and Earth System Sciences*, 16(1):241–254.

[414] Silverman, B. W. (1986). *Density Estimation for Statistics and Data Analysis*. CRC Press, Boca Raton, Fla.

[415] Sklar, M. (1959). Fonctions de repartition an dimensions et leurs marges. *Publ. inst. statist. univ. Paris*, 8:229–231.

[416] Smith, S. W. (1997). *The scientist and engineer's guide to digital signal processing*. California Technical Publishing.

[417] Smolka, A. (2006). Natural disasters and the challenge of extreme events: risk management from an insurance perspective. *Philosophical Transactions of the Royal Society A: Mathematical, Physical and Engineering Sciences*, 364(1845):2147–2165.

[418] Sneyers, R. (1990). Technical note No 143 on the statistical analysis of series of observations. *World Meteorological Organization, Geneva, Switzerland*.

[419] SNIRH (2020 (accessed February 3, 2020)). *Sistema Nacional de Informação de Recursos Hídricos (2020): APA - Agência Portuguesa do Ambiente*.

[420] Soares, P. M., Cardoso, R. M., Ferreira, J. J., and Miranda, P. M. (2015). Climate change and the Portuguese precipitation: ENSEMBLES regional climate models results. *Climate dynamics*, 45(7-8):1771–1787.

[421] Soares, P. M., Cardoso, R. M., Miranda, P. M., Viterbo, P., and Belo-Pereira, M. (2012). Assessment of the ENSEMBLES regional climate models in the representation of precipitation variability and extremes over Portugal. *Journal of Geophysical Research: Atmospheres*, 117(D7).

[422] Soltani, M., Rousta, I., and Taheri, S. M. (2013). Using Mann-Kendall and time series techniques for statistical analysis of long-term precipitation in Gorgan weather station. *World Appl. Sci. J*, 28(7):902–908.

[423] Stahl, K., Blauhut, V., Kohn, I., Acácio, V., Assimacopoulos, D., Bifulco, C., De Stefano, L., Dias, S., Eilertz, D., Freilingsdorf, B., et al. (2012). A European drought impact report inventory (EDII): design and test for selected recent droughts in Europe. Technical report, Wageningen Universiteit, Hydrology and Quantitative Water Management WIMEK.

[424] Stooksbury, D. E., Idso, C. D., and Hubbard, K. G. (1999). The Effects of Data Gaps on the Calculated Monthly Mean Maximum and Minimum Temperatures in the Continental United States: A Spatial and Temporal Study. *Journal of Climate*, 12(5):1524–1533.

[425] Sun, X., Renard, B., Thyer, M., Westra, S., and Lang, M. (2015). A global analysis of the asymmetric effect of ENSO on extreme precipitation. *Journal of Hydrology*, 530:51–65.

[426] Sutton, R. T., Norton, W. A., and Jewson, S. P. (2000). The North Atlantic Oscillation—what role for the ocean? *Atmospheric Science Letters*, 1(2):89–100.

[427] Svoboda, M., Hayes, M., and Wood, D. (2012). Standardized precipitation index user guide. *World Meteorological Organization Geneva, Switzerland*.

[428] Tabari, H. (2020). Climate change impact on flood and extreme precipitation increases with water availability. *Scientific reports*, 10(1):1–10.

[429] Tabari, H., Madani, K., Arnbjerg-Nielsen, K., and Willems, P. (2019). Disentangling natural and forced components of extreme rainfall hazards over Europe. In *Geophysical Research Abstracts*, volume 21.

[430] Tabari, H. and Willems, P. (2018a). Anomalous extreme rainfall variability over Europe—interaction between climate variability and climate change. In *International Conference on Urban Drainage Modelling*, pages 375–379. Springer.

[431] Tabari, H. and Willems, P. (2018b). Lagged influence of Atlantic and Pacific climate patterns on European extreme precipitation. *Scientific reports*, 8(1):5748.

[432] Tallaksen, L. M. (2000). Streamflow drought frequency analysis. In *Drought and drought mitigation in Europe*, pages 103–117. Springer.

[433] Tallaksen, L. M., Hisdal, H., and Van Lanen, H. A. (2009). Space–time modelling of catchment scale drought characteristics. *Journal of Hydrology*, 375(3-4):363–372.

[434] Tallaksen, L. M., Madsen, H., and Clausen, B. (1997). On the definition and modelling of streamflow drought duration and deficit volume. *Hydrological Sciences Journal*, 42(1):15–33.

[435] Tallaksen, L. M. and Van Lanen, H. (2004). *Hydrological drought: processes and estimation methods for streamflow and groundwater*, volume 48. Elsevier.

[436] Taws, S. L., Marsh, R., Wells, N. C., and Hirschi, J. (2011). Re-emerging ocean temperature anomalies in late-2010 associated with a repeat negative NAO. *Geophysical Research Letters*, 38(20).

[437] Taylor, F. W. (2005). *Elementary climate physics*. Oxford Univ. Press.

[438] Teixeira, J., Carvalho, A., Carvalho, M., Luna, T., and Rocha, A. (2014). Sensitivity of the WRF model to the lower boundary in an extreme precipitation event–Madeira island case study. *Natural Hazards and Earth System Sciences*, 14(8):2009–2025.

[439] Terzago, S., Fratianni, S., and Cremonini, R. (2013). Winter precipitation in Western Italian Alps (1926–2010). *Meteorology and Atmospheric Physics*, 119(3):125–136.

[440] Thanh, N. T. (2019). Evaluation of multi-precipitation products for multi-time scales and spatial distribution during 2007-2015. *Civil Engineering Journal*, 5(1):255–267.

[441] Thiessen, A. H. (1911). Precipitation averages for large areas. *Monthly weather review*, 39(7):1082–1089.

[442] Thornthwaite, C. W. (1948). An approach toward a rational classification of climate. *Geographical review*, 38(1):55–94.

[443] Timbal, B. (2009). The continuing decline in south-east Australian rainfall—Update to May 2009. *CAWCR Research Letters*, 2(4-11).

[444] Tosunoglu, F. and Can, I. (2016). Application of copulas for regional bivariate frequency analysis of meteorological droughts in Turkey. *Natural Hazards*, 82(3):1457–1477.

[445] Tramblay, Y., El Adlouni, S., and Servat, E. (2013). Trends and variability in extreme precipitation indices over Maghreb countries. *Natural Hazards and Earth System Sciences*, 13(12):3235–3248.

[446] Trigo, R. M. and DaCamara, C. C. (2000). Circulation weather types and their influence on the precipitation regime in Portugal. *International Journal of Climatology: A Journal of the Royal Meteorological Society*, 20(13):1559–1581.

[447] Trigo, R. M., Pozo-Vázquez, D., Osborn, T. J., Castro-Díez, Y., Gámiz-Fortis, S., and Esteban-Parra, M. J. (2004). North Atlantic Oscillation influence on precipitation, river flow and water resources in the Iberian Peninsula. *International Journal of Climatology: A Journal of the Royal Meteorological Society*, 24(8):925–944.

[448] Trigo, R. M., Zêzere, J. L., Rodrigues, M. L., and Trigo, I. F. (2005). The influence of the North Atlantic Oscillation on rainfall triggering of landslides near Lisbon. *Natural Hazards*, 36(3):331–354.

[449] Trouet, V., Esper, J., Graham, N. E., Baker, A., Scourse, J. D., and Frank, D. C. (2009). Persistent positive North Atlantic Oscillation mode dominated the medieval climate anomaly. *science*, 324(5923):78–80.

[450] Turrado, C. C., López, M. d. C. M., Lasheras, F. S., Gómez, B. A. R., Rollé, J. L. C., and Juez, F. J. d. C. (2014). Missing data imputation of solar radiation data under different atmospheric conditions. *Sensors*, 14(11):20382–20399.

[451] Unal, Y., Kindap, T., and Karaca, M. (2003). Redefining the climate zones of Turkey using cluster analysis. *International journal of climatology*, 23(9):1045–1055.

[452] Uvo, C. B. (2003). Analysis and regionalization of northern European winter precipitation based on its relationship with the North Atlantic Oscillation. *International Journal of Climatology: A Journal of the Royal Meteorological Society*, 23(10):1185–1194.

[453] Van-Buuren, S. (2018). *Flexible imputation of missing data*. Chapman and Hall/CRC.

[454] Van-Buuren, S. and Groothuis-Oudshoorn, K. (2010). mice: Multivariate imputation by chained equations in R. *Journal of statistical software*, pages 1–68.

[455] Van-Buuren, S. and Oudshoorn, K. (1999). *Flexible mutlivariate imputation by MICE*. Leiden: TNO.

[456] Van Loon, A., Van Lanen, H., Hisdal, H., Tallaksen, L., Fendeková, M., Oosterwijk, J., Horvát, O., and Machlica, A. (2010). Understanding hydrological winter drought in Europe. *Global Change: Facing Risks and Threats to Water Resources, IAHS Publ*, 340:189–197.

[457] Van Loon, A., Van Lanen, H., Tallaksen, L., Hanel, M., Fendekova, M., Machlica, A., Sapriza, G., Koutroulis, A., Huijgevoort, M., Jódar, J., Hisdal, H., and Tsanis, I. (2011). *Propagation of drought through the hydrological cycle*. The WATCH project.

[458] Van Montfort, M. and Witter, J. (1986). The generalized pareto distribution applied to rainfall depths. *Hydrological Sciences Journal*, 31(2):151–162.

[459] Venter, G. (2002). Tails of Copulas. *Proceedings of the Casualty Actuarial Society*, 89.

[460] Veron, S., Mouchet, M., Govaerts, R., Haevermans, T., and Pellens, R. (2019). Vulnerability to climate change of islands worldwide and its impact on the tree of life. *Scientific reports*, 9(1):1–14.

[461] Vicente-Serrano, S. (2005a). El Niño and La Niña influence on droughts at different timescales in the Iberian Peninsula. *Water Resources Research*, 41(12).

[462] Vicente-Serrano, S. (2005b). *Las sequías climáticas en el valle medio del Ebro: Factores atmosféricos, evolución temporal y variabilidad espacial*. Consejo de Protección de la Naturaleza de Aragón.

[463] Vicente-Serrano, S. (2006). Differences in spatial patterns of drought on different time scales: an analysis of the Iberian Peninsula. *Water resources management*, 20(1):37–60.

[464] Vicente-Serrano, S., Aguilar, E., Martínez, R., Martín-Hernández, N., Azorín-Molina, C., Sánchez-Lorenzo, A., El Kenawy, A., Tomás-Burguera, M., Morán-Tejeda, E., López-Moreno, J., et al. (2017). The complex influence of ENSO on droughts in Ecuador. *Climate dynamics*, 48(1-2):405–427.

[465] Vicente-Serrano, S., López-Moreno, J., Lorenzo-Lacruz, J., El Kenawy, A., Azorin-Molina, C., Morán-Tejeda, E., Pasho, E., Zabalza, J., Beguería, S., and Angulo-Martínez, M. (2011). The NAO impact on droughts in the Mediterranean region. In *Hydrological, socioeconomic and ecological impacts of the North Atlantic Oscillation in the mediterranean region*, pages 23–40. Springer.

[466] Vicente-Serrano, S. M., Beguería, S., and López-Moreno, J. I. (2010). A multiscalar drought index sensitive to global warming: the standardized precipitation evapotranspiration index. *Journal of climate*, 23(7):1696–1718.

[467] Vieira, I., Barreto, V., Figueira, C., Lousada, S., and Prada, S. (2018). The use of detention basins to reduce flash flood hazard in small and steep volcanic watersheds–a simulation from Madeira Island. *Journal of Flood Risk Management*, 11:S930–S942.

[468] Villafuerte II, M., Matsumoto, J., Akasaka, I., Takahashi, H. G., Kubota, H., and Cinco, T. A. (2014). Long-term trends and variability of rainfall extremes in the Philippines. *Atmospheric research*, 137:1–13.

[469] Vink, G., Frank, L., Pannekoek, J., and Van Buuren, S. (2014). Predictive mean matching imputation of semicontinuous variables. *Statistica Neerlandica*, 68(1):61–90.

[470] Visbeck, M. H., Hurrell, J. W., Polvani, L., and Cullen, H. M. (2001). The North Atlantic Oscillation: past, present, and future. *Proceedings of the National Academy of Sciences*, 98(23):12876–12877.

[471] Voss, R., May, W., and Roeckner, E. (2002). Enhanced resolution modelling study on anthropogenic climate change: changes in extremes of the hydrological cycle. *International Journal of Climatology*, 22(7):755–777.

[472] Waheed, S. Q., Alobaidy, M. N., and Grigg, N. S. (2021). Characterizing Influence of Hydrologic Data Correlations on Climate Change Decision Variables: Evidence from Diyala River Basin in Iraq. *Journal of Hydrologic Engineering*, 26(3):04021001.

[473] Walker, G. and Bliss, W. (1932). World Weather V. Memories of the Royal eteorological. *Society*, 44:53–84.

[474] Wallace, J. M. and Gutzler, D. S. (1981). Teleconnections in the geopotential height field during the Northern Hemisphere winter. *Monthly weather review*, 109(4):784–812.

[475] Wang, C., Deser, C., Yu, J.-Y., DiNezio, P., and Clement, A. (2017). El Niño and southern oscillation (ENSO): a review. *Coral reefs of the eastern tropical Pacific*, pages 85–106.

[476] Wang, S. and Sobel, A. H. (2017). Factors controlling rain on small tropical islands: Diurnal cycle, large-scale wind speed, and topography. *Journal of the Atmospheric Sciences*, 74(11):3515–3532.

[477] Wang, W., Chen, Y., Becker, S., and Liu, B. (2015). Linear trend detection in serially dependent hydrometeorological data based on a variance correction Spearman rho method. *Water*, 7(12):7045–7065.

[478] Wang, W., Ertsen, M. W., Svoboda, M. D., and Hafeez, M. (2016). Propagation of drought: from meteorological drought to agricultural and hydrological drought. *Advances in Meteorology*, 2016.

[479] Wang, W., Lee, X., Xiao, W., Liu, S., Schultz, N., Wang, Y., Zhang, M., and Zhao, L. (2018). Global lake evaporation accelerated by changes in surface energy allocation in a warmer climate. *Nature Geoscience*, 11:410–414.

[480] Wang, X., Lang, X., and Jiang, D. (2020a). Linkage of future regional climate extremes to global warming intensity. *Climate Research*, 81:43–54.

[481] Wang, Y., Xu, Y., Tabari, H., Wang, J., Wang, Q., Song, S., and Hu, Z. (2020b). Innovative trend analysis of annual and seasonal rainfall in the Yangtze River Delta, eastern China. *Atmospheric Research*, 231:104673.

[482] Wanner, H., Brönnimann, S., Casty, C., Gyalistras, D., Luterbacher, J., Schmutz, C., Stephenson, D. B., and Xoplaki, E. (2001). North Atlantic Oscillation–concepts and studies. *Surveys in geophysics*, 22(4):321–381.

[483] Wen, L., Rogers, K., Ling, J., and Saintilan, N. (2011). The impacts of river regulation and water diversion on the hydrological drought characteristics in the Lower Murrumbidgee River, Australia. *Journal of Hydrology*, 405(3-4):382–391.

[484] Wesonga, R. (2015). On multivariate imputation and forecasting of decadal wind speed missing data. *SpringerPlus*, 4(1):1–8.

[485] Westra, S., Alexander, L. V., and Zwiers, F. W. (2013). Global increasing trends in annual maximum daily precipitation. *Journal of Climate*, 26(11):3904–3918.

[486] White, D., Richman, M., and Yarnal, B. (1991). Climate regionalization and rotation of principal components. *International Journal of Climatology*, 11(1):1–25.

[487] White, I., Royston, P., and Wood, A. (2011). Multiple imputation using chained equations: issues and guidance for practice. *Statistics in medicine*, 30(4):377–399.

[488] Wikarmpapraharn, C., Kositsakulchai, E., et al. (2010). Relationship between ENSO and rainfall in the Central Plain of Thailand. *Kasetsart Journal (Natural Science)*, 44:744–755.

[489] Wilby, R., O'hare, G., and Barnsley, N. . (1997). The North Atlantic Oscillation and British Isles climate variability, 1865–1996. *Weather*, 52(9):266–276.

[490] Wise, J. (1955). The autocorrelation function and the spectral density function. *Biometrika*, 42(1/2):151–159.

[491] WMO (1992). International Meteorological Vocabulary. World Meteorological Organization -No. 182. Technical report, WMO/OMM/IMGW, 182, Geneva.

[492] WMO (2009). (World Meteorological Organization. Guide to hydrological practices, volume II management of water resources and application of hydrological practices.

[493] WMO (2017a). WMO Drought Initiatives: High-Level Meeting on National Drought Policy (HMNDP) and Integrated Drought Management Programme (IDMP) (2017).

[494] WMO (2017b). WMO Guidelines on the Calculation of Climate Normals. Technical report, World Meteorological Organization (WMO)/OMM/IMGW, 182, Geneva.

[495] Wong, G., Lambert, M. F., and Metcalfe, A. V. (2007). Trivariate copulas for characterisation of droughts. *Anziam Journal*, 49:C306–C323.

[496] Wu, Z., Xu, H., Li, Y., Wen, L., Li, J., Lu, G., and Li, X. (2018). Climate and drought risk regionalisation in China based on probabilistic aridity and drought index. *Science of the Total Environment*, 612:513–521.

[497] Xia, Y., Fabian, P., Stohl, A., and Winterhalter, M. (1999). Forest climatology: estimation of missing values for Bavaria, Germany. *Agricultural and Forest Meteorology*, 96(1-3):131–144.

[498] Xia, Y., Fabian, P., Winterhalter, M., and Zhao, M. (2001). Forest climatology: estimation and use of daily climatological data for Bavaria, Germany. *Agricultural and Forest Meteorology*, 106(2):87–103.

[499] Xu, H., Kim, H.-M., Nye, J. A., and Hameed, S. (2015a). Impacts of the North Atlantic Oscillation on sea surface temperature on the Northeast US Continental Shelf. *Continental Shelf Research*, 105:60–66.

[500] Xu, K., Yang, D., Xu, X., and Lei, H. (2015b). Copula based drought frequency analysis considering the spatio-temporal variability in Southwest China. *Journal of Hydrology*, 527:630–640.

[501] Yang, Y. and Tian, F. (2009). Abrupt change of runoff and its major driving factors in Haihe River Catchment, China. *Journal of Hydrology*, 374(3-4):373–383.

[502] Yarnal, B. (1993). *Synoptic climatology in environmental analysis: a primer*. Belhaven.

[503] Ye, H. (2018). Changes in duration of dry and wet spells associated with air temperatures in Russia. *Environmental Research Letters*, 13(3):034036.

[504] Yevjevich, V. M. (1967). An objective approach to definitions and investigations of continental hydrologic droughts. *Hydrology papers (Colorado State University); no. 23*.

[505] Young, T. and Mohlenkamp, M. (2008). Introduction to Numerical Methods and Matlab Programming. *Lecture Notes, Ohio University*.

[506] Yu, B. and Neil, D. (1993). Long-term variations in regional rainfall in the south-west of Western Australia and the difference between average and high intensity rainfalls. *International Journal of Climatology*, 13(1):77–88.

[507] Zeleňáková, M., Purcz, P., Portela, M. M., Hlavatá, H., and Gargar, I. (2014). Investigation of the trends in Rainfall Data in Slovakia, Portugal and Libya. *Parte: http://hdl. handle. net/10316.2/34789*.

[508] Zelenhasić, E. and Salvai, A. (1987). A method of streamflow drought analysis. *Water resources research*, 23(1):156–168.

[509] Zhang, L. and Singh, V. P. (2007). Bivariate rainfall frequency distributions using Archimedean copulas. *Journal of Hydrology*, 332(1-2):93–109.

[510] Zhang, S., Liu, D., Huang, Q., Wei, X., Feng, J., and Lin, M. (2017). The effect of time series length on runoff characteristics analysis. In *IOP Conference Series: Earth and Environmental Science*, volume 82, page 012047. IOP Publishing.

[511] Zhang, W. and Villarini, G. (2017). Heavy precipitation is highly sensitive to the magnitude of future warming. *Climatic Change*, 145(1-2):249–257.

[512] Zhang, Z. (2016). Multiple imputation with multivariate imputation by chained equation (MICE) package. *Annals of translational medicine*, 4(2).

THIS PAGE INTENTIONALLY LEFT BLANK

Appendix A

Long-Term Rainfall Trends and Their Variability in Portugal in the Last 106 Years [1]

This chapter has been published as: Portela, M. M., Espinosa, L. A., and Zelenakova, M. (2020). Long-Term Rainfall Trends and Their Variability in Mainland Portugal in the Last 106 Years. *Climate*, 8(12): 146, https://doi.org/10.3390/cli8120146

Abstract

This study addresses the long-term rainfall trends, their temporal variability and uncertainty over mainland Portugal, a small country in the most western European coast. The study was based on monthly, seasonal and annual rainfall series spanning for the period of 106 years, between October 1913 and September 2019 ((herein after referred to as global period), at 532 rain gauges evenly distributed over the country (c.a. 6 rain gauges per 1000 km^2). To understand the rainfall behaviour over time, an initial subperiod with 55 years and a final subperiod with 51 years were also analysed along with the global period. The trends identification and the assessment of their magnitude were derived utilising the non-parametric Mann–Kendall (MK) test coupled with the Sen's slope estimator method. The results showed that, after the initial subperiod with prevailing increasing rainfall, the trends were almost exclusively decreasing. They were also so pronounced that counterbalanced the initial rainfall increase and resulted in equally decreasing trends for the global period. The study also shows that, approximately from late 1960 on, the rainy season pattern has changed, with the last months prior to the dry season showing a sustained decrease of their relative contributions to the annual rainfalls. Overall, the results support the hypothesis of less uncertainty on the pronounced decrease of rainfall over mainland Portugal in recent years which is expected to continue. They also show that the asymmetry between a less wet North, yet still wet, and an arid South is becoming much more marked.

Keywords:

Climate change; mainland Portugal; rainfall trends; Mann-Kendall test; Sen's slope test.

[1] The references related to Appendix A are included in the Bibliography.

A.1 Introduction

Progressively more noticeable signs of climate change have been detected in recent years, in the form of increased climate variability, more and worse extreme hydrological events, rising temperature and sea level, among others [44, 101, 317]. Such signs have become large enough to exceed the bounds of their historical natural variability.

According to the periodical reports of the Intergovernmental Panel on Climate Change, IPCC [255, 310, 31], the increasing sea surface temperature and the consequent intensification of the hydrological cycle [33] has a significant effect on the rainfall, which is expected to increase globally [214]. Nevertheless, at regional and local scales, decreasing trends in rainfall are also expected [255, 242]. This is the case of the Iberian Peninsula, in which mainland Portugal is located, where the rainfall amounts are projected to decrease throughout the 21st century, and become more clustered into extreme rainfall events [281, 298, 420, 267, 381, 382].

Regarding the recent climate evolution, the high northern latitudes have registered rainfall increases, while from 10°S to 30°N decreases were reported from the 1970s onward [33]. This also applies to Europe, with increasing rainfall in its higher latitudes and decreasing rainfall in the Mediterranean region particularly in its western and central parts [378]. Such decrease in the rainfall is aligned with the general trend throughout the 21st century pointed out by Gibelin and Déqué [148] and Giorgi and Lionello [151].

Specifically for the Mediterranean region, there are several studies making use of ground-based data about rainfall, drought characteristics, and moisture availability trends during the 20th century, e.g., [295, 90, 319, 130, 237], but few have addressed climate variability in the early years of the 21st century, e.g., [17, 311, 329]. However, such type of studies needs to be continuously updated, as the changes of most of the hydrological variables are related to active and ongoing processes that may be more or less visible depending on the materials and models, time-windows, and lengths of the analysed time series data.

Rainfall is the source of water of the hydrological cycle [383, 242]. Hence, the detection and quantification of trends and of abrupt changes (within-the-year or among years) in its series are fundamental issues to understand the susceptibility of the hydrological environment to the effects of the climate change, namely in terms of fresh water availability. With this in mind, long-term and recent rainfall trends at different time scales, and their fluctuation and uncertainty are analysed for mainland Portugal aiming at understanding how they changed over time.

A decrease in the rainfall has been generally pointed out for mainland Portugal. However, the results from the general circulation models (GCM) applied to different climate scenarios show substantial differences, meaning that there is a considerable uncertainty about future projections of the rainfall amounts and that the numerical models of climate change prediction are in need of further insights [381, 382]. To reduce uncertainty in rainfall changes studies, the use of spatially-dense ground-based observations can be an alternative to the GCM. For this purpose, long data series must be available at a high number of monitoring points to ensure a comprehensive description of the temporal and spatial variability of the rainfall at different timescales over the study region [75, 152].

However, the majority of the studies on the topic for Portugal have been based on a few rain gauges or on rainfall series generally with short records length. This was the case of the novel studies of Portela and Carvalho Quintela [327, 328], which used monthly rainfall series, almost from the beginning to the end of the 20th century (average length of the records of 90 years), but only at 11 rain gauges scattered over the country. Following the previous studies, it is worth mentioning de Lima et al. [87], that used 107 rain gauges with 69 years of monthly data, from 1941 to 2000; Rodrigo and Trigo [359], that addressed rainfall trends over the Iberian Peninsula, from 1951 to 2002, based on 22 rain gauges, 7 of which located in Portugal; and the wide-ranging analysis of Santos and Portela [379], that used 94 years, from 1910 to 2004, of monthly rainfall series at 144 rain gauges regularly distributed over the country. The last authors showed that the high spatial rainfall variability hampers the establishment of an overall pattern of the rainfall changes. In fact, most of the detected monthly and annual rainfall trends had no statistical significance (except for March with generalised pronounced decrease), but instead were within the limits of the natural temporal rainfall variability.

Other contributions on the subject for mainland Portugal using ground-based observations are those of de Lima *et al.* [85, 86], based on only 10 rain gauges over Portugal, albeit with long recording series, and of Santo et al. [378], and de Lima et al. [88] that used daily data from 1941 to 2007 at 57 rain gauges to ascertain seasonal variations and trends in the intensity, frequency and duration of daily rainfall extremes. Portela et al. [330] summarises previous studies done by the authors to Portugal, including trend analysis applied to streamflow series, and Nunes and Lourenço [296] analyses the monthly and annual rainfall trends from 1960 to 2011 at 42 rain gauges. A more recent study by Portela et al. [329] used 108 years of monthly records at 62 rain gauges densely covering part of southern Portugal (study area of 16000 km^2, i.e., approx. 18% of mainland Portugal) where the rainfall decrease is a major problem due to the water scarcity that already characterises the region [315]. Such study revealed that, in general, the upward rainfall trends in the early years of the 20th century switched to pronounced significant downward trends in recent years. It also revealed that the intra-annual rainfall pattern is changing, namely in what concerns the more contributory months of the year.

The present research work updates the results from the previous studies, with emphasis on those of Portela et al. [329] by expanding them to the entire country, employing up-to-date ground-based data covering both, a long period (106 years, from 1913/1914 to 2018/2019) and a large number of rain gauges (532 rain gauges, c.a., 6 rain gauges per 1000 km^2) thus, providing a comprehensive assessment of the temporal and spatial rainfall variability over Portugal.

Following this introduction, Section A.2 presents the study area, the rainfall data that supported the research, the procedure applied to fill in the monthly rainfall gaps, and the models used to characterise the rainfall trends. Section A.3 reports the results achieved. Finally, Section A.4 provides a discussion and some relevant conclusions from the trend analysis.

The main findings of this research evidence a widespread decrease of the rainfall over Portugal, especially from 1960 onwards, that is also resulting in a more pronounced asymmetry between a still relatively wet North and a dry South. The overall rainfall decrease is becoming less uncertain, reinforcing the evidence of a future with less fresh water availability and, consequently, the need of widespread

public awareness and participation towards common water-saving practices. The public institutions and those responsible for the water resources policies also need to increase their capacity building aiming at urgent implementation of mitigation and adaptation measures and of new water resources planning and management policies.

A.2 Materials and methods

A.2.1 Study area

The rainfall trend analysis considered mainland Portugal, with approx. 89000 km^2, as study area. The country is located in the western part of the Iberian Peninsula (37° to 42°N and 6° to 9.5°W), facing the Atlantic Ocean, in the transitional region between the sub-tropical anticyclone and the subpolar depression zones (Figure A-1). The major natural factors that condition the climate of the country are the latitude, the topography, ranging from approx. 0 to 2000 m.a.m.s.l., and the effect of the North Atlantic Ocean as the most eastern regions of the country are only c.a. 220 km away from it [446, 36]. The mean annual rainfall over Portugal varies from more than 2800 mm, in the north-western region, to less than 400 mm, in the southern region, following a complex spatial pattern (N–S / E–W), in close connection with the relief [385].

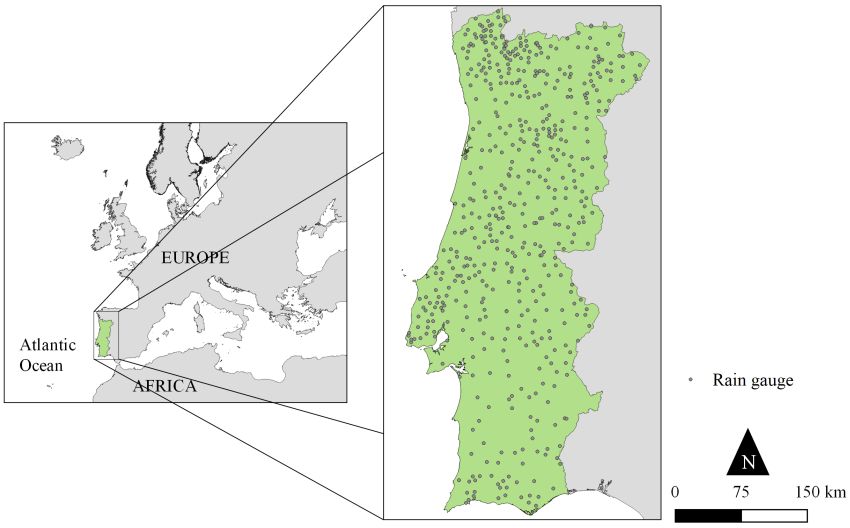

Figure A-1: General location of mainland Portugal and of the rain gauges with complete monthly data in the period of 106 years, from 1913/1914 to 2018/2019 used in the study (532 rain gauges).

A.2.2 Rainfall dataset

The original rainfall records used in the study span from October 1910 to September 2019 (109 hydrological years, each starting October 1st), but later adopting the reference period from October 1913 to September 2019. The records were acquired from 764 rain gauges of the public database of the Portuguese Environment Agency, the *Sistema Nacional de Informação de Recursos Hídricos* (SNIRH) [419]. All the rain gauges have incomplete series, as briefly characterised in Figures A-2 and A-3.

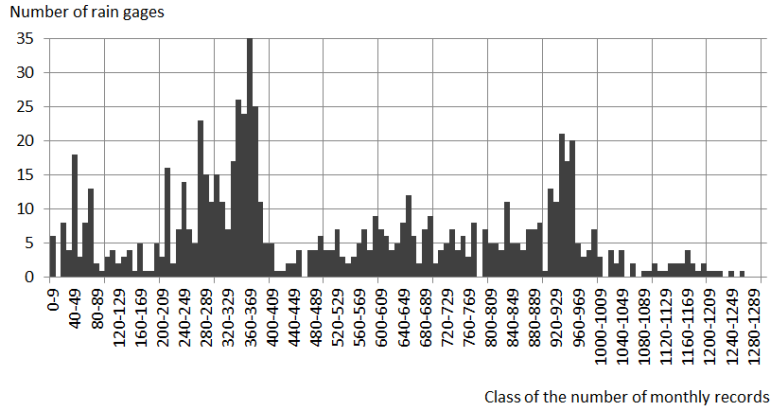

Figure A-2: SNIRH database [419]. Number of rain gauges, out of 764 rain gauges, per class of available number of monthly records, from October 1910 to September 2019 (total number of months of $109 \times 12 = 1308$).

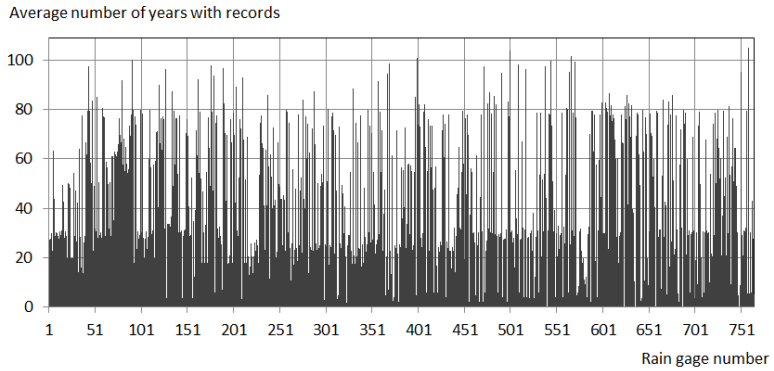

Figure A-3: SNIRH database [419]. Average number of years per rain gauge with monthly records, from October 1910 to September 2019.

Figure A-2 shows a histogram of the number of rain gauges per class of number of available monthly records from October 1910 on. The amplitude of the classes is equal to 10, except for the last class whose upper limit coincides with the number of months of the recording period ($109 \times 12 = 1308$ months). Figure A-3 indicates the average number of years with monthly records in each rain gauge, obtained by dividing the number of available monthly records by 12. The number of rain gauges with, in average, 20, 40 and 60 years with monthly records is 641, 374 and 242, respectively. Although the previous characterisation does not provide any information about the regularity of the distribution of the records along the different months, it shows that there is a considerable amount of monthly rainfall series, although with several gaps.

To fill the gaps aiming at obtaining continuous rainfall series a linear regression model based on an each-gap specific equation was applied [385, 329]. For a rainfall gap in month m of year n, in a given rain gauge, R_i, the model identifies the candidate rain gauges, R_j, with $j = 1, ..., k$ and $j \neq i$, where k is the number of rain gauges, with records in month m of year n and, therefore, that can be used to fill the gap. These gauges are next ranked according to the correlation coefficient between paired rainfall series in month m in years other than n, at the rain gauge with the gap, R_i, and at each of the candidate rain gauges, R_j.

From the candidate rain gauges, the one with the highest correlation coefficient between the previous paired monthly rainfall series is used to fill the gap based on a linear regression model applied to those series, provided two requisites are met: the length of the two paired rainfall series in month m and the correlation coefficient between those series must be higher than prefixed minimum values, so that the regression model is valid and the dependency structure significant. Regarding the length, a minimum value of $m = 15$ years was adopted. Because 83 out of the 764 rain gauges had less than 15 rainfall records in any month, they were discarded from the filling-gap procedure, which therefore proceeded with 681 rain gauges.

Regarding the correlation coefficient, two values were considered: 0.7 for the months from October to June, where rainfall is expected to occur in Portugal, and 0.6 for the months from July to September with negligible rainfall amounts (approx. 7% of the annual amount), often due to erratic short duration rainfall events over very small areas. In the establishment of the linear regression models only recorded values are considered (and not the values resulting from the gap filling procedure).

For the period from 1913/1914 to 2018/2019, the previous approach led to 288 rain gauges with complete series and to 244 rain gauges, each with less than 10 monthly gaps. Taking into account the very small number of still remaining gaps compared to the number of months or even to the number of years of the period (in each rain gauge, less than 10 months out of $106 \times 12 = 1272$ months, and less than 1 year, out of 106 years), it was decided to assign the historical monthly averages (i.e., averages prior the gap-filling procedure) to those gaps. This resulted in the set of 532 rain gauges schematically located in Figure A-1, covering almost uniformly the country (c.a. 6 rain gauges per 1000 km^2), with continuous monthly rainfall data over a global period of 106 years.

A.2.3 Long-term trend analysis models

The well-known rank-based non-parametric Mann-Kendall test was applied to assess the significant trends [247, 211]. The adopted significance level was $\alpha = 0.05$. The magnitude of the monotonic trends was measured based on the Sen's slope estimator test [396]. A positive value of the Sen's slope estimator indicates an increasing (or upward) trend and a negative value a decreasing (or downward) trend in the time series.

In order to produce maps with the spatial variability of the magnitude of the trends at a given time scale, the Sen's estimator was computed for all the corresponding rainfall time series regardless the statistical significance of the results from Mann-Kendall test.

A.3 Results

A.3.1 Rainfall characterisation

Figure A-4 presents a simplified characterisation of the intra-annual distribution of the rainfall over mainland Portugal based on the continuous monthly rainfall data at the 532 rain gauges used in the study (Figure A-1). Each seasonal rainfall was weighted according to the grid generated by the cubic

spline interpolation [259, 107]. As the study adopted hydrological years (starting each October and finishing next September), the definition of the quarters, Q, and of the semesters, S, is as follows: Q1 – October to December; Q2 – January to March; Q3 – April to June; Q4 – July to September; S1 – October to March; and S2 – April to September. In the table, the rainfalls are expressed in absolute values and in dimensionless values obtained by dividing the average rainfall in each month and season by the mean annual rainfall that result from the entire set of data, i.e., approx. 961 mm.

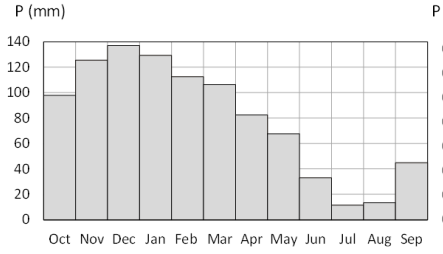

Season		Rainfall, P (mm)	P/Pyear (-)
Month	October	98	0.102
	November	125	0.131
	December	137	0.142
	January	129	0.135
	February	113	0.117
	March	106	0.111
	April	82	0.086
	May	68	0.070
	June	33	0.034
	July	12	0.012

Season		Rainfall, P (mm)	P/Pyear (-)
Month	August	13	0.014
	September	45	0.047
Quarter	Q1	360	0.375
	Q2	348	0.362
	Q3	183	0.190
	Q4	70	0.073
Semester	S1	708	0.737
	S2	253	0.263
Year (Pyear)		961	1.000

Figure A-4: Average monthly (figure and table) and seasonal (table) rainfalls at the 532 rain gauge locations of Figure A-1 in the period from 1913/1914 to 2018/2019 expressed in mm and by their relative contribution to the mean annual rainfall. Q1 to Q4 stand for the quarters and S1 and S2 for the semesters of the hydrological year.

According to Figure A-4, the average contribution of the wet semester, S1, from October to March, to the annual amount of rainfall is ca. 74%, approximately equally distributed by its two first quarters, Q1 and Q2. The less contributing quarter of the year is the last one, Q4, from July to September, which only accounts for ca. 7% of the mean annual rainfall. These results are in accordance with the rainfall characterisation of the National Water Plan [322].

Along with the analysis for the 106-year global period (from 1913/1914 to 2018/2019), two subperiods were also considered: (i) the initial 55 years, from October 1913 to September 1968, and (ii) the final 51 years, from October 1968 to September 2019. This partition was done to ascertain if the rainfall trends became more pronounced recently, as reported by [329] for southern Portugal. The starting year of the final subperiod coincides with the one previously adopted in the study for the south of the country, based on the application of the Sequential Mann Kendall test [62, 418], although to a period slightly different from the one now adopted (from October 1910 to September 2017). This is also in accordance with the findings by [25], showing that a number of important characteristics of the global atmospheric circulation and climate changed in a near-monotonic fashion over the decade centered on the late 1960s.

The map of the mean annual rainfall over mainland Portugal derived from the cubic spline interpolation technique applied to the mean annual rainfalls at the 532 rain gauges is presented in Figure A-5. Besides the global period, the two previous subperiods were included for a better perception of the annual rainfall changes. The cubic spline interpolation was applied to the mean annual rainfall in mainland Portugal, because it gives a smoother interpolation, when dealing with high-density rain gauge network, compared to the other interpolation methods [505].

Based on Figure A-5 it is easy to follow the spatio-temporal rainfall changes, with generally wetter conditions in the 55-year initial subperiod (Figure A-5b) even in the inner southern of Portugal, and drier conditions in the 51-year final subperiod (Figure A-5c). The decrease of the mean annual rainfall

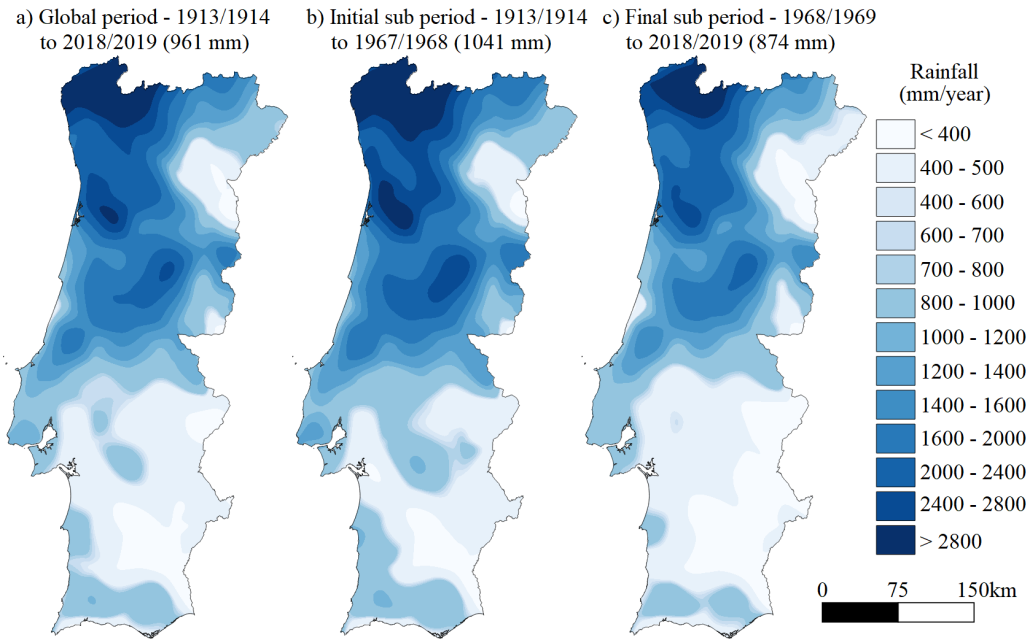

Figure A-5: Mean annual rainfall maps for the global period (106 years) and for the initial (55 years) and final (51 years) subperiods based on the 532 rain gauges schematically located in Figure A-1 (between brackets, the weighted mean annual rainfall in each period given by the cubic spline interpolation).

from one period to the other is almost 170 mm. This affects the whole country, but also emphasises the asymmetry in the rainfall distribution between the wetter north and the drier south, the latter being recognised as suffering a progressive desertification process [321, 69].

A.3.2 Mann-Kendall test and Sen's slope estimates

The trends at the 532 rain gauges were characterised via the Mann-Kendall and Sen's slope estimator tests at the annual level but also at the quarterly (Q1 to Q4) and semi-annual (S1 and S2) timescales aiming to ascertain the intra-annual signs of the climate change [386, 329]. For each of the periods and time scales, Table A.1 summarises the number of rain gauges with significant trends and the corresponding extreme (maximum, for increasing trends, and minimum, for decreasing trends) and mean values of the Sen's slope estimates. The results related to negative (downward) and positive (upward) trends are highlighted in blue and yellow, respectively. Additionally, Figures A-6 to A-8 present the spatial distribution of the values of the Sen's slope, regardless their statistical significance.

Table A.1 clearly indicates that, after the initial 55-year period mostly with positive significant rainfall trends, a more recent 51-year period almost exclusively with negative significant trends occurred. The only exception are the summer months of July and August, which nevertheless have very small contributions to the annual rainfall (1.2 and 1.4%, respectively — Figure A-4). The negative trends in the final subperiod were so pronounced that they counterbalanced the positive trends in the first period and resulted in more frequent negative trends for the whole period, albeit less marked. This is the case, for instance, of the annual rainfall with 505 rain gauges with a mean significant downward trend of -11.42 mm/year in the final subperiod, whereas the equivalent numbers for the global period are 428 and -4.27 mm/year, respectively. These results are aligned with those of [329] for the south of Portugal.

Table A.1: Summary of the significant trends for the 106-year period and for its initial 55 years and final 51 years. Number of rain gauges with significant trends. Maximum (positive), minimum (negative) and average values of the Sen's slope estimates for the significant increasing (in blue) and decreasing (in yellow) trends, respectively.

	106-year global period (1913/1914 to 2018/2019)					55-year initial subperiod (1913/1914 to 1967/1968)					51-year final subperiod (1968/1969 to 2018/2019)				
Period of the year	Positive trends		Negative trends			Positive trends		Negative trends			Positive trends		Negative trends		
	Number of rain gauges	Maximum value (mm/year)	Number of rain gauges	Maximum value (mm/year)	Mean value (mm/year)	Number of rain gauges	Maximum value (mm/year)	Number of rain gauges	Maximum value (mm/year)	Mean value (mm/year)	Number of rain gauges	Maximum value (mm/year)	Number of rain gauges	Maximum value (mm/year)	Mean value (mm/year)
Oct	9	0.67	2	-0.71	0.24	8	2.75	0	–	1.31	0	–	17	-3.19	-2.17
Nov	0	–	263	-2.89	-0.85	24	4.45	0	–	2.12	0	–	134	-5.51	-2.25
Dec	1	0.15	231	-2.94	-0.95	6	1.99	3	-2.95	0.20	0	–	179	-6.29	-2.40
Jan	1	0.26	124	-2.74	-0.86	6	1.90	1	-0.55	0.83	0	–	479	-9.45	-2.72
Feb	0	–	189	-2.57	-0.58	3	2.92	0	–	2.10	0	–	353	-5.92	-2.09
Mar	0	–	517	-2.92	-0.92	13	3.36	0	–	1.49	0	–	89	-3.13	-1.31
Apr	0	–	65	-0.94	-0.48	10	1.77	0	–	1.06	0	–	25	-1.93	-0.97
May	0	–	145	-1.50	-0.56	2	0.49	10	-1.92	-0.76	0	–	312	-4.87	-1.59
Jun	0	–	230	-0.99	-0.34	11	0.89	2	-0.85	0.22	0	–	338	-2.9	-0.72
Jul	23	0.40	113	-0.98	-0.30	42	0.50	220	-0.98	-0.38	10	0.92	30	-0.97	-0.18
Aug	58	0.90	14	-0.96	0.16	64	0.90	12	-0.80	0.20	42	0.90	3	-0.46	0.29
Sep	4	0.84	72	-0.79	-0.36	12	1.19	0	–	0.45	0		79	-2.67	-1.26
Q1	1	1.00	221	-5.58	-2.15	23	9.93	8	-6.88	0.07	0	–	175	-14.68	-6.00
Q2	0	–	492	-7.28	-2.15	25	13.54	0	–	0.28	0	–	492	-19.97	-5.26
Q3	0	–	193	-3.77	-1.08	12	1.90	0	–	0.03	0	–	372	-9.46	-2.83
Q4	7	0.68	73	-1.38	-0.59	21	2.30	1	-0.28	0.03	0	–	127	-4.84	-1.89
S1	0	–	446	-12.19	-3.61	63	21.14	3	-10.39	0.69	0	–	461	-36.84	-8.74
S2	0	–	189	-4.16	-1.40	31	5.24	0	–	0.11	0	–	399	-12.71	-3.44
Year	0	–	428	-15.36	-4.27	74	26.58	3	-11.60	0.89	0	–	505	-49.98	-11.42

The comparison of Figures A-6 to A-8 reinforces the results of Table A.1 by highlighting the exceptional and, for some timescales, widespread extent of the decreasing trends in the last 51 years, specially in contrast with the initial 55 years. The results for the quarters, semesters and year are especially marked, with reduction of the rainfall in some rain gauges often greater than 9 mm/year in the last 51 years. The figures also point out some important information regarding the monthly distribution of the rainfall. In fact, when looking at the 106-year global period, March appears as the month with the highest number of significant and pronounced trends. However, when considering the most recent subperiod it is notorious that the more noticeable trends occur in the months before, namely in January and especially in February. The shift between February and March is also evident based on the number of rain gauges with significant decreasing trends, as reported in Table A.1: for the global period, 189 in February and 517 in March; the equivalent values for the last 51 years are 479 and 353. These results suggest that the decrease of the rainfall is moving "backwards" and progressively affecting the months before March.

The identified "backwards" behaviour resulted in aggravated decreasing rainfall trends in the last 51 years compared to the global period. For Q2, i.e., from January to March, the average decrease of the rainfall in the last subperiod is 2.4 times the one in the global period (-5.26 mm/year versus -2.15 mm/year), despite having the same number of rain gauges with significant trends (492).

A comparison for the remaining quarters between the last 51 years and the 106-year global period shows the noteworthy aggravation in the rainfall decrease in Q1 (-6.00 mm/year versus -2.15 mm/year) and in the increase of the number of rain gauges with significant trends for both Q3 (372 versus 193) and Q4 (127 versus 73). In these two last quarters, an aggravation in the rainfall decrease also occurs (with absolute values of the trends approx. 2.6 and 3.2 times more, respectively), although with less pronounced decreases in terms of the rainfall itself.

Regarding the semesters, the ratio between average trends in the last 51 years and in the global period is approx. 2.4, clearly showing more pronounced rainfall decreases. The aggravation in the rainfall decrease in S1 (-8.74 mm/year versus -3.61 mm/year) and the increase in the number of rain gauges with

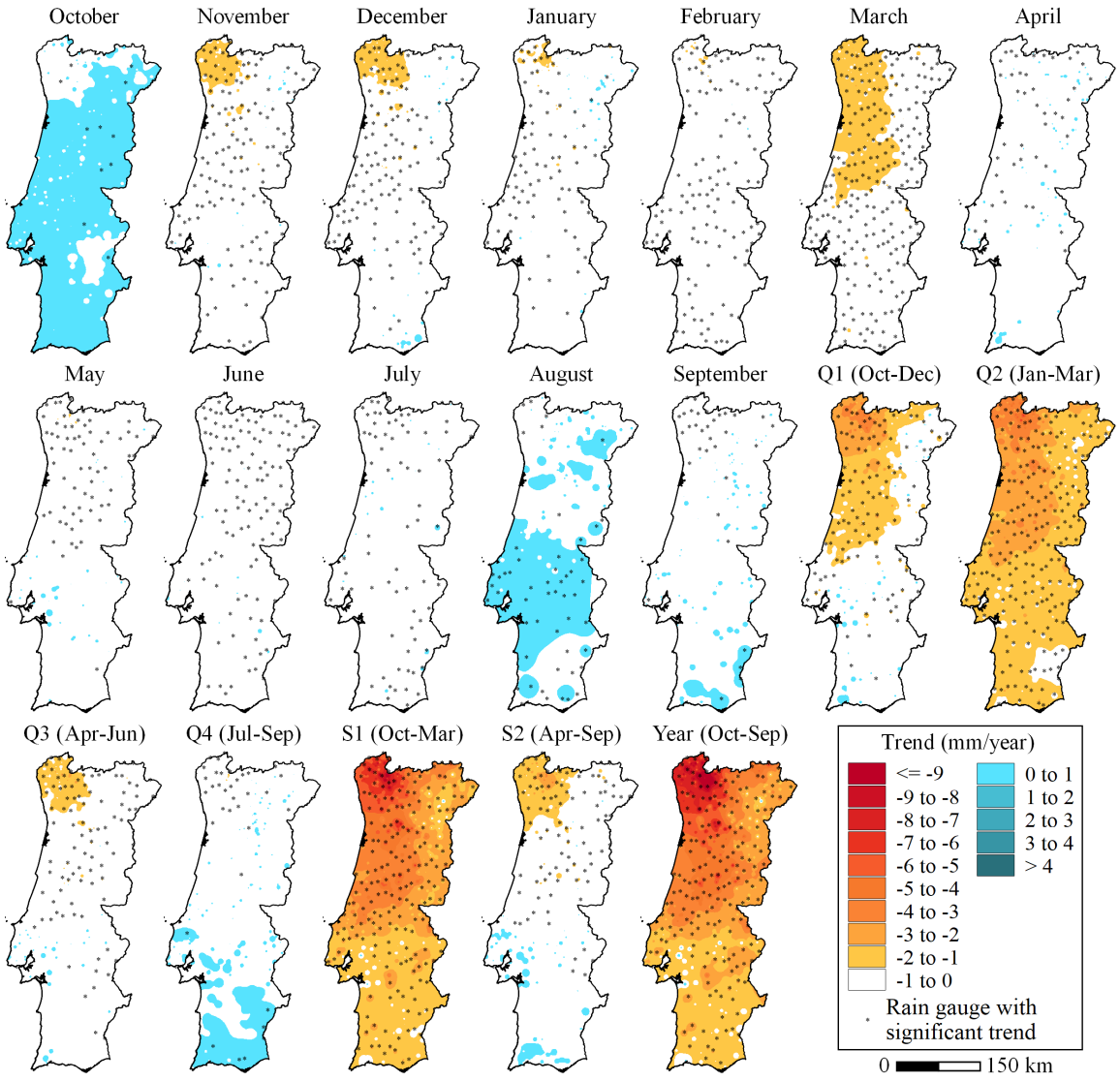

Figure A-6: Spatial distribution of the Sen's slope for the monthly, quarterly (Q1 to Q4), semi-annual (S1 and S2) and annual rainfall in the global period, from 1913/1914 to 2018/2019 (106 years). Only the rain gauges with significant trends are schematically located in the maps.

significant trends in S2 (399 versus 189) should also be stressed. The comparison for the annual rainfall shows an increase in the number of rain gauges with significant trends (505 versus 428 rain gauges) and an aggravation in the averages of those trends (-11.42 mm/year versus -4.27 mm/year).

A.3.3 Sequential variability of the rainfall

To understand the intra-annual behaviour of the rainfall, a complementary approach, namely the simple moving average technique, was applied to the weighted rainfalls at the 532 rain gauges for the different timescales based on a running length of $n = 30$ years. The weight assigned to each rain gauges was given by the Voronoi or Thiessen polygons [441, 397]. For the global period of 106 years, the number of moving averages for each time scale is $106 - 30 + 1 = 77$.

The moving average technique allows smoothening out short-term fluctuations and to highlight longer-term trends or cycles in a long temporal series [212]. Periods of 30 years (as considered for the running

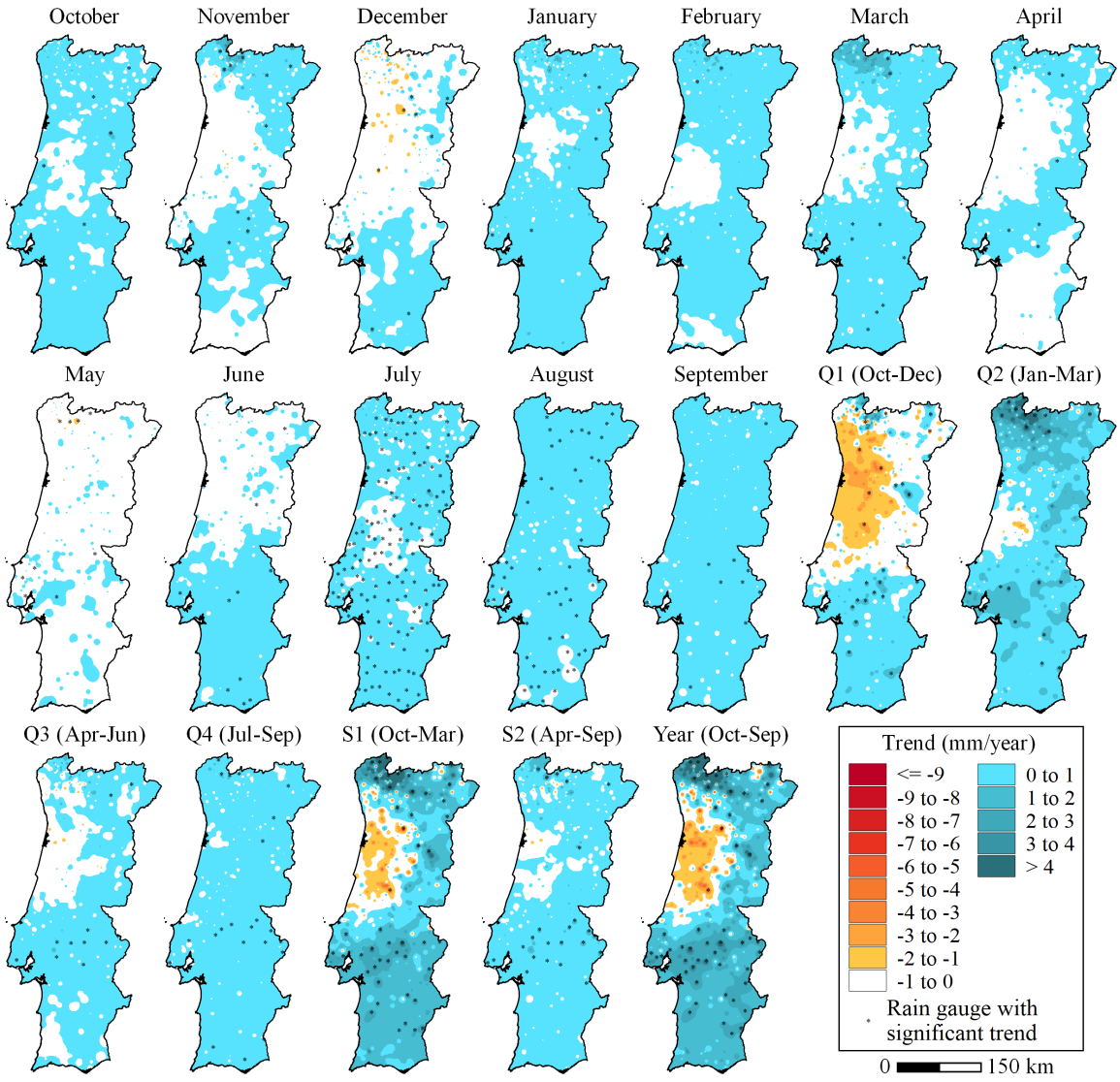

Figure A-7: Spatial distribution of the Sen's slope for the monthly, quarterly (Q1 to Q4), semi-annual (S1 and S2) and annual rainfall in the initial subperiod, from 1913/1914 to 1967/1968 (55 years). Only the rain gauges with significant trends are schematically located in the maps.

length) are also adopted in the computation of the climatological standard normals aiming at to ascertain the climatic conditions likely to be experienced in a given location [491, 494].

Figure A-9 shows the results for the six initial months, the quarters, and the semesters of the hydrological year, and for this year itself. The results for the months of the dry semester, from April to September, were not represented due to their small contribution to the annual rainfall amount (approx. 26%). The rainfalls at the different timescales were made comparable by dividing them by the mean annual rainfall of 961 mm presented in Figure A-4. In Figure A-9 each moving average was assigned to the first civil year of the 16th hydrological year of the corresponding 30-year period (first moving average from 1913/1914 to 1942/1943 assigned to 1928 and last moving average from 1989/90 to 2019/2019 assigned to 2004).

For the quarterly, semi-annual and annual timescales, Figure A-9 shows the decreasing behavior of the rainfall towards the present. The downward trends are particularly marked in the wet season (Q1,

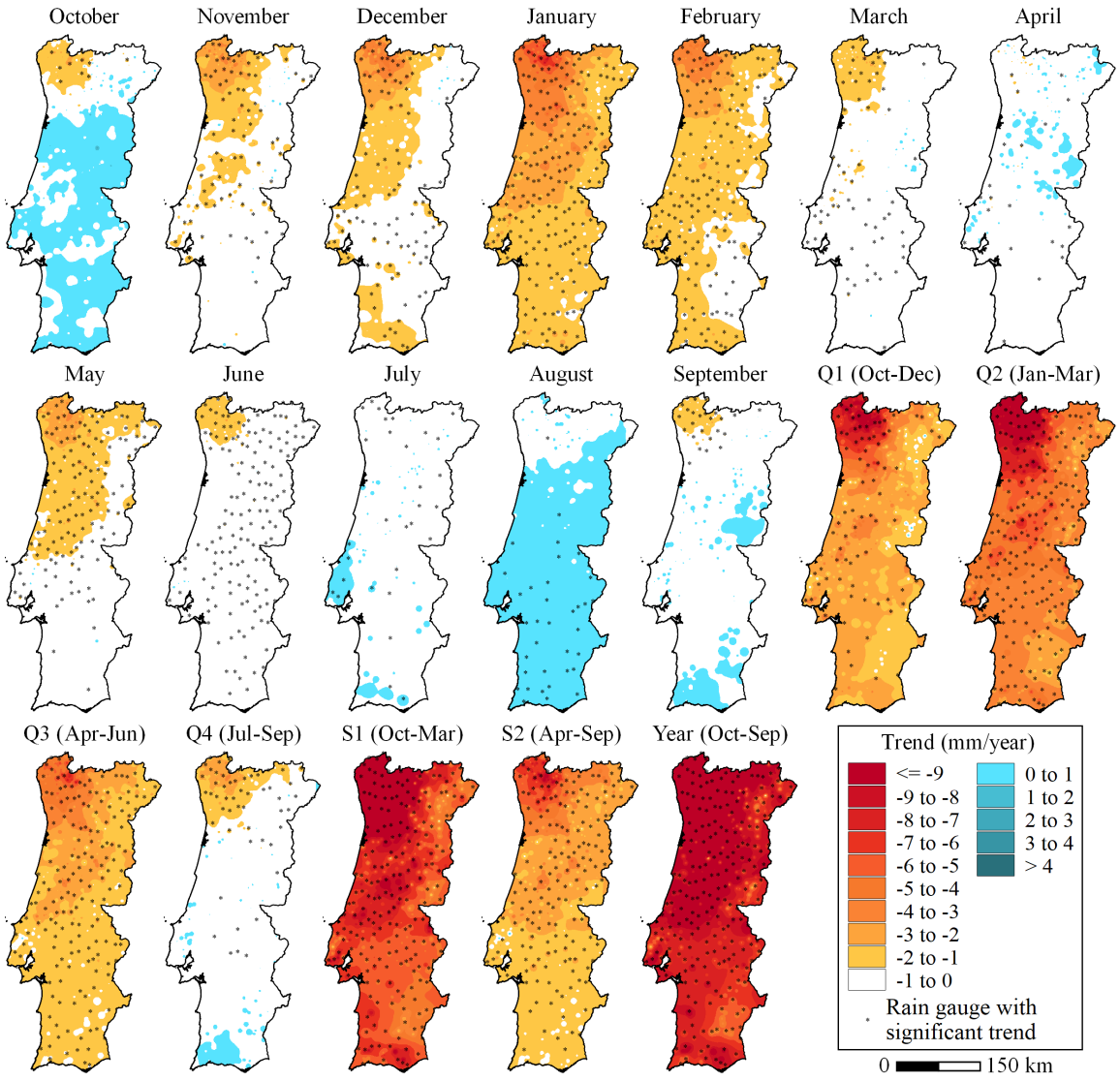

Figure A-8: Spatial distribution of the Sen's slope for the monthly, quarterly (Q1 to Q4), semi-annual (S1 and S2) and annual rainfall in the final subperiod, from 1968/1969 to 2018/2019 to (51 years). Only the rain gauges with significant trends are schematically located in the maps.

Q2 and S1), which explains the trends at the annual level. Due to the prevailing Mediterranean-type climatic conditions in Portugal, the wet season rainfall amount is the determining factor in the water budgets of the hydrological cycle, namely in terms of the natural and artificial storage replenishment. This season also plays a key role in triggering drought episodes, because the environmental and socio-economic systems are not prepared for an unexpected lack of winter rainfall, although they are to cope with the natural summer dryness [383].

The last three months of the wet season (i.e., Q2, from January to March) bring out new insights into the previous behavior. In fact, the rainfall decrease in March — particularly noticeable in the moving averages of the 30-year periods from 1940/1941 on — seems to have stabilised after the periods starting in 1970/1971, albeit with much smaller values than the long-term historical average. The pronounced decreasing rainfall tendency in March seems to have "moved" backwards affecting the months of January and February. Such "displacement" is particularly evident in the moving averages starting on the late

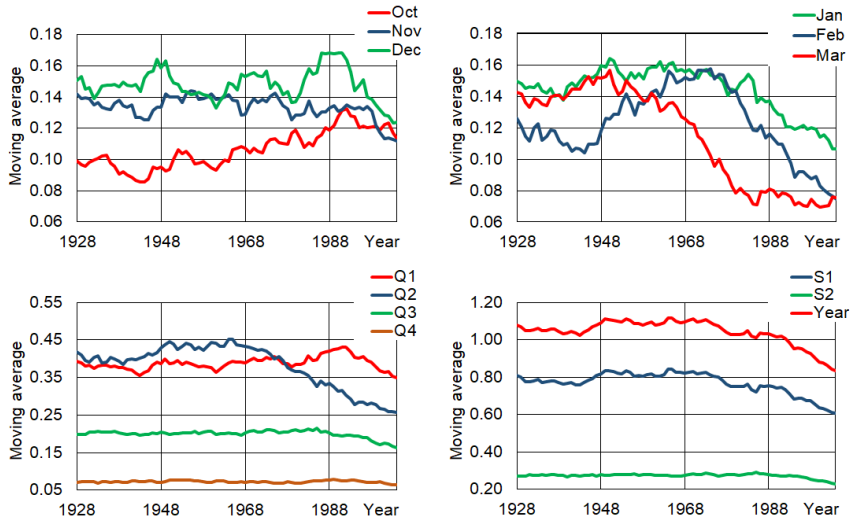

Figure A-9: Dimensionless moving average of the rainfall in different periods of the year, from 1913/1914 on, for a running length of 30 years. Each moving was made dimensionless by reference to the mean annual rainfall and assigned to the first civil year of the 16th hydrological year of the corresponding 30-year period.

years (in the case of January) and on the early years (in the case of February) of the decade beginning in 1970/1971, clearly indicating that the intra-annual rainfall pattern is changing. These downward trends seem to be sustained in recent years, resulting, for instance, in an average rainfall from January to March in the last 30-year period (1989/1990 to 2018/2019) of 246 mm, i.e., ca. 71% of the long-term average of 348 mm and 61% of the average of 402 mm in the first 30-year period of the moving averages (1913/1914 to 1942/1943). The more pronounced decreasing trends detected for the final subperiod, from 1967/1968 on (Figure A-8), are also visible in the moving averages along the same period, which in Figure A-9 are assigned to the years from 1982 on (i.e., 1967+15).

For each of the months from January to March, during which the intra-annual pattern of the rainfall is changing, an additional analysis was done based on the moving averages of the rainfalls at the set of 532 individual rain gauges instead of considering only spatially weighted rainfalls. In this respect, each set of 532 moving averages referred to the same year (from 1913/1914 to 1989/1990, starting years of the first and last 30-year moving averages, respectively) was characterised by the corresponding median, average, and empirical quantiles for the non exceedance probabilities of 5% (Q5%), and 95% (Q95%), as shown in Figure A-10. The average curves of this figure coincide with those of Figure A-9.

For any month of Figure A-10, there is always a great dispersion of the moving average values in the set of 532 rain gauges. Along the years, the averages are always higher than the corresponding medians, and the Q95% values are much higher than the averages, while the Q5% values are closer to the averages. This means that (i) the data is skewed to the left, (ii) there is a long tail of low scores on the right side of the empirical distributions, and (iii) there are a few exceptional high values "pushing up" the averages. The results for the set of 532 rain gauges confirm the behaviour towards the present previously stressed for March, i.e., a stabilising tendency around much smaller values than the long-term averages. For February and January, it is also notorious a "dynamic" behaviour, with markedly decreasing tendencies which are apparently still ongoing and with no further stabilisation. The figure also shows that the

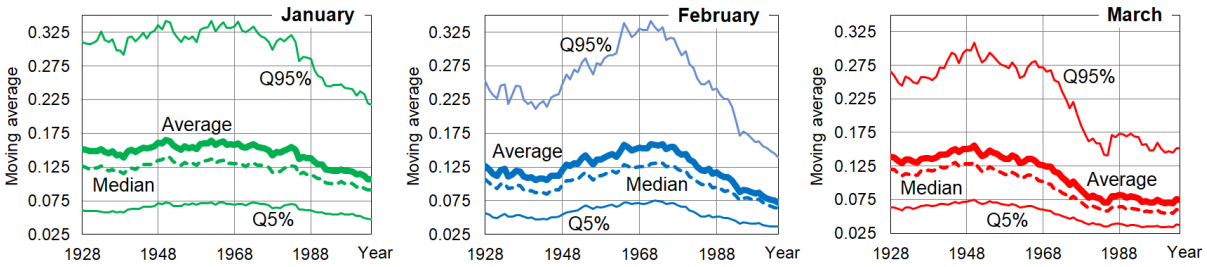

Figure A-10: Median, mean and empirical quantiles for the non-exceedance probabilities of 5% (Q5%) and 95% (Q95%) of the dimensionless moving averages of the rainfall in January, February and March, from 1913/1914 on, at the 532 rain gauges (running length of 30 years). Each moving was made dimensionless by reference to the average of the mean annual rainfalls and assigned to the first civil year of the 16th hydrological year of the corresponding 30-year period.

amplitude between the quantiles Q95% and Q5% is consistently decreasing as the moving averages relate to more recent periods. Such decrease indicates less variability in the rainfall behaviour within the set of 532 rain gauges, and accordingly, less uncertainty in the overall expected decrease of the rainfall over Portugal.

A.4 Discussion and conclusions

Understanding past rainfall variations and being able to anticipate the expected rainfall changes over different time-scales are of utmost importance because the hydrological processes driven by the rainfall (e.g., evapotranspiration and surface and ground water flow) affect the whole water resources system. The analysis of ground-based rainfall observations can help to comply with such purposes given the corresponding series are updated, long enough [75], and supported by a dense monitoring network able of describing the spatial rainfall variability [152]. This is the case of the present research work which, at the authors' best knowledge, represents the most thorough and comprehensive study on rainfall trends over mainland Portugal, using ground-based data, addressing the long-term monthly, seasonal and annual rainfall changes and the recent rainfall trends dynamics.

This study shows that in the last five decades the rainfall has been markedly decreasing over mainland Portugal. Such decrease has been progressively affecting the more contributing months of the wet season, in absolute terms but also with regard to their relative contribution to annual rainfall, thus strongly conditioning the intra-annual rainfall pattern. This behaviour is particularly pronounced before the long dry season start, i.e., in the last wet period of the hydrological year (Q2, January to March), a fundamental period for the replenishing of the water, both in the soil and in the artificial reservoirs. The analysis of the set of 532 rain gauges throughout the 106-year period showed that the amplitude of the rainfall decrease has gradually narrowed, meaning less uncertainty about its behaviour.

When considering the global 106-year period, but especially the most recent 51-year subperiod, from 1968/1969 on (Figures A-5 and A-8), the study revealed a coherent monthly spatial pattern of the trends, with each month showing almost a same rainfall trend over the country. For the months of the rainy season, except for October, the trends are consistently negative. Such homogeneous behaviour indicates the vulnerability of the country to the rainfall decrease given it is not expected that some regions may

become wetter, thus counterbalancing those becoming drier.

To understand the relevance of the previous vulnerability, rainfall anomalies were assigned to each rain gauge and spatially represented based on the cubic spline interpolation (Figure A-11). In each rain gauge, the anomaly was defined as the mean annual rainfall in the last 51 years minus the mean annual rainfall in the initial 55 years. Each anomaly was expressed in absolute terms (Figure A-11a) and made dimensionless (Figure A-11b), by dividing by the average in the initial period (dimensionless anomaly relative to the 55-year initial period).

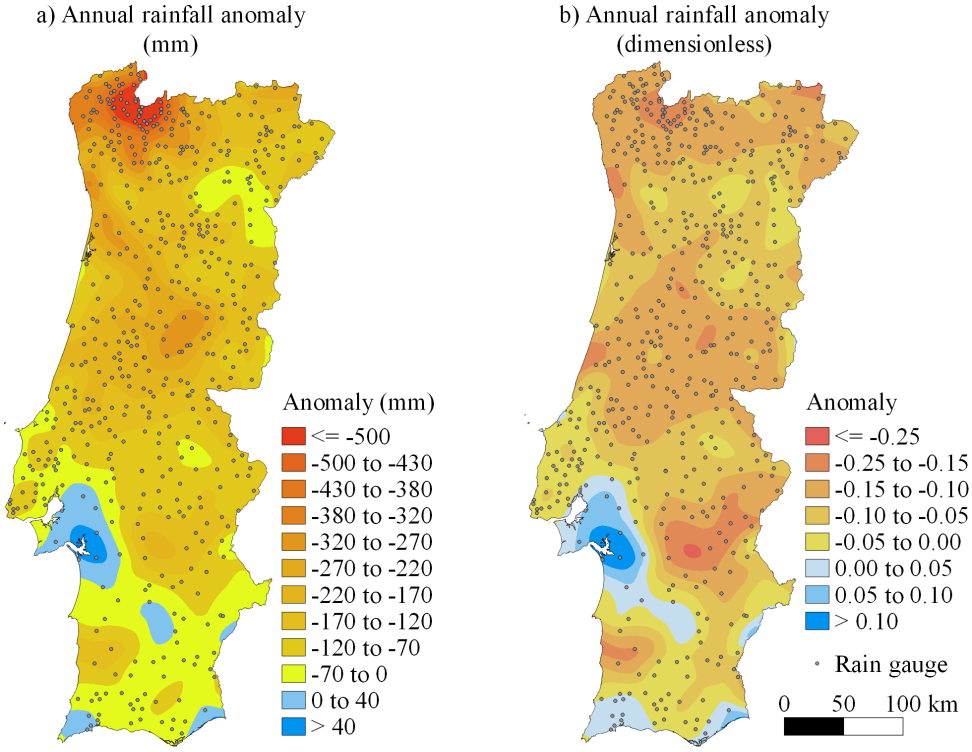

Figure A-11: Mean annual rainfall anomalies: difference between mean annual rainfalls in the 51-year subperiod, from 1968/16969 to 2018/2019, and in the 55-year period, from 1913/14 to 1967/1968 (left side); previous difference relative to the mean annual rainfall in the 55-year initial period (right side)

Figure A-11a shows that, except for very small regions, the country experienced a mean annual rainfall decrease from one subperiod to another above 120 mm. In the northwest wettest region such decreases exceeds 500 mm. Figure A-11b allows to understand the relevance of the magnitude of those results. It shows that a same dimensionless rainfall reduction affects both wetter and drier regions meaning that some of these last regions are becoming much drier than the former ones. Such behaviour reinforces the difference between a less wet, yet wetter, north and a definitely drier arid south. This agrees with the findings of the global assessment of wetting/drying trends during the period 1948–2005 of Greve et al. [163] that identified the southwest regions of the Iberian Peninsula as one hot spot of the pattern "dry gets drier" (the DD paradigm).

The recent rainfall reduction, from late 1960 on, depicted in Figure A-11, agrees with the widespread drying tendency across North Africa and southern Europe, extending from the Atlantic coast to the Middle East, detected by Hoerling et al. [188] when comparing the periods 1902–1970 and 1971–2010.

The rainfall tendency to decrease in subtropical latitudes mentioned in some IPCC reports [255, 310,

31], has been verified in this case for Portugal despite the complex spatial and temporal rainfall distribution. This agreement was achieved with the use of spatially-dense long-running rainfall series rarely available with the necessary resolution compared to general low resolution global atmosphere reanalysis datasets — such as the Multi-Source Weighted-Ensemble Precipitation (MSWEP) global dataset from 1979 to 2015 [34]. Although ground-based rainfall data analysis and reanalysis normally exhibit differences due to the different inferential processes and resolution [307], a comparison between the here obtained trends and those via global models' reanalysis datasets [361], shows a consistent rainfall reduction from December to March in recent years. However, these findings need to be interpreted with caution depending on the data source used. The results for the final subperiod are also in accordance to a study based on downscaling [82], denoting a significant decrease in the rainfall amount in certain regions of the Iberian Peninsula during the last third of the 20^{th} century.

Despite it is difficult to make a global synthesis of the results obtained from the different observation periods, data, methods implemented, etc., there is prima-facie evidence about the generalised rainfall decrease in Portugal. This is reinforced by the global evidence, based on likely emission scenarios [65], of a future with less fresh water availability in subtropical latitudes. It also stresses the urge for widespread public awareness and participation towards common water-saving practices. Public participation is a key factor, also because it calls for updated information and political commitment towards the implementation of mitigation and adaptation measures and of new water resources planning and management policies. Both challenges are presently far from being achieved for mainland Portugal [51].